

1 LEVERAGING MULTI-MESSENGER ASTROPHYSICS FOR DARK MATTER SEARCHES

By

Daniel Nicholas Salazar-Gallegos

A DISSERTATION

Submitted to
Michigan State University
in partial fulfillment of the requirements
for the degree of

Physics—Doctor of Philosophy
Computational Mathematics in Science and Engineering—Dual Major

Today

ABSTRACT

3 I did Dark Matter with HAWC and IceCube. I also used Graph Neural Networks

⁴ Copyright by

⁵ DANIEL NICHOLAS SALAZAR-GALLEGOS

⁶ Today

ACKNOWLEDGMENTS

8 I love my friends. Thanks to everyone that helped me figure this out. Amazing thanks to the people
9 at LANL who supported me. Eames, etc Dinner Parties Jenny and her child Kaydince Kirsten, Pat,
10 Andrea Family. You're so far but so critical to my formation. Unconditional love. Roommate

TABLE OF CONTENTS

12	LIST OF TABLES	vii
13	LIST OF FIGURES	viii
14	LIST OF ABBREVIATIONS	xvi
15	CHAPTER 1 INTRODUCTION	1
16	CHAPTER 2 DARK MATTER IN THE COSMOS	2
17	2.1 Introduction	2
18	2.2 Dark Matter Basics	3
19	2.3 Evidence for Dark Matter	4
20	2.4 Searching for Dark Matter: Particle DM	11
21	2.5 Sources for Indirect Dark Matter Searches	16
22	2.6 Multi-Messenger Dark Matter	18
23	CHAPTER 3 HIGH ALTITUDE WATER CHERENKOV (HAWC) OBSERVATORY	21
24	3.1 The Detector	21
25	3.2 Events Reconstruction and Data Acquisition	21
26	3.3 Remote Monitoring	21
27	CHAPTER 4 ICECUBE NEUTRINO OBSERVATORY	22
28	4.1 The Detector	22
29	4.2 Events Reconstruction and Data Acquisition	22
30	4.3 Northern Test Site	22
31	CHAPTER 5 GLORY DUCK: MULTI-WAVELENGTH SEARCH FOR DARK MATTER ANNIHILATION TOWARDS DWARF SPHEROIDAL GALAXIES	23
32	5.1 Introduction	23
33	5.2 Dataset and Background	25
34	5.3 Analysis	26
35	5.4 Likelihood Methods	31
36	5.5 HAWC Results	37
37	5.6 Glory Duck Combined Results	40
38	5.7 HAWC Systematics	45
39	5.8 J -factor distributions	46
40	5.9 Discussion and Conclusions	52
43	CHAPTER 6 MULTITHREADING HAWC ANALYSES FOR DARK MATTER SEARCHES	56
44	6.1 Introduction	56
45	6.2 Dataset and Background	56
46	6.3 Analysis	58

48	6.4 Likelihood Methods	61
49	6.5 Computational Methods: Multithreading	62
50	6.6 Analysis Results	68
51	6.7 Systematics	73
52	6.8 Conclusion and Discussion	73
53	CHAPTER 7 HEAVY DARK MATTER ANNIHILATION SEARCH WITH ICE-CUBE'S NORTH SKY TRACK DATA	75
54		
55	7.1 Introduction	75
56	7.2 Dataset and Background	76
57	7.3 Analysis	77
58	7.4 Likelihood Methods	85
59	7.5 Background Simulation	86
60	CHAPTER 8 NU DUCK	105
61	APPENDIX A MULTI-EXPERIMENT SUPPLEMENTARY FIGURES	106
62	APPENDIX B MULTITHREADING DARK MATTER ANALYSES SUPPLEMENTARY MATERIAL	107
63		
64	B.1 Remaining Spectral Models	107
65	B.2 <code>mpu_analysis.py</code>	108
66	B.3 Comparison with Glory Duck	117
67	APPENDIX C ICECUBE HEAVY DARK MATTER ANALYSIS SUPPLEMENTARY MATERIAL	120
68		
69	C.1 Docker Image for Oscillating Neutrino Spectra	120
70	C.2 Spline Fitting Statuses	123
71	C.3 Full Test statistic Background Simulation Per Source	124
72	BIBLIOGRAPHY	125

LIST OF TABLES

<p>74 Table 5.1 Summary of the relevant properties of the dSphs used in the present work. Column 1 lists the dSphs. Columns 2 and 3 present their heliocentric distance and galactic coordinates, respectively. Columns 4 and 5 report the J-factors of each source given from the \mathcal{GS} and \mathcal{B} independent studies and their estimated $\pm 1\sigma$ uncertainties. The values $\log_{10} J$ (\mathcal{GS} set) [45] correspond to the mean J-factor values for a source extension truncated at the outermost observed star. The values $\log_{10} J$ (\mathcal{B} set) [47] are provided for a source extension at the tidal radius of each dSph. Bolded sources are within HAWC's field of view and provided to the Glory Duck analysis.</p> <p>83 Table 5.2 Summary of dSph observations by each experiment used in this work. A ‘-’ indicates the experiment did not observe the dSph for this study. For Fermi-LAT, the exposure at 1 GeV is given. For HAWC, $\Delta\theta$ is the absolute difference between the source declination and HAWC latitude. HAWC is more sensitive to sources with smaller $\Delta\theta$. For IACTs, we show the zenith angle range, the total exposure, the energy range, the angular radius θ of the signal or ON region, the ratio of exposures between the background-control (OFF) and signal (ON) regions (τ), and the significance of gamma-ray excess in standard deviations, σ.</p> <p>92 Table 6.1 Summary of the relevant properties of the dSphs used in the present work. Column 1 lists the dSphs. Columns 2 and 3 present their heliocentric distance and galactic coordinates, respectively. Column 4 reports the J-factors of each source given from the \mathcal{LS} studies and estimated $\pm 1\sigma$ uncertainties. The values $\log_{10} J$ (\mathcal{LS} set) [65] correspond to the mean J-factor values for a source extension truncated at 0.5°.</p> <p>98 Table 6.2 Timing summaries for analyses for serial and multithreaded processes. M tasks is the number of functional-parallel tasks ran for the computation. $T_{p,c}$ is a single run time in hours:minutes:seconds for runs utilizing p nodes and c threads. Runs are run interactively on the same computer to maximize consistency. Empty entries are indicated with ‘-’. (.) entries are estimated entries extrapolated from data earlier in the column.</p> <p>104 Table 6.3 Speed up summaries for analyses for serial and multithreaded processes. M tasks is the number of functional-parallel tasks ran for the computation. $S_{p,c}$ is a single speedup comparison for runs utilizing p nodes and c threads. $[\cdot]$ are the estimated speedups calculated from Tab. 6.2, Eq. (6.10), and Eq. (6.5). Empty entries are indicated with ‘-’.</p> <p>109 Table 7.1 TODO: fill me daddy</p> <p>110 Proof I know how to include</p>	<p>31</p> <p>32</p> <p>62</p> <p>66</p> <p>66</p> <p>68</p> <p>83</p>
--	---

111

LIST OF FIGURES

112	Figure 2.1	Rotation curve fit to NGC 6503 from [7]. Dashed line is the contribution 113 from visible matter. Dotted curves are from gas. Dash-dot curves are from 114 dark matter (DM). Solid line is the composite contribution from all matter 115 and DM sources. Data are indicated with bold dots with error bars. Data 116 agree strongly with a matter + DM composite prediction.	5
117	Figure 2.2	Light from distant galaxy is bent in unique ways depending on the distribution 118 of mass between the galaxy and Earth. Yellow dashed lines indicate where 119 the light would have gone if the matter were not present [8].	7
120	Figure 2.3	(left) Optical image of galactic cluster 1E0657-558. (right) X-ray image of the 121 cluster with redder meaning hotter and higher baryon density. (both) Green 122 contours are reconstruction of gravity contours from weak lensing. White 123 rings are the best fit mass maxima at 68.3%, 95.5%, and 99.7% confidence. 124 The matter maxima of the clusters are clearly separated from x-ray maxima. [9]	8
125	Figure 2.4	Plank CMB sky. Sky map features small variations in temperature in primor- 126 dial light. These anisotropies are used to make inferences about the universe's 127 energy budget and developmental history. [10]	9
128	Figure 2.5	Observed Cosmic Microwave Background power spectrum as a function of 129 multipole moment from Plank [10]. Blue line is best fit model from Λ CDM. 130 Red points and lines are data and error, respectively.	10
131	Figure 2.6	Predicted power spectra of CMB for different $\Omega_m h^2$ values for fixed baryon 132 density from [11]. (left) Low $\Omega_m h^2$ increases the prominence of first and 133 second peaks. (middle) $\Omega_m h^2$ is most similar to the observed power spectrum. 134 The second and third peaks are similar in height. (right) $\Omega_m h^2$ is large which 135 suppresses the first peak and raises the prominence of the third peak.	10
136	Figure 2.7	The Standard Model (SM) of particle physics. Figure taken from http://www.quantumdiaries.org/2014/03/14/the-standard-model-a-beautiful-but-flawed-theory/	12
139	Figure 2.8	Simplified Feynman diagram demonstrating with different ways DM can 140 interact with SM particles. The 'X's refer to the DM particles whereas the 141 SM refer to fundamental particles in the SM. The large circle in the center 142 indicates the vertex of interaction and is purposely left vague. The colored 143 arrows refer to different directions of time as well as their respective labels. 144 The arrows indicate the initial and final state of the DM -SM interaction in time.	13

145	Figure 2.9 A single jet event in ATLAS detector from 2017 [16]. Jet momentum was 146 observed to be 1.9 TeV. Missing transverse momentum was observed to be 147 1.9 TeV compared to the initial transverse momentum of the event was 0. 148 Implied MET is traced by a red dashed line in event display.	14
149	Figure 2.10 More detailed pseudo-Feynman diagram of particle cascade from dark matter 150 annihilation into 2 quarks. The quarks hadronize and down to stable particles 151 like γ or the anti-proton (p^-). Diagram pulled from ICRC 2021 presentation 152 on DM annihilation search [17].	15
153	Figure 2.11 Dark Matter (DM) decay spectrum for $b\bar{b}$ initial state and γ final state. Redder 154 spectra are for larger DM masses. Bluer spectra are light DM masses. x is a 155 unitless factor defined as the ratio of the mass of DM, m_χ , and the final state 156 particle energy E_γ . Figure from [19].	17
157	Figure 2.12 Different dark matter density profiles compared. Some models produce ex- 158 ceptionally large densities at small r [20].	18
159	Figure 2.13 The Milky Way Galaxy in photons (γ) and neutrinos (ν) [22]. The Galactic 160 center is at $l=0^\circ$ and is the brightest region in all panels. (top) An Optical 161 color image of the Milky Way galaxy seen from Earth. Clouds of gas and dust 162 obscure some light from stars. (2nd down) Integrated flux of γ -rays observed 163 by the Fermi-LAT telescope [23]. (middle) Expected neutrino emission 164 that corresponds with Fermi-LAT observations. (2nd up) Expected neutrino 165 emission profile after considering detector systematics of IceCube. (bottom) 166 Observed neutrino emission from region of the galactic plane. Substantial 167 neutrino emission was detected.	19
168	Figure 2.14 Dark Matter annihilation spectra for different final state particle and standard 169 model annihilation channels [24]. Photons (red), e^\pm (green), \bar{p} (blue), ν (black).	20
170	Figure 5.1 Sensitivities of five gamma-ray experiments compared to percentages of the 171 Crab nebula's emission and dark matter annihilation. Solid lines present 172 estimated sensitivities to power law spectra [FACT CHECK THIS]for each 173 experiment. Green lines are Fermi-LAT sensitivities where lighter green is 174 the sensitivity to the galactic center and dark green is its sensitivity to higher 175 declinations. Orange, red, and purple solid lines represent the MAGIC, HESS, 176 and VERITAS 50 hour sensitivities respectively. The maroon and brown lines 177 are the HAWC 1 year and 5 year sensitivities. Across four decades of gamma- 178 ray energy, these experiments have similar sensitivities on the order 10^{-12} 179 $\text{erg cm}^{-2}\text{s}^{-1}$. The dotted lines are estimated dark matter fluxes assuming 180 $m_\chi = 5 \text{ TeV}$ DM annihilating to bottom quarks (red), tau leptons (blue), 181 and W bosons (green). Faded gray lines outline percentage flux of the Crab 182 nebula. Figure is an augmented version of [25]	24

183	Figure 5.2	Effect of Electroweak (EW) corrections on expected DM annihilation spectrum for $\chi\chi \rightarrow W^-W^+$. Solid lines are spectral models that consider EW corrections. Dash-dot lines are spectral models without EW corrections. Red lines are models for $M_\chi = 1$ TeV. Blue lines represent models for $M_\chi = 100$ TeV. All models are sourced from the PPPC4DMID [44].	28
188	Figure 5.3	$\frac{dJ}{d\Omega}$ maps for Segue1 (top) and Coma Berenices (bottom). Origin is centered on the specific dwarf spheroidal galaxies (dSph). X and Y axes are the angular separation from the center of the dwarf. Plots of the remaining 11 dSph HAWC studied are linked in Fig. A.1.	30
192	Figure 5.4	Illustration of the combination technique showing a comparison between $-2 \ln \lambda$ provided by four instruments (colored lines) from the observation of the same dSph without any J nuisance and their sum, <i>i.e.</i> the resulting combined likelihood (thin black line). According to the test statistics of Equation (5.6), the intersection of the likelihood profiles with the line $-2 \ln \lambda = 2.71$ indicates the 95% C.L. upper limit on $\langle \sigma v \rangle$. The combined likelihood (thin black line) shows a smaller value of upper limit on $\langle \sigma v \rangle$ than those derived by individual instruments. We also show how the uncertainties on the J factor effects the combined likelihood and degrade the upper limit on $\langle \sigma v \rangle$ (thick black line). All likelihood profiles are normalized so that the global minimum $\widehat{\langle \sigma v \rangle}$ is 0. We note that each profile depends on the observational conditions in which a target object was observed. The sensitivity of a given instrument can be degraded and the upper limits less constraining if the observations are performed in non-optimal conditions such as a high zenith angle or a short exposure time.	35
207	Figure 5.5	38
208	Figure 5.6	HAWC TS values for best fit $\langle \sigma v \rangle$ versus m_χ for seven SM annihilation channels with J factors from \mathcal{GS} . The solid black line shows the combined best fit TS values. The colored, dashed lines are the TS values for each of the 13 sources HAWC studied.	39
212	Figure 5.7	HAWC Brazil bands at 95% confidence level on $\langle \sigma v \rangle$ versus DM mass for seven annihilation channels with J -factors from \mathcal{GS} [53]. The solid line represents the combined limit from 13 dSphs. The dashed line is the expected limit. The green band is the 68% containment. The yellow band is the 95% containment.	40

217	Figure 5.8	Upper limits at 95% confidence level on $\langle \sigma v \rangle$ in function of the DM mass for 218 eight annihilation channels, using the set of J factors from Ref. [53] (\mathcal{GS} set 219 in Table 5.1). The black solid line represents the observed combined limit, 220 the black dashed line is the median of the null hypothesis corresponding 221 to the expected limit, while the green and yellow bands show the 68% and 222 95% containment bands. Combined upper limits for each individual detector 223 are also indicated as solid, colored lines. The value of the thermal relic 224 cross-section in function of the DM mass is given as the red dotted-dashed 225 line [54].	41
226	Figure 5.9	Same as Fig. 5.8, using the set of J factors from Ref. [47, 55] (\mathcal{B} set in Table 5.1).	42
227	Figure 5.10	Comparisons of the combined limits at 95% confidence level for each of the 228 eight annihilation channels when using the J factors from Ref. [53] (\mathcal{GS} set in 229 Table 5.1), plain lines, and the J factor from Ref. [47, 55] (\mathcal{B} set in Table 5.1), 230 dashed lines. The cross-section given by the thermal relic is also indicated [54].	44
231	Figure 5.11	Comparisons of the combined limits at 95% confidence level for a point source 232 analysis and extended source using [53] \mathcal{GS} J-factor distributions and PPPC 233 [44] annihilation spectra. Shown are the limits for Segue1 which will have 234 the most significant impact on the combined limit. 6 of the 7 DM annihilation 235 channels are shown. Solid lines are extended source studies. Dashed lines 236 are point source studies. Overall, the extended source analysis improves the 237 limit by a factor of 2.	46
238	Figure 5.12	Same as Fig. 5.11 on Coma Berenices. This dSph also contributes signifi- 239 cantly to the limit. The limits are identical in this case.	47
240	Figure 5.13	Comparison of combined limits when correcting for HAWC's pointing sys- 241 tematic. All DM annihilation channels are shown. The solid black line is the 242 ratio between published limit to the declination corrected limit. The blue solid 243 line or "Combined_og" represented the limits computed for Glory Duck. The 244 solid orange line or "Combined_ad" represented the limits computed after 245 correcting for the pointing systematic.	48
246	Figure 5.14	Differential map of dJ/Ω from model built in Section 5.8.1 and profiles 247 provided directly from authors. (Top) Differential from Segue1. (bottom) 248 Differential from Coma Berenices. Note that their scales are not the same. 249 Segue1 shows the deepest discrepancies which is congruent with its large 250 uncertainties. Both models show anuli where unique models become apparent.	49

251	Figure 5.15 HAWC limits for Coma Berenices (top) and Segue1 (bottom) for two different 252 map sets. Blue lines are limits calculated on maps with poor model repre- 253 sentation. Orange lines are limits calculated on spatial profiles provided by 254 the authors of [45]. Black line is the ratio of the poor spatial model limits to 255 the corrected spatial models. The left y-axis measures $\langle\sigma v\rangle$ for the blue and 256 orange lines. The right y-axis measures the ratio and is unitless.	50
257	Figure 5.16 Comparisons between the J -factors versus the angular radius for the com- 258 putation of J factors from Ref. [53] (\mathcal{GS} set in Table 5.1) in blue and for 259 the computation from Ref. [47, 55] (\mathcal{B} set in Tab. 5.1) in orange. The solid 260 lines represent the central value of the J -factors while the shaded regions 261 correspond to the 1σ standard deviation.	53
262	Figure 5.17 Comparisons between the J -factors versus the angular radius for the computa- 263 tion of J factors from Ref. [53] (\mathcal{GS} set in Tab. 5.1) in blue and for the 264 computation from Ref. [47, 55] (\mathcal{B} set in Tab. 5.1) in orange. The solid 265 lines represent the central value of the J -factors while the shaded regions 266 correspond to the 1σ standard deviation.	54
267	Figure 6.1 Difference between spectral hypotheses from PPPC [44] and HDM [64]. 268 Shown is the expected DM annihilation spectrum for $\chi\chi \rightarrow W^-W^+$. Solid 269 lines are spectral models with EW corrections from the PPPC. Dash-dot lines 270 are spectral models from HDM. Red lines are models for $M_\chi = 1$ TeV. Blue 271 lines represent models for $M_\chi = 100$ TeV.	59
272	Figure 6.2 Photon spectra for $\chi\chi \rightarrow \gamma\gamma$ (left) and $\chi\chi \rightarrow ZZ$ (right) after Gaussian 273 convolution of line features. Both spectra have δ -features at photon energies 274 equal to the DM mass. Bluer lines are annihilation spectra with lower DM 275 mass. Redder lines are spectra from larger DM mass. All Spectral models are 276 sourced from the Heavy Dark Matter models [64]. Axes are drawn roughly 277 according to the energy sensitivity of HAWC.	60
278	Figure 6.3 $\frac{dJ}{d\Omega}$ maps for Coma Berenices, Draco, Segue1, and Sextans. Columns are 279 divided for the $\pm 1\sigma$ uncertainties in $dJ/d\Omega$ around the mean value from \mathcal{LS} 280 [65]. Origin is centered on the specific dwarf spheroidal galaxies (dSph). θ 281 and ϕ axes are the angular separation from the center of the dwarf	61
282	Figure 6.4 Infographic on how jobs and DM computation was organized in Section 5.3. 283 Jobs were built for each permutation of CHANS and SOURCES shown by the 284 left block in the figure. Each job, which took on the order 2 hrs to compute, 285 had the following work flow: 1. Import HAWC analysis software, 2 min to 286 run. 2. Load HAWC count maps, 5 min to run. 3. Load HAWC energy and 287 spatial resolutions, 4 min. 5. Load DM spatial source templates and spectral 288 models, less than 1 s. 6. Perform likelihood fit on data and model, about 8 289 min per DM mass. 7. Write results to file, less than 1s.	63

290	Figure 6.5	Graphic of Gustafson parallel coding pattern. f_s is the fraction of a program, in time, spent on serial computation. f_p is the fraction of computing time that is parallelizable. T_p is the total time for a parallel program to run. T_1 is the total time for a parallel program to run if only 1 processor is allocated. P_N is the N -th processor where it's row is the computation the processor performs. The Gustafson pattern is most similar to what is implemented for this analysis. Figure is pulled from [67].	64
297	Figure 6.6	Task chart for one multithreaded job developed for this project. Green blocks indicate a shared resource across the threads AND computation performed serially. Red blocks indicate functional parallel processing within each thread. 3 threads are represented here, yet many more can be employed during the full analysis. Jobs are defined by the SOURCE as these require unique maps to be loaded into the likelihood estimator. The m_χ , CHAN, and $\langle\sigma v\rangle$ variables are entered into the thread pool and allocated as evenly as possible across the threads.	66
305	Figure 6.7	HAWC upper limits at 95% confidence level on $\langle\sigma v\rangle$ versus DM mass for $\chi\chi \rightarrow b\bar{b}, t\bar{t}, u\bar{u}, d\bar{d}, s\bar{s}, c\bar{c}, gg, W^+W^-$, and hh . Limits are with \mathcal{LS} J - factors [65]. The solid line represents the observed combined limit. Dashed lines represent limits from individual dSphs.	69
309	Figure 6.8	HAWC upper limits at 95% confidence level on $\langle\sigma v\rangle$ versus DM mass for $\chi\chi \rightarrow \nu_e\bar{\nu}_e, \nu_\mu\bar{\nu}_\mu, \nu_\tau\bar{\nu}_\tau, e\bar{e}, \mu\bar{\mu}, \tau\bar{\tau}, \gamma\gamma$ and ZZ . Limits use \mathcal{LS} J factors [65]. The solid line represents the observed combined limit. Dashed lines represent limits from individual dSphs.	70
313	Figure 6.9	HAWC TS values for best fit $\langle\sigma v\rangle$ versus m_χ for SM annihilation channels: $\chi\chi \rightarrow b\bar{b}, t\bar{t}, u\bar{u}, d\bar{d}, s\bar{s}, c\bar{c}, gg, W^+W^-$, and hh . Limits use \mathcal{LS} J factors. The solid black line shows the combined best fit TS values. The colored, dashed lines are the TS values from each dSph.	71
317	Figure 6.10	HAWC TS values for best fit $\langle\sigma v\rangle$ versus m_χ for SM annihilation channels: $\chi\chi \rightarrow \nu_e\bar{\nu}_e, \nu_\mu\bar{\nu}_\mu, \nu_\tau\bar{\nu}_\tau, e\bar{e}, \mu\bar{\mu}, \tau\bar{\tau}, \gamma\gamma$ and ZZ . Limits use \mathcal{LS} J factors. The solid black line shows the combined best fit TS values. The colored, dashed lines are the TS values from each dSph.	72
321	Figure 6.11	Comparison of HAWC limits from this analysis to Glory Duck (Fig. 5.5) for 3 dSphs and 3 SM annihilation channels: $b\bar{b}, \tau\bar{\tau}$, and $e\bar{e}$. Each sector shows the 95% confidence limit from Glory Duck (blue line) and this analysis (orange line) in the top plot. The lower plot features the ratio in log scale of Glory Duck to this analysis in a red solid line. Horizontal dashed lines are for ratios of 1.0 (black) and $\sqrt{2}$ (blue). Ratios larger than 1.0 are for limits smaller, or stricter, than Glory Duck. Ratios larger than $\sqrt{2}$ indicates limits are stricter than a simple doubling of the Glory Duck data.	74

329	Figure 7.1	Neutrino spectra at production (left panels) and after oscillation at Earth 330 (right panels). Blue, orange, and green lines are the ν_e , ν_μ , and ν_τ spectra 331 respectively. Top panels show the spectra in $\frac{dN}{dE}$. Lower panels plot the flavor 332 ratio to $\nu_e + \nu_\mu + \nu_\tau$. SM annihilation channels $b\bar{b}$, $\tau\bar{\tau}$, and $\nu_\mu\bar{\nu}_\mu$ are shown 333 for $M_\chi = 1$ PeV, TeV, and EeV.	79
334	Figure 7.2	Signal recovery for 100 TeV DM annihilation into $\nu_\mu\bar{\nu}_\mu$ for a source at Dec 335 = 16.06°. n_{inj} is the number of injected signal events in simulation. n_s is 336 the number of reconstructed signal events from the simulation. Although 337 the uncertainties are small and tight, the reconstructed n_s are systematically 338 underestimated.	80
339	Figure 7.3	Top left panel shows the two kernels overlayed the original spectrum from 340 Charon. delta I is the difference in the integral of the peaks with respect to the 341 original spectrum. The vertical red line indicated where the original neutrino 342 line is maximized. Lower right shows the signal recovers of the DM model 343 using the Gaussian kernel with parameters enumerated above.	81
344	Figure 7.4	Example spline that failed the fit. Failed splined are corrected on a case by 345 case basis unless the SM channel has a systematic problem fitting the splines. 346 In this case, I made a bookkeeping error and loaded the incorrected neutrino 347 flavor	83
348	Figure 7.5	Summary of input spectral models that were smoothed with Gaussian kernel. 349 Spectral models are for $\chi\chi \rightarrow e\bar{e}$, $\mu\bar{\mu}\tau\bar{\tau}$, $\nu_e\bar{\nu}_e$, $\nu_\mu\bar{\nu}_\mu$, and $\nu_\tau\bar{\nu}_\tau$. These spectra 350 are the composite ($\nu_\mu + \nu_\tau$) of neutrino flavors. Every spectral model used for 351 this analysis is featured as a colored solid line. Bluer lines are for lower DM 352 mass spectral models. DM masses range from 681 GeV to 100 PeV. HDM 353 [64], χ arov [68], and Photospline [70] are used to generate these spectra. 354 Energy (x-axis) was chosen to roughly represent the energy sensitivity of NST. .	84
355	Figure 7.6	Test statistic (TS) distributions for Segue 1 and $\chi\chi \rightarrow b\bar{b}$. Each subplot, 356 except the final, is the TS distribution for a specific DM mass listed in the 357 subplot. Orange dashed lines are the traces for a χ^2 distribution with 1 degree 358 of freedom. $\epsilon[\cdot]$ is the fraction of trials smaller than the bracketed value. The 359 final subplot plots the all DM spectral models, similar to Fig. 7.5, used as 360 input for the TS distributions.	88
361	Figure 7.7	Same as Fig. 7.6 for Segue 1 $\chi\chi \rightarrow \tau\bar{\tau}$	89
362	Figure 7.8	Same as Fig. 7.6 for Segue 1 $\chi\chi \rightarrow \nu_\mu\bar{\nu}_\mu$	90
363	Figure 7.9	Same as Fig. 7.6 for Ursa Major II 1 $\chi\chi \rightarrow b\bar{b}$	91
364	Figure 7.10	Same as Fig. 7.6 for Ursa Major II 1 $\chi\chi \rightarrow \tau\bar{\tau}$	92

365	Figure 7.11 Same as Fig. 7.6 for Ursa Major II 1 $\chi\chi \rightarrow \nu_\mu\bar{\nu}_\mu$	93
366	Figure 7.12 Same as Fig. 7.6 for 15, \mathcal{GS} J-factor, stacked sources and $\chi\chi \rightarrow b\bar{b}$	94
367	Figure 7.13 Same as Fig. 7.6 for 15, \mathcal{GS} J-factor, stacked sources and $\chi\chi \rightarrow t\bar{t}$	95
368	Figure 7.14 Same as Fig. 7.6 for 15, \mathcal{GS} J-factor, stacked sources and $\chi\chi \rightarrow u\bar{u}$	96
369	Figure 7.15 Same as Fig. 7.6 for 15, \mathcal{GS} J-factor, stacked sources and $\chi\chi \rightarrow d\bar{d}$	97
370	Figure 7.16 Same as Fig. 7.6 for 15, \mathcal{GS} J-factor, stacked sources and $\chi\chi \rightarrow e\bar{e}$	98
371	Figure 7.17 Same as Fig. 7.6 for 15, \mathcal{GS} J-factor, stacked sources and $\chi\chi \rightarrow \mu\bar{\mu}$	99
372	Figure 7.18 Same as Fig. 7.6 for 15, \mathcal{GS} J-factor, stacked sources and $\chi\chi \rightarrow \tau\bar{\tau}$	100
373	Figure 7.19 Same as Fig. 7.6 for 15, \mathcal{GS} J-factor, stacked sources and $\chi\chi \rightarrow W^+W^-$	101
374	Figure 7.20 Same as Fig. 7.6 for 15, \mathcal{GS} J-factor, stacked sources and $\chi\chi \rightarrow ZZ$	102
375	Figure 7.21 Same as Fig. 7.6 for 15, \mathcal{GS} J-factor, stacked sources and $\chi\chi \rightarrow \nu_e\bar{\nu}_e$	103
376	Figure 7.22 Same as Fig. 7.6 for 15, \mathcal{GS} J-factor, stacked sources and $\chi\chi \rightarrow \nu_\mu\bar{\nu}_\mu$	104
377	Figure A.1 Sister figure to Figure 5.3. Sources in the first row from left to right: Boötes I, Canes Venatici I, II. In second row: Draco, Hercules, Leo I. In the first row: Leo II, Leo IV, Sextans. In the final row: Ursa Major I, Ursa Major II.	106
380	Figure B.1 Sister figure to Figure 6.2 for remaining SM primary annihilation channels studied for this thesis. These did not require any post generation smoothing and so are directly pulled from [64] with a binning scheme most helpful for a HAWC analysis.	107
384	Figure B.2 TODO: fill this out	117
385	Figure B.3 TODO: fill this out	118
386	Figure B.4 TODO: fill this out	119
387	Figure C.1 TODO: fill me daddy	123
388	Figure C.2 TODO: Fill this out eventually. I think I want all the plots generated first[NEEDS A SOURCE][FACT CHECK THIS]	124

LIST OF ABBREVIATIONS

- 391 **MSU** Michigan State University
392 **LANL** Los Alamos National Laboratory
393 **DM** Dark Matter
394 **SM** Standard Model
395 **HAWC** High Altitude Water Cherenkov Observatory
396 **dSph** Dwarf Spheroidal Galaxy

CHAPTER 1

INTRODUCTION

398 Is the text not rendering right? Ah ok it knows im basically drafting the doc still

CHAPTER 2

399

DARK MATTER IN THE COSMOS

400 2.1 Introduction

401 The dark matter problem can be summarized in part by the following thought experiment.

402 Let us say you are the teacher for an elementary school classroom. You take them on a field
403 trip to your local science museum and among the exhibits is one for mass and weight. The exhibit
404 has a gigantic scale, and you come up with a fun problem for your class.

405 You ask your class, "What is the total weight of the classroom? Give your best estimation to
406 me in 30 minutes, and then we'll check your guess on the scale. If your guess is within 10% of the
407 right answer, we will stop for ice cream on the way back."

408 The students are ecstatic to hear this, and they get to work. The solution is some variation of
409 the following strategy. The students should give each other their weight or best guess if they do
410 not know. Then, all they must do is add each student's weight and get a grand total for the class.

411 The measurement on the giant scale should show the true weight of the class. When comparing
412 the measured weight to your estimation, multiply the measurement by 1.0 ± 0.1 to get the $\pm 10\%$
413 tolerances for your estimation.

414 Two of your students, Sandra and Mario, return to you with a solution.

415 They say, "We weren't sure of everyone's weight. We used 65 lbs. for the people we didn't
416 know and added everyone who does know. There are 30 of us, and we got 2,000 lbs.! That's a ton!"

417 You estimated 1,900 lbs. assuming the average weight of a student in your class was 60 lbs.
418 So, you are pleased with Sandra's and Mario's answer. You instruct your students to all gather on
419 the giant scale and read off the weight together. To all your surprise, the scale reads *10,000 lbs.*!
420 10,000 is significantly more than a 10% error from 2,000. In fact, it is approximately 5 times more
421 massive than either your or your students' estimates. You think to yourself and conclude there
422 must be something wrong with the scale. You ask an employee to check the scale and verify it is
423 well calibrated. They confirm that the scale is in working order. You weigh a couple of students
424 individually to assess that the scale is well calibrated. Sandra weighs 59 lbs., and Mario weighs

425 62 lbs., typical weights for their age. You then weigh each student individually and see that their
426 weights individually do not deviate greatly from 60 lbs. So, where does all the extra weight come
427 from?

428 This thought experiment serves as an analogy to the Dark Matter problem. The important
429 substitution to make however is to replace the students with stars and the classroom with a galaxy,
430 say the Milky Way. Individually the mass of stars is well measured and defined with the Sun as our
431 nearest test case. However, when we set out to measure the mass of a collection of stars as large as
432 galaxies, our well-motivated estimation is wildly incorrect. There simply is no way to account for
433 this discrepancy except without some unseen, or dark, contribution to mass and matter in galaxies.
434 I set out in my thesis to narrow the possibilities of what this Dark Matter could be.

435 This chapter is organized like the following... **TODO: Text should look like ... Chapter x has**
436 **blah blah blah.**

437 2.2 Dark Matter Basics

438 Presently, a more compelling theory of cosmology that includes Dark Matter (DM) in order
439 to explain a variety of observations is Λ Cold Dark Matter, or Λ CDM. I present the evidence
440 supporting Λ CDM in Section 2.3 yet discuss the conclusions of the Λ CDM model here. According
441 to Λ CDM fit to observations on the Cosmic Microwave Background (CMB), DM is 26.8% of the
442 universe's current energy budget. Baryonic matter, stuff like atoms, gas, and stars, contributes to
443 4.9% of the universe's current energy budget [1, 2, 3].

444 DM is dark; it does not interact readily with light at any wavelength. DM also does not interact
445 noticeably with the other standard model forces (Strong and Weak) at a rate that is readily observed
446 [3]. DM is cold, which is to say that the average velocity of DM is below relativistic speeds [1].
447 'Hot' DM would not likely manifest the dense structures we observe like galaxies, and instead
448 would produce much more diffuse galaxies than what is observed [3, 1]. DM is old; it played a
449 critical role in the formation of the universe and the structures within it [1, 2].

450 Observations of DM have so far been only gravitational. The parameter space available to what
451 DM could be therefore is extremely broad. The broad DM parameter space is iteratively tested in

452 DM searches by supposing a hypothesis that has not yet been ruled out and performing observations
453 to test them. When the observations yield a null result, the parameter space is constrained further.
454 I present some approaches for DM searches in Section 2.4.

455 **2.3 Evidence for Dark Matter**

456 Dark Matter (DM) has been a looming problem in physics for almost 100 years. Anomalies
457 have been observed by astrophysicists in galactic dynamics as early as 1933 when Fritz Zwicky
458 noticed unusually large velocity dispersion in the Coma cluster. Zwicky's measurement was the
459 first recorded to use the Virial theorem to measure the mass fraction of visible and invisible matter
460 in celestial bodies [4]. From Zwicky in [5], "*If this would be confirmed, we would get the surprising*
461 *result that dark matter is present in much greater amount than luminous matter.*" Zwicky's and
462 others' observation did not instigate a crisis in astrophysics because the measurements did not
463 entirely conflict with their understanding of galaxies [4]. In 1978, Rubin, Ford, and Norbert
464 measured rotation curves for ten spiral galaxies [6]. Rubin et al.'s 1978 publication presented a
465 major challenge to the conventional understanding of galaxies that could no longer be dismissed by
466 measurement uncertainties. Evidence has been mounting ever since for this exotic form of matter.
467 The following subsections provide three compelling pieces of evidence in support of the existence
468 of DM.

469 **2.3.1 First Clues: Stellar Velocities**

470 Zwicky, and later Rubin, measured the stellar velocities of various galaxies to estimate their
471 virial mass. The Virial Theorem upon which these observations are interpreted is written as

$$2T + V = 0. \quad (2.1)$$

472 Where T is the kinetic energy and V is the potential energy in a self-gravitating system. The
473 classical Newton's law of gravity from stars and gas was used for gravitational potential modeled in
474 the observed galaxies:

$$V = -\frac{1}{2} \sum_i \sum_{j \neq i} \frac{m_i m_j}{r_{ij}}. \quad (2.2)$$

475 Zwicky et al. measured just the velocities of stars apparent in optical wavelengths [5]. Rubin et al.
 476 added by measuring the velocity of the hydrogen gas via the 21 cm emission line of Hydrogen [6].
 477 The velocities of the stars and gas are used to infer the total mass of galaxies and galaxy clusters
 478 via Equation (2.1). An inferred mass is obtained from the luminosity of the selected sources. The
 479 two inferences are compared to each other as a luminosity to mass ratio which typically yielded [1]

$$\frac{M}{L} \sim 400 \frac{M_{\odot}}{L_{\odot}} \quad (2.3)$$

480 M_{\odot} and L_{\odot} referring to stellar mass and stellar luminosity, respectively. These ratios clearly indicate
 481 a discrepancy in apparent light and mass from stars and gas and their velocities.

482 Rubin et al. [6] demonstrated that the discrepancy was unlikely to be an underestimation of
 483 the mass of the stars and gas. The inferred "dark" mass was up to 5 times more than the luminous
 484 mass. This dark mass also needed to extend well beyond the extent of the luminous matter.

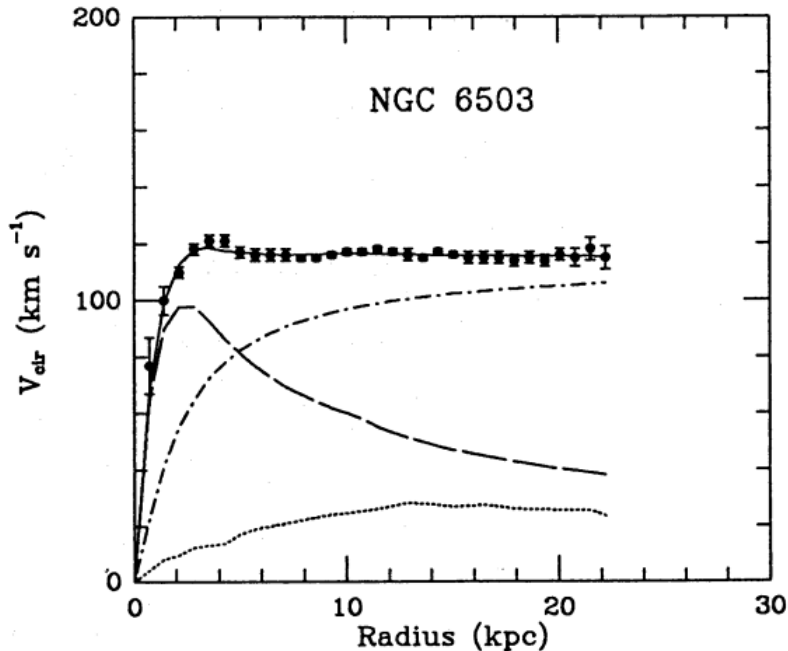


Figure 2.1 Rotation curve fit to NGC 6503 from [7]. Dashed line is the contribution from visible matter. Dotted curves are from gas. Dash-dot curves are from dark matter (DM). Solid line is the composite contribution from all matter and DM sources. Data are indicated with bold dots with error bars. Data agree strongly with a matter + DM composite prediction.

485 Figure 2.1 features one of many rotation curves plotted from the stellar velocities within galaxies.

486 The measured rotation curves mostly feature a flattening of velocities at higher radius which is not
487 expected if the gravity was only coming from gas and luminous matter. The extension of the
488 flat velocity region also indicates that the DM is distributed far from the center of the galaxy.
489 Modern velocity measurements include significantly larger objects, galactic clusters, and smaller
490 objects, dwarf galaxies. Yet, measurements along this regime are leveraging the Virial theorem
491 with Newtonian potential energies. We know Newtonian gravity is not a comprehensive description
492 of gravity. New observational techniques have been developed since 1978, and those are discussed
493 in the following sections.

494 **2.3.2 Evidence for Dark Matter: Gravitational Lensing**

495 Modern evidence for dark matter comes from new avenues beyond stellar velocities. Grav-
496 itational lensing from DM is a new channel from general relativity. General relativity predicts
497 aberrations in light caused by massive objects. In recent decades we have been able to measure the
498 lensing effects from compact objects and DM halos. Figure 2.2 shows how different massive ob-
499 jects change the final image of a faraway galaxy resulting from gravitational lensing. Gravitational
500 lensing developed our understanding of dark matter in two important ways.

501 Gravitational lensing provides additional compelling evidence for DM. The observation of two
502 merging galactic clusters in 2006, shown in Figure 2.3, provided a compelling argument for DM
503 outside the Standard Model. These clusters merged recently in astrophysical time scales. Galaxies
504 and star cluster have mostly passed by each other as the likelihood of their collision is low. Therefore,
505 these massive objects will mostly track the highest mass, dark and/or baryonic, density. Yet, the
506 intergalactic gas is responsible for the majority of the baryonic mass in the systems [4]. These gas
507 bodies will not phase through and will heat up as they collide together. The hot gas is located via
508 x-ray emission from the cluster. Two observations of the clusters were performed independently of
509 each other.

510 The first was the lensing of light around the galaxies due to their gravitational influences.
511 When celestial bodies are large enough, the gravity they exert bends space and time itself. The
512 warped space-time lenses light and will deflect in an analogous way to how glass lenses will bend

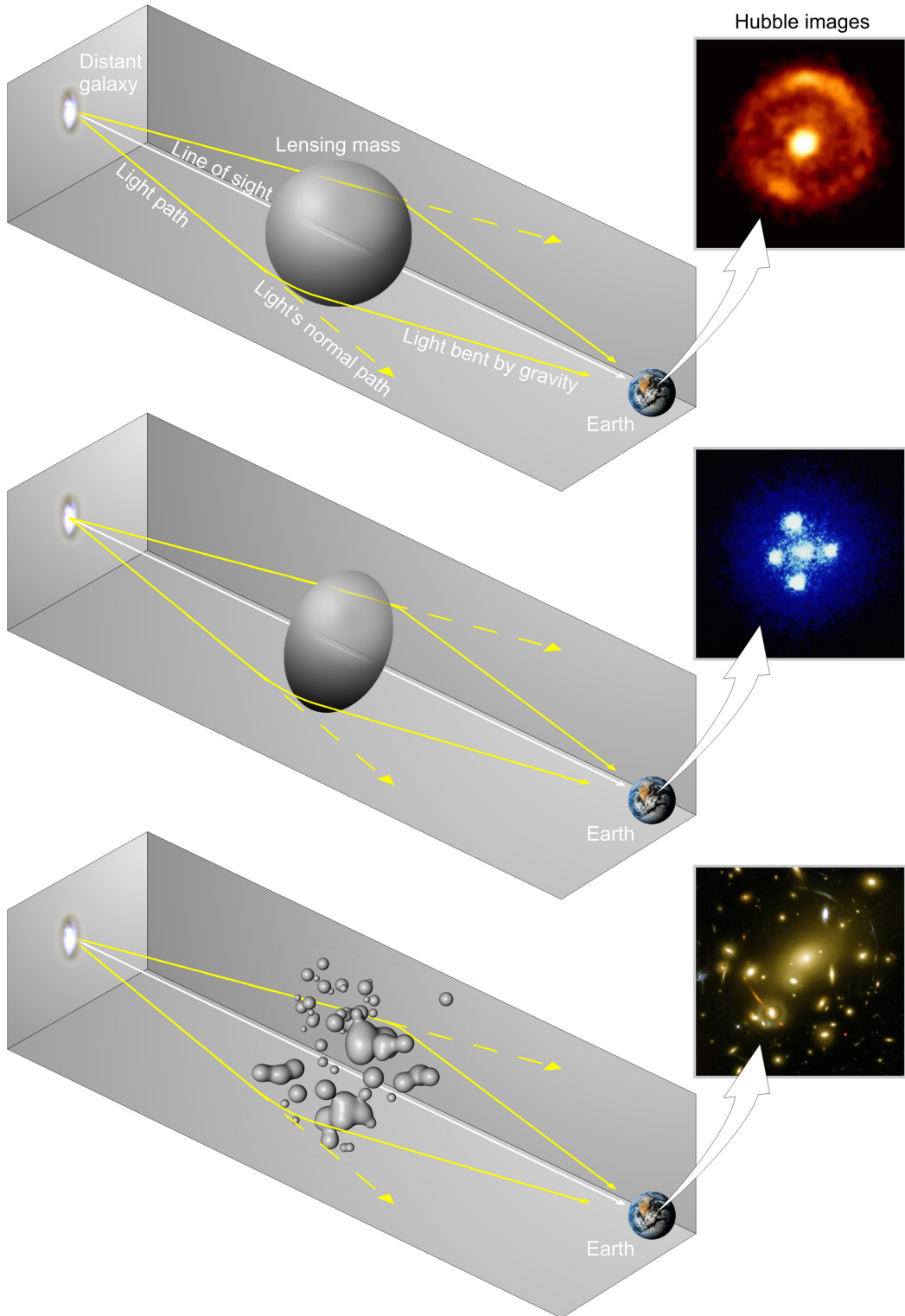


Figure 2.2 Light from distant galaxy is bent in unique ways depending on the distribution of mass between the galaxy and Earth. Yellow dashed lines indicate where the light would have gone if the matter were not present [8].

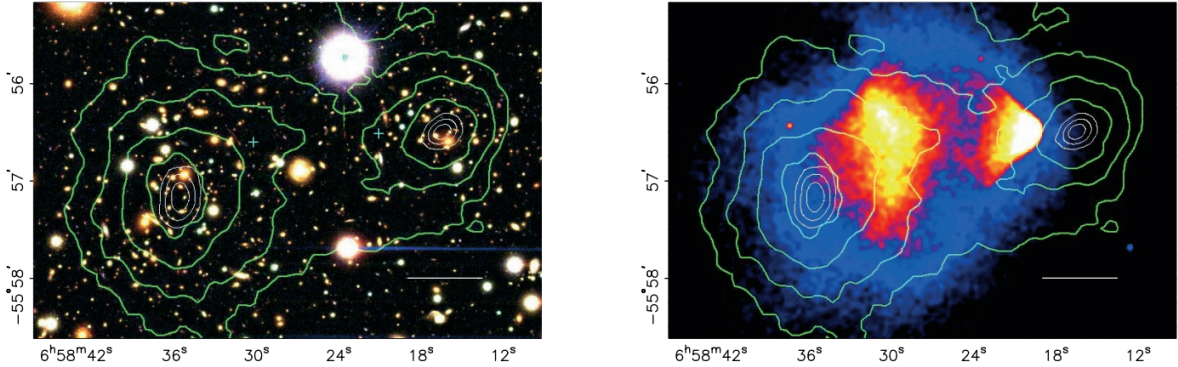


Figure 2.3 (left) Optical image of galactic cluster 1E0657-558. (right) X-ray image of the cluster with redder meaning hotter and higher baryon density. (both) Green contours are reconstruction of gravity contours from weak lensing. White rings are the best fit mass maxima at 68.3%, 95.5%, and 99.7% confidence. The matter maxima of the clusters are clearly separated from x-ray maxima. [9]

513 light, see Figure 2.2. With a sufficient understanding of light sources behind a massive object, we
 514 can reconstruct the contours of the gravitational lenses. The gradient of the contours shown in
 515 Figure 2.3 then indicates how dense the matter is and where it is.

516 The x-ray emission can then be observed from the clusters. Since these galaxies are mostly gas
 517 and are merging, then the gas should be getting hotter. If they are merging, the x-ray emissions
 518 should be the strongest where the gas is mostly moving through each other. Hence, X-ray emission
 519 maps out where the gas is in the merging galaxy cluster.

520 The lensing and x-ray observations were done on the Bullet cluster featured on Figure 2.3.
 521 The x-ray emissions do not align with the gravitational contours from lensing. The incongruence
 522 in mass density and baryon density suggests that there is a lot of matter somewhere that does
 523 not interact with light. Moreover, this dark matter cannot be baryonic [9]. The Bullet Cluster
 524 measurement did not really tell us what DM is exactly, but it did give the clue that DM also does
 525 not interact with itself very strongly. If DM did interact strongly with itself, then it would have been
 526 more aligned with the x-ray emission [9]. There have been follow-up studies of galaxy clusters with
 527 similar results. The Bullet Cluster and others like it provide a persuasive case against something
 528 possibly amiss in our gravitational theories.

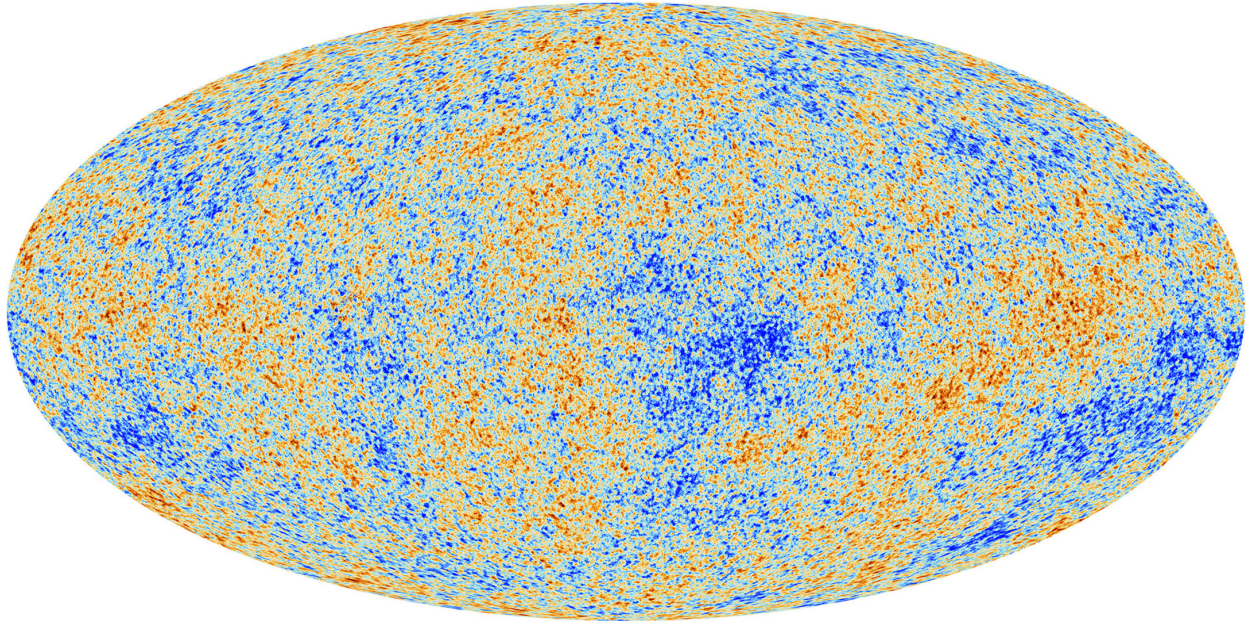


Figure 2.4 Plank CMB sky. Sky map features small variations in temperature in primordial light. These anisotropies are used to make inferences about the universe’s energy budget and developmental history. [10]

529 **2.3.3 Evidence for Dark Matter: Cosmic Microwave Background**

530 The Cosmic Microwave Background (CMB) is the primordial light from the early universe
531 when Hydrogen atoms formed from the free electron and proton soup in the early universe. The
532 CMB is the earliest light we can observe; released when the universe was about 380,000 years old.
533 Then we look at how the simulated universes look like compared to what we see. Figure 2.4 is the
534 most recent CMB image from the Plank satellite after subtracting the average value and masking the
535 galactic plane [10]. Redder regions indicate a slightly hotter region in the CMB, and blue indicates
536 colder. The intensity variations are on the order of 1 in 1000 with respect to the average value.

537 The Cosmic Microwave Background shows that the universe had DM in it from an incredibly
538 early stage. To measure the DM, Dark Energy, and matter fractions of the universe from the CMB,
539 the image is analyzed into a power spectrum, which shows the amplitude of the fluctuations as
540 a function of spherical multipole moments. Λ CDM provides the best fit to the power spectra of
541 the CMB as shown in Figure 2.5. The CMB power spectrum is quite sensitive to the fraction
542 of each energy contribution in the early universe. Low l modes are dominated by variations
543 in gravitational potential. Intermediate l emerge from oscillations in photon-baryon fluid from

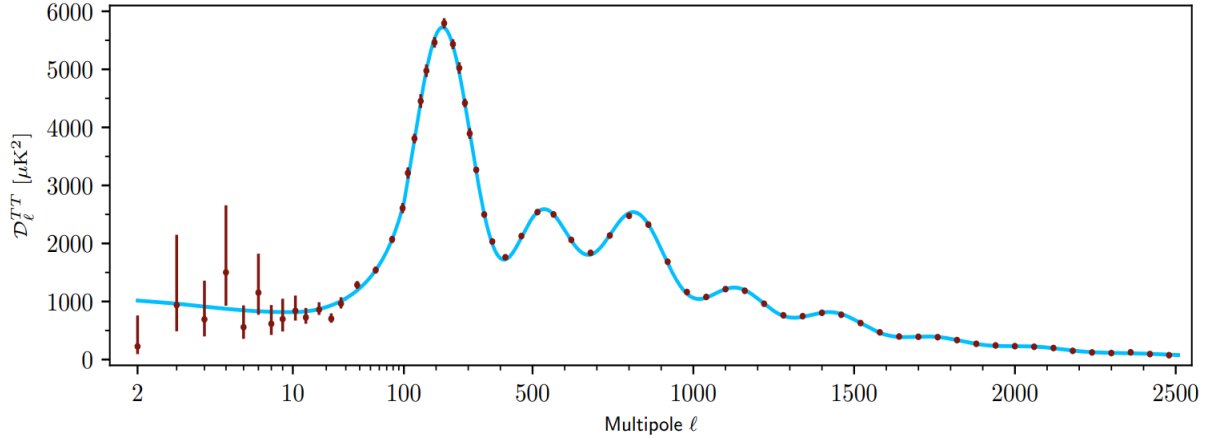


Figure 2.5 Observed Cosmic Microwave Background power spectrum as a function of multipole moment from Plank [10]. Blue line is best fit model from Λ CDM. Red points and lines are data and error, respectively.

544 competing baryon pressures and gravity. High l is a damped region from the diffusion of photons
 545 during electron-proton recombination. [1]

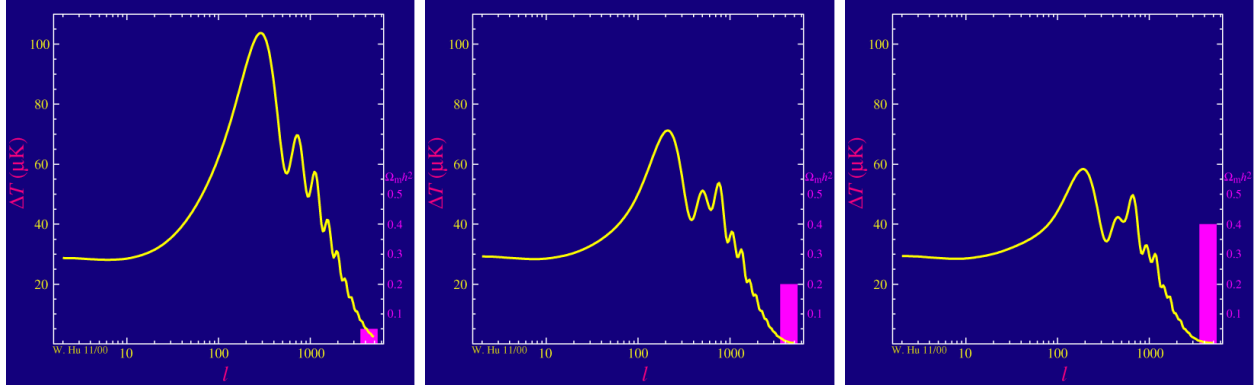


Figure 2.6 Predicted power spectra of CMB for different $\Omega_m h^2$ values for fixed baryon density from [11]. (left) Low $\Omega_m h^2$ increases the prominence of first and second peaks. (middle) $\Omega_m h^2$ is most similar to the observed power spectrum. The second and third peaks are similar in height. (right) $\Omega_m h^2$ is large which suppresses the first peak and raises the prominence of the third peak.

546 The harmonics would look quite different for a universe with less DM. Figure 2.6 demonstrates
 547 the effect $\Omega_m h^2$ has on the expected power spectrum for fixed baryon matter density. [11] Sweeping
 548 $\Omega_m h^2$ in this way clearly shows the effect dark matter has on the CMB power spectrum. The
 549 observations fit well with the Λ CDM model, and the derived fractions are as follows. The matter
 550 fraction: $\Omega_m = 0.3153$; and the baryon fraction: $\Omega_b = 0.04936$ [10]. Plank's observations also
 551 provide a measure of the Hubble constant, H_0 . H_0 especially has seen a growing tension in the

552 past decade that continues to deepened with observations from instruments like the James Webb
553 Telescope [12, 13]. As Hubble tensions deepen, we may find that perhaps Λ **CDM**, despite its
554 successes, is missing some critical physics.

555 Overall, the Newtonian motion of stars in galaxies, weak lensing from galactic clusters, and
556 power spectra from primordial light form a compelling body of research in favor of dark matter.
557 It takes another leap of theory and experimentation to make observations of DM that are non-
558 gravitational in nature. In Section 2.3, the evidence for DM implies strongly that the DM is matter
559 and not a lost parameter in the gravitational fields between massive objects. Finally, if we take one
560 axiom: that this matter has quantum behavior, such as being described by some Bohr wavelength
561 and abiding by some fermion or boson statistics; then we arrive at particle dark matter. One particle
562 DM hypothesis is the Weakly Interacting Massive Particle (WIMP). This DM candidate theory is
563 discussed further in the next section and is the focus of this thesis.

564 **2.4 Searching for Dark Matter: Particle DM**

565 Section 2.4 shows the Standard Model of particle physics and is currently the most accurate
566 model for the dynamics of fundamental particles like electrons and photons. The current status
567 of the SM does not have a viable DM candidate. When looking at the standard model, we can
568 immediately exclude any charged particle because charged particles interact strongly with light.
569 Specifically, this will rule out the following charged, fundamental particles: $e, \mu, \tau, W, u, d, s, c, t, b$
570 and their corresponding antiparticles. Recalling from Section 2.2 that DM must be long-lived and
571 stable over the age of the universe which excludes all SM particles with decay half-lives at or shorter
572 than the age of the universe. The lifetime constraint additionally eliminates the Z and H bosons.
573 Finally, the candidate DM needs to be somewhat massive. Recall from Section 2.2 that DM is cold
574 or not relativistic through the universe. This eliminates the remaining SM particles: $\nu_{e,\mu,\tau}, g, \gamma$ as
575 DM candidates. Because there are no DM candidates within the SM, the DM problem strongly
576 hints to physics beyond the SM (BSM).

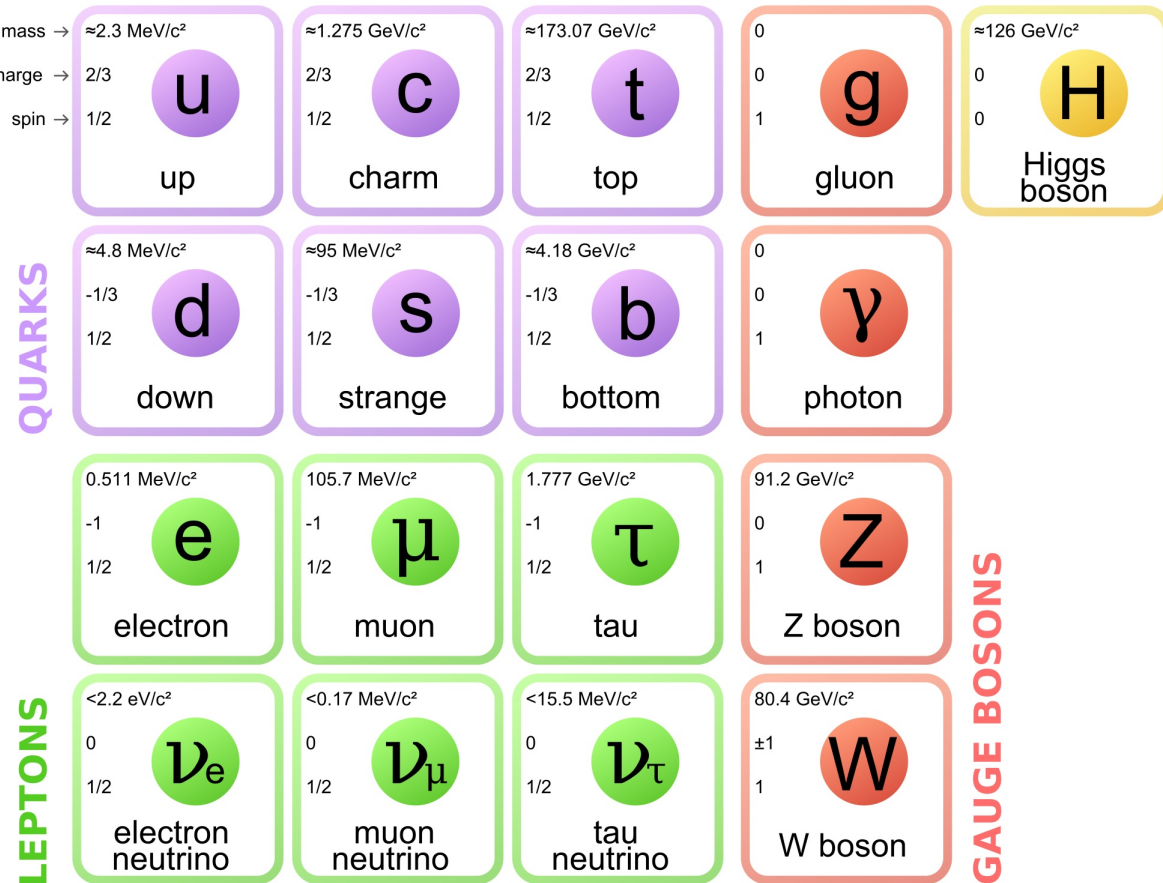


Figure 2.7 The Standard Model (SM) of particle physics. Figure taken from <http://www.quantumdiaries.org/2014/03/14/the-standard-model-a-beautiful-but-flawed-theory/>

577 2.4.1 Shake it, Break it, Make it

578 When considering DM that couples in some way with the SM, the interactions are roughly
 579 demonstrated by interaction demonstrated in Figure 2.8. The figure is a simplified Feynman
 580 diagram where the arrow of time represents the interaction modes of: **Shake it, Break it, Make it**.

581 **Shake it** refers to the direct detection of dark matter. Direct detection interactions start with
 582 a free DM particle and an SM particle. The DM and SM interact via elastic or inelastic collision
 583 and recoil away from each other. The DM remains in the dark sector and imparts some momentum
 584 onto the SM particle. The hope is that the momentum imparted onto the SM particle is sufficiently
 585 high enough to pick up with extremely sensitive instruments. Because we cannot create the DM in
 586 the lab, a direct detection experiment must wait until DM is incident on the detector. Most direct
 587 detection experiments are therefore placed in low-background environments with inert detection

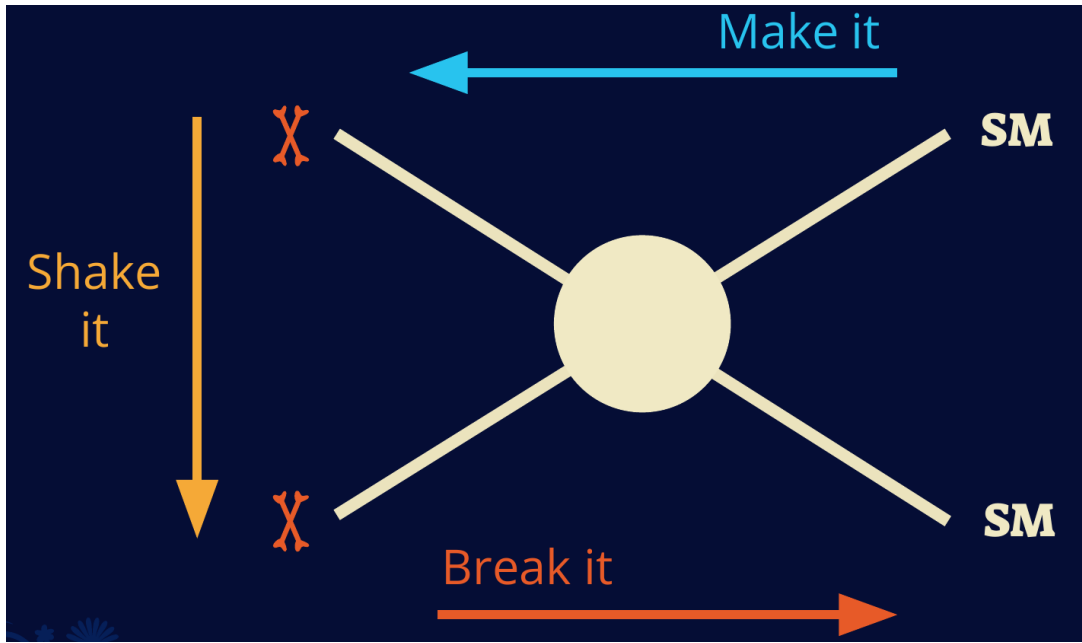


Figure 2.8 Simplified Feynman diagram demonstrating different ways DM can interact with SM particles. The 'X's refer to the DM particles whereas the SM refer to fundamental particles in the SM. The large circle in the center indicates the vertex of interaction and is purposely left vague. The colored arrows refer to different directions of time as well as their respective labels. The arrows indicate the initial and final state of the DM -SM interaction in time.

588 media like the noble gas Xenon. [14]

589 **Make it** refers to the production of DM from SM initial states. The experiment starts with
 590 particles in the SM. These SM particles are accelerated to incredibly high energies and then collide
 591 with each other. In the confluence of energy, DM hopefully emerges as a byproduct of the SM
 592 annihilation. Often it is the collider experiments that are energetic enough to hypothetically produce
 593 DM. These experiments include the world-wide collaborations ATLAS and CMS at CERN where
 594 proton collide together at extreme energies. The DM searches, however, are complex. DM likely
 595 does not interact with the detectors and lives long enough to escape the detection apparatus of
 596 CERN's colliders. This means any DM production experiment searches for an excess of events
 597 with missing momentum or energy in the events. An example event with missing transverse
 598 momentum is shown in Figure 2.9. The missing momentum with no particle tracks implies a
 599 neutral particle carried the energy out of the detector. However, there are other neutral particles
 600 in the SM, like neutrons or neutrinos, so any analysis has to account for SM signatures of missing

601 momentum. [15]

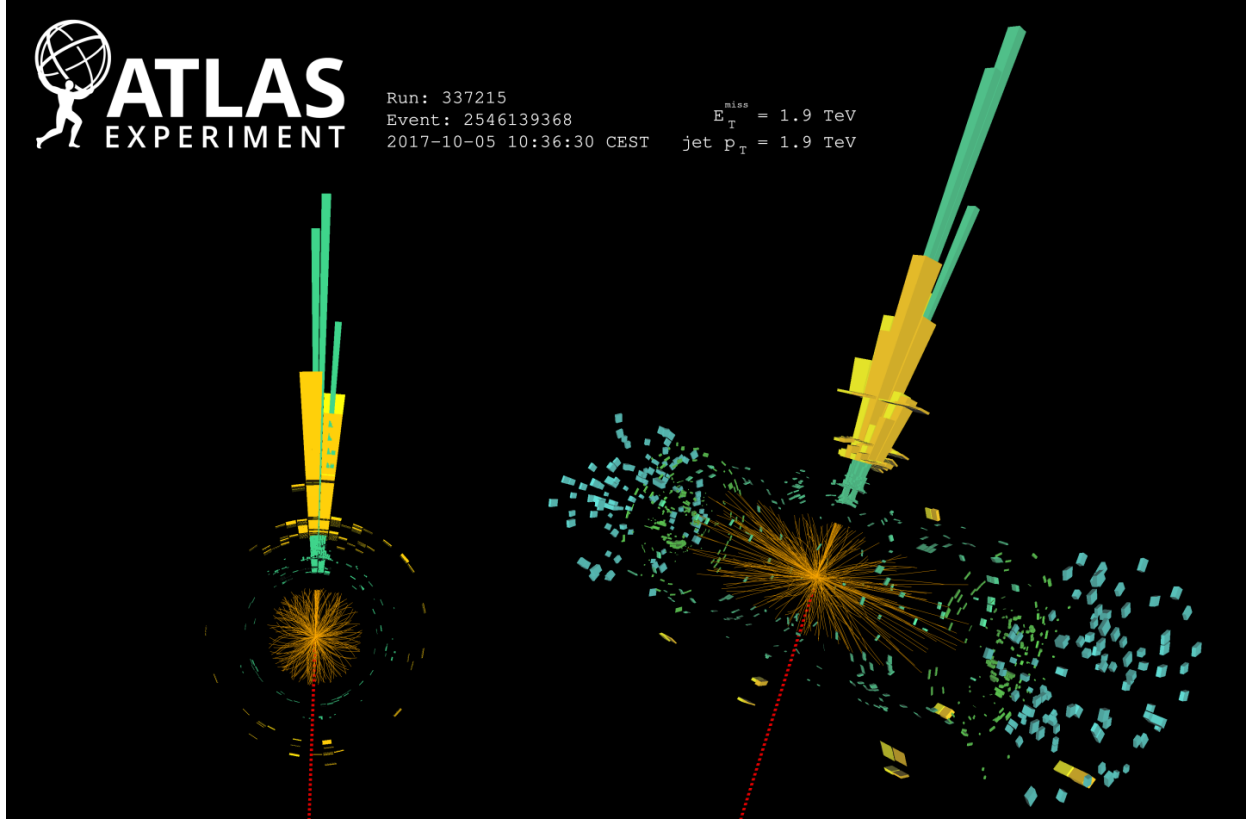


Figure 2.9 A single jet event in ATLAS detector from 2017 [16]. Jet momentum was observed to be 1.9 TeV. Missing transverse momentum was observed to be 1.9 TeV compared to the initial transverse momentum of the event was 0. Implied MET is traced by a red dashed line in event display.

602 2.4.2 Break it: Standard Model Signatures of Dark Matter through Indirect Searches

603 **Break it** refers to the creation of SM particles from the dark sector, and it is the primary focus
604 of this thesis. The interaction begins with DM or in the dark sector. The hypothesis is that this
605 DM will either annihilate with itself or decay and produce an SM byproduct. This method is
606 often referred to as the Indirect Detection of DM because we have no lab to directly control or
607 manipulate the DM. Therefore, most indirect DM searches are performed using observations of
608 known DM densities among the astrophysical sources. The strength is that we have the whole of the
609 universe and its 13.6-billion-year lifespan to use as a detector and particle accelerator. Additionally,
610 locations of dark matter are well cataloged since it was astrophysical observations that presented

611 the problem of DM in the first place.

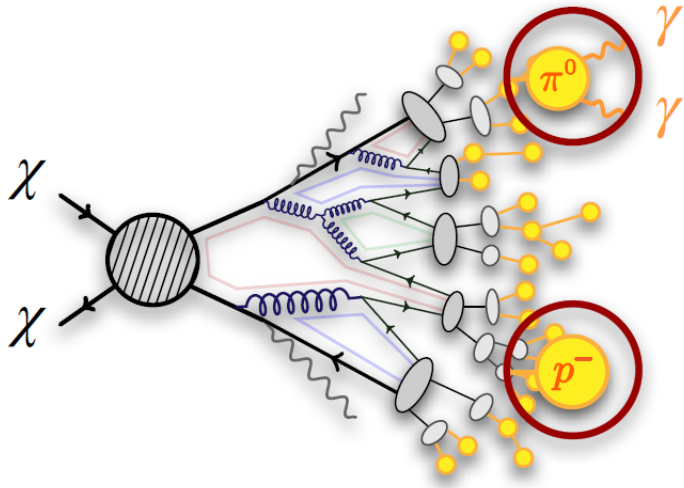


Figure 2.10 More detailed pseudo-Feynman diagram of particle cascade from dark matter annihilation into 2 quarks. The quarks hadronize and down to stable particles like γ or the anti-proton (p^-). Diagram pulled from ICRC 2021 presentation on DM annihilation search [17].

612 However, anything can happen in the universe. There are many difficult to deconvolve back-
613 grounds when searching for DM. One prominent example is the galactic center. We know the
614 galactic center has a large DM content because of stellar kinematics in our Milky Way and DM halo
615 simulations. Yet, any signal from the galactic center is challenging to parse apart from the extreme
616 environment of our supermassive black hole, unresolved sources, and diffuse emission from the
617 interstellar medium [18]. Despite the challenges, any DM model that yields evidence in the other
618 two observation methods, **Shake it or Make it** must be corroborated with indirect observations of
619 the known DM sources. Without corroborating evidence, DM observation in the lab is hard-pressed
620 to demonstrate that it is the model contributing to the DM seen at the universal scale.

621 In the case of WIMP DM, signals are described in terms of primary SM particles produced
622 from DM decay or annihilation. The SM initial state particles are then simulated down to stable
623 final states such as the γ , ν , p , or e which can traverse galactic lengths to reach Earth.

624 Figure 2.10 shows the quagmire of SM particles that emerges from SM initial states that are not
625 stable [17]. There are many SM particles with varying energies that can be produced in such an

626 interaction. For any arbitrary DM source and stable SM particle, the SM flux from DM annihilating
 627 to a neutral particle in the SM, ϕ , from a region in the sky is described by the following.

$$\frac{d\Phi_\phi}{dE_\phi} = \frac{\langle\sigma v\rangle}{8\pi m_\chi^2} \frac{dN_\phi}{dE_\phi} \times \int_{\text{source}} d\Omega \int_{l.o.s} \rho_\chi^2 dl(r, \theta') \quad (2.4)$$

628 In Equation (7.1), $\langle\sigma v\rangle$ is the velocity-weighted annihilation cross-section of DM to the SM. m_χ
 629 refers to the mass of DM, noted with Greek letter χ . $\frac{dN_\phi}{dE_\phi}$ is the N particle flux weighted by the
 630 particle energy. An example is provided in Figure 2.11 for the γ final state. The integrated terms
 631 are performed over the solid angle, $d\Omega$, and line of sight, l.o.s. ρ is the density of DM for a
 632 location (r, θ') in the sky. The terms left of the ' \times ' are often referred to as the particle physics
 633 component. The terms on the right are referred to as the astrophysical component. For decaying
 634 DM, the equation changes to...

$$\frac{d\Phi_\phi}{dE_\phi} = \frac{1}{4\pi\tau m_\chi} \frac{dN_\phi}{dE_\phi} \times \int_{\text{source}} d\Omega \int_{l.o.s} \rho_\chi dl(r, \theta') \quad (2.5)$$

635 In Equation (6.1), τ is the decay lifetime of the DM. Just as in Equation (7.1), the left and right
 636 terms are the particle physics and the astrophysical components respectively. The integrated
 637 astrophysical component of Equation (7.1) is often called the J-Factor. Whereas the integrated
 638 astrophysical component of Equation (6.1) is often called the D-Factor.

639 Exact DM $\text{DM} \rightarrow \text{SM SM}$ branching ratios are not known, so it is usually assumed to go 100%
 640 into an SM particle/anti-particle. Additionally, when a DM annihilation or decay produces one of
 641 the neutral, long-lived SM particles (ν or γ), the particle is traced back to a DM source. For DM
 642 above GeV energies, there are very few SM processes that can produce particles with such a high
 643 energy. Seeing such a signal would almost certainly be an indication of the presence of dark matter.
 644 Fortunately, the universe provides us with the largest volume and lifetime ever for a particle physics
 645 experiment.

646 2.5 Sources for Indirect Dark Matter Searches

647 The first detection of DM relied on optical observations. Since then, we have developed new
 648 techniques to find DM dense regions. As described in Section 2.3.1, many DM dense regions were
 649 through observing galactic rotation curves. Our Milky Way galaxy is among DM dense regions

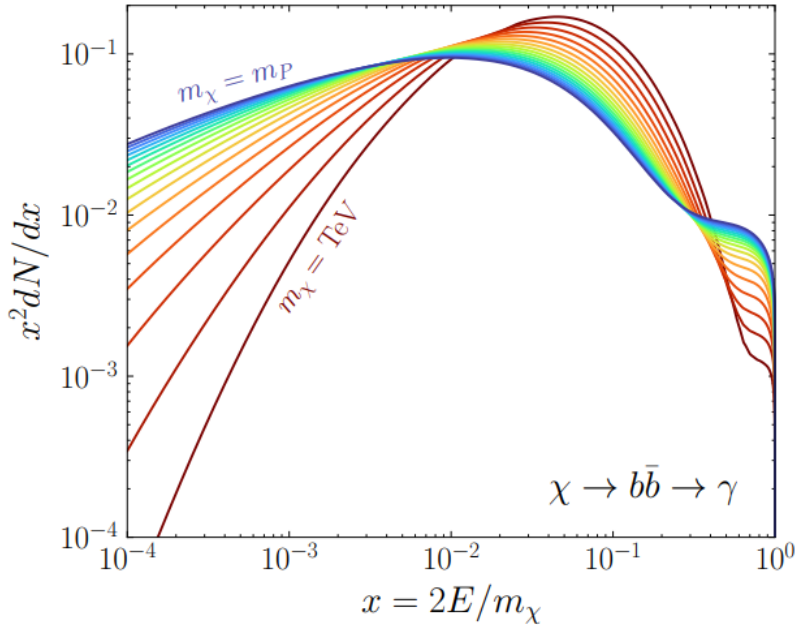


Figure 2.11 Dark Matter (DM) decay spectrum for $b\bar{b}$ initial state and γ final state. Redder spectra are for larger DM masses. Bluer spectra are light DM masses. x is a unitless factor defined as the ratio of the mass of DM, m_χ , and the final state particle energy E_γ . Figure from [19].

discovered, and it is the largest nearby DM dense region to look at. Additionally, the DM halo surrounding the Milky Way is clumpy [18]. There are regions in the DM halo of the Milky Way that have more DM than others that have captured gas over time. These sub-halos were dense enough collapse gas and form stars. These apparent sub galaxies are known as dwarf spheroidal galaxies and are the main sources studied in this thesis. Each source type comes with different trade-offs. Galactic Center studies will be very sensitive to the assumed distribution of DM. The central DM density can vary substantially as demonstrated in Figure 2.12. At distances close to the center of the galaxy, or small r , the differences in DM densities can be 3-4 orders of magnitude. Searches toward the galactic center will therefore be quite sensitive to the assumed DM distribution.

Searches toward Dwarf Spheroidal Galaxies (dSph's) suffer from uncertainties in the DM density less than the galactic center studies. This is mostly from their diminutive size being smaller than the angular resolution of most γ -ray observatories [18]. The DM content dSph's are typically determined with the Virial theorem, Equation (2.1), and are usually majority DM [18] in mass. DSph's tend to be ideal sources to look at for DM searches. Their environments are quiet with little

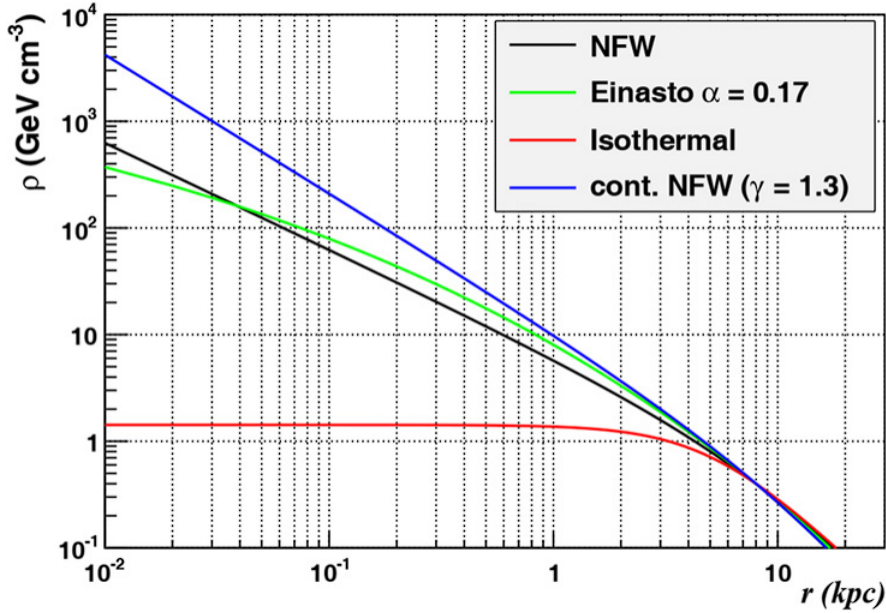


Figure 2.12 Different dark matter density profiles compared. Some models produce exceptionally large densities at small r [20].

664 astrophysical background. Unlike the galactic center, the most active components of dSph's are the
 665 stars within them versus a violent accretion disc around a black hole. All this together means that
 666 dSph's are among the best sources to look at for indirect DM searches. dSph's are the targets of
 667 focus for this thesis.

668 2.6 Multi-Messenger Dark Matter

669 Astrophysics entered a new phase in the past few decades that leverages our increasing sensitivity
 670 to SM channels and general relativity (GR). Up until the 21st century, astrophysical observations
 671 were performed with photons (γ) only. Astrophysics with this 'messenger' is fairly mature now.
 672 Novel observations of the universe have since only adjusted the sensitivity of the wavelength of
 673 light that is observed except at MeV energies. Gems like the CMB [10], and more have ultimately
 674 been observations of different wavelengths of light. Multi-messenger astrophysics proposes using
 675 other SM particles such the p^{+-} , or ν or gravitation waves predicted by general relativity.

676 The experiment LIGO had a revolutionary discovery in 2016 with the first detection of a binary
 677 black hole merger [21]. This opened the collective imagination to observing the universe through
 678 gravitational waves. There has also been a surge of interest in the neutrino (ν) sector. IceCube

679 demonstrated that we are sensitive to neutrinos in regions that correlate with significant photon
 680 emission like the galactic plane [22]. Neutrinos, like gravitational waves and light, travel mostly
 681 unimpeded from their source to our observatories. This makes pointing to the originating source
 682 of these messengers much easier than it is for cosmic rays which are deflected from their source by
 683 magnetic fields.

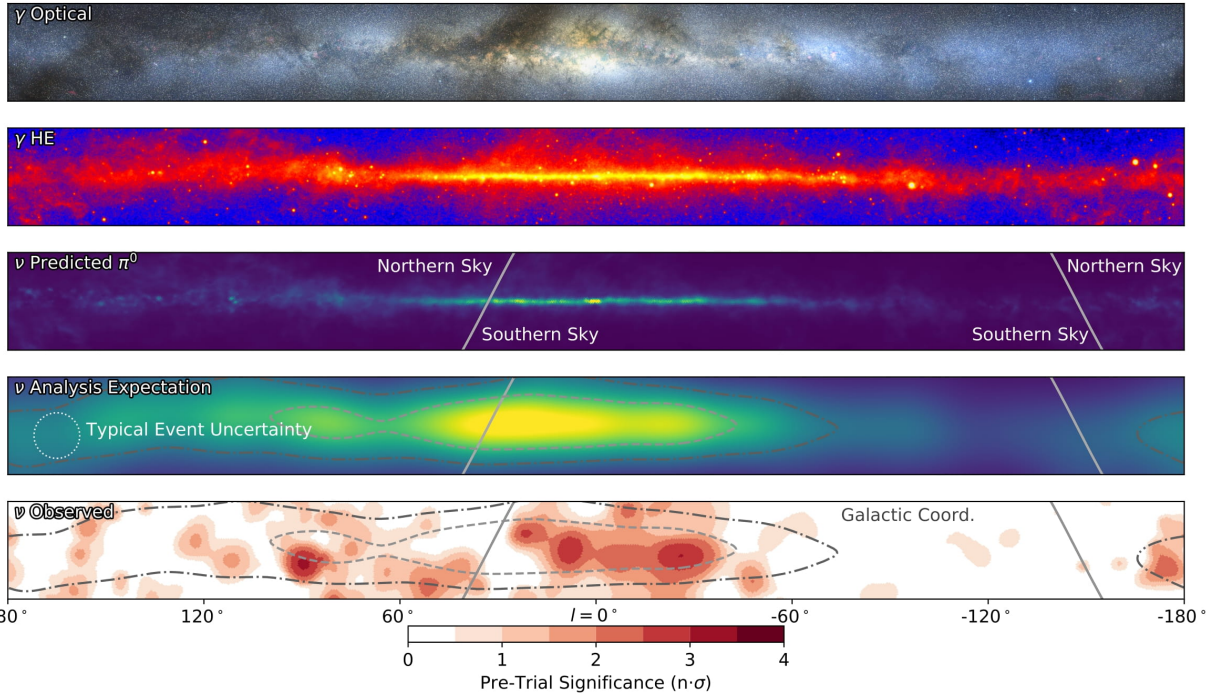


Figure 2.13 The Milky Way Galaxy in photons (γ) and neutrinos (ν) [22]. The Galactic center is at $l=0^\circ$ and is the brightest region in all panels. (top) An Optical color image of the Milky Way galaxy seen from Earth. Clouds of gas and dust obscure some light from stars. (2nd down) Integrated flux of γ -rays observed by the Fermi-LAT telescope [23]. (middle) Expected neutrino emission that corresponds with Fermi-LAT observations. (2nd up) Expected neutrino emission profile after considering detector systematics of IceCube. (bottom) Observed neutrino emission from region of the galactic plane. Substantial neutrino emission was detected.

684 The IceCube collaboration recently published a groundbreaking result of the Milky Way in
 685 neutrinos. The recent result from IceCube, shown in Figure 2.13, proves that we can make
 686 observations under different messenger regimes. The top two panels show the appearance of the
 687 galactic plane to different wavelengths of light. Some sources are more apparent in some panels,
 688 while others are not. This new channel is powerful because neutrinos are readily able to penetrate
 689 through gas and dust in the Milky Way. This new image also refines our understanding of how high

690 energy particles are produced. For example, the fit to IceCube data prefers neutrino production
 691 from the decay of π^0 [22].

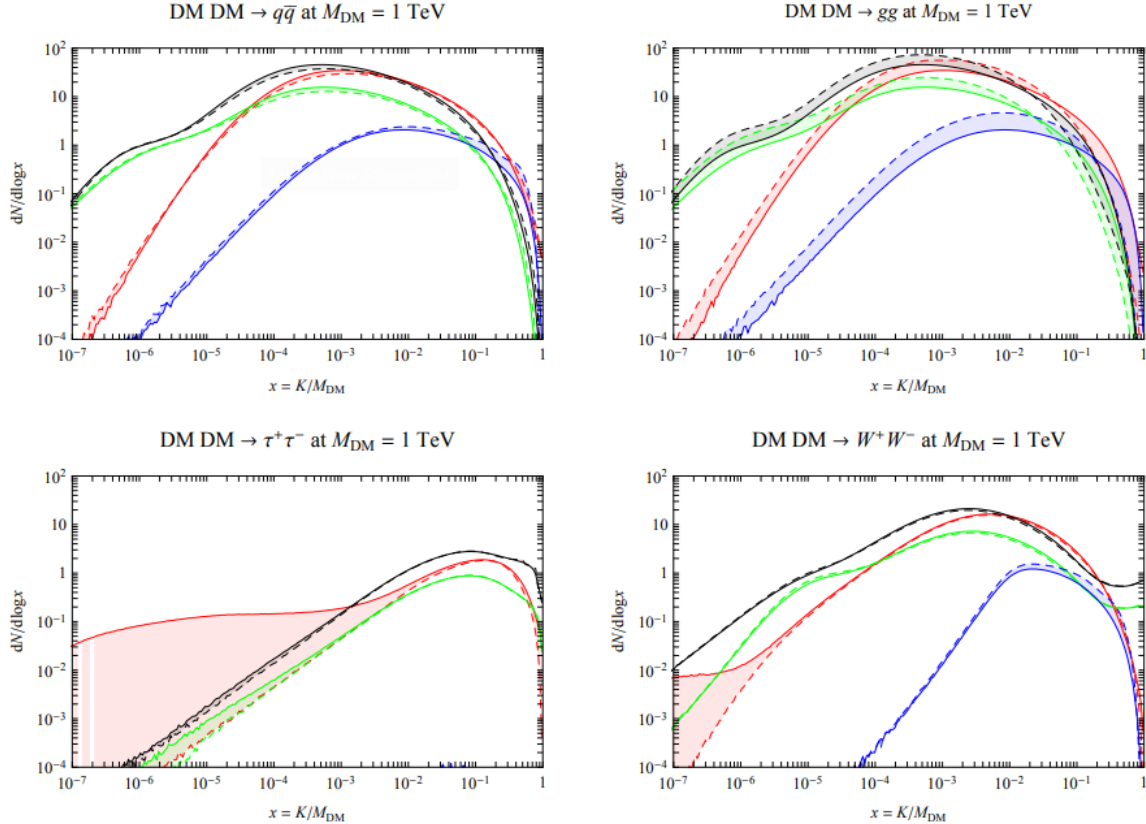


Figure 2.14 Dark Matter annihilation spectra for different final state particle and standard model annihilation channels [24]. Photons (red), e^\pm (green), \bar{p} (blue), ν (black).

692 Exposing our observations to more cosmic messengers greatly increases our sensitivity to
 693 rare processes. In the case of DM, Figure 2.14, there are many SM particles produced in DM
 694 annihilation. Among the final state fluxes are gammas and neutrinos. Charged particles are also
 695 produced however they would not likely make it to Earth since they will be deflected by magnetic
 696 fields between the source and Earth. This means observatories that can see the neutral messengers
 697 are especially good for DM searches and for combining data for a multi-messenger DM search.

CHAPTER 3

698 **HIGH ALTITUDE WATER CHERENKOV (HAWC) OBSERVATORY**

699 **3.1 The Detector**

700 **3.2 Events Reconstruction and Data Acquisition**

701 **3.2.1 G/H Discrimination**

702 **3.2.2 Angle**

703 **3.2.3 Energy**

704 **3.3 Remote Monitoring**

705 **3.3.1 ATHENA Database**

706 **3.3.2 HOMER**

707

CHAPTER 4

ICECUBE NEUTRINO OBSERVATORY

708 **4.1 The Detector**

709 **4.2 Events Reconstruction and Data Acquisition**

710 **4.2.1 Angle**

711 **4.2.2 Energy**

712 **4.3 Northern Test Site**

713 **4.3.1 PIgeon remote dark rate testing**

714 **4.3.2 Bulkhead Construction**

CHAPTER 5

GLORY DUCK: MULTI-WAVELENGTH SEARCH FOR DARK MATTTER ANNIHILATION TOWARDS DWARF SPHEROIDAL GALAXIES

5.1 Introduction

The field of astrophysics now has several instruments and observatories sensitive to high energy gamma-rays. The energy sensitivity for the modern gamma-ray program spans many orders of magnitude. Figure 5.1 demonstrates these similar sensitivities across energies for the five experiments: Fermi-LAT, HAWC, HESS, MAGIC, and VERITAS.

Each of the five experiments featured in Figure 5.1 have independently searched for DM annihilation from dwarf spheroidal galaxies (dSph) and set limits. Intriguingly, there are regions of substantial overlap in their energy sensitivities. This clearly motivates an analysis that combines data from these five. Each experiment has unique gamma-ray detection methods and their weaknesses and strengths can be leveraged with each other. The HAWC gamma-ray observatory is extensively introduced in chapter 3, so it is not introduced here. A brief description of the remaining experiments are in the following paragraphs.

The Large Area Telescope (LAT) is a pair conversion telescope mounted on the NASA Fermi satellite in orbit \sim 550 km above the Earth [26]. LAT's field of view covers about 20% of the whole sky, and it sweeps the whole sky approximately every 3 hours. LAT's gamma-ray energy sensitivity ranges from 20 MeV up to 1 TeV. Previous DM searches towards dSphs using Fermi-LAT are published in [27] and [28]

The High Energy Spectroscopic System (HESS), Major Atmospheric Gamma Imaging Cherenkov (MAGIC), and Very Energetic Radiation Imaging Telescope Array System (VERITAS) are arrays of Imaging Atmospheric Cherenkov Telescopes (IACT). These telescopes observe the Cherenkov light emitted from gamma-ray showers in the Earth's atmosphere. The field of view for these telescopes is no larger than 5° with energy sensitivities ranging from 30 GeV up to 100 TeV [29, 30, 31]. IACTs are able to make precise observations in selected regions of the sky, however can only be operated in ideal dark conditions. HESS's observations of the dwarves

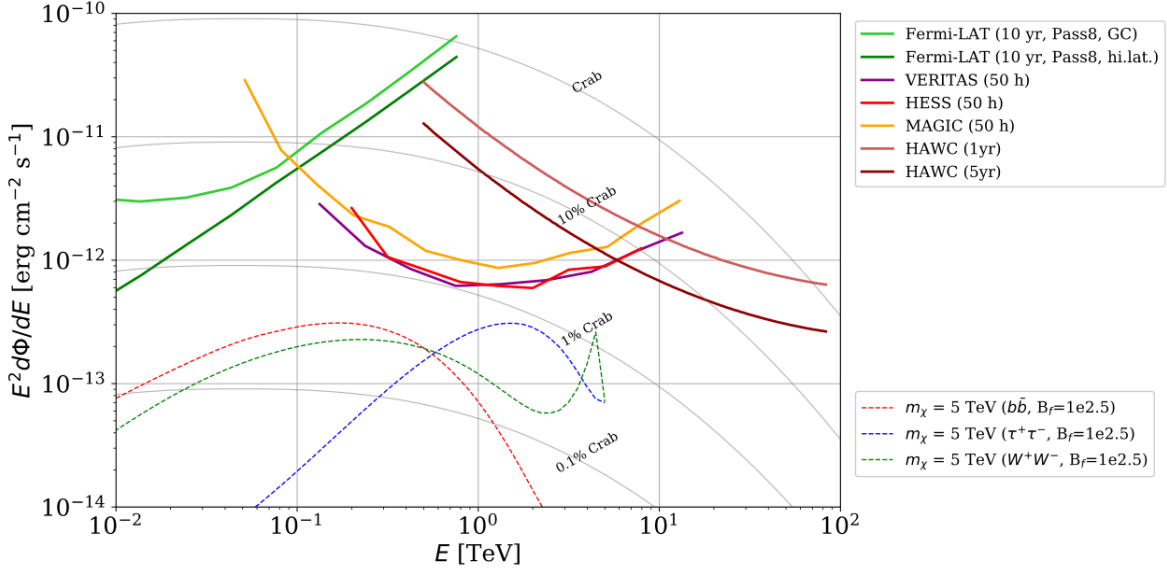


Figure 5.1 Sensitivities of five gamma-ray experiments compared to percentages of the Crab nebula’s emission and dark matter annihilation. Solid lines present estimated sensitivities to power law spectra [FACT CHECK THIS] for each experiment. Green lines are Fermi-LAT sensitivities where lighter green is the sensitivity to the galactic center and dark green is its sensitivity to higher declinations. Orange, red, and purple solid lines represent the MAGIC, HESS, and VERITAS 50 hour sensitivities respectively. The maroon and brown lines are the HAWC 1 year and 5 year sensitivities. Across four decades of gamma-ray energy, these experiments have similar sensitivities on the order 10^{-12} erg $\text{cm}^{-2}\text{s}^{-1}$. The dotted lines are estimated dark matter fluxes assuming $m_\chi = 5$ TeV DM annihilating to bottom quarks (red), tau leptons (blue), and W bosons (green). Faded gray lines outline percentage flux of the Crab nebula. Figure is an augmented version of [25]

741 Sculptor and Carina were between January 2008 and December 2009. HESS’s observations of
 742 Coma Berenices were from 2010 to 2013, and Fornax was observed in 2010 [32, 33, 34]. MAGIC
 743 provided deep observations of Segue1 between 2011 and 2013 [35]. MAGIC also provides data
 744 for three dwarves: Coma Berenices, Draco, and Ursa Major II where observations were made
 745 in: January - June 2019 [36], March - September 2018 [36], and 2014 - 2016 [37] respectively.
 746 VERITAS provided data for Boötes I, Draco, Segue 1, and Ursa Minor from 2009 to 2016 [38].

747 This chapter presents the Glory Duck analysis, the name given for the search for dark matter
 748 annihilation from dSph by combining data from the five gamma-ray observatories: Fermi-LAT,
 749 HAWC, HESS, MAGIC, and VERITAS. Specifically, the methods in analysis and modeling are
 750 presented for the HAWC gamma-ray observatory. This work was published to the Journal of
 751 Cosmology and Astroparticle Physics and presented at the International Cosmic Ray Conference

752 in 2019, 2021, and 2023 [39, 40, 41] and others.

753 **5.2 Dataset and Background**

754 This section enumerates the data and background methods used for HAWC's study of dSphs.

755 Section 5.2.1 and Section 5.2.2 are most useful for fellow HAWC collaborators looking to replicate

756 the Glory Duck analysis.

757 **5.2.1 Itemized HAWC files**

758 • Detector Resolution: `response_aerie_svn_27754_systematics_best_mc_test_no`
759 `broadpulse_10pctlogchargesmearing_0.63qe_25kHzNoise_run5481_curvatu`
760 `re0_index3.root`

761 • Data Map: `maps-20180119/liff/maptree_1024.root`

762 • Spectral Dictionary: `DM_CirrelliSpectrum_dict_gammas.npy`

763 • Analysis wiki: https://private.hawc-observatory.org/wiki/index.php/Glory_Duck_Multi-Experiment_Dark_Matter_Search

765 **5.2.2 Software Tools and Development**

766 This analysis was performed using HAL and 3ML [42, 43] in Python version 2. I built software
767 to implement the *A Poor Particle Physicist Cookbook for Dark Matter Indirect Detection* (PPPC)
768 [44] DM spectral model and dSphs spatial model from [45] for HAWC analysis. A NumPy version
769 of this dictionary was made for both Py2 and Py3. The code base for creating this dictionary is
770 linked on my GitLab sandbox:

771 • Py2: [Dictionary Generator \(Deprecated\)](#)

772 • Py3: [PPPC2Dict](#)

773 The analysis was performed using the f_{hit} framework performed in the HAWC Crab paper
774 [42]. The Python2 NumPy dictionary file for gamma-ray final states is `dmCirSpecDict.npy`. The
775 corresponding Python3 file is `DM_CirrelliSpectrum_dict_gammas.npy`. These files can also

776 be used for decay channels and the PPPC describes how [44]. All other software used for data
777 analysis, DM profile generation, and job submission to SLURM are also kept in my sandbox for
778 [the Glory Duck](#) project.

779 **5.2.3 Data Set and Background Description**

780 The HAWC data maps used for this analysis contain 1017 days of data between runs 2104
781 (2014-11-26) and 7476 (2017-12-20). They were generated from pass 4.0 reconstruction. The
782 analysis is performed using the f_{hit} energy binning scheme with bins (1-9) similar to what was done
783 for the Crab and previous HAWC dSph analysis [42, 46]. Bin 0 was excluded as it has substantial
784 hadronic contamination and poor angular resolution.

785 This analysis was done on dSphs because of their large DM mass content relative to baryonic
786 mass. We consider the following to estimate the background to this study.

- 787 • The dSphs are small in HAWC’s field of view, so the analysis is not sensitive to large or small
788 scale anisotropies.
- 789 • The dSphs used in this analysis are off the galactic plane.
- 790 • The dSphs are baryonically faint relative to their expected dark matter content and are not
791 expected to contain high energy gamma-ray sources.

792 Therefor we make no additional assumptions on the background from our sources and use
793 HAWC’s standard direct integration method for background estimation [42]. It is possible for
794 gamma rays from DM annihilation to scatter in transit to HAWC via Inverse Compton Scattering
795 (ICS). This was investigated and its impact on the flux is basically zero. Supporting information
796 on this is in Section 5.7.1

797 **5.3 Analysis**

798 The expected differential photon flux from DM-DM annihilation to standard model particles,
799 $d\Phi_\gamma/dE_\gamma$, over solid angle, Ω is described by the familiar equation.

$$\frac{d\Phi_\gamma}{dE_\gamma} = \frac{\langle\sigma v\rangle}{8\pi m_\chi^2} \frac{dN_\gamma}{dE_\gamma} \times \int_{\text{source}} d\Omega \int_{l.o.s} \rho_\chi^2 dl(r, \theta') \quad (5.1)$$

800 Where $\langle \sigma v \rangle$ is the velocity weighted annihilation cross-section. $\frac{dN}{dE}$ is the expected differential
 801 number of photons produced at each energy per annihilation. m_χ is the rest mass of the supposed
 802 DM particle. ρ_χ is the DM density. J is the astrophysical J-factor and is defined as

$$J = \int d\Omega \int_{l.o.s} dl \rho_\chi^2(r, \theta') \quad (5.2)$$

803 l is the distance to the source from Earth. r is the radial distance from the center of the source. θ' is
 804 the half angle defining a cone containing the DM source. How each component is synthesized and
 805 considered for HAWC's analysis is presented in the following sections. Section 5.3.1 presents the
 806 particle physics model for DM annihilation. Section 5.3.2 presents the spatial distributions built
 807 for each dSph.

808 **5.3.1 $\frac{dN_\gamma}{dE_\gamma}$ - Particle Physics Component**

809 For these spectra, we import the PPPC with Electroweak (EW) corrections [44]. The spectrum
 810 is implemented as a model script in astromodels for 3ML. The EW corrections were previously not
 811 considered for HAWC and are significant for DM annihilating to EW coupled SM particles such
 812 as all leptons, and the γ , Z , and W bosons [46]. Figure 5.2 demonstrates the significance of EW
 813 corrections for W boson annihilation. Across EW SM channels, the gamma-ray spectra become
 814 harder than spectra without EW corrections. Tables from the PPPC were reformatted into Python
 815 NumPy dictionaries for collaboration-wide use. A class in astromodels was developed to include
 816 the EW correction from the PPPC and is aptly named `PPPCSpectra` within `DM_models.py`.

817 **5.3.2 J - Astrophysical Component**

818 The J-factor profiles for each source are imported from Geringer-Sameth (referred to with \mathcal{GS})
 819 [45]. These were pulled from the publication as $J(\theta)$, where θ is the angular separation from the
 820 center of the source. HAWC requires maps in terms of $\frac{dJ}{d\Omega}$, so the conversion from the maps was
 821 done in the following way...

822 First, convert the angular distances to solid angles

$$\Omega = 2 \cdot \pi(1 - \cos(\theta)) \quad (5.3)$$

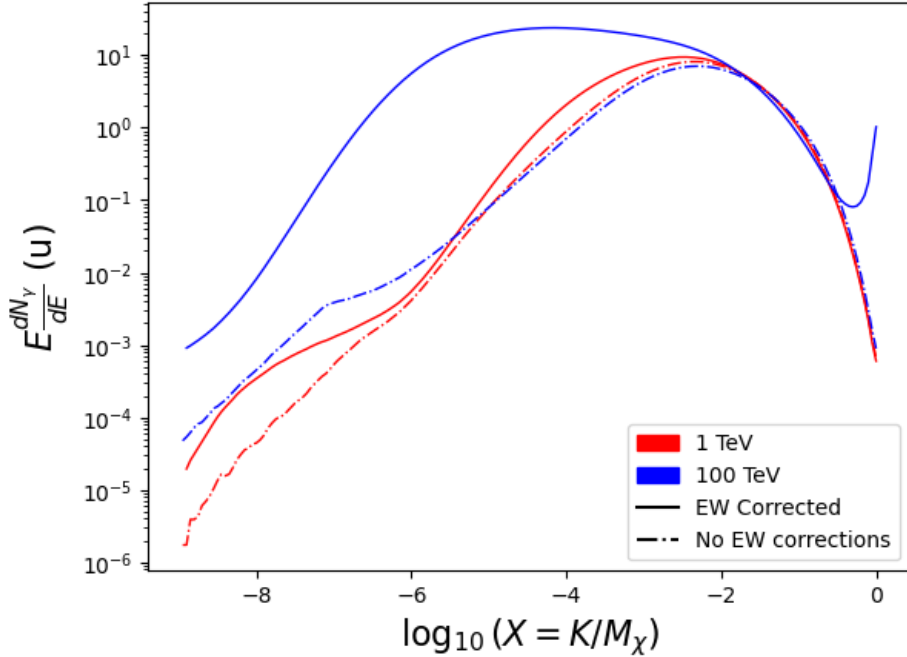


Figure 5.2 Effect of Electroweak (EW) corrections on expected DM annihilation spectrum for $\chi\chi \rightarrow W^-W^+$. Solid lines are spectral models that consider EW corrections. Dash-dot lines are spectral models without EW corrections. Red lines are models for $M_\chi = 1$ TeV. Blue lines represent models for $M_\chi = 100$ TeV. All models are sourced from the PPPC4DMID [44].

823 which reduces with a small angle approximation to $\pi\theta^2$. Next, the central difference for both the
 824 ΔJ and $\Delta\Omega$ value were calculated from the discretized $J(\theta)$ with the central difference stencil:

$$\Delta\phi_i = \phi_{i+1} - \phi_{i-1} \quad (5.4)$$

825 Where ϕ is either Ω or J . These were done separately in case the grid spacing in θ was not uniform.
 826 Finally, these lists are divided so that we are left with an approximation of the $dJ/d\Omega$ profile that
 827 is a function of θ . Admittedly, this is an approximation method for the map which introduces small
 828 errors compared to the true profile estimate. This was checked as a systematic against the author's
 829 profiling of the spatial distribution and is documented in Section 5.8.1.

830 With $\frac{dJ}{d\Omega}(\theta)$, a map is generated, first by filling in the north-east quadrant of the map. This
 831 quadrant is then reflected twice, vertically then horizontally, to fill the full map. Maps are then
 832 normalized by dividing the discrete 2D integral of the map. The 2D integral was a simple height

833 of bins, Newton's integral:

$$p^2 \cdot \sum_{i,j=0}^{N,M} \frac{dJ}{d\Omega}(\theta_{i,j}, \phi_{i,j}) \quad (5.5)$$

834 These maps are HEALpix maps with NSIDE 16384 and saved in the `.fits` format.

835 Another DM spatial distribution model from Bonnivard (\mathcal{B}) [47] was used for the Glory Duck
836 study. However, to save computational time, limits from \mathcal{GS} were scaled to \mathcal{B} instead of each
837 experiment performing a full study a second time. How these models compare is demonstrated
838 for each dSph in Figure 5.16 and Figure 5.17 Plots of these maps are provided for each source
839 in chapter A Examples of the two most impactful dSphs derived from \mathcal{GS} , Segue1 and Coma
840 Berenices are featured in Figure 5.3

841 5.3.3 Source Selection and Annihilation Channels

842 We use many of the dSphs presented in HAWC's previous dSph DM search [46]. HAWC's
843 sources for Glory Duck include Boötes I, Coma Berenices, Canes Venatici I + II, Draco, Hercules,
844 Leo I, II, + IV, Segue 1, Sextans, and Ursa Major I + II. A full description of all sources used
845 in Glory Duck is found in Table 5.1. Triangulum II was excluded from the Glory Duck analysis
846 because of large uncertainties in its J factor. Ursa Minor was excluded from HAWC's contribution
847 to the combination because the source extension model extended Ursa Minor beyond HAWC's field
848 of view. Ursa Minor was not expected to contribute significantly to the combined limit, so work
849 was not invested in a solution to include Ursa Minor.

850 This analysis improves on the previous HAWC dSph paper [46] in the following ways. Pre-
851 viously, the dSphs were treated and implemented as point sources. For this analysis, dSphs are
852 modeled and treated as extended source. The impact of this change with respect to the upper limit
853 is source dependent and is explored in Section 5.7.2. Previously, the particle physics model used for
854 gamma-ray spectra from DM annihilation did not have EW corrections where the PPPC includes
855 them. Finally, the gamma-ray ray dataset is much larger. The study performed here analyzes over
856 1000 days of data compared to 507.

857 The SM annihilation channels probed for the Glory Duck combination include $b\bar{b}$, $e\bar{e}$, $\mu\bar{\mu}$, $\tau\bar{\tau}$,
858 $t\bar{t}$, W^+W^- , and ZZ . A summary of all sources, with a description of each experiments' sensitivity

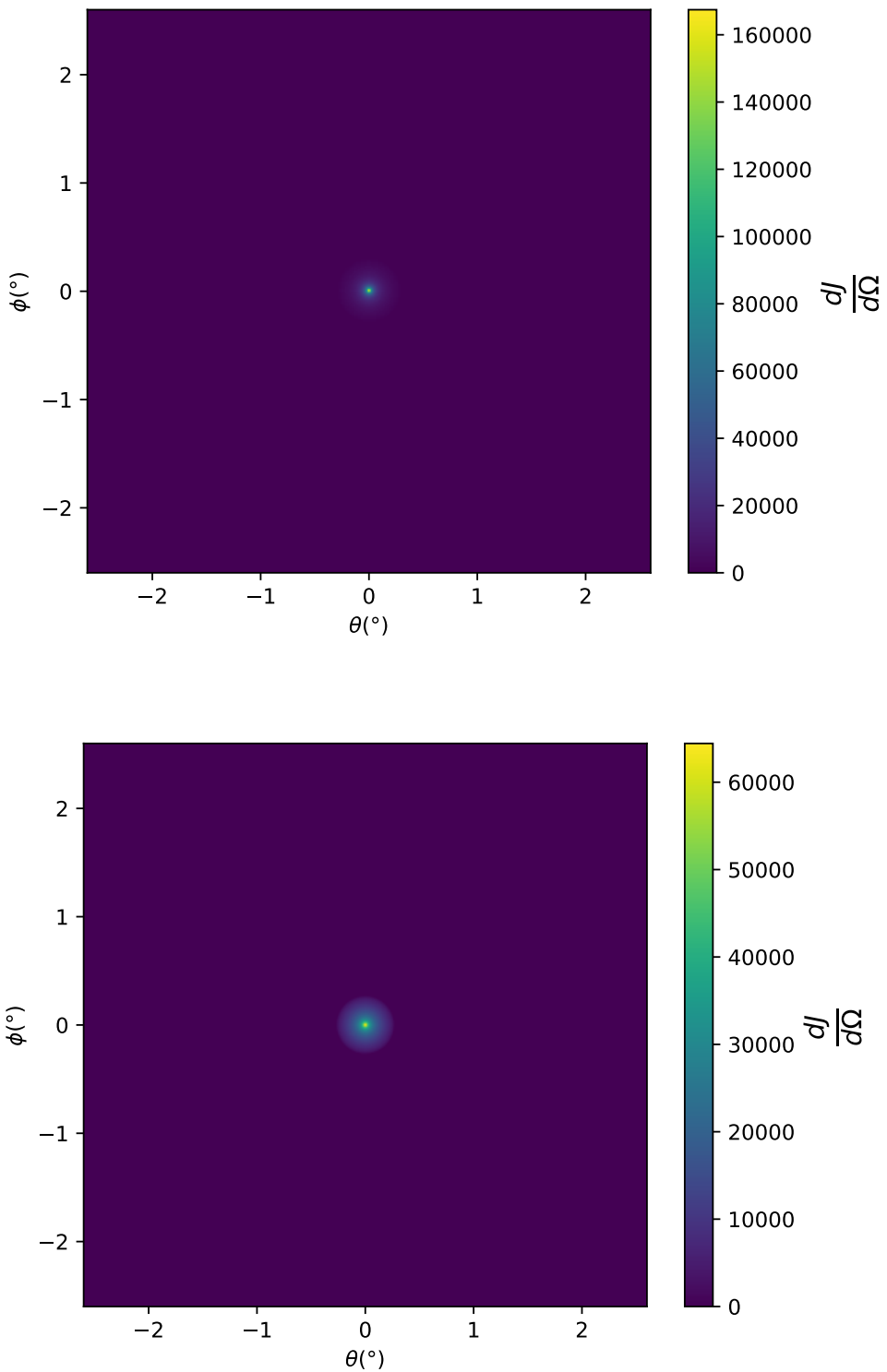


Figure 5.3 $\frac{dJ}{d\Omega}$ maps for Segue1 (top) and Coma Berenices (bottom). Origin is centered on the specific dwarf spheroidal galaxies (dSph). X and Y axes are the angular separation from the center of the dwarf. Plots of the remaining 11 dSph HAWC studied are linked in Fig. A.1.

Table 5.1 Summary of the relevant properties of the dSphs used in the present work. Column 1 lists the dSphs. Columns 2 and 3 present their heliocentric distance and galactic coordinates, respectively. Columns 4 and 5 report the J -factors of each source given from the \mathcal{GS} and \mathcal{B} independent studies and their estimated $\pm 1\sigma$ uncertainties. The values $\log_{10} J$ (\mathcal{GS} set) [45] correspond to the mean J -factor values for a source extension truncated at the outermost observed star. The values $\log_{10} J$ (\mathcal{B} set) [47] are provided for a source extension at the tidal radius of each dSph. **Bolded sources are within HAWC’s field of view and provided to the Glory Duck analysis.**

Name	Distance (kpc)	l, b ($^{\circ}$)	$\log_{10} J$ (\mathcal{GS} set) $\log_{10}(\text{GeV}^2 \text{cm}^{-5} \text{sr})$	$\log_{10} J$ (\mathcal{B} set) $\log_{10}(\text{GeV}^2 \text{cm}^{-5} \text{sr})$
Boötes I	66	358.08, 69.62	$18.24^{+0.40}_{-0.37}$	$18.85^{+1.10}_{-0.61}$
Canes Venatici I	218	74.31, 79.82	$17.44^{+0.37}_{-0.28}$	$17.63^{+0.50}_{-0.20}$
Canes Venatici II	160	113.58, 82.70	$17.65^{+0.45}_{-0.43}$	$18.67^{+1.54}_{-0.97}$
Carina	105	260.11, -22.22	$17.92^{+0.19}_{-0.11}$	$18.02^{+0.36}_{-0.15}$
Coma Berenices	44	241.89, 83.61	$19.02^{+0.37}_{-0.41}$	$20.13^{+1.56}_{-1.08}$
Draco	76	86.37, 34.72	$19.05^{+0.22}_{-0.21}$	$19.42^{+0.92}_{-0.47}$
Fornax	147	237.10, -65.65	$17.84^{+0.11}_{-0.06}$	$17.85^{+0.11}_{-0.08}$
Hercules	132	28.73, 36.87	$16.86^{+0.74}_{-0.68}$	$17.70^{+1.08}_{-0.73}$
Leo I	254	225.99, 49.11	$17.84^{+0.20}_{-0.16}$	$17.93^{+0.65}_{-0.25}$
Leo II	233	220.17, 67.23	$17.97^{+0.20}_{-0.18}$	$18.11^{+0.71}_{-0.25}$
Leo IV	154	265.44, 56.51	$16.32^{+1.06}_{-1.70}$	$16.36^{+1.44}_{-1.65}$
Leo V	178	261.86, 58.54	$16.37^{+0.94}_{-0.87}$	$16.30^{+1.33}_{-1.16}$
Leo T	417	214.85, 43.66	$17.11^{+0.44}_{-0.39}$	$17.67^{+1.01}_{-0.56}$
Sculptor	86	287.53, -83.16	$18.57^{+0.07}_{-0.05}$	$18.63^{+0.14}_{-0.08}$
Segue I	23	220.48, 50.43	$19.36^{+0.32}_{-0.35}$	$17.52^{+2.54}_{-2.65}$
Segue II	35	149.43, -38.14	$16.21^{+1.06}_{-0.98}$	$19.50^{+1.82}_{-1.48}$
Sextans	86	243.50, 42.27	$17.92^{+0.35}_{-0.29}$	$18.04^{+0.50}_{-0.28}$
Ursa Major I	97	159.43, 54.41	$17.87^{+0.56}_{-0.33}$	$18.84^{+0.97}_{-0.43}$
Ursa Major II	32	152.46, 37.44	$19.42^{+0.44}_{-0.42}$	$20.60^{+1.46}_{-0.95}$
Ursa Minor	76	104.97, 44.80	$18.95^{+0.26}_{-0.18}$	$19.08^{+0.21}_{-0.13}$

859 to the source, is provided in Table 5.2.

860 5.4 Likelihood Methods

861 5.4.1 HAWC Likelihoods

862 For every analysis bin in energy, f_{hit} bins (1-9), and location, we can expect N signal events and
863 B background events. The expected number of excess signal events from dark matter annihilation,

Table 5.2 Summary of dSph observations by each experiment used in this work. A ‘-’ indicates the experiment did not observe the dSph for this study. For Fermi-LAT, the exposure at 1 GeV is given. For HAWC, $|\Delta\theta|$ is the absolute difference between the source declination and HAWC latitude. HAWC is more sensitive to sources with smaller $|\Delta\theta|$. For IACTs, we show the zenith angle range, the total exposure, the energy range, the angular radius θ of the signal or ON region, the ratio of exposures between the background-control (OFF) and signal (ON) regions (τ), and the significance of gamma-ray excess in standard deviations, σ .

Source name	Fermi-LAT	HAWC	H.E.S.S, MAGIC, VERITAS						
	Exposure (10^{11} s m 2)	$ \Delta\theta $ (°)	IACT	Zenith (°)	Exposure (h)	Energy range (GeV)	θ (°)	τ	S (σ)
Boötes I	2.6	4.5	VERITAS	15 – 30	14.0	100–41000	0.10	8.6	-1.0
Canes Venatici I	2.9	14.6	–	–	–	–	–	–	–
Canes Venatici II	2.9	15.3	–	–	–	–	–	–	–
Carina	3.1	–	H.E.S.S.	27 – 46	23.7	310 – 70000	0.10	18.0	-0.3
Coma Berenices	2.7	4.9	H.E.S.S.	47 – 49	11.4	550 – 70000	0.10	14.4	-0.4
			MAGIC	5 – 37	49.5	60 – 10000	0.17	1.0	–
			MAGIC	29 – 45	52.1	70 – 10000	0.22	1.0	–
Draco	3.8	38.1	VERITAS	25 – 40	49.8	120 – 70000	0.10	9.0	-1.0
Fornax	2.7	–	H.E.S.S.	11 – 25	6.8	230 – 70000	0.10	45.5	-1.5
Hercules	2.8	6.3	–	–	–	–	–	–	–
Leo I	2.5	6.7	–	–	–	–	–	–	–
Leo II	2.6	3.1	–	–	–	–	–	–	–
Leo IV	2.4	19.5	–	–	–	–	–	–	–
Leo V	2.4	–	–	–	–	–	–	–	–
Leo T	2.6	–	–	–	–	–	–	–	–
Sculptor	2.7	–	H.E.S.S.	10 – 46	11.8	200 – 70000	0.10	19.8	-2.2
Segue I	2.5	2.9	MAGIC	13 – 37	158.0	60 – 10000	0.12	1.0	-0.5
			VERITAS	15 – 35	92.0	80 – 50000	0.10	7.6	0.7
Segue II	2.7	–	–	–	–	–	–	–	–
Sextans	2.4	20.6	–	–	–	–	–	–	–
Ursa Major I	3.4	32.9	–	–	–	–	–	–	–
Ursa Major II	4.0	44.1	MAGIC	35 – 45	94.8	120 – 10000	0.30	1.0	-2.1
Ursa Minor	4.1	–	VERITAS	35 – 45	60.4	160 – 93000	0.10	8.4	-0.1

864 S , is estimated by convolving Equation (7.1) with HAWC's energy response and pixel point spread
 865 functions. I then compute the test statistic (TS) with the log-likelihood ratio test,

$$\text{TS} = -2 \ln \left(\frac{\mathcal{L}_0}{\mathcal{L}^{\max}} \right) \quad (5.6)$$

867 where \mathcal{L}_0 is the null hypothesis, or no DM emission, likelihood. \mathcal{L}^{\max} is the best fit signal
 868 hypothesis where $\langle \sigma v \rangle$ maximizes the likelihood. We calculate the likelihood of each source and
 869 model, assuming events are Poisson distributed, with

$$\mathcal{L} = \prod_i \frac{(B_i + S_i)^{N_i} e^{-(B_i + S_i)}}{N_i!} \quad (5.7)$$

870 where S_i is the sum of expected number of signal counts. B_i is the number of background counts
 871 observed. N_i is the total number of counts.

872 I also calculate an upper limit on $\langle \sigma v \rangle$ by calculating the 95% confidence level (CL). For the
 873 CL, we define a parameter, TS_{95} , as

$$\text{TS}_{95} \equiv \sum_{\text{bins}} \left[2N \ln \left(1 + \frac{\epsilon S_{\text{ref}}}{B} \right) - 2\epsilon S_{\text{ref}} \right] \quad (5.8)$$

874 where the expected signal counts from a dSph is scaled by ϵ . S_{ref} is the expected number of excess
 875 counts in a bin from DM emission from a dSph with a corresponding annihilation cross-section,
 876 $\langle \sigma v \rangle$. We scan ϵ such that

$$2.71 = \text{TS}_{\max} - \text{TS}_{95} \quad (5.9)$$

877 5.4.2 Glory Duck Joint Likelihood

878 The joint likelihood for the 5-experiment combination was done similarly as Section 5.4.1. We
 879 calculate upper limits on $\langle \sigma v \rangle$ from the TS, Eq. (5.6), and define the likelihood ratio more generally

$$\lambda(\langle \sigma v \rangle | \mathcal{D}_{\text{dSphs}}) = \frac{\mathcal{L}(\langle \sigma v \rangle; \hat{\nu} | \mathcal{D}_{\text{dSphs}})}{\mathcal{L}(\widehat{\langle \sigma v \rangle}; \hat{\nu} | \mathcal{D}_{\text{dSphs}})} \quad (5.10)$$

880 $\mathcal{D}_{\text{dSphs}}$ is the totality of observations across experiments and dSphs. ν are the nuisance parameters
 881 which are the J factors in this study. $\widehat{\langle \sigma v \rangle}$ and $\hat{\nu}$ are the respective estimate that maximize \mathcal{L}
 882 globally. Finally, $\hat{\nu}$ is the set of nuisance parameters that maximize \mathcal{L} for a fixed value of $\langle \sigma v \rangle$.

883 The *complete* joint likelihood, \mathcal{L} that encompasses all observations from all instruments and
 884 dSphs can be factorized into *partial* functions for each dSph l (with $\mathcal{L}_{\text{dSph},l}$) and its J factor (\mathcal{J}_l):

$$\mathcal{L}(\langle \sigma v \rangle; \nu | \mathcal{D}_{\text{dSphs}}) = \prod_{l=1}^{N_{\text{dSphs}}} \mathcal{L}_{\text{dSph},l}(\langle \sigma v \rangle; J_l, \nu_l | \mathcal{D}_l) \times \mathcal{J}_l(J_l | J_{l,\text{obs}}, \sigma_{\log J_l}). \quad (5.11)$$

885 For this study, $N_{\text{dSphs}} = 20$ is the number of dSphs studied. \mathcal{D}_l are the gamma-ray observations
 886 of dSph, l . ν_l are the nuisance parameters modifying the gamma-ray observations of dSph, l ,
 887 but excludes \mathcal{J}_l . \mathcal{J}_l is the J factor for dSph, l , as defined in Equation (5.2), and it is a nuisance
 888 parameter whose value is unknown. $\log_{10} J_{l,\text{obs}}$ and $\sigma_{\log J_l}$ are obtained from fitting a log-normal
 889 function of $J_{l,\text{obs}}$ to the posterior distribution of J_l [48]. $\log_{10} J_{l,\text{obs}}$ and $\sigma_{\log J_l}$ values are provided
 890 in Table 5.1. The term \mathcal{J}_l constraining J_l is written as:

$$\mathcal{J}_l(J_l | J_{l,\text{obs}}, \sigma_{\log J_l}) = \frac{1}{\ln(10)J_{l,\text{obs}}\sqrt{2\pi}\sigma_{\log J_l}} \exp\left(-\frac{(\log_{10} J_l - \log_{10} J_{l,\text{obs}})^2}{2\sigma_{\log J_l}^2}\right). \quad (5.12)$$

891 Both the \mathcal{GS} and \mathcal{B} , displayed in Table 5.1, sets of J factors are used in this analysis. Equation (5.12)
 892 is also normalized, so it can also be interpreted as a probability density function (PDF) for $J_{l,\text{obs}}$.
 893 From Equation (7.1), we can also see that $\langle \sigma v \rangle$ and J_l are degenerate when computing $\mathcal{L}_{\text{dSph},l}$.
 894 Therefore, as noted in [49], it is sufficient to compute $\mathcal{L}_{\text{dSph},l}$ versus $\langle \sigma v \rangle$ for a fixed value of J_l .
 895 We used $J_{l,\text{obs}}(\mathcal{GS})$ reported in Tab. 5.1, in order to perform the profile of \mathcal{L} with respect to J_l .
 896 The degeneracy implies that for any $J'_l \neq J_{l,\text{obs}}$ (in practice in our case we used $J'_l = J_{l,\text{obs}}(\mathcal{B})$ to
 897 compute results from a different set of J factors):

$$\mathcal{L}_{\text{dSph},l}(\langle \sigma v \rangle; J'_l, \nu_l | \mathcal{D}_l) = \mathcal{L}_{\text{dSph},l}\left(\frac{J'_l}{J_{l,\text{obs}}} \langle \sigma v \rangle; J_{l,\text{obs}}, \nu_l | \mathcal{D}_l\right), \quad (5.13)$$

898 which is a straightforward rescaling operation that reduces the computational needs of the profiling
 899 operation since:

$$\mathcal{L}(\langle \sigma v \rangle; \hat{\nu} | \mathcal{D}_{\text{dSphs}}) = \prod_{l=1}^{N_{\text{dSphs}}} \max_{J_l} \left[\mathcal{L}_{\text{dSph},l}(\langle \sigma v \rangle; J_l, \hat{\nu}_l | \mathcal{D}_l) \times \mathcal{J}_l(J_l | J_{l,\text{obs}}, \sigma_{\log J_l}) \right]. \quad (5.14)$$

900 In addition, Eq. (5.13) enables the combination of data from different gamma-ray instruments and
 901 observed dSphs via tabulated values of $\mathcal{L}_{\text{dSph},l}$, or equivalently of λ from Eq. (5.10) as was done in

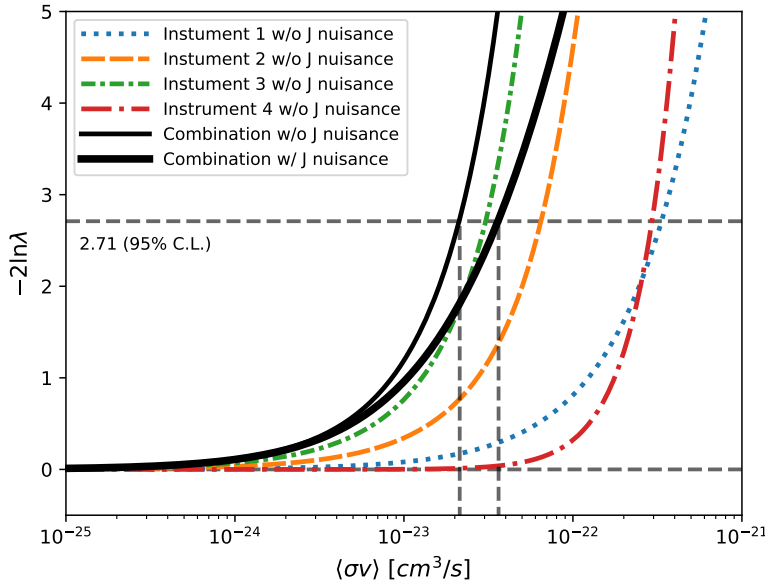


Figure 5.4 Illustration of the combination technique showing a comparison between $-2 \ln \lambda$ provided by four instruments (colored lines) from the observation of the same dSph without any J nuisance and their sum, *i.e.* the resulting combined likelihood (thin black line). According to the test statistics of Equation (5.6), the intersection of the likelihood profiles with the line $-2 \ln \lambda = 2.71$ indicates the 95% C.L. upper limit on $\langle \sigma v \rangle$. The combined likelihood (thin black line) shows a smaller value of upper limit on $\langle \sigma v \rangle$ than those derived by individual instruments. We also show how the uncertainties on the J factor effects the combined likelihood and degrade the upper limit on $\langle \sigma v \rangle$ (thick black line). All likelihood profiles are normalized so that the global minimum $\widehat{\langle \sigma v \rangle}$ is 0. We note that each profile depends on the observational conditions in which a target object was observed. The sensitivity of a given instrument can be degraded and the upper limits less constraining if the observations are performed in non-optimal conditions such as a high zenith angle or a short exposure time.

902 this work, versus $\langle \sigma v \rangle$. $\mathcal{L}_{\text{dSph},l}$ is computed for a fixed value of J_l and profiled with respect to all
 903 instrumental nuisance parameters ν_l , these nuisance parameters are discussed in more detail below.
 904 These values are produced by each detector independently and therefore there is no need to share
 905 sensitive low-level information used to produce them, such as event lists. Figure 5.4 illustrates the
 906 multi-instrument combination technique used in this study with a comparison of the upper limit
 907 on $\langle \sigma v \rangle$ obtained from the combination of the observations of four experiments towards one dSph
 908 versus the upper limit from individual instruments. It also shows graphically the effect of the
 909 J -factor uncertainty on the combined observations.

910 The *partial* joint likelihood function for gamma-ray observations of each dSph ($\mathcal{L}_{\text{dSph},l}$) is

written as the product of the likelihood terms describing the $N_{\text{exp},l}$ observations performed with any of our observatories:

$$\mathcal{L}_{\text{dSph},l} (\langle \sigma v \rangle; J_l, \nu_l | \mathcal{D}_l) = \prod_{k=1}^{N_{\text{exp},l}} \mathcal{L}_{lk} (\langle \sigma v \rangle; J_l, \nu_{lk} | \mathcal{D}_{lk}), \quad (5.15)$$

where each \mathcal{L}_{lk} term refers to an observation of the l -th dSph with associated k -th instrument responses. $N_{\text{exp},l}$ varies from dSph to dSph and can be inferred from Table 5.2.

Each collaboration separately analyzes their data for \mathcal{D}_{lk} corresponding to dSph l and gamma-ray detector k , using as many common assumptions as possible in the analysis. HAWC's treatment was described earlier in Section 5.4.1 whereas the specifics of the remaining experiments is left to the publication. We compute the values for the likelihood functions \mathcal{L}_{lk} (see Eq. (5.15)) for a fixed value of J_l and profile over the rest of the nuisance parameters ν_{lk} . Then, values of λ from Eq. (5.10) are computed as a function of $\langle \sigma v \rangle$, and shared using a common format. Results are computed for seven annihilation channels, W^+W^- , ZZ , $b\bar{b}$, $t\bar{t}$, e^+e^- , $\mu^+\mu^-$, and $\tau^+\tau^-$ over 62 m_χ values between 5 GeV and 100 TeV provided in [44]. The $\langle \sigma v \rangle$ range is defined between 10^{-28} and $10^{-18} \text{cm}^3 \cdot \text{s}^{-1}$, with 1001 logarithmically spaced values. The likelihood combination, i.e. Equation (5.11), and profile over the J -factor to compute the profile likelihood ratio λ , Equation (5.10), are carried out with two different public analysis software packages, namely `gLike` [50] and `LklCom` [51], that provide the same results [52].

As mentioned previously, each experiment computes the \mathcal{L}_{lk} from Equation (5.10) differently. The remainder of this section highlights the differences in this calculation across the experiments. Four experiments, namely *Fermi*-LAT, H.E.S.S., HAWC and MAGIC, use a binned likelihood to compute the \mathcal{L}_{lk} . For these experiments, for each observation \mathcal{D}_{lk} of a given dSph l carried out using a given gamma-ray detector k , the binned likelihood function is:

$$\mathcal{L}_{lk} (\langle \sigma v \rangle; J_l, \nu_{lk} | \mathcal{D}_{lk}) = \prod_{i=1}^{N_E} \prod_{j=1}^{N_P} \left[\mathcal{P}(s_{lk,ij}(\langle \sigma v \rangle, J_l, \nu_{lk}) + b_{lk,ij}(\nu_{lk}) | N_{lk,ij}) \right] \times \mathcal{L}_{lk,\nu} (\nu_{lk} | \mathcal{D}_{\nu_{lk}}) \quad (5.16)$$

where N_E and N_P are the number of considered bins in reconstructed energy and arrival direction, respectively; \mathcal{P} represents a Poisson PDF for the number of gamma-ray candidate events $N_{lk,ij}$

934 observed in the i -th bin in energy and j -th bin in arrival direction, when the expected number is
 935 the sum of the expected mean number of signal events s_{ij} (produced by DM annihilation) and of
 936 background events b_{ij} ; $\mathcal{L}_{lk,\nu}$ is the likelihood term for the extra ν_{lk} nuisance parameters that vary
 937 from one instrument k to another. The expected counts for signal events s_{ij} for a given dSph l and
 938 detector k is given by:

$$s_{ij}(\langle\sigma\nu\rangle, J) = \int_{E'_{\min,i}}^{E'_{\max,i}} dE' \int_{P'_{\min,j}}^{P'_{\max,j}} d\Omega' \int_0^\infty dE \int_{\Delta\Omega_{tot}} d\Omega \int_0^{T_{\text{obs}}} dt \frac{d^2\Phi(\langle\sigma\nu\rangle, J)}{dEd\Omega} \text{IRF}(E', P' | E, P, t) \quad (5.17)$$

939 where E' and E are the reconstructed and true energies, P' and P the reconstructed and true
 940 arrival directions; $E'_{\min,i}$, $P'_{\min,j}$, $E'_{\max,i}$, and $P'_{\max,j}$ are their lower and upper limits of the i -th
 941 energy bin and the j -th arrival direction bin; T_{obs} is the (dead-time corrected) total observation
 942 time; t is the time along the observations; $d^2\Phi/dEd\Omega$ is the DM flux in the source region (see
 943 Equation (7.1)); and $\text{IRF}(E', P' | E, P, t)$ is the IRF, which can be factorized as the product of the
 944 effective collection area of the detector $A_{\text{eff}}(E, P, t)$, the PDFs for the energy estimator $f_E(E' | E, t)$,
 945 and arrival direction $f_P(P' | E, P, t)$ estimators. Note that for Fermi-LAT, HAWC, MAGIC, and
 946 VERITAS the effect of the finite angular resolution is taken into account through the convolution
 947 of $d\Phi/dEd\Omega$ with f_P in Equation (5.17), whereas in the cases of H.E.S.S. f_P is approximated by a
 948 delta function. This approximation has been made in order to maintain compatibility of the result
 949 with what has been previously published. The difference introduced by this approximation is $< 5\%$
 950 for all considered dSphs. A more comprehensive review of the differences between the analyses of
 951 different instruments can be found in [25].

952 5.5 HAWC Results

953 13 of the 20 dSphs considered for the Glory Duck analysis are within HAWC's field of view.
 954 These dSph are analyzed for emission from DM annihilation according to the likelihood method
 955 described in Section 5.4. The 13 likelihood profiles are then stacked to synthesize a combined
 956 limit on the dark matter cross-section, $\langle\sigma\nu\rangle$. This combination is done for the 7 SM annihilation
 957 channels used in the Glory Duck analysis. Figure 5.5 shows the combined limit for all annihilation
 958 channels with HAWC only observations. We also perform 300 studies of Poisson trials on the

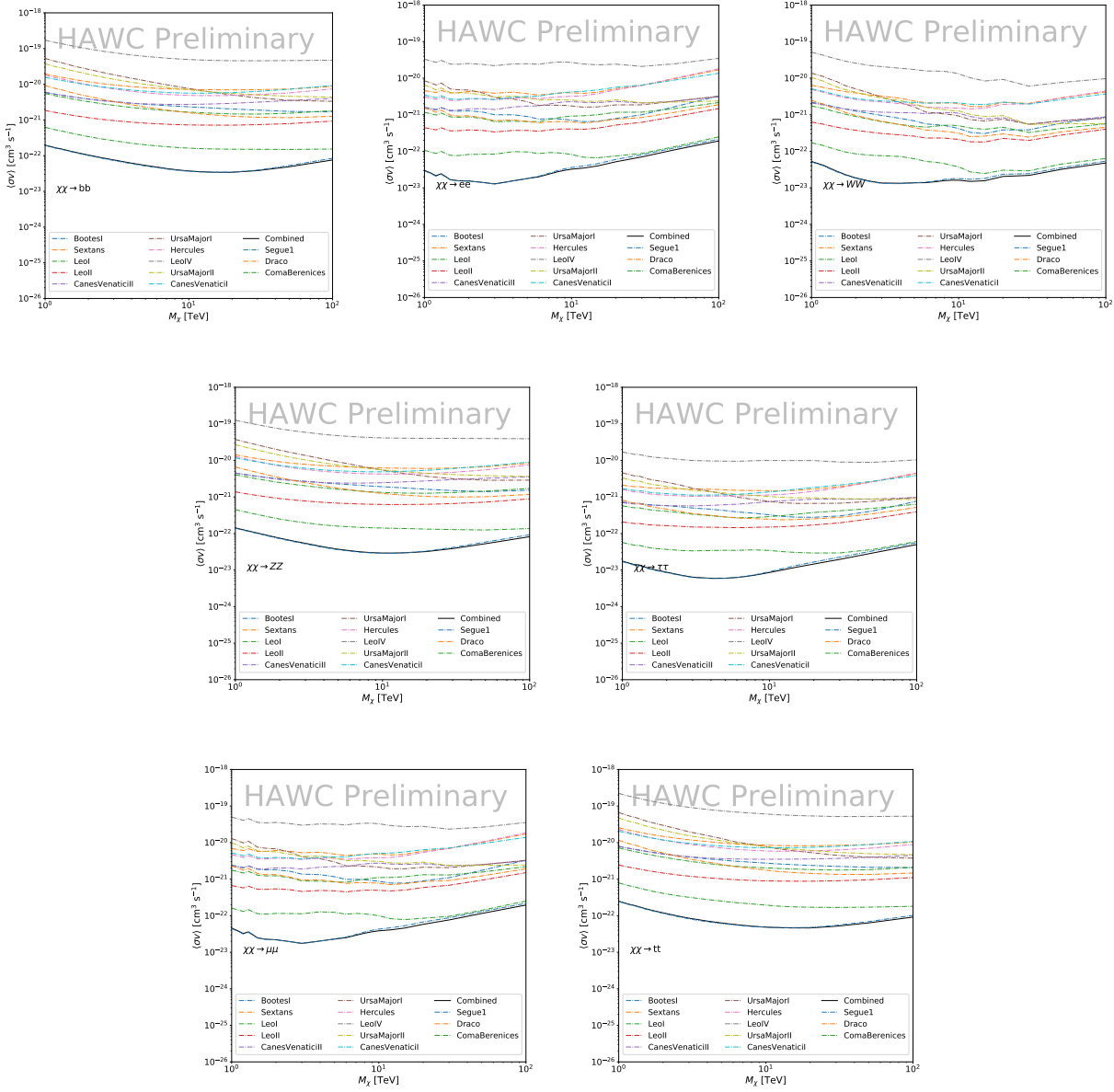


Figure 5.5

background. These trials are used to produce HAWC Brazil bands which were shared with the other collaborators for combined Brazil Bands. The results on fitting to HAWC's Poisson trials of the DM hypothesis is shown in Figure 5.7 for all the DM annihilation channels studied for Glory Duck.

No DM was found in HAWC observations. HAWC's limits are dominated by the dSphs Segue1 and Coma Berenices. The remaining 11 dSphs do not contribute significantly to the limit because

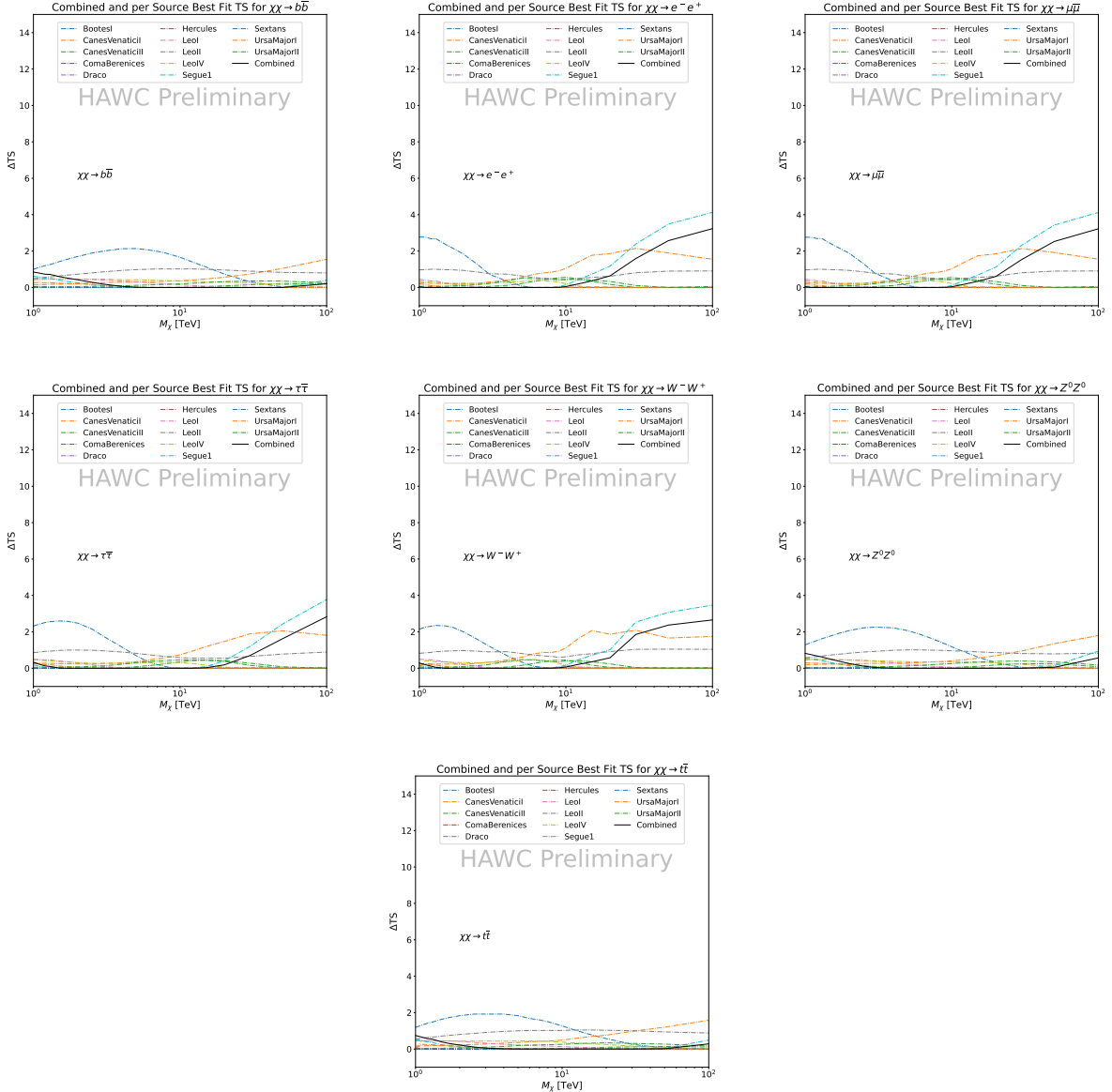


Figure 5.6 HAWC TS values for best fit $\langle\sigma v\rangle$ versus m_χ for seven SM annihilation channels with J factors from \mathcal{GS} . The solid black line shows the combined best fit TS values. The colored, dashed lines are the TS values for each of the 13 sources HAWC studied.

965 they are at high zenith and/or have much smaller J factors. Even though some remaining dSphs
 966 have large J factors, they are towards the edge of HAWC's field of view where HAWC analysis is
 967 less sensitive.

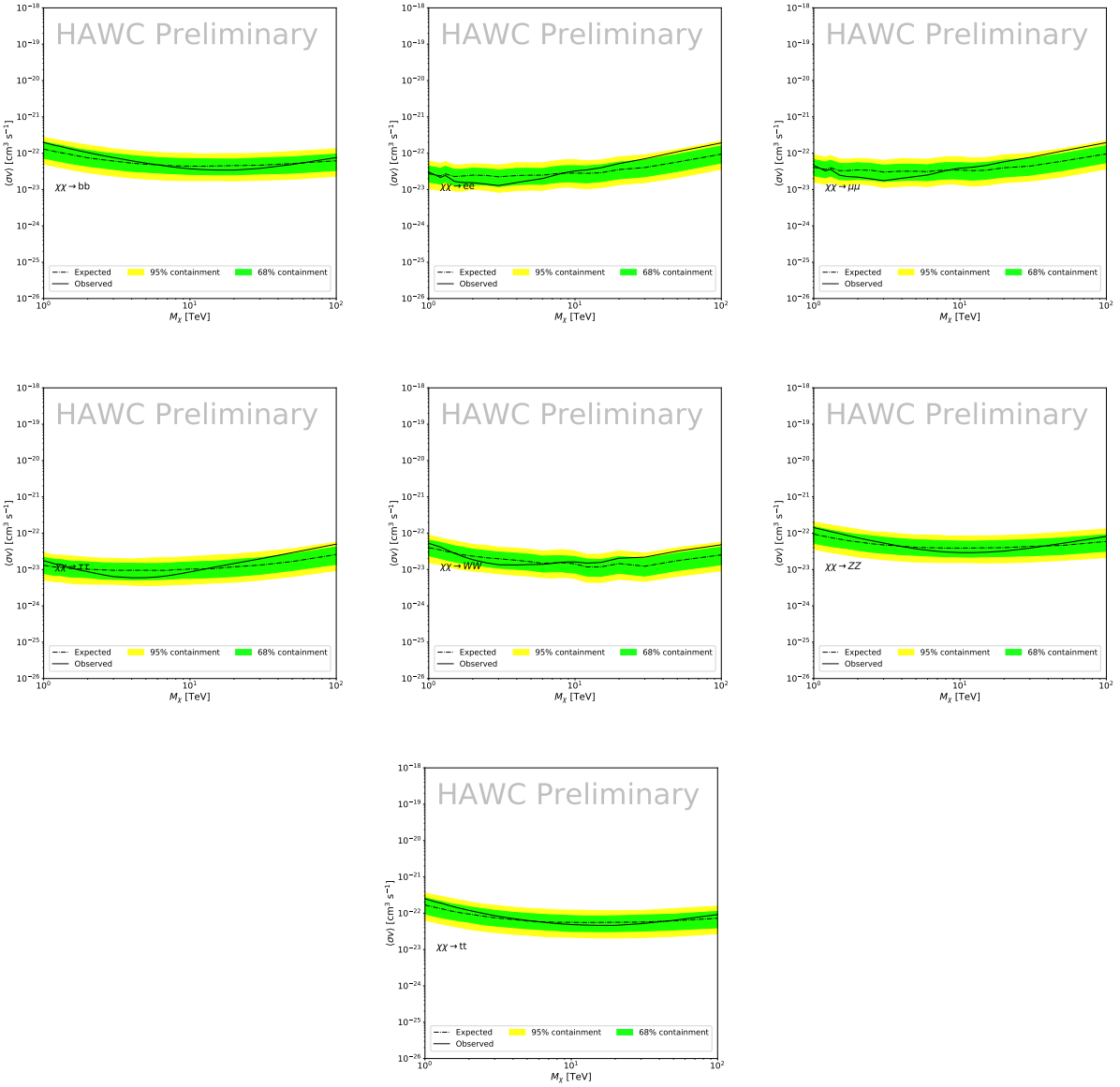


Figure 5.7 HAWC Brazil bands at 95% confidence level on $\langle\sigma v\rangle$ versus DM mass for seven annihilation channels with J -factors from \mathcal{GS} [53]. The solid line represents the combined limit from 13 dSphs. The dashed line is the expected limit. The green band is the 68% containment. The yellow band is the 95% containment.

968 5.6 Glory Duck Combined Results

969 The crux of this analysis is that HAWC's results are combined with 4 other gamma-ray observa-
 970 tories: Fermi-LAT, H.E.S.S., MAGIC, and VERITAS. No significant DM emission was observed
 971 by any of the five instruments. We present the upper limits on $\langle\sigma v\rangle$ assuming seven independent
 972 DM self annihilation channels, namely W^+W^- , Z^+Z^- , $b\bar{b}$, $t\bar{t}$, e^+e^- , $\mu^+\mu^-$, and $\tau^+\tau^-$. The 68%

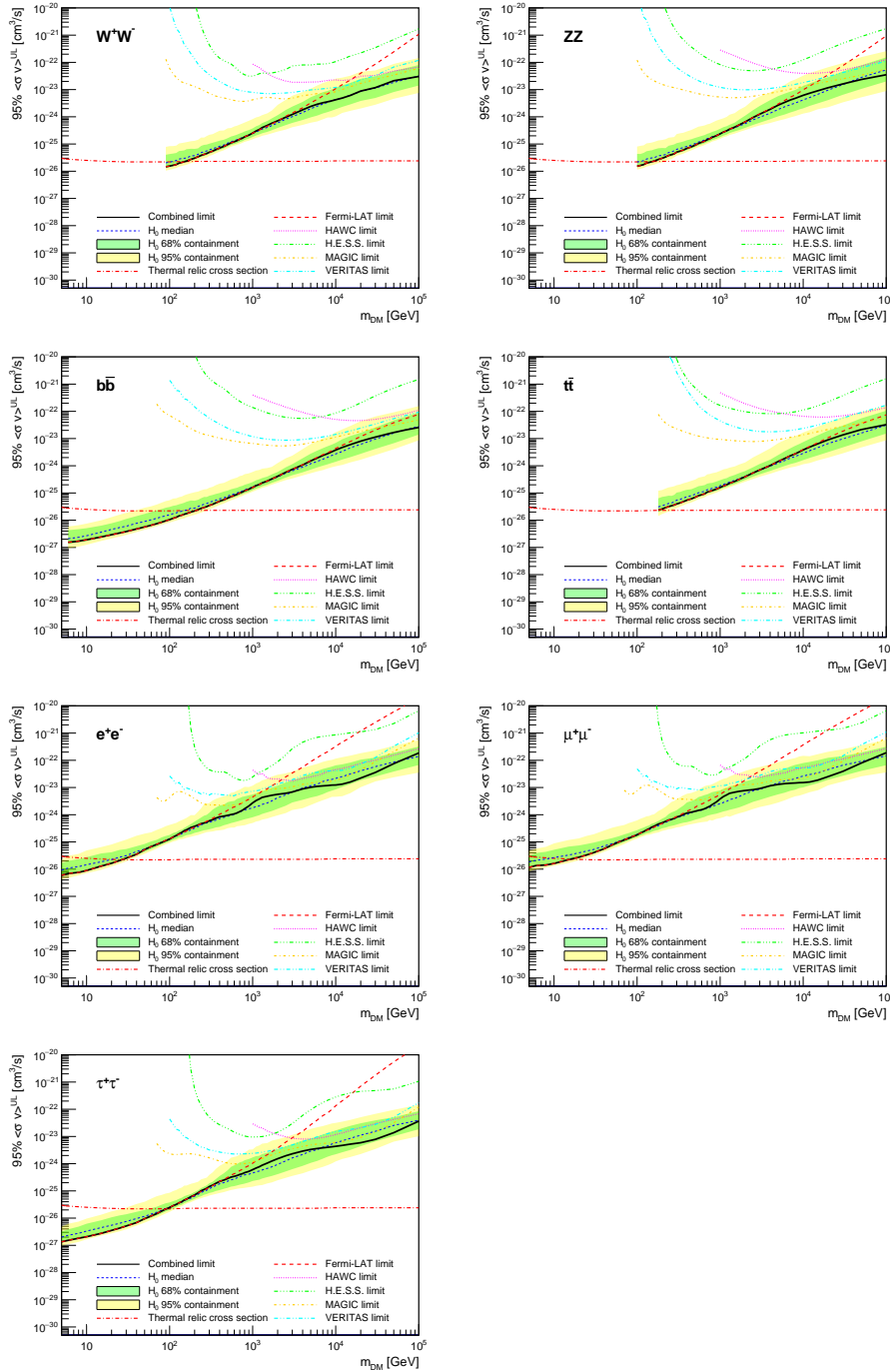


Figure 5.8 Upper limits at 95% confidence level on $\langle\sigma v\rangle$ in function of the DM mass for eight annihilation channels, using the set of J factors from Ref. [53] (\mathcal{GS} set in Table 5.1). The black solid line represents the observed combined limit, the black dashed line is the median of the null hypothesis corresponding to the expected limit, while the green and yellow bands show the 68% and 95% containment bands. Combined upper limits for each individual detector are also indicated as solid, colored lines. The value of the thermal relic cross-section in function of the DM mass is given as the red dotted-dashed line [54].

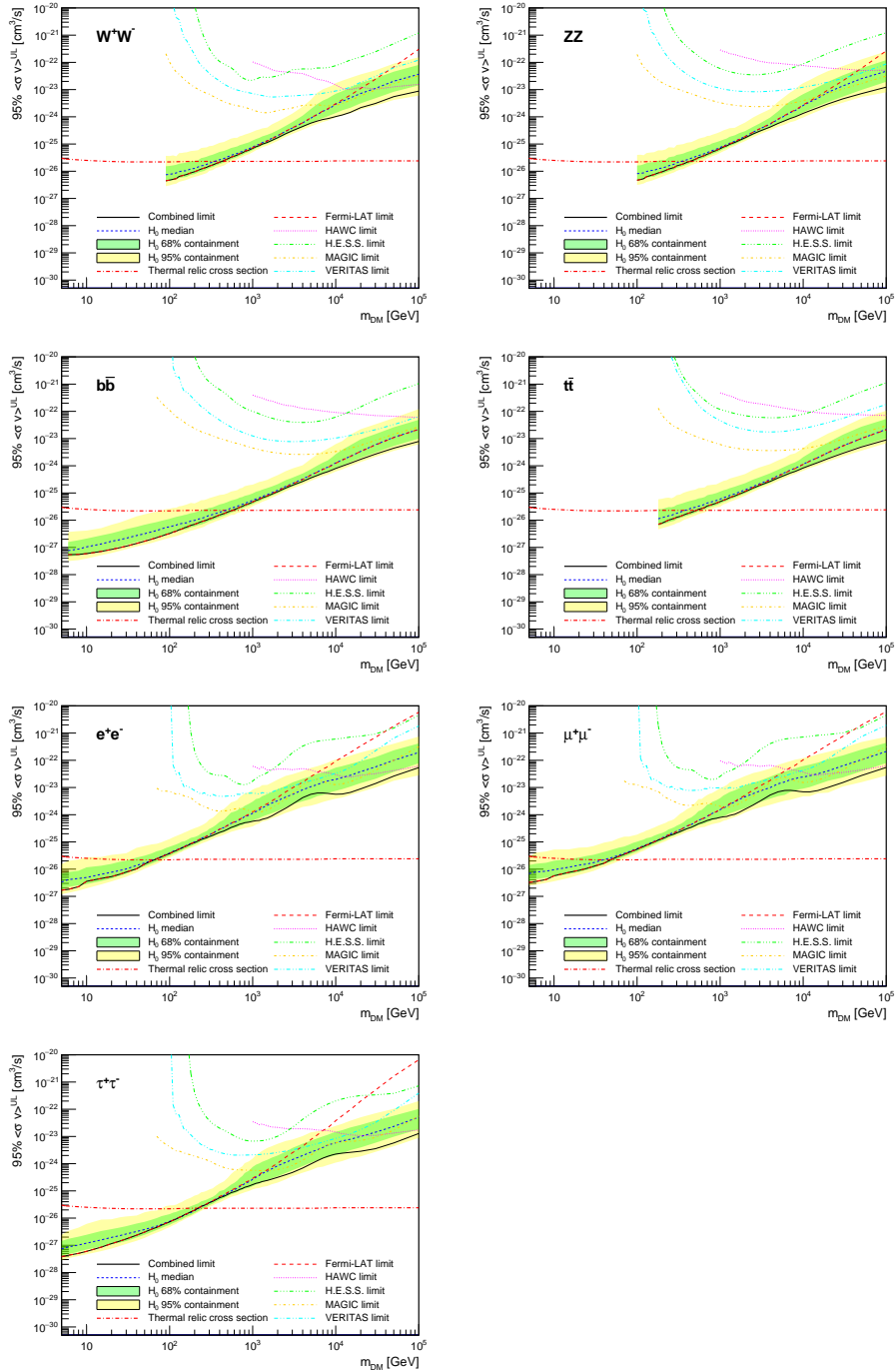


Figure 5.9 Same as Fig. 5.8, using the set of J factors from Ref. [47, 55] (\mathcal{B} set in Table 5.1).

and 95% containment bands are produced from 300 Poisson realizations of the null hypothesis corresponding to each of the combined datasets. These 300 realizations are combined identically to dSph observations. The containment bands and the median are extracted from the distribution of resulting limits on the null hypothesis. These 300 realizations are obtained either by fast simu-

977 lations of the OFF observations, for H.E.S.S., MAGIC, VERITAS, and HAWC, or taken from real
978 observations of empty fields of view in the case of Fermi-LAT [48, 56, 57].

979 The obtained limits are shown in Figure 5.8 for the $\mathcal{G}\mathcal{S}$ set of J -factors [53] and in Figure 5.9
980 for the \mathcal{B} set of J -factors [47, 55]. The combined limits are presented with their 68% and 95%
981 containment bands, and are expected to be close to the median limit when no signal is present.
982 We observe agreement with the null hypothesis for all channels, within 2σ standard deviations,
983 between the observed limits and the expectations given by the median limits. Limits obtained from
984 each detector are also indicated in the figures, where limits for all dSphs observed by the specific
985 instrument have been combined.

986 Below ~ 300 GeV, the *Fermi*-LAT dominates the DM limits for all annihilation channels. From
987 ~ 300 GeV to ~ 2 TeV, *Fermi*-LAT continues to dominate for the hadronic and bosonic DM channels,
988 yet the IACTs (H.E.S.S., MAGIC, and VERITAS) and *Fermi*-LAT all contribute to the limit for
989 leptonic DM channels. For DM masses between ~ 2 TeV to ~ 10 TeV, the IACTs dominate leptonic
990 DM annihilation channels, whereas both the *Fermi*-LAT and the IACTs dominate bosonic and
991 hadronic DM annihilation channels. From ~ 10 TeV to ~ 100 TeV, both the IACTs and HAWC
992 contribute significantly to the leptonic DM limit. For hadronic and bosonic DM, the IACTs and
993 *Fermi*-LAT both contribute strongly.

994 We notice that the limits computed using the \mathcal{B} set of J -factor are always better compared to the
995 ones calculated with the $\mathcal{G}\mathcal{S}$ set. For the W^+W^- , Z^+Z^- , $b\bar{b}$, and $t\bar{t}$ channels, the ratio between the
996 limits computed with the two sets of J -factor is varying between a factor of ~ 3 and ~ 5 depending
997 on the energy, with the largest ratio around 10 TeV. For the channels e^+e^- , $\mu^+\mu^-$, and $\tau^+\tau^-$, the
998 ratio lies between ~ 2 to ~ 6 , being maximum around 1 TeV. Examining Figure 5.16 and Figure 5.17
999 in Section 5.8, these differences are explained by the fact that the \mathcal{B} set provides higher J -factors
1000 for the majority of the studied dSphs, with the notable exception of Segue I. The variation on the
1001 ratio of the limits for the two sets is due to different dSph dominating the limits depending on the
1002 energy. This pushes the range of thermal cross-section which can be excluded to higher mass. This
1003 comparison demonstrates the magnitude of systematic uncertainties associated with the choice of

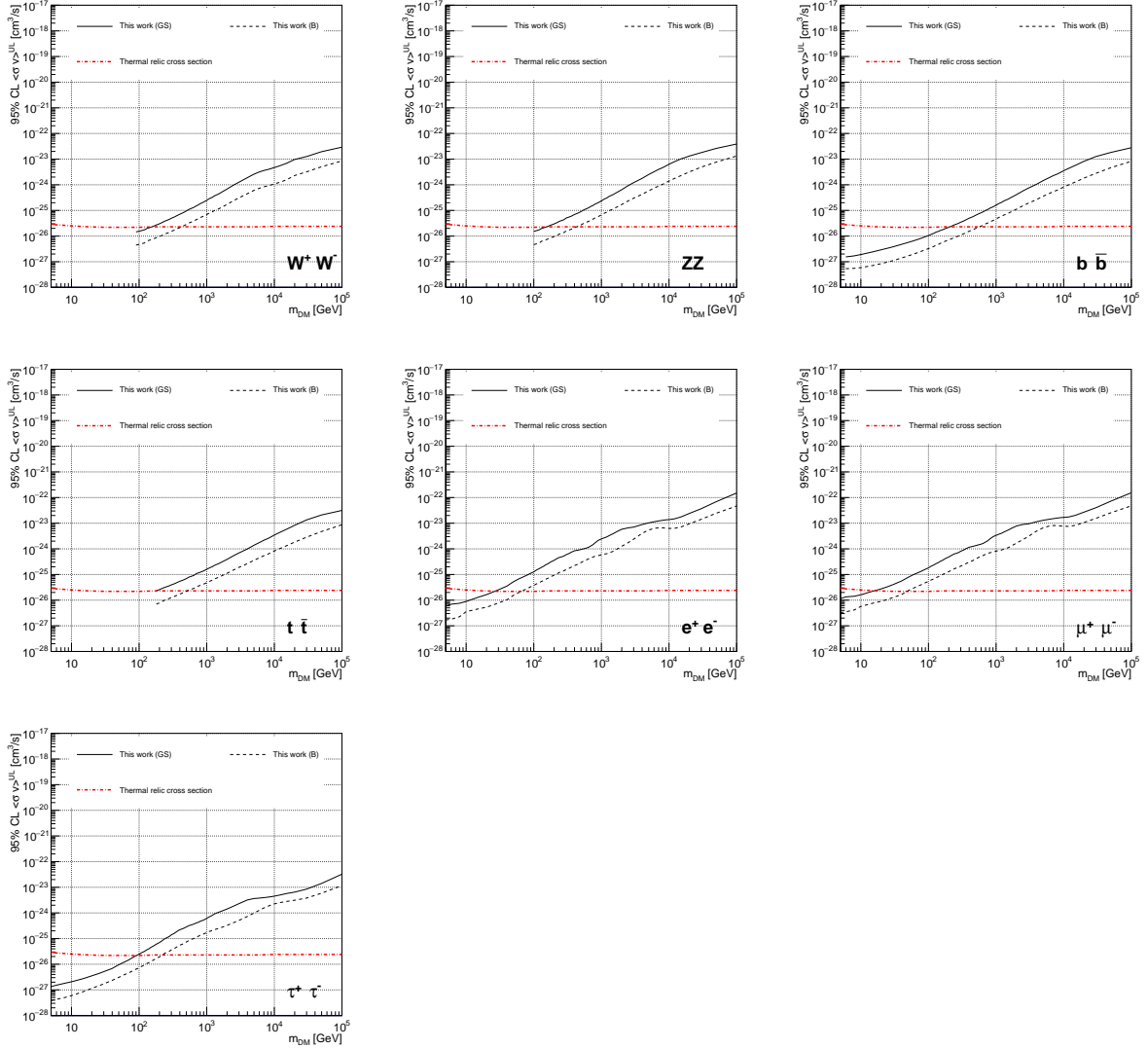


Figure 5.10 Comparisons of the combined limits at 95% confidence level for each of the eight annihilation channels when using the J factors from Ref. [53] (\mathcal{GS} set in Table 5.1), plain lines, and the J factor from Ref. [47, 55] (\mathcal{B} set in Table 5.1), dashed lines. The cross-section given by the thermal relic is also indicated [54].

1004 the J -factor

1005 This comparison demonstrates the magnitude of systematic uncertainties associated with the
 1006 choice of the J -factor calculation. The \mathcal{GS} and \mathcal{B} sets present a difference in the limits for all
 1007 channels of about This difference is explained, see Figure 5.16 and Figure 5.17 in Appendix, by the
 1008 fact that the \mathcal{B} set provides higher J factors for all dSph except for Segue I. This pushes the range
 1009 of thermal cross-section which can be excluded to higher mass.

1010 **5.7 HAWC Systematics**

1011 **5.7.1 Inverse Compton Scattering**

1012 The DM-DM annihilation channels produce many high energy electrons regardless of the
1013 primary annihilation channel. These high energy electrons can produce high energy gamma-rays
1014 through Inverse Compton Scattering (ICS). If this effect is strong, it would change the morphology
1015 of the source and increase the total expected gamma-ray counts from any source. The PPPC [44]
1016 provides tools in Mathematica for calculating the impact of ICS for an arbitrary location in the
1017 sky for a specified annihilation channel. We calculated the change in gamma-ray counts for DM
1018 annihilation to primary $e\bar{e}$ for RA and Dec corresponding to Segue1 and Coma Berenices. These
1019 dSphs were chosen because they are the strongest contributors to the limit. $e\bar{e}$ was selected because
1020 it would have the largest number of high energy electrons. The effect was found to be on the order
1021 of 10^{-7} on the gamma-ray spectrum. As a result, this systematic is not considered in our analysis.

1022 **5.7.2 Point Source Versus Extended Source Limits**

1023 The previous DM search toward dSph approximated the dSphs as point sources [46]. In
1024 this analysis, the dSphs are implemented as extended with J-factor distributions following those
1025 produced by [53]. The resolution of the cited map is much finer than HAWC's angular resolution.
1026 The vast majority of the J-factor distribution is represented on the central HAWC pixel of the dSph
1027 spatial map. However, the neighboring 8 pixels are not negligible and contribute to our limit.

1028 Figure 5.11 shows a substantial improvement to the limit for Segue1. Fig. 5.12 however showed
1029 identical limits. These disparities are best explained by the relative difference in their J-Factors.
1030 Both dSphs pass almost overhead the HAWC detector, however Segue1 has the larger J-Factor
1031 between the two. Adjacent pixels to the central pixel will therefore contribute to the limits. This is
1032 the case for other dSph that are closer to overhead the HAWC detector.

1033 Comparison plots for all sources and the combined limit can be found in the sandbox for the
1034 Glory Duck project.

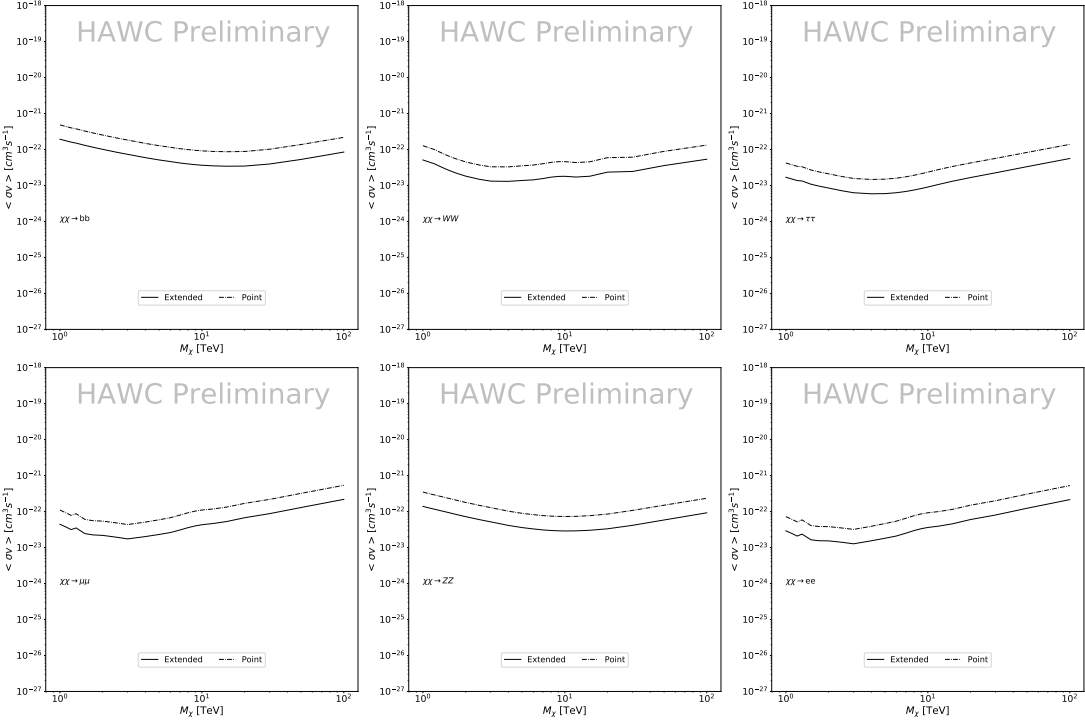


Figure 5.11 Comparisons of the combined limits at 95% confidence level for a point source analysis and extended source using [53] \mathcal{GS} J-factor distributions and PPPC [44] annihilation spectra. Shown are the limits for Segue1 which will have the most significant impact on the combined limit. 6 of the 7 DM annihilation channels are shown. Solid lines are extended source studies. Dashed lines are point source studies. Overall, the extended source analysis improves the limit by a factor of 2.

1035 5.7.3 Impact of Pointing Systematic

1036 During the analysis it was discovered that reconstruction of gamma-rays. Slides describing this
 1037 systematic can be found [here](#). Shown on the presentation is dependence on the pointing systematic
 1038 on declination. New spatial profiles were generated for every dSph and limits were computed for
 1039 the adjusted declination.

1040 Section 5.7.3 demonstrates the impact of this systematic for all DM annihilation channels
 1041 studied by HAWC. The impact is a tiny improvement, yet mostly identical, to the combined limits.

1042 5.8 J-factor distributions

1043 5.8.1 Numerical integration of \mathcal{GS} maps

1044 It was discovered well after the HAWC analysis was completed that the published tables from
 1045 \mathcal{GS} [45] quoted median J-factors were computed in a non-trivial manner. The assumption myself

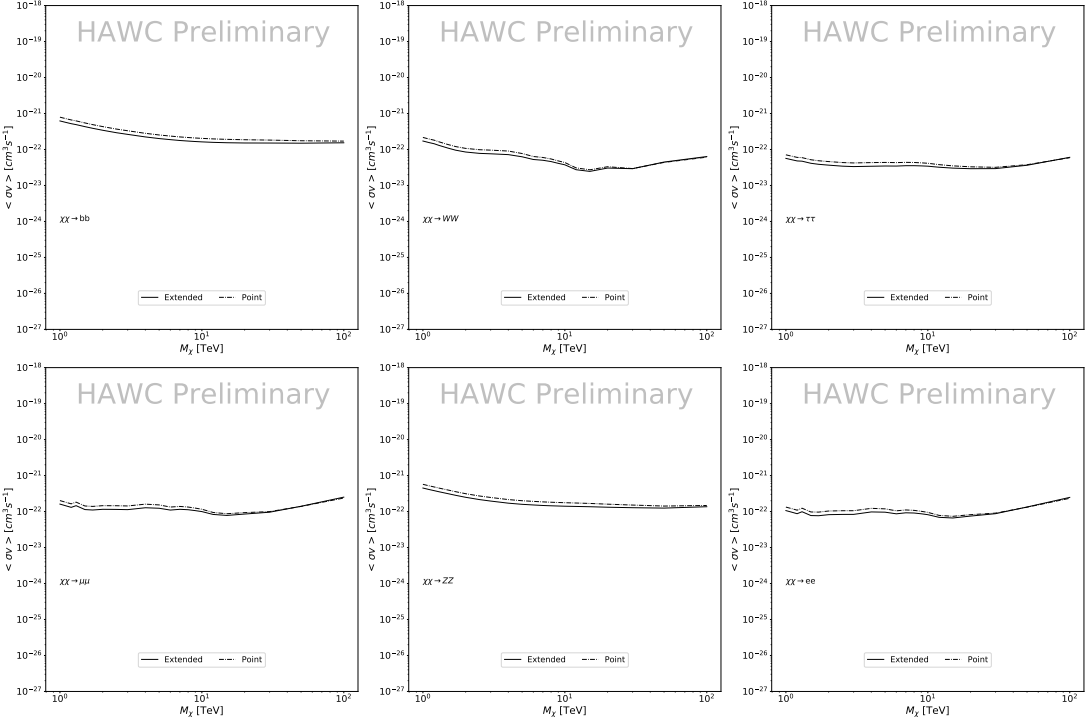


Figure 5.12 Same as Fig. 5.11 on Coma Berenices. This dSph also contributes significantly to the limit. The limits are identical in this case.

and collaborators had been that the published tables represented the J -factor as a function of θ for the best global fit model on a per-source basis. However, this is not the case. Instead, what is published are the best fit model for each dwarf that only considers stars up to the angular separation θ . Therefore, the model is changing for each value of θ for each dwarf. Yet, the introduced features from unique models at each θ are much smaller than the angular resolution of HAWC. It is not expected for these effects to impact the limits and TS greatly as a result.

Median J -factor model profiles were provided by the authors. New maps were generated and analyzed for Segue1 and Coma Berenices. Figure 5.14 shows the differential between maps generated with the method from Section 5.8.1 and from the authors of [45]. These maps were reanalyzed for all SM DM annihilation channels. Upper limits for these channels are shown in Figure 5.15

From Figure 5.15, we can see that the impact of these model difference was no substantial. The observed impact was a fractional effect which is much smaller than the impact from selecting another DM spatial distribution model as was shown in Figure 5.10.

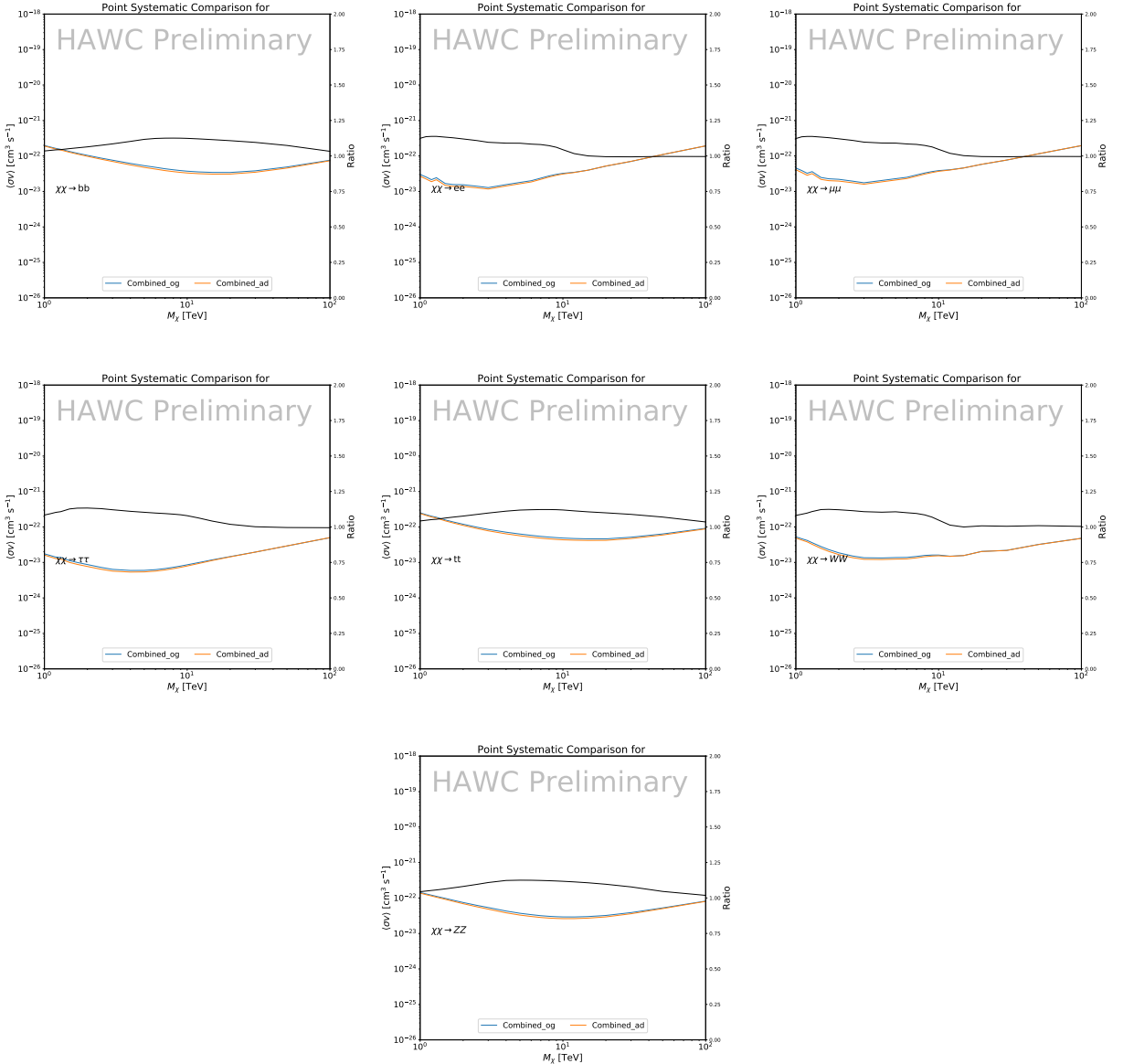


Figure 5.13 Comparison of combined limits when correcting for HAWC's pointing systematic. All DM annihilation channels are shown. The solid black line is the ratio between published limit to the declination corrected limit. The blue solid line or "Combined_og" represented the limits computed for Glory Duck. The solid orange line or "Combined_ad" represented the limits computed after correcting for the pointing systematic.

1060 5.8.2 $\mathcal{G}\mathcal{S}$ Versus \mathcal{B} spatial models

1061 We show in this appendix a comparison between the J -factors computed by Geringer-Sameth
 1062 *et al.* [53] (the $\mathcal{G}\mathcal{S}$ set) and the ones computed by Bonnivard *et al.* [47, 55] (the \mathcal{B} set). The
 1063 $\mathcal{G}\mathcal{S}$ J -factors are computed through a Jeans analysis of the kinematic stellar data of the selected

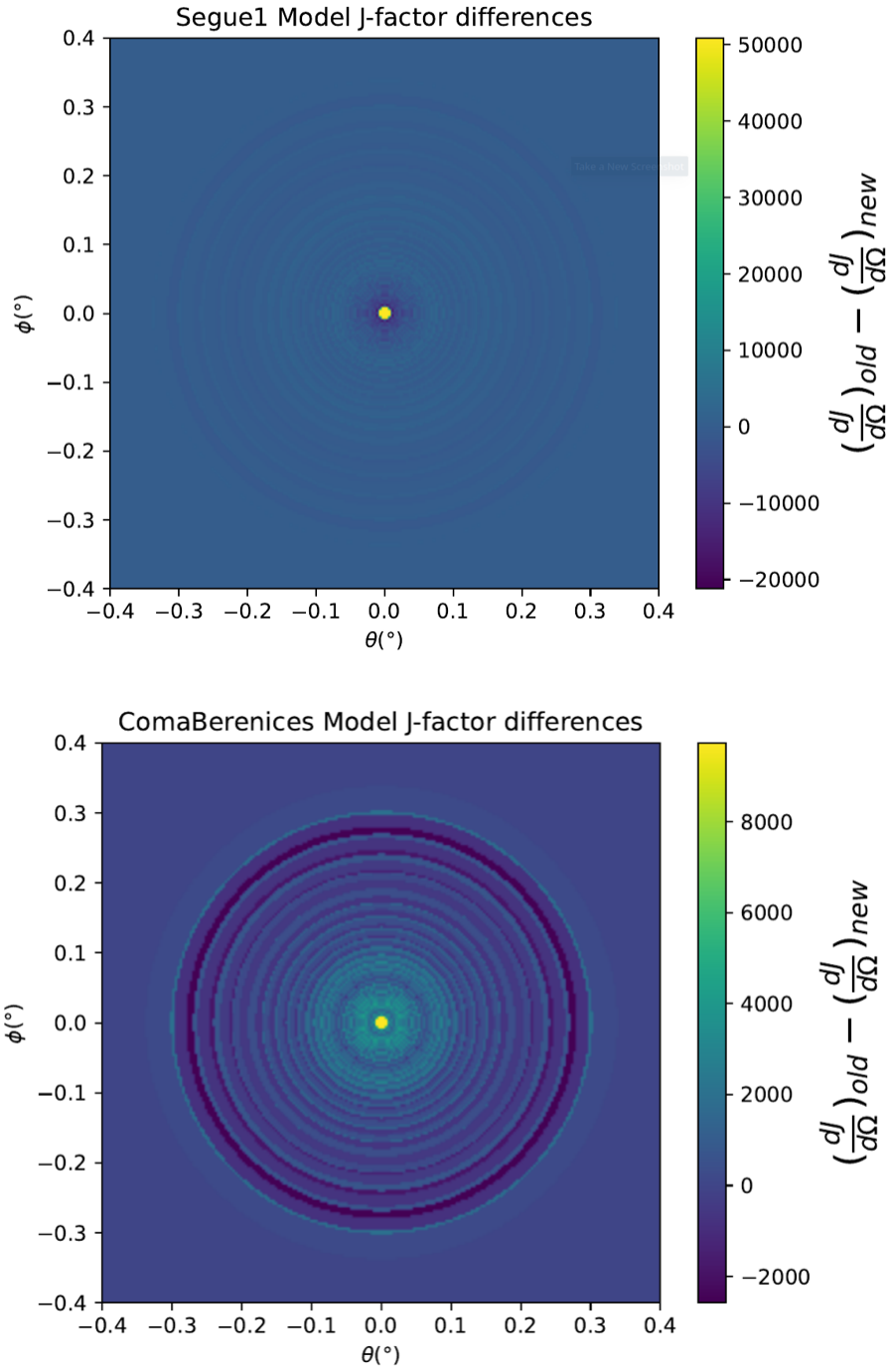


Figure 5.14 Differential map of dJ/Ω from model built in Section 5.8.1 and profiles provided directly from authors. (Top) Differential from Segue1. (bottom) Differential from Coma Berenices. Note that their scales are not the same. Segue1 shows the deepest discrepancies which is congruent with its large uncertainties. Both models show anuli where unique models become apparent.

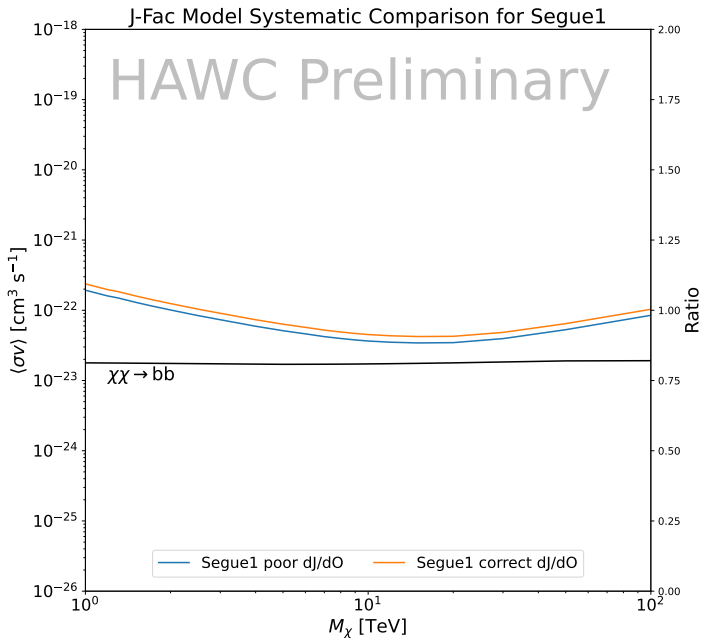
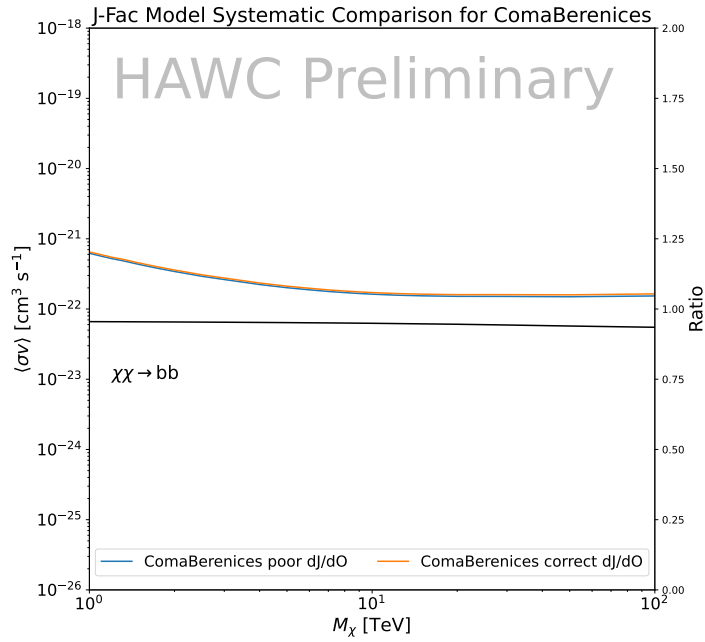


Figure 5.15 HAWC limits for Coma Berenices (top) and Segue1 (bottom) for two different map sets. Blue lines are limits calculated on maps with poor model representation. Orange lines are limits calculated on spatial profiles provided by the authors of [45]. Black line is the ratio of the poor spatial model limits to the corrected spatial models. The left y-axis measures $\langle \sigma v \rangle$ for the blue and orange lines. The right y-axis measures the ratio and is unitless.

1064 dSphs, assuming a dynamic equilibrium and a spherical symmetry for the dSphs. They adopted
1065 the generalized DM density distribution, known as Zhao-Hernquist, introduced by [58], carrying
1066 three additional index parameters to describe the inner and outer slopes, and the break of the
1067 density profile. Such a profile parametrization allows the reduction of the theoretical bias from
1068 the choice of a specific radial dependency on the kinematic data. In other words, the increase of
1069 free parameters with the use of the Zhao-Hernquist profile allows a better description of the mass
1070 density distribution of dark matter.

1071 In addition, a constant velocity anisotropy profile and a Plummer light profile [59] for the stellar
1072 distribution were assumed. The velocity anisotropy profile depends on the radial and tangential
1073 velocity dispersion. However, its determination remains challenging since only the line-of-sight
1074 velocity dispersion can be derived from velocity measurements. Therefore, the parametrization of
1075 the anisotropy profile is obtained from simulated halos (see [60] for more details). They provide the
1076 values of the J -factors of regions extending to various angular radius up to the outermost member
1077 star.

1078 The \mathcal{B} J -factors were computed through a Jeans analysis taking into account the systematic
1079 uncertainties induced by the DM profile parametrization, the radial velocity anisotropy profile, and
1080 the triaxiality of the halo of the dwarf galaxies. They performed a more complete study of the dSph
1081 kinematics and dynamics than \mathcal{GS} for the determination of the J -factor. Conservative values of the
1082 J -factors where obtained using an Einasto DM density profile [61], a realistic anisotropy profile
1083 known as the Baes & Van Hese profile [62] which takes into account that the inner regions can be
1084 significantly non-isotropic, and a Zhao-Hernquist light profile [58].

1085 For both sets, J -factor values are provided for all dSphs as a function of the radius of the
1086 integration region [53, 47, 55]. Table 5.1 shows the heliocentric distance and Galactic coordinates
1087 of the twenty dSphs, together with the two sets of J -factor values integrated up to the outermost
1088 observed star for \mathcal{GS} and the tidal radius for \mathcal{B} . Both J -factor sets were derived through a Jeans
1089 analysis based on the same kinematic data, except for Draco where the measurements of [63] have
1090 been adopted in the computation of the \mathcal{B} value. The computations for producing the \mathcal{GS} and \mathcal{B}

1091 samples differ in the choice of the DM density, velocity anisotropy, and light profiles, for which the
1092 set \mathcal{B} takes into account some sources of systematic uncertainties.

1093 Figure 5.16 and Figure 5.17 show the comparisons for the J -factor versus the angular radius
1094 for each of the 20 dSphs used in this study. The uncertainties provided by the authors are also
1095 indicated in the figures. For the \mathcal{GS} set, the computation stops at the angular radius corresponding
1096 to the outermost observed star, while for the \mathcal{B} set, the computation stops at the angular radius
1097 corresponding to the tidal radius.

1098 5.9 Discussion and Conclusions

1099 In this multi-instrument analysis, we have used observations of 20 dSphs from the gamma-ray
1100 telescopes Fermi-LAT, H.E.S.S., MAGIC, VERITAS, and HAWC to perform a collective DM
1101 search annihilation signals. The data were combined across sources and detectors to significantly
1102 increase the sensitivity of the search. We have observed no significant deviation from the null, no
1103 DM, hypothesis, and so present our results in terms of upper limits on the annihilation cross-section
1104 for seven potential DM annihilation channels.

1105 Fermi-LAT brings the most stringent constraints for continuum channels below approximately
1106 1 TeV. The remaining detectors dominate at higher energies. Overall, for multi-TeV DM mass,
1107 the combined DM constraints from all five telescopes are 2-3 times stronger than any individual
1108 telescope for multi-TeV DM.

1109 Derived from observations of many dSphs, our results produce robust limits given the DM
1110 content of the dSphs is relatively well constrained. The obtained limits span the largest mass
1111 range of any WIMP DM search. Our combined analysis improves the sensitivity over previously
1112 published results from each detector which produces the most stringent limits on DM annihilation
1113 from dSphs. These results are based on deep exposures of the most promising known dSphs with
1114 the currently most sensitive gamma-ray instruments. Therefore, our results constitute a legacy of
1115 a generation of gamma-ray instruments on WIMP DM searches towards dSphs. Our results will
1116 remain the reference in the field until a new generation of more sensitive gamma-ray instruments
1117 begin operations, or until new dSphs with higher J -factors are discovered.

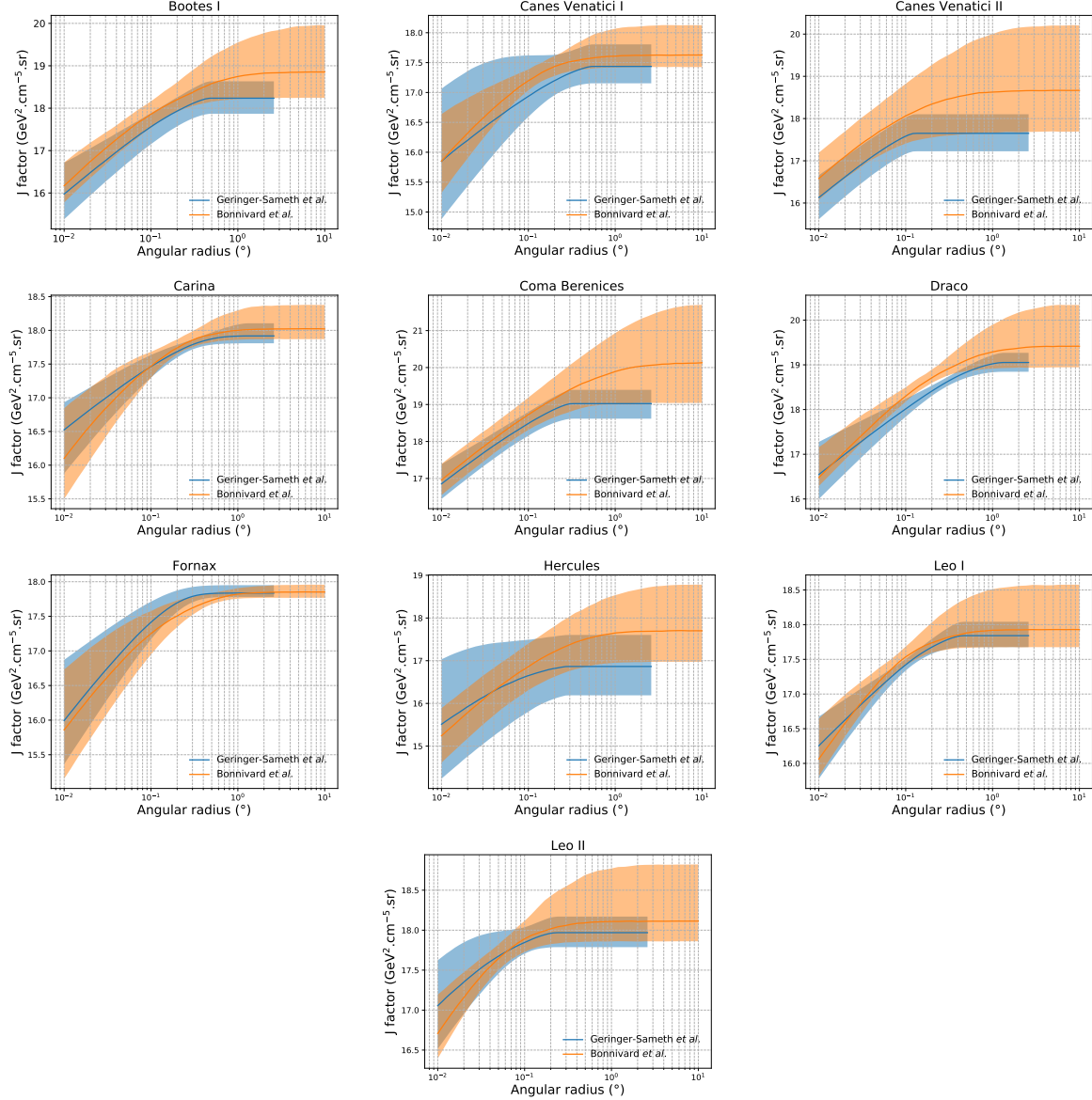


Figure 5.16 Comparisons between the J -factors versus the angular radius for the computation of J factors from Ref. [53] (\mathcal{GS} set in Table 5.1) in blue and for the computation from Ref. [47, 55] (\mathcal{B} set in Tab. 5.1) in orange. The solid lines represent the central value of the J -factors while the shaded regions correspond to the 1σ standard deviation.

This analysis serves as a proof of concept for future multi-instrument and multi-messenger combination analyses. With this collaborative effort, we have managed to sample over four orders in magnitude in gamma-ray energies with distinct observational techniques. Determining the nature of DM continues to be an elusive and difficult problem. Larger datasets with diverse measurement techniques could be essential to tackling the DM problem. A future collaboration using similar

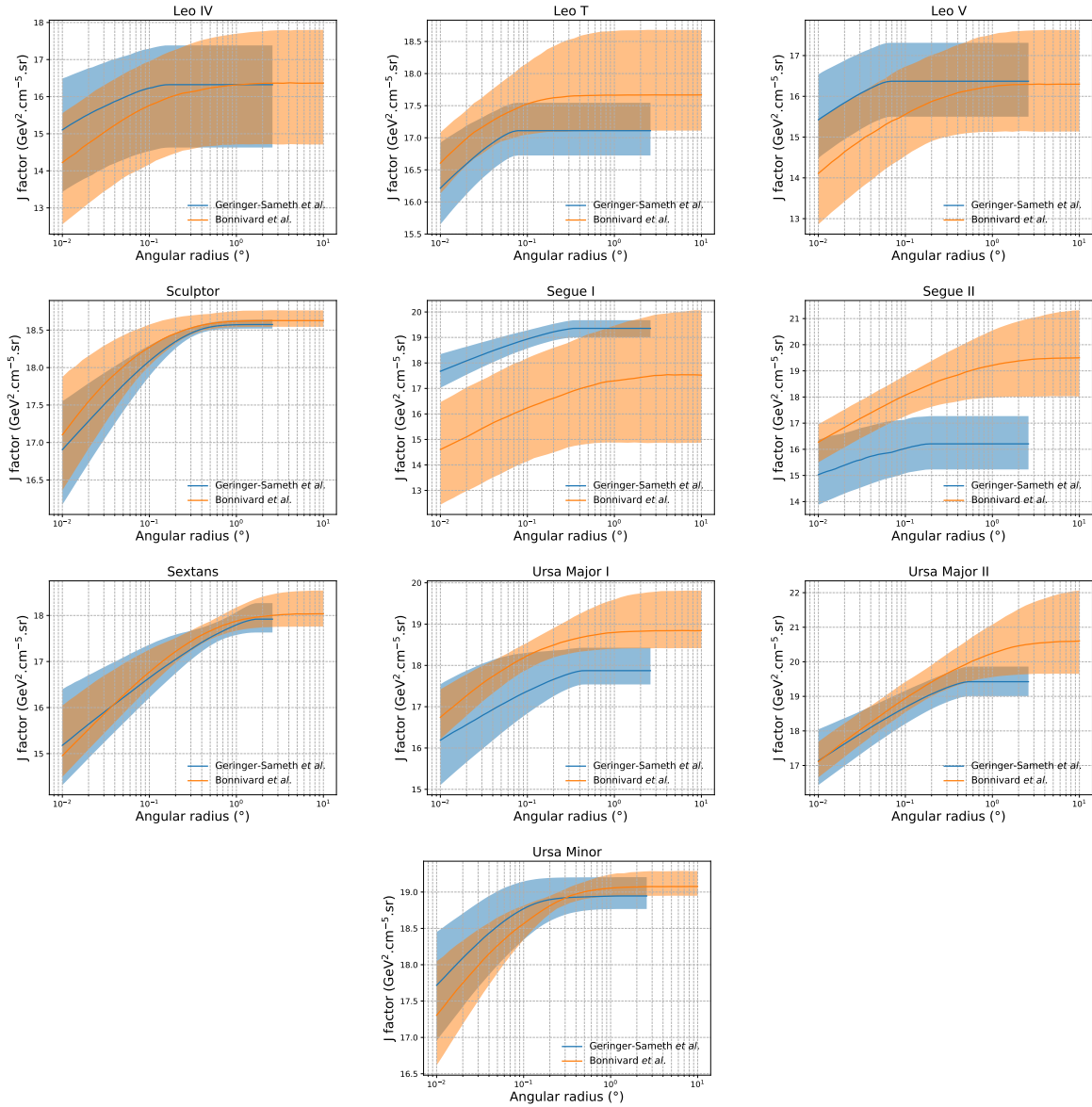


Figure 5.17 Comparisons between the J -factors versus the angular radius for the computation of J factors from Ref. [53] (\mathcal{GS} set in Tab. 5.1) in blue and for the computation from Ref. [47, 55] (\mathcal{B} set in Tab. 5.1) in orange. The solid lines represent the central value of the J -factors while the shaded regions correspond to the 1σ standard deviation.

techniques as the ones described in this paper could grow even beyond gamma rays. The models we used for this study include annihilation channels with neutrinos in the final state. Advanced studies could aim to merge our results with those from neutrino observatories with large data sets. Efforts are already underway to add data from the IceCube, ANTARES, and KM3NeT observatories to these gamma-ray results.

1128 From this work, a selection of the best candidates for observations, according to the latest
1129 knowledge on stellar dynamics and modelling techniques for the derivation of the J -factors on
1130 the potential dSphs targets, is highly desirable at the time that new experiments are starting their
1131 dark matter programs using dSphs. Given the systematic uncertainty inherent to the derivation of
1132 the J -factors, an informed observational strategy would be to select both objects with the highest
1133 J -factors that could lead to DM signal detection, and objects with robust J -factor predictions, i.e.
1134 with kinematic measurements on many bright stars, which would strengthen the DM interpretation
1135 reliability of the observation outcome.

1136 This analysis combines data from multiple telescopes to produce strong constraints on astro-
1137 physical objects. From this perspective, these methods can be applied beyond just DM searches.
1138 Almost every astrophysical study can benefit from multi-telescope, multi-wavelength gamma-ray
1139 studies. We have enabled these telescopes to study the cosmos with greater precision and detail.
1140 Many astrophysical searches can benefit from multi-instrument gamma-ray studies, for which our
1141 analysis lays the foundation.

CHAPTER 6

MULTITHREADING HAWC ANALYSES FOR DARK MATTER SEARCHES

6.1 Introduction

HAWC's current software suite, plugins to 3ML, does not fully utilize computational advancements of recent decades. Said advancements include the proliferation of Graphical Processing Units (GPUs), and multithreading on multicore processors. The analysis described in chapter 5 took up to 3 months of human time waiting for the full gambit of data analysis and simulation of background to run. Additionally, with the addition of a 2D binning scheme, f_{hit} and NN, the time needed to compute expected to grow. Although excessive computing time was, in part, from an intense use of a shared computing cluster, it was evident that there was room for improvement. In HAWC's next generation dSph DM search, I decided to develop codes that would utilize the multicore processors on modern high performance computing clusters. The results of this work are featured in this chapter and brought a human timing improvement to computation that scales as $1/N$ where N is the number of threads.

6.2 Dataset and Background

This section enumerates the data and background methods used for HAWC's multithreaded study of dSphs. Section 6.2.1 and Section 6.2.2 are most useful for fellow HAWC collaborators looking to replicate a multithreaded dSph DM search.

6.2.1 Itemized HAWC files

- Detector Resolution: `refit-Pass5-Final-NN-detRes-zenith-dependent.root`
- Data Map: `Pass5-Final-NN-maptree-ch103-ch1349-zenith-dependent.root`
- Spectral Dictionary: `HDMspectra_dict_gamma.npy`

6.2.2 Software Tools and Development

This analysis was performed using HAL and 3ML [42, 43] in Python version 3. I built software in collaboration with Michael Martin and Letrell Harris to implement the *Dark Matter Spectra from*

1166 *the Electroweak to the Planck Scale* (HDM) [64] and dSphs spatial model from [65] for HAWC
1167 analysis. A NumPy dictionary of HDM was made for Py3. The corresponding Python3 file is
1168 `HDMspectra_dict_gamma.npy`. These files can also be used for decay channels and tools are
1169 provided in HDM’s [git repository](#) [64]. The analysis was performed using the Neural Network
1170 energy estimator for Pass 5.F. A description of this estimator was provided in chapter 3. **TODO:**
1171 **Define a subsection when it’s written**, and its key improvements are an improved energy estimation
1172 and improved sensitivities at higher zenith angles. All other software used for data analysis, DM
1173 profile generation, and job submission to SLURM are also kept in my sandbox in the [Dark Matter](#)
1174 [HAWC](#) project. The above repository also incorporates the model inputs used previously in Glory
1175 Duck, described in chapter 5

1176 **6.2.3 Data Set and Background Description**

1177 The HAWC data maps used for this analysis contain 2565 days of data between runs 2104 (**TODO: Day start**) and 7476 (**TODO: Day end**). They were generated from pass 5.f reconstruction.
1179 The analysis is performed using the NN energy estimator with bin list:

1180 B1C0Ea, B1C0Eb, B1C0Ec, B1C0Ed, B1C0Ee, B2C0Ea, B2C0Eb, B2C0Ec, B2C0Ed, B2C0Ee,
1181 B3C0Ea, B3C0Eb, B3C0Ec, B3C0Ed, B3C0Ee, B3C0Ef, B4C0Eb, B4C0Ec, B4C0Ed, B4C0Ee,
1182 B4C0Ef, B5C0Ec, B5C0Ed, B5C0Ee, B5C0Ef, B5C0Eg, B6C0Ed, B6C0Ee, B6C0Ef, B6C0Eg,
1183 B6C0Eh, B7C0Ee, B7C0Ef, B7C0Eg, B7C0Eh, B7C0Ei, B8C0Ee, B8C0Ef, B8C0Eg, B8C0Eh,
1184 B8C0Ei, B8C0Ej, B9C0Ef, B9C0Eg, B9C0Eh, B9C0Ei, B9C0Ej, B10C0Eg, B10C0Eh,
1185 B10C0Ei, B10C0Ej, B10C0Ek, B10C0El

1186 Bin 0 was excluded as it has substantial hadronic contamination and poor angular resolution.

1187 Background considerations and source selection was identical to Section 5.2, and no additional
1188 arguments are provided here. Many of the HAWC systematics explored in Section 5.7 also apply
1189 for this DM search and are not added upon here.

1190 **6.3 Analysis**

1191 The analysis and its systematics are almost identical to Section 5.3. Importantly, we use the
1192 same Equation (7.1) and Equation (5.2) for estimating the gamma-ray flux at HAWC from our
1193 sources. We add on to the previous study with a search for DM decay. The flux equations for DM
1194 decay are

$$\frac{d\Phi_\gamma}{dE_\gamma} = \frac{1}{4\pi\tau m_\chi} \frac{dN_\gamma}{dE_\gamma} \times \int_{\text{source}} d\Omega \int_{l.o.s} \rho_\chi dl(r, \theta') \quad (6.1)$$

1195 with a new quantity, the D factor, defined as

$$D = \int d\Omega \int_{l.o.s} dl \rho_\chi(r, \theta') \quad (6.2)$$

1196 Software was written to accommodate DM decay from dSphs, however decay profiles were not
1197 received from $\mathcal{L}\mathcal{S}$ by the time of writing this thesis.

1198 **6.3.1 $\frac{dN_\gamma}{dE_\gamma}$ - Particle Physics Component**

1199 For these spectra, we import HDM with Electroweak (EW) corrections and additional correc-
1200 tions for neutrinos above the EW scale [64]. The spectrum is implemented as a model script in
1201 astromodels for 3ML. A comprehensive description of EW corrections and neutrino considerations
1202 are provided later in [TODO: refeance MM nu duck](#).

1203 Figure 6.1 demonstrates the impact of changes from HDM on DM annihilation to W bosons.
1204 A class in astromodels was developed to include HDM and is aptly named `HDMspectra` within
1205 `DM_models.py`. The SM DM annihilation channels studied here are $\chi\chi \rightarrow:$

1206 $e^+e^-, \mu^+\mu^-, \tau^+\tau^-, b\bar{b}, t\bar{t}, gg, W^+W^-, ZZ, c\bar{c}, u\bar{u}, d\bar{d}, s\bar{s}, \nu_e\bar{\nu}_e, \nu_\mu\bar{\nu}_\mu, \nu_\tau\bar{\nu}_\tau, \gamma\gamma, hh.$

1207 For $\gamma\gamma$ and ZZ , a substantial fraction of the signal photons are expected to have total energy equal
1208 m_χ [64]. This introduces a δ -function that is much narrower than the energy resolution of the
1209 HAWC detector. To ensure that this feature is not lost in the likelihood fits, the 'line' feature is
1210 convolved with a Gaussian kernel with a 1σ width of $0.05 \cdot m_\chi$ and total kernel window of $\pm 4\sigma$.
1211 This differs from HAWC's previous line study where 30% of HAWC's energy resolution was used
1212 for the kernel [66]. The NN energy estimator's strength compared to f_{hit} at low gamma-ray energy

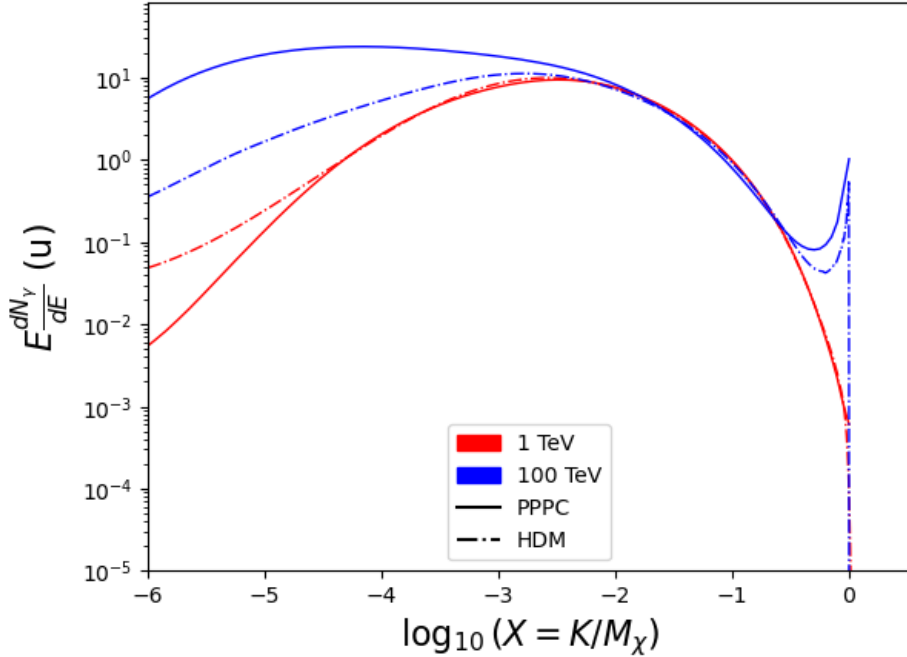


Figure 6.1 Difference between spectral hypotheses from PPPC [44] and HDM [64]. Shown is the expected DM annihilation spectrum for $\chi\chi \rightarrow W^-W^+$. Solid lines are spectral models with EW corrections from the PPPC. Dash-dot lines are spectral models from HDM. Red lines are models for $M_\chi = 1$ TeV. Blue lines represent models for $M_\chi = 100$ TeV.

enables smaller resolutions in addition to low energy tails in the spectral models [64]. $\chi\chi \rightarrow \gamma\gamma$ and ZZ spectral hypotheses are shown in Figure 6.2. Spectral models for the remaining annihilation channels are plotted for each m_χ in Figure B.1.

6.3.2 J and D- Astrophysical Components

The J-factor profiles for each source are imported from Louis Strigari et al. (referred to with \mathcal{LS}) [65]. Profiles in $\frac{dJ}{d\Omega}(\theta)$ up to $\theta = 0.5^\circ$ were provided directly from the authors. Map generation from these profiles were almost identical to Section 5.3.2 except that a higher order trapezoidal integral was used for the normalization of the square, uniformly-spaced map:

$$p^2 \cdot \sum_{i=0}^N \sum_{j=0}^M w_{i,j} \frac{d\mathcal{K}}{d\Omega}(\theta_{i,j}, \phi_{i,j}) \quad (6.3)$$

\mathcal{K} is either J or D for the spatial distributions of annihilation or decay respectively. p is the angular side of one pixel in the map. $w_{i,j}$ is a weight assigned the following ways:

$w_{i,j} = 1$ if $(\theta_{i,j}, \phi_{i,j})$ is fully within the region of integration

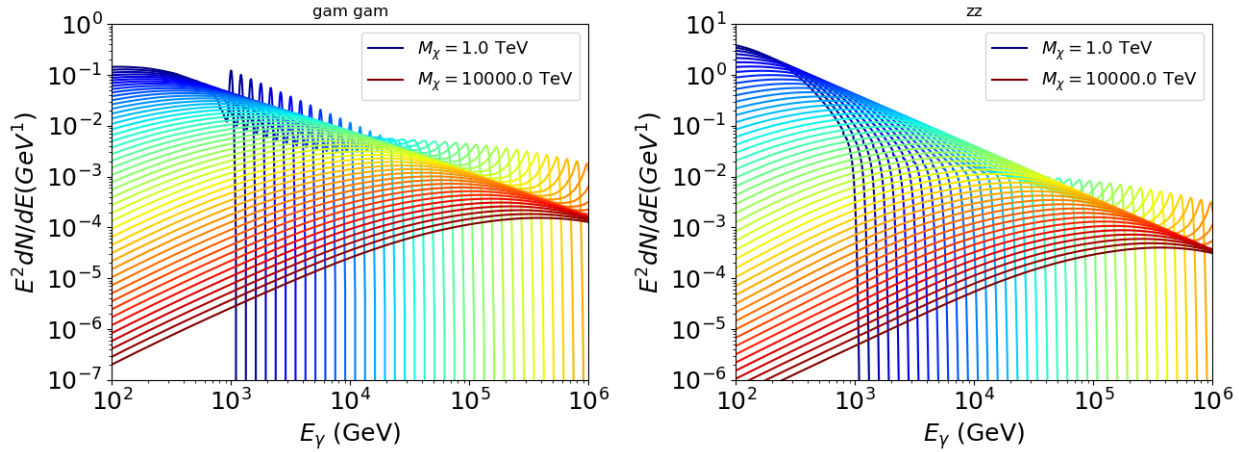


Figure 6.2 Photon spectra for $\chi\chi \rightarrow \gamma\gamma$ (left) and $\chi\chi \rightarrow ZZ$ (right) after Gaussian convolution of line features. Both spectra have δ -features at photon energies equal to the DM mass. Bluer lines are annihilation spectra with lower DM mass. Redder lines are spectra from larger DM mass. All Spectral models are sourced from the Heavy Dark Matter models [64]. Axes are drawn roughly according to the energy sensitivity of HAWC.

1224 $w_{i,j} = 1/2$ if $(\theta_{i,j}, \phi_{i,j})$ is on an edge of the region of integration

1225 $w_{i,j} = 1/4$ if $(\theta_{i,j}, \phi_{i,j})$ is on a corner of the region of integration

1226 Figure 6.3 shows the median and $\pm 1\sigma$ maps used as input for DM annihilation studied by \mathcal{LS} .

1227 **6.3.3 Source Selection and Annihilation Channels**

1228 HAWC's sources for this multithreaded analysis include Coma Berenices, Draco, Segue 1, and
 1229 Sextans \mathcal{LS} observes up to 43 sources in its publication, however only 4 of the best fit profiles were
 1230 provided at the time this thesis was written. A full description of each source used in this analysis
 1231 is found in Table 6.1.

1232 This analysis improves on chapter 5 in the following ways. Previously, the particle physics
 1233 model used for gamma-ray spectra from DM annihilation was from the PPPC [44] which missed
 1234 important considerations relevant for the neutrino sector. HDM is used to account for this shortfall
 1235 [64]. HDM also models DM to the Planck scale which permits HAWC to probe PeV scale DM.
 1236 For this study, we sample DM masses: 1 TeV - 10 PeV with 6 mass bins per decade in DM mass.
 1237 In the case of line spectra ($\chi\chi \rightarrow \gamma\gamma$, or ZZ), we double the mass binning to 12 DM mass bins
 1238 per decade in DM mass. A larger source catalog is used that uses a Navarro–Frenk–White (NFW)

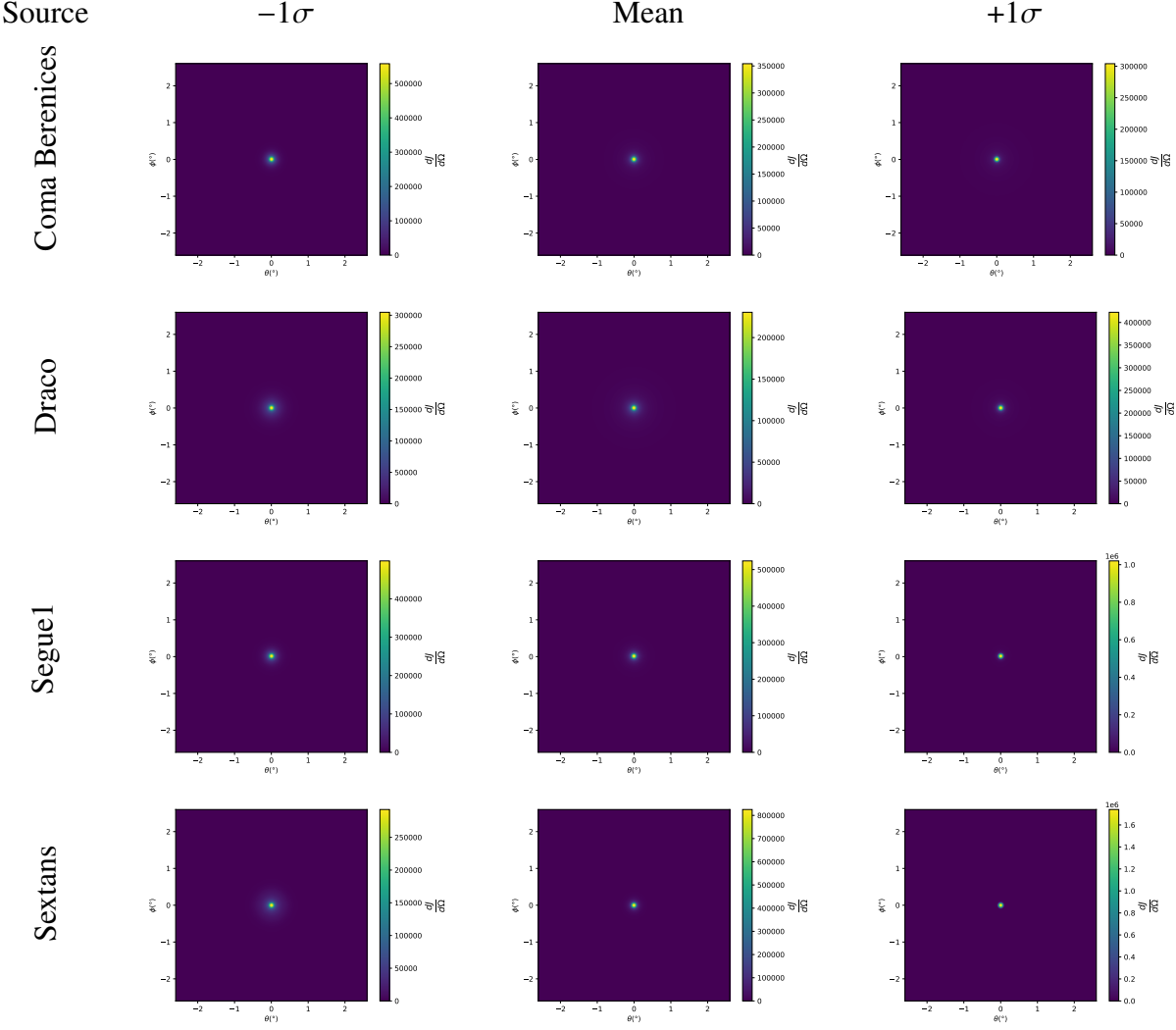


Figure 6.3 $\frac{dJ}{d\Omega}$ maps for Coma Berenices, Draco, Segue1, and Sextans. Columns are divided for the $\pm 1\sigma$ uncertainties in $dJ/d\Omega$ around the mean value from \mathcal{LS} [65]. Origin is centered on the specific dwarf spheroidal galaxies (dSph). θ and ϕ axes are the angular separation from the center of the dwarf

1239 spatial DM distribution from \mathcal{LS} [65]. Because NFW has fewer parameters than what is used
 1240 for \mathcal{GS} , \mathcal{LS} is able to fit ultra-faint dwarves, expanding the number of sources available for DM
 1241 searches. Finally, the gamma-ray ray dataset is much larger. The study performed here analyzes
 1242 2565 days of data compared to 1017 days analyzed in chapter 5.

1243 6.4 Likelihood Methods

1244 These are identical to Section 5.4.1 and no additional changes are made to the likelihood. Bins
 1245 in this analysis are expanded to include HAWC’s NN energy estimator.

1246 **6.5 Computational Methods: Multithreading**

1247 Previously, as in Section 5.3, the likelihood was minimized for one model at a time. One
 1248 model in this case representing a DM annihilation channel, DM mass, and dSph. In an effort
 1249 to conserve human and CPU time, jobs submitted for high performance computing contained a
 1250 list of DM masses to iterate over for likelihood fitting. Jobs were then trivially parallelized for
 1251 each permutation of the two lists: CHANS (SM annihilation channel) and SOURCES (dSph spatial
 1252 templates). The lists for CHANS and SOURCES are found in Section 6.3.1 and Table 6.1, respectively.
 1253 Initially, 11 DM mass bins were serially sampled for one job defined by a [SM channel, dSph] set.
 1254 Computing the likelihoods would take between 1.5 to 2 hrs, stochastically, for a job. We expect to
 1255 compute likelihoods for data and 300 Poisson background trials. The estimated CPU time based on
 1256 the above for all SM annihilation channels (17) and 25 sources (all \mathcal{LS} sources within HAWC's
 1257 field of view) amounted to 127,925 jobs. In total, 1,407,175 likelihood fits and profiles would
 1258 be computed for the 11 mass bins we wished to study. The estimated CPU time ranged between
 1259 10k CPU days - 8k CPU days. Human time is more challenging to estimate as job allocation is
 1260 stochastic and highly dependent on what other users are submitting, yet it is unlikely that all jobs
 1261 would run simultaneously. Therefore, we can expect human time to be about as long as was seen
 1262 in chapter 5 which was on the order of months to fully compute on a smaller analysis. A visual aid
 1263 to describe how jobs were organized is provided in Figure 6.4.

Name	Distance (kpc)	l, b ($^{\circ}$)	$\log_{10} J$ (\mathcal{LS} set) $\log_{10}(\text{GeV}^2 \text{cm}^{-5} \text{sr})$
Coma Berenices	44	241.89, 83.61	$19.00^{+0.36}_{-0.35}$
Draco	76	86.37, 34.72	$18.83^{+0.12}_{-0.12}$
Segue I	23	220.48, 50.43	$19.12^{+0.49}_{-0.58}$
Sextans	86	243.50, 42.27	$17.73^{+0.13}_{-0.12}$

Table 6.1 Summary of the relevant properties of the dSphs used in the present work. Column 1 lists the dSphs. Columns 2 and 3 present their heliocentric distance and galactic coordinates, respectively. Column 4 reports the J -factors of each source given from the \mathcal{LS} studies and estimated $\pm 1\sigma$ uncertainties. The values $\log_{10} J$ (\mathcal{LS} set) [65] correspond to the mean J -factor values for a source extension truncated at 0.5° .

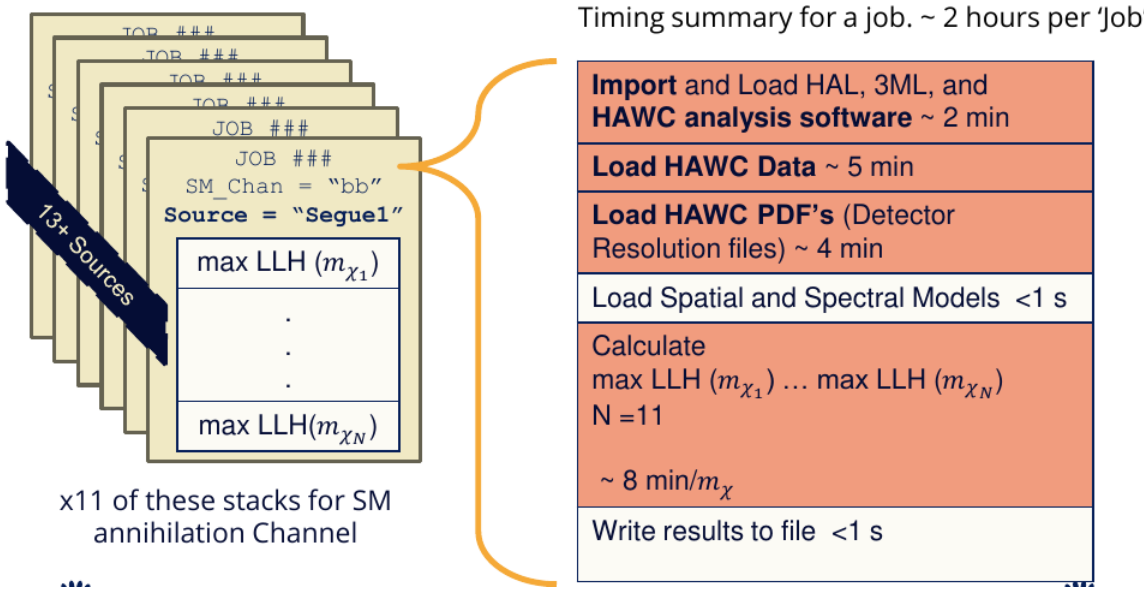


Figure 6.4 Infographic on how jobs and DM computation was organized in Section 5.3. Jobs were built for each permutation of CHANS and SOURCES shown by the left block in the figure. Each job, which took on the order 2 hrs to compute, had the following work flow: 1. Import HAWC analysis software, 2 min to run. 2. Load HAWC count maps, 5 min to run. 3. Load HAWC energy and spatial resolutions, 4 min. 5. Load DM spatial source templates and spectral models, less than 1 s. 6. Perform likelihood fit on data and model, about 8 min per DM mass. 7. Write results to file, less than 1s.

1264 The computational needs for this next generation DM analysis are extreme and is unlike other
 1265 analyses performed on HAWC. It became clear that there was a lot to gain from optimizing how
 1266 the likelihoods are computed. This section discusses how multi-threading was applied to solve and
 1267 reduce HAWC’s computing of likelihoods for large parameter spaces like in DM searches.

1268 6.5.1 Relevant Foundational Information

1269 The profiling of the likelihood for HAWC is done via gradient descent where the normalization
 1270 of Equation (7.1) (linearly correlated with $\langle \sigma v \rangle$) is rescaled in the descent. Additionally, we sample
 1271 the likelihood space for a defined list of $\langle \sigma v \rangle$ ’s described in Section 5.4.2. The time to compute
 1272 these values is not predictable or consistent because many variables can change across the full
 1273 model-space. Comprehensively, these variables are:

- 1274 • m_χ : DM rest mass
- 1275 • CHAN : DM SM annihilation channel.

1276 • SOURCE : dSph within HAWC's field of view. This involves a spatial template AND coordinate
1277 in HAWC data.

1278 • $\langle\sigma v\rangle$: Effectively the flux normalization and free parameter in the likelihood fit.

1279 Therefore, we develop an asynchronous, functional-parallel coding pattern. Asynchronous mean-
1280 ing that the instructions and computing within a function are independent and permitted to be out
1281 of sync with sibling computations. Functional-parallel meaning that instructions are the subject of
1282 parallelization rather than threading the likelihood computation. This is close to trivial parametriza-
1283 tion seen in Figure 6.4 except that we seek to consolidate the loading stages (software, data, and
1284 detector resolution loading). Reducing the total instances of loading stages and distributing access
1285 to the reduced loads across multiple asynchronous threads is expected to reduce serial processing
1286 time and the overhead implicit to each job in addition to saving human time.

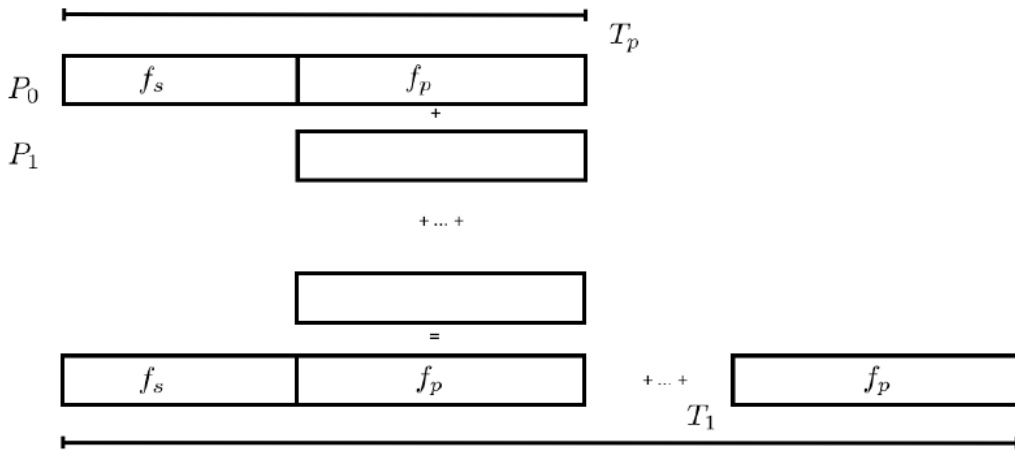


Figure 6.5 Graphic of Gustafson parallel coding pattern. f_s is the fraction of a program, in time, spent on serial computation. f_p is the fraction of computing time that is parallelizable. T_p is the total time for a parallel program to run. T_1 is the total time for a parallel program to run if only 1 processor is allocated. P_N is the N -th processor where it's row is the computation the processor performs. The Gustafson pattern is most similar to what is implemented for this analysis. Figure is pulled from [67].

1287 We need a way to measure and compare the expected speedup and efficiency gain for this
1288 asynchronous coding pattern. I pull inspiration for timing measurement from [67] and use *Amdahl's
1289 law with hybrid programming*. Hybrid programming meaning that the computation is a mix of

1290 distributed and shared memory programming. If we assume the code is fully parallelizable over p
1291 processors and c threads, the ideal speedup is simply pc and ideal run-time is $T_1/(pc)$. T_1 is the
1292 total time for a parallel program to run if only 1 processor is allocated. However, the coding pattern
1293 contains some amount of unavoidable serial computation, as shown in Figure 6.5. In our case, the
1294 run time is estimated to be

$$T_{p,c} = \frac{T_1}{pc} (1 + F_s(c - 1)). \quad (6.4)$$

1295 F_s is the fraction of CPU time dedicated to serial computation. The expected speedup is

$$S_{p,c} \equiv \frac{T_1}{T_{p,c}} = \frac{pc}{1 + F_s(c - 1)}. \quad (6.5)$$

1296 From Equation (6.5), we can see that the speed-up scales with p/F_s . We are free to minimize
1297 F_s asymptotically by enlarging the total models that are submitted to the thread pool, thereby
1298 shrinking the CPU fraction dedicated to serial operation. We are also free to define exactly how
1299 many threads and processors we utilize, yet eventually hit a hard cap at the hardware available on
1300 our computing cluster. HAWC uses Intel Xeon processors with 48 cores and 96 threads. This
1301 means when N-threads (c) are defined, $N \bmod 2$ cores (p) are needed. We see that a successful
1302 code scales well as the expected speedup is inversely correlated with F_s . As the total number of
1303 models sampled grows, the speedup will also.

1304 **6.5.2 Implementation**

1305 The multithreaded code was written in Python3 and is documented in the `dark_matter_hawc`
1306 [repository](#) within the script named `mpu_analysis.py`. A version of the script as of April 25
1307 **TODO: make sure to update on this date** is also provided in Section B.2 It has many dependencies
1308 including the HAWC analysis software. Figure 6.6 displays the workflow of a job with 3 threads.
1309 Within a job, SOURCE is kept fixed . CHAN(S) remains 17 elements long. More m_χ are sampled
1310 from 11 bins up to 49 (for $\gamma\gamma$ and ZZ) and 25 (for remaining CHANS) which amounts to 12 or 6
1311 mass bins per decade. The DM mass, m_χ , and SM annihilation channels, CHANS, are permuted into
1312 a 473 element list which is split evenly across N threads where N ranges between 5 - 16. Within a
1313 thread, for each m_χ -CHAN tuple, 1001 $\langle\sigma v\rangle$ values are sampled in the likelihood, and the value of

Timing summary for a multi-threaded job.

Import and Load HAL, 3ML, and HAWC analysis software ~ 2 min		
Load HAWC Data ~ 5 min		
Load HAWC PDF's (Detector Resolution files) ~ 4 min		
Load Spatial Model < 1s		
Load Spectra Models <1 s	Load Spectra Models <1 s	Load Spectra Models <1 s
Calculate max LLH (Chan_0, m_{χ_1}) ... max LLH (Chan_?, m_{χ_N}) N = TOTAL/N_THREADS ~ 8 min/Spec_model	Calculate max LLH (Chan_?, m_{χ_1}) ... max LLH (Chan_?, m_{χ_N}) N = TOTAL/N_THREADS ~ 8 min/Spec_model	Calculate max LLH (Chan_?, m_{χ_1}) ... max LLH (Chan_?, m_{χ_N}) N = TOTAL/N_THREADS ~ 8 min/Spec_model
Write results to file <1 s	Write results to file <1 s	Write results to file <1 s
Join Threads and terminate < 1s		

Figure 6.6 Task chart for one multithreaded job developed for this project. Green blocks indicate a shared resource across the threads AND computation performed serially. Red blocks indicate functional parallel processing within each thread. 3 threads are represented here, yet many more can be employed during the full analysis. Jobs are defined by the SOURCE as these require unique maps to be loaded into the likelihood estimator. The m_{χ} , CHAN, and $\langle \sigma v \rangle$ variables are entered into the thread pool and allocated as evenly as possible across the threads.

1314 $\langle \sigma v \rangle$ that maximizes the likelihood is found. Although rare, fits that failed are handled on a case
1315 by case basis.

1316 6.5.3 Performance

M Tasks	$T_{p,c}$ (hr:min:s)			
	$T_{1,1}$	$T_{1,2}$	$T_{1,8}$	$T_{1,16}$
50	1:40:37.5	0:52:43.7	0:19:13.8	0:13:44.0
74	2:22:30.0	1:15:00.6	0:25:21.3	0:15:49.8
100	(3:07:51.9)	1:40:10.5	0:30:44.4	0:20:01.4
200	(6:02:20.6)	-	1:00:32.0	0:30:35.0
473	(13:58:40.3)	-	TODO: run this	1:07:53.2

Table 6.2 Timing summaries for analyses for serial and multithreaded processes. M tasks is the number of functional-parallel tasks ran for the computation. $T_{p,c}$ is a single run time in hours:minutes:seconds for runs utilizing p nodes and c threads. Runs are run interactively on the same computer to maximize consistency. Empty entries are indicated with '-'. (·) entries are estimated entries extrapolated from data earlier in the column.

1317 We see a tremendous reduction to human time waiting for our dSph analyses to run. Table 6.2

1318 shows the timing summaries for analyses of different sizes and thread counts. Additionally, the
 1319 efficiency gained when consolidating the serial loading of data is also apparent in our ability to
 1320 study many more tasks in about the same amount of wall time as a smaller serial computation. Trials
 1321 represented in the table were run on an AMD Opteron® processor 6344 with 48 cores, 2 threads
 1322 per core; 2.6 GHz clock. This is not the same architecture used for analysis on the computing
 1323 cluster however they are similar enough that results shown here are reasonably representative of
 1324 computing on the HAWC computing cluster. I use the Tab. 6.2 for the inferences and conclusions
 1325 in the following paragraphs.

1326 First, we want to find T_s , the time of serial computation. From Fig. 6.5, the timing for our
 1327 coding pattern can be written as

$$T_s + Mt_p = T_{1,1}^M. \quad (6.6)$$

1328 M is the number of functional-parallel tasks (represented as column 1 of Tab. 6.2), and t_p is the
 1329 average time to complete a single parallel task. $T_{1,1}^M$ is the total time for a parallel program to run if
 1330 only 1 processor is allocated for M parallel task. With two runs of different M ($M1$ and $M2$), we
 1331 can use a system of equations to derive

$$T_s = T_{1,1}^{M1} - M1 \left(\frac{T_{1,1}^{M1} - T_{1,1}^{M2}}{M1 - M2} \right). \quad (6.7)$$

1332 We also extract t_p using the same methods:

$$t_p = \frac{T_{1,1}^{M1} - T_{1,1}^{M2}}{M1 - M2}. \quad (6.8)$$

1333 From Tab. 6.2, we set $M1 = 50$ and $M2 = 74$ and take their corresponding $T_{1,1}$ from the table to
 1334 calculate T_s and t_p .

$$T_s = 803.1\text{s} \text{ and } t_p = 104.6\text{s} \quad (6.9)$$

1335 Now, we have specific estimation for the fraction of serial computing time, F_s :

$$F_s = \frac{803.1}{803.1 + 104.6 \cdot M}. \quad (6.10)$$

1336 The maximum M for this study is 473 which evaluates using Eq. (6.10): $F_s = 0.016$ or 1.6% of
 1337 computing time. Table 6.3 shows the resulting speedups.

M Tasks	F_s	$S_{1,2}$	$S_{1,8}$	$S_{1,16}$
50	1.33 E-1	1.90 [1.76]	5.23 [4.14]	6.35 [5.34]
74	9.40 E-2	1.90 [1.83]	5.62 [4.82]	9.00 [6.64]
100	7.13 E-2	1.88 [1.87]	6.11 [5.34]	9.38 [7.73]
200	3.70 E-2	- [1.93]	5.98 [6.36]	11.85 [10.29]
473	1.60 E-2	- [1.97]	[7.20]	12.35 [12.91]

Table 6.3 Speed up summaries for analyses for serial and multithreaded processes. M tasks is the number of functional-parallel tasks ran for the computation. $S_{p,c}$ is a single speedup comparison for runs utilizing p nodes and c threads. [·] are the estimated speedups calculated from Tab. 6.2, Eq. (6.10), and Eq. (6.5). Empty entries are indicated with '-'.

1338 We see a speedup that generally exceeds expectations from Eq. (6.5) for real trail runs. We also
 1339 see that there are diminishing returns as the number of threads increases. For small jobs with large c ,
 1340 both the expected and observed speedup are significantly smaller than c . One thing not considered
 1341 in Eq. (6.5) is the time incurred via communication latency. Communication latency increases
 1342 with the number of threads and contributes to diminishing returns. Additionally, these values are
 1343 for single runs and do not consider the stochastic variation expected in a shared high performance
 1344 computing resource. Therefor, these results are not strictly conclusive, yet demonstrate the merits
 1345 of multi-threading. We see very clearly that there is a lot to gain, and this new coding pattern will
 1346 expand HAWC's analysis capabilities.

1347 6.6 Analysis Results

1348 3 of the 43 \mathcal{LS} dSphs considered for the multithreaded analysis. These dSph are analyzed for
 1349 emission from DM annihilation according to the likelihood method described in Section 5.4. The 3
 1350 likelihood profiles are then stacked to synthesize a combined limit on the dark matter cross-section,
 1351 $\langle\sigma v\rangle$. This combination is done for the 17 SM annihilation channels. Figure 6.7 and Fig. 6.8 show
 1352 the combined limits for all annihilation channels with HAWC's observations. Test statistics of the
 1353 best fit $\langle\sigma v\rangle$ values for each DM mass and SM annihilation channels are shown in Fig. 6.9 and
 1354 Fig. 6.10. We also compare these limits to HAWC's Glory Duck limits shown in Section 5.5. The
 1355 comparison to Glory Duck are featured in Fig. 6.11 for all the DM annihilation channels studied
 1356 for Glory Duck. A full comparison is provided in the appendix in Fig. B.2, Fig. B.3, and Fig. B.4.
 1357 Here, we show updated limits for $\chi\chi \rightarrow b\bar{b}, e\bar{e}, \mu\bar{\mu}, \tau\bar{\tau}, t\bar{t}, W^+W^-$, $\gamma\gamma$ and ZZ . For the first time

ever, we show limits for $\chi\chi \rightarrow c\bar{c}$, $s\bar{s}$, $u\bar{u}$, $d\bar{d}$, $\nu_e\bar{\nu}_e$, $\nu_\mu\bar{\nu}_\mu$, $\nu_\tau\bar{\nu}_\tau$, gg , and hh .

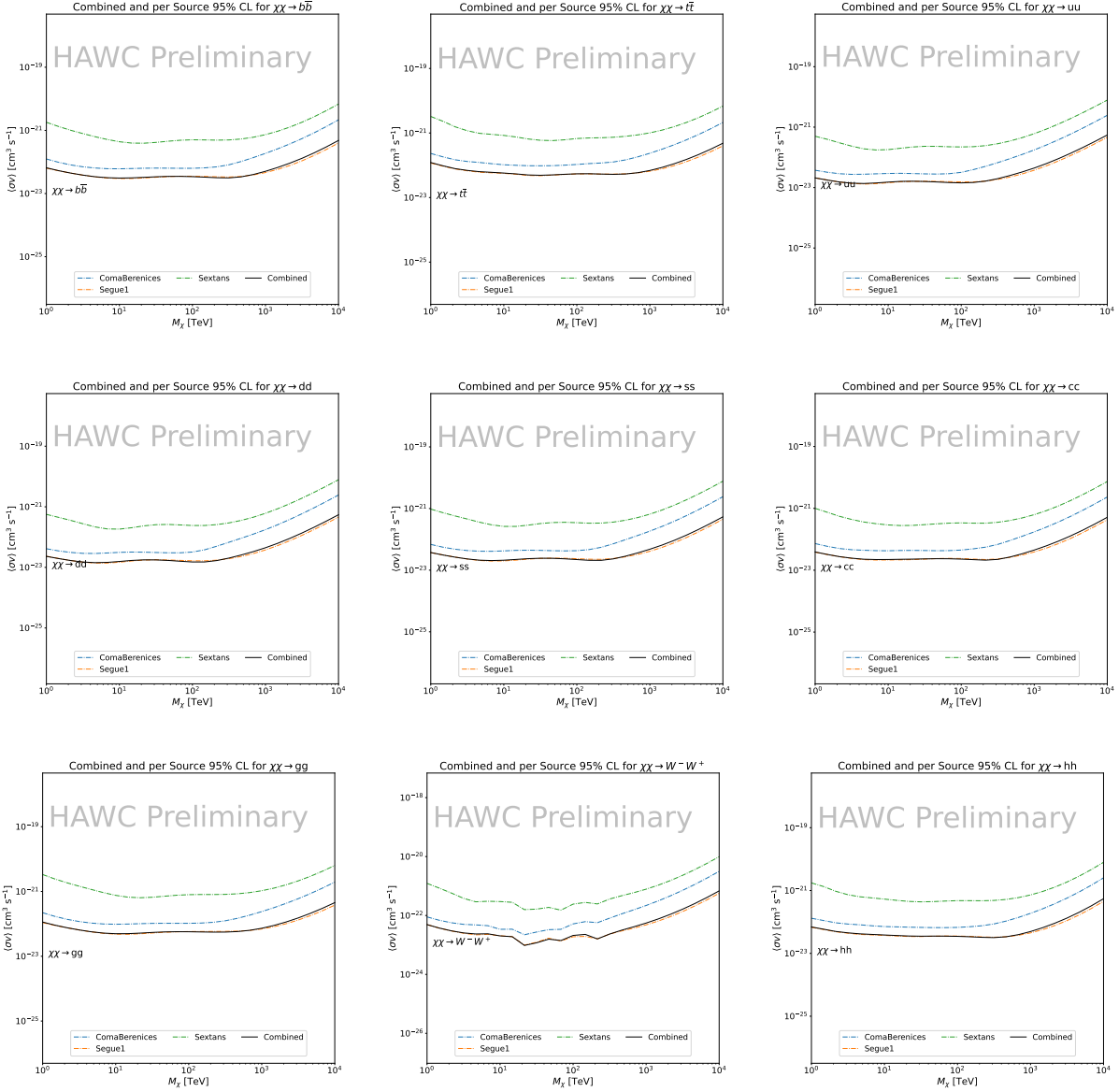


Figure 6.7 HAWC upper limits at 95% confidence level on $\langle\sigma v\rangle$ versus DM mass for $\chi\chi \rightarrow b\bar{b}$, $t\bar{t}$, $u\bar{u}$, $d\bar{d}$, $s\bar{s}$, $c\bar{c}$, gg , W^+W^- , and hh . Limits are with \mathcal{LS} J -factors [65]. The solid line represents the observed combined limit. Dashed lines represent limits from individual dSphs.

No DM was found in HAWC observations. The largest excess found in HAWC data was for DM annihilating to W -bosons for $m_\chi = 10 \text{ TeV}$ at 2σ . HAWC's limits and excesses are dominated by Segue1. Coma Berenices shows excess at higher DM mass, yet no similar excesses were observed in Segue1. Sextans did not contribute significantly to signal excess or the combined limit as it is

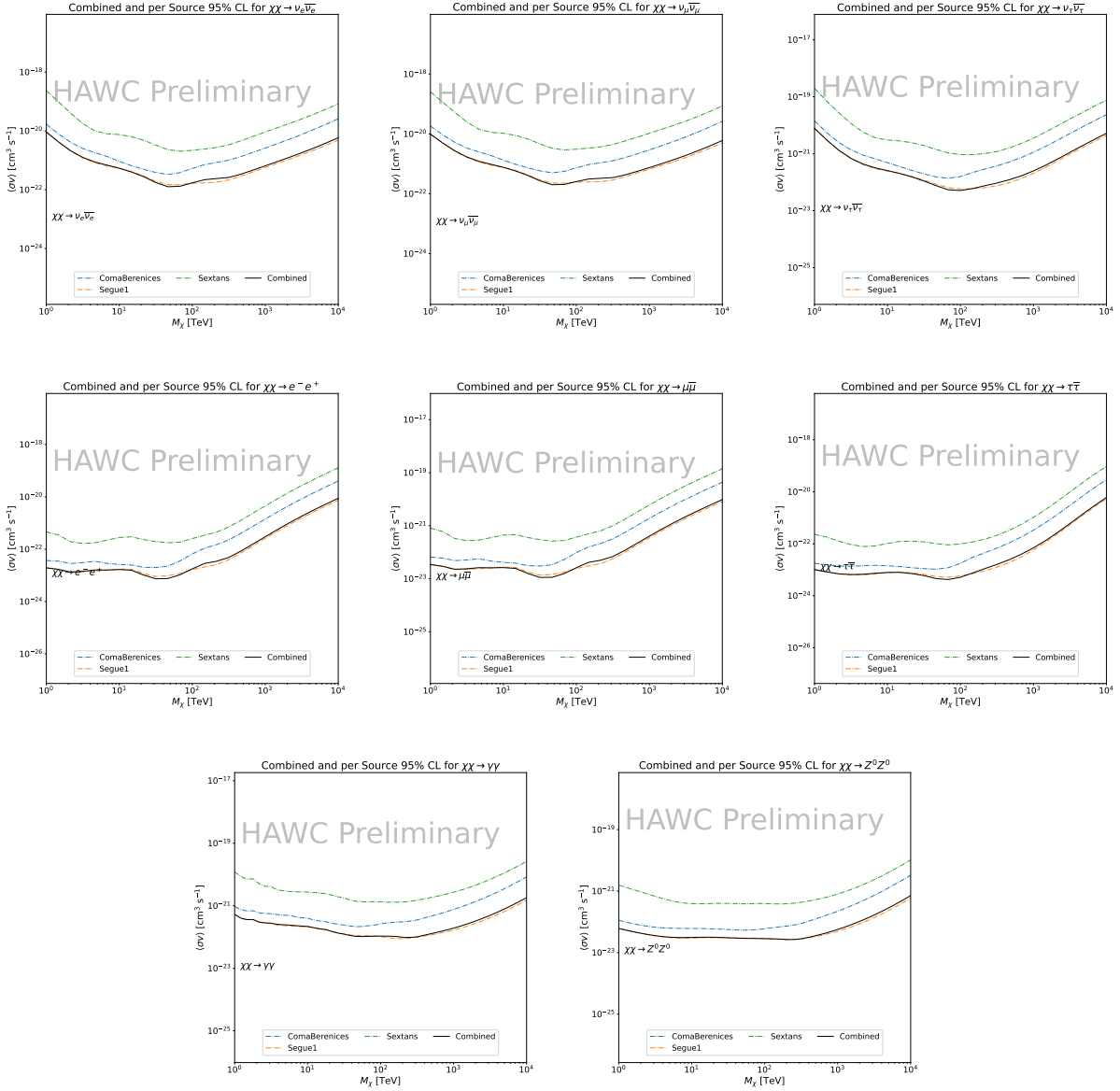


Figure 6.8 HAWC upper limits at 95% confidence level on $\langle\sigma v\rangle$ versus DM mass for $\chi\chi \rightarrow \nu_e \bar{\nu}_e$, $\nu_\mu \bar{\nu}_\mu$, $\nu_\tau \bar{\nu}_\tau$, $e^- e^+$, $\mu \bar{\mu}$, $\tau \bar{\tau}$, $\gamma\gamma$ and ZZ . Limits use $\mathcal{L}S J$ factors [65]. The solid line represents the observed combined limit. Dashed lines represent limits from individual dSphs.

at high zenith. Draco was not included as the PDF of some of our analysis bins were wider than what is reasonable for a point source analysis. Draco is at a high zenith for HAWC, so the effort required to include it was not justified by the benefits.

We were not able to generate background trials in time of writing this thesis. These are not shown and are an immediate next step for this analysis before publication.

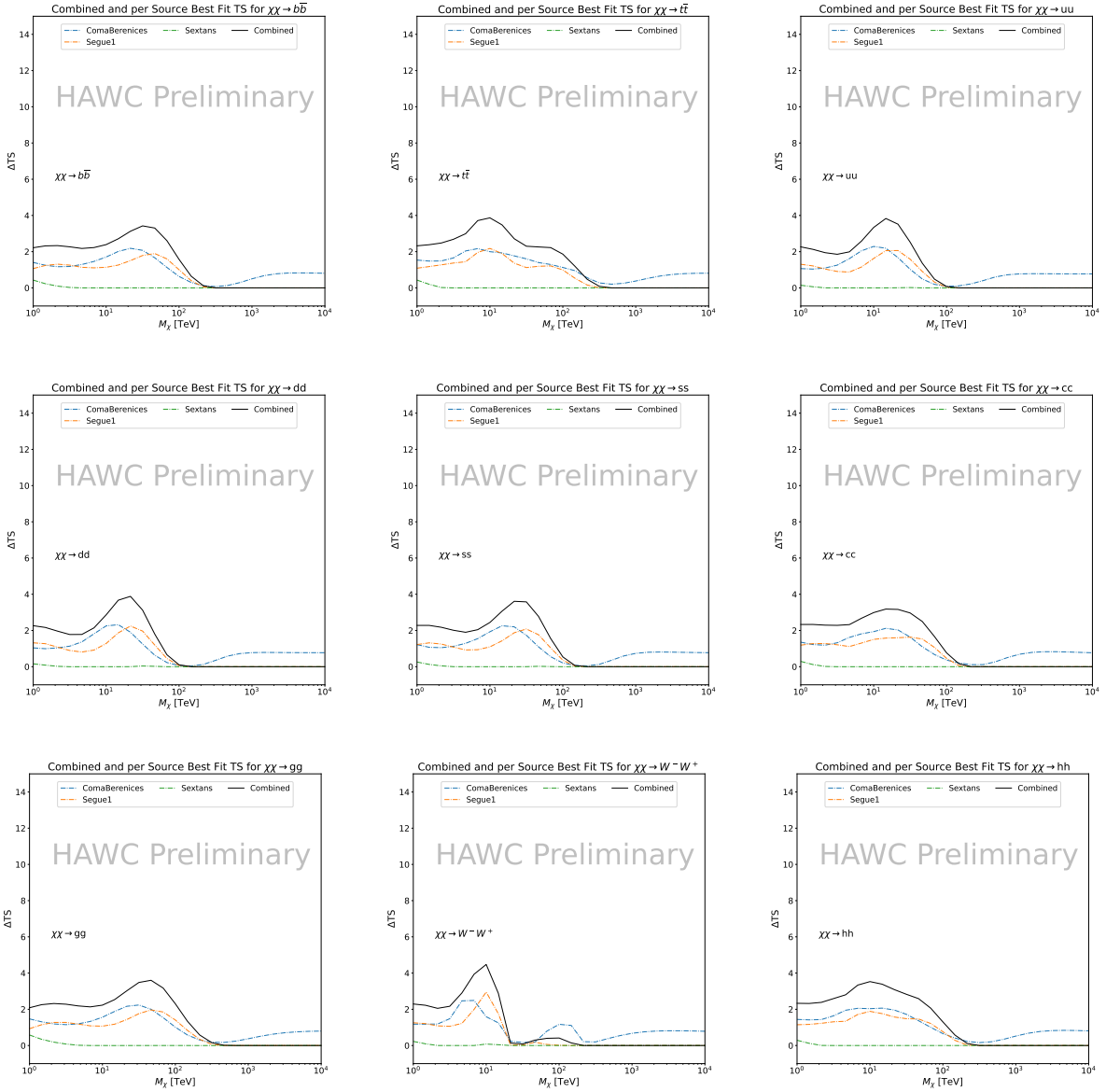


Figure 6.9 HAWC TS values for best fit $\langle\sigma v\rangle$ versus m_χ for SM annihilation channels: $\chi\chi \rightarrow b\bar{b}$, $t\bar{t}$, $u\bar{u}$, $d\bar{d}$, $s\bar{s}$, $c\bar{c}$, gg , W^-W^+ , and hh . Limits use $\mathcal{L}\mathcal{S} J$ factors. The solid black line shows the combined best fit TS values. The colored, dashed lines are the TS values from each dSph.

When comparing these results to Section 5.5, we see an overall decrease to the confidence limit therefore improvement to HAWC's expected sensitivity. This improvement is generally stronger than a doubling of data, or a factor $\sqrt{2}$ decrease. The comparison is somewhat complex and dependent on the dSph and SM annihilation channel. Figure 6.11 shows the comparisons of limits calculated for this analysis and Glory Duck (Section 5.5). Segue 1 and Coma Berenices are low

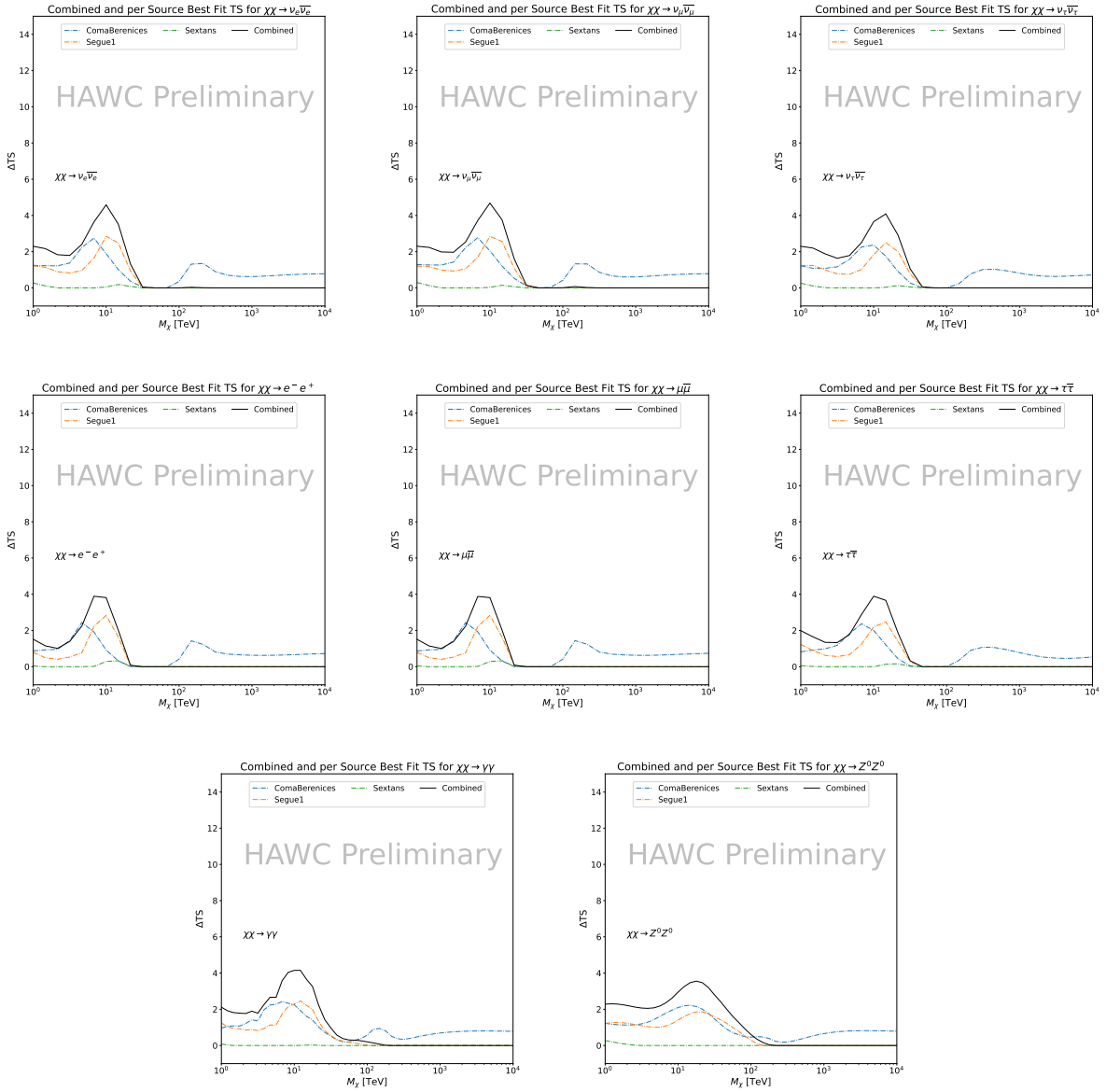


Figure 6.10 HAWC TS values for best fit $\langle\sigma v\rangle$ versus m_χ for SM annihilation channels: $\chi\chi \rightarrow \nu_e \bar{\nu}_e$, $\nu_\mu \bar{\nu}_\mu$, $\nu_\tau \bar{\nu}_\tau$, $e^- e^+$, $\mu \bar{\mu}$, $\tau \bar{\tau}$, $\gamma\gamma$ and ZZ . Limits use $\mathcal{L}\mathcal{S} J$ factors. The solid black line shows the combined best fit TS values. The colored, dashed lines are the TS values from each dSph.

zenith where improvements to HAWC's analysis come only from energy estimation. Differences between these two are dominantly from their differences in J -factor, half-light radii of the dSphs, and the particle physics inputs. Substantial gains in HAWC's analysis methods (pass 5.F) were made at high zenith which is important for sources like Sextans. The HDM particle physics model produces almost identical spectra to the PPPC for $\chi\chi \rightarrow e^- e^+$, so can be used to compare limits

1378 between dSph. Overhead sources see minimal improvement to the limits, while high zenith sources
1379 see an order of magnitude improvement for all DM masses. Softer SM annihilation channels see
1380 broad improvements to the limit compared to harder channels.

1381 **6.7 Systematics**

1382 These are identical to what was performed earlier in Glory Duck, Section 5.7. We are also
1383 sensitive to the choice in spatial template, and this was explored in Section 5.7.2 and Section 5.8.2.

1384 **6.8 Conclusion and Discussion**

1385 In this multithreaded analysis, we have used observations of 3 dSphs from HAWC to perform
1386 a collective DM search for annihilation signals. The data were combined across sources to signifi-
1387 cantly increase the sensitivity of the search. Advanced computational techniques were deployed to
1388 accelerate wall-time spent analyzing by an order of magnitude. We have observed no significant
1389 deviation from the null, no DM, hypothesis, and so present our results in terms of upper limits on
1390 the annihilation cross-section for seventeen potential DM annihilation channels across four decades
1391 of DM mass.

1392 This analysis serves as a proof of concept for multithreaded HAWC analyses with large parameter
1393 spaces. Larger datasets with fast techniques will be essential to tackling the DM problem. The
1394 models we used for this study include annihilation channels with neutrinos in the final state.
1395 Advanced studies could aim to merge our results with those from neutrino observatories with large
1396 data sets.

1397 A full HAWC analysis will include systematic studies of the J -factor distributions. Additionally,
1398 because of the timing reduction, the study can be doubled in size to include DM decay. We have no
1399 yet received the remaining spatial profiles to the $\mathcal{L}\mathcal{S}$ catalog, and limits can be quickly computed
1400 once these are received. Finally, statistical studies with Poisson variation of HAWC’s background
1401 are essential to a comprehensive understanding of our observed excesses.

Segue1

Coma Berenices

Sextans

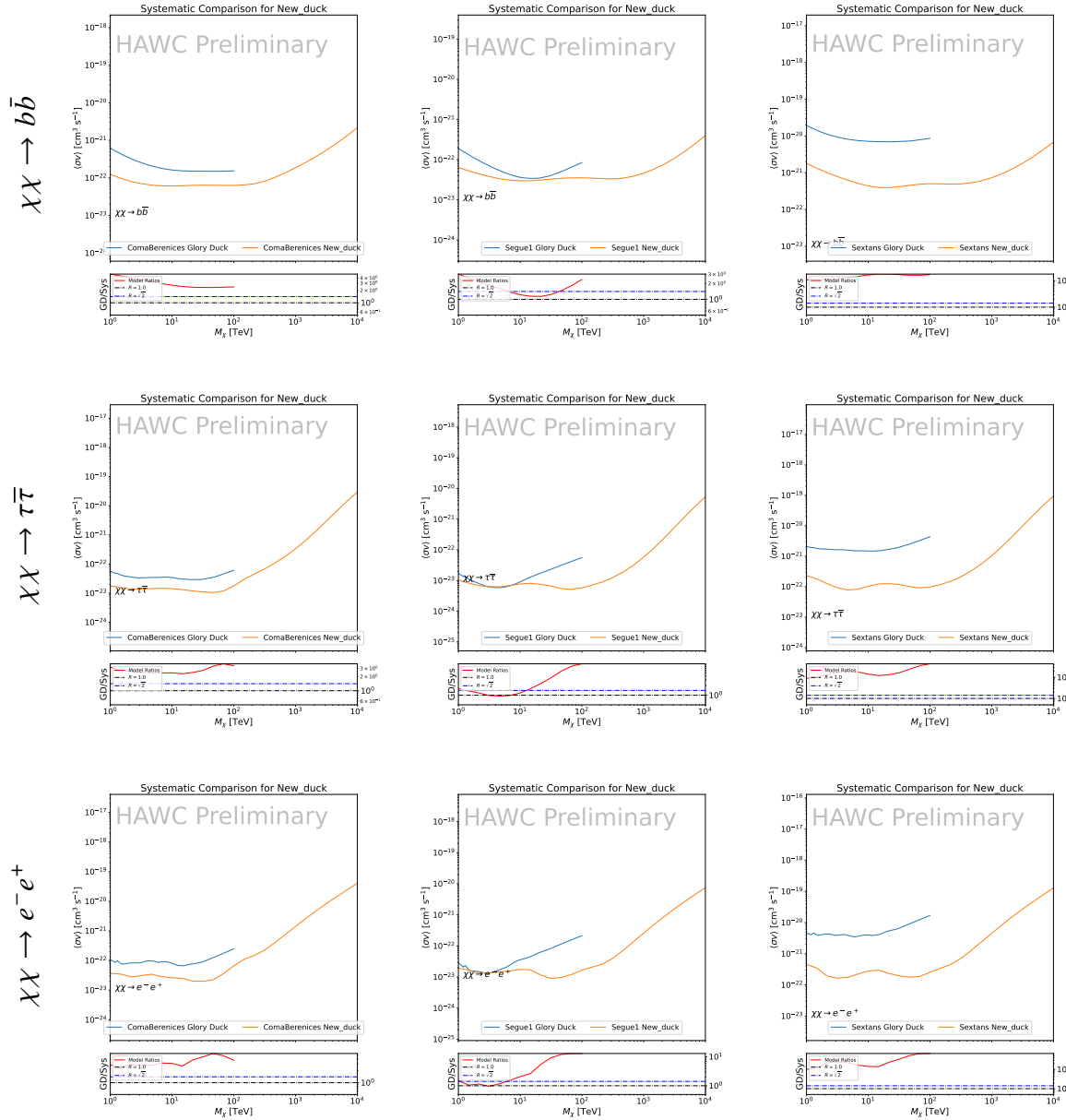


Figure 6.11 Comparison of HAWC limits from this analysis to Glory Duck (Fig. 5.5) for 3 dSphs and 3 SM annihilation channels: $b\bar{b}$, $\tau\bar{\tau}$, and $e\bar{e}$. Each sector shows the 95% confidence limit from Glory Duck (blue line) and this analysis (orange line) in the top plot. The lower plot features the ratio in log scale of Glory Duck to this analysis in a red solid line. Horizontal dashed lines are for ratios of 1.0 (black) and $\sqrt{2}$ (blue). Ratios larger than 1.0 are for limits smaller, or stricter, than Glory Duck. Ratios larger than $\sqrt{2}$ indicates limits are stricter than a simple doubling of the Glory Duck data.

CHAPTER 7

HEAVY DARK MATTER ANNIHILATION SEARCH WITH ICECUBE'S NORTH SKY TRACK DATA

7.1 Introduction

Neutrinos are another astrophysical messenger than can travel long distances without interaction. Uniquely, they interact less readily than photons especially above PeV energies. Neutrinos thereofre provide another window through which we can perform dark matter searches. Neutrinos come in three flabors and so this triples the multiplicity of the particles we are searching for.

Icecube has not done a DM annihilation analysis towards dwarf galaxies for a while. **TODO:**

cite 2013 paper. This is in spite of the potentially crucial sensitivity afforded from neutrino spectral lines **TODO: cite dan hooper and neutrino lines.** A lot has changed in IC3 since that last analysis (we have more strings, we have much more sophisticated analysis methods, and the theory modeling has made significant leaps.) Therefore it is time to finally do a DM search toward dSphs. The hope is that by laying down the important statistical foundation as well, that this work can be meshed with gamma-ray data. IceCube is sensitive to annihilating DM to the DM ranges above 1 TeV and can produce competitive results relative to gamma ray observatories in spectral models that produce sharp neutrino features. The goal of this analysis is to perform a DM annihilation search using the new datasets NST. The search will only be towards dwarf spheroidal galaxies (dSph). These sources are known for their low backgrounds and high DM contents. Since the dataset is sensitive to the north and south, as many dSph as possible will be included. Additionally, with annihilation, these sources can be treated as point sources with little loss to sensitivity or model dependence on how the DM is distributed. DM masses from 500 GeV to 100 PeV are considered for this analysis. All standard model annihilation channels available from the HDMspectra are studied in this analysis.

Additional work is done to extract the Likelihood profiles for each DM, source hypothesis so that these data can be combined with gamma-ray observatories. This work is considered a separate project as the statistical treatment is unique from many IceCube analyses. The wiki for [the

1428 combined analysis] **TODO: instead point to chapter**This chapter presents the analysis work for
1429 IC3 for DM searches toward dSphs. This section describes the various steps and features of the
1430 analysis. It is structure first introduces the data and how it is treated, then systematic studies of the
1431 dwarves individually. Finally, the stacked analysis and results are presented.

1432 **7.2 Dataset and Background**

1433 This section enumerates the data and background methods used for IceCube's study of dSphs.
1434 Section 7.2.1 and Section 7.2.2 are most useful for fellow IceCube collaborators looking to replicate
1435 this analysis.

1436 **7.2.1 Itemized IceCube files**

- 1437 • Software Environment: CVMFS Py3-v4.1.1
- 1438 • Data Sample: Northern Tracks NY86v5p1
- 1439 • Analysis Software: csky ([nu_dark_matter](#))
- 1440 • Analysis wiki: https://wiki.icecube.wisc.edu/index.php/Dark_Matter_Annihilation_Search_towards_dwarf_spheroidals_with_NST_and_DNN_Cascades
- 1442 • Project repository

1443 **7.2.2 Software Tools and Development**

1444 This analysis was performed inside IceCube's CVMFS (3.4.1.1) software environment using
1445 csky for likelihood calculations. Csky did not come with dark matter spectral models nor could
1446 accomodate custom flux models. We developed these capacities for single source and stacked
1447 source studies for this analysis. The analysis code is held in a separate repository from csky. The
1448 [nu_dark_matter](#) branch of csky manages the input of custom dark matter spectra and accompanied
1449 DM astrophysical source then calculates likelihoods with a selected data sample. The [IceCube Dark](#)
1450 [Matter dSph repository](#) manages the generation of spectral models for neutrinos, physics parameter
1451 extraction from n_{sig} , J -factor per source inputs, and bookkeeping for the large parameter space.
1452 The project repository required a secondary software environment for neutrino oscillations. How

1453 to launch and run those calculations are documented in the project repository and the Docker image
1454 is additionally saved in Section C.1

1455 **7.2.3 Data Set and Background Description**

1456 For this analysis, I use the Northern Sky Tracks (NST) Sample (Version V005-P01). The sample
1457 contains up-going track-like events, usually from ν_μ and ν_τ and has a superior angular resolution
1458 compared to the cascade dataset. This sample covers 10.4 years of data (IC86_2011-2021). The
1459 accepted neutrino energy range used for the analysis is unique from most other IceCube searches
1460 because DM spectra are very hard. The sampled energy range is $1 < \log(E_\nu/\text{GeV}) < 9.51$ with
1461 step size 0.125.

1462 The strength of a dwarf analysis is that there is no additional background consideration beyond
1463 nominal, baseline background estimations. For NST, the nominal contribution comes from atmo-
1464 spheric neutrinos and isotropic astrophysical neutrinos. We estimate the background by scrambling
1465 NST data along Right Ascension.

1466 **7.3 Analysis**

1467 The expected differential neutrino flux from DM-DM annihilation to standard model particles,
1468 $d\Phi_\nu/dE_\nu$, over solid angle, Ω is described by the familiar equation.

$$\frac{d\Phi_\nu}{dE_\nu} = \frac{\langle\sigma v\rangle}{8\pi m_\chi^2} \frac{dN_\nu}{dE_\nu} \times \int_{\text{source}} d\Omega \int_{l.o.s} \rho_\chi^2 dl(r, \theta') \quad (7.1)$$

1469 This is identical to past examples except that there are 3 neutrino flavors, so there are a corresponding
1470 3 flux equations. Section 5.3 has a complete description of all the terms. Additionally, neutrinos
1471 oscillate between flavors which needs to be considered for the expected neutrino flux at Earth.
1472 Section 7.3.1 presents the particle physics model for DM annihilation. Section 7.3.2 presents the
1473 spatial distributions built for each dSph.

1474 **7.3.1 $\frac{dN_\nu}{dE_\nu}$ - Particle Physics Component**

1475 Neutrino spectra from heavy dark matter annihilation were generated using HDMSSpectra [64]
1476 and χ arrov [68]. HDMSSpectra simulates the decay and annihilation of heavy dark matter, for
1477 different dark matter masses and SM primary annihilation channels. The simulation includes

1478 electroweak radiative corrections and higher order loop corrections with quarks. This publication
 1479 also pushes the simulated DM mass to the Plank scale (1 EeV), however this study will not explore
 1480 that high.

1481 An important novel feature in the spectra is that neutrino line channels will be accompanied
 1482 with a low energy tail. Thus the earth will not fully attenuate a neutrino SM channel signal from
 1483 high declination sources where the neutrino flux must first traverse through the Earth. The SM
 1484 annihilation channels that feature lines include all leptonic channels. ($\nu_{e,\mu,\tau}$, e , μ , and τ) We use
 1485 [Xarov](#) to propagate and oscillate the neutrinos from the source to Earth. Because these sources are
 1486 quite large in absolute terms, and also far (order 10 kpc or more), the resulting flavor spectra are
 1487 the averages of the transition probabilities [68]:

$$P(\nu_\alpha \rightarrow \nu_\beta) \approx \begin{bmatrix} 0.55 & 0.18 & 0.27 \\ 0.18 & 0.44 & 0.38 \\ 0.27 & 0.38 & 0.35 \end{bmatrix} \quad (7.2)$$

1488 When calculating the expected contribution to n_s , only ν_μ , ν_τ are considered as NST's effective
 1489 area to ν_e is essentially 0 [69]. With these consideration, the expected composite neutrino spectrum
 1490 is sum of the two flavors: $\nu_\mu + \nu_\tau$. The spectral tables are then converted to splines to condense
 1491 information, enable random sampling of the spectra, and enable faster computation times. The
 1492 spectral splines are finally implemented as a DM class in csky. Examples of the spectra before and
 1493 after propagation are shown in Fig. 7.1.

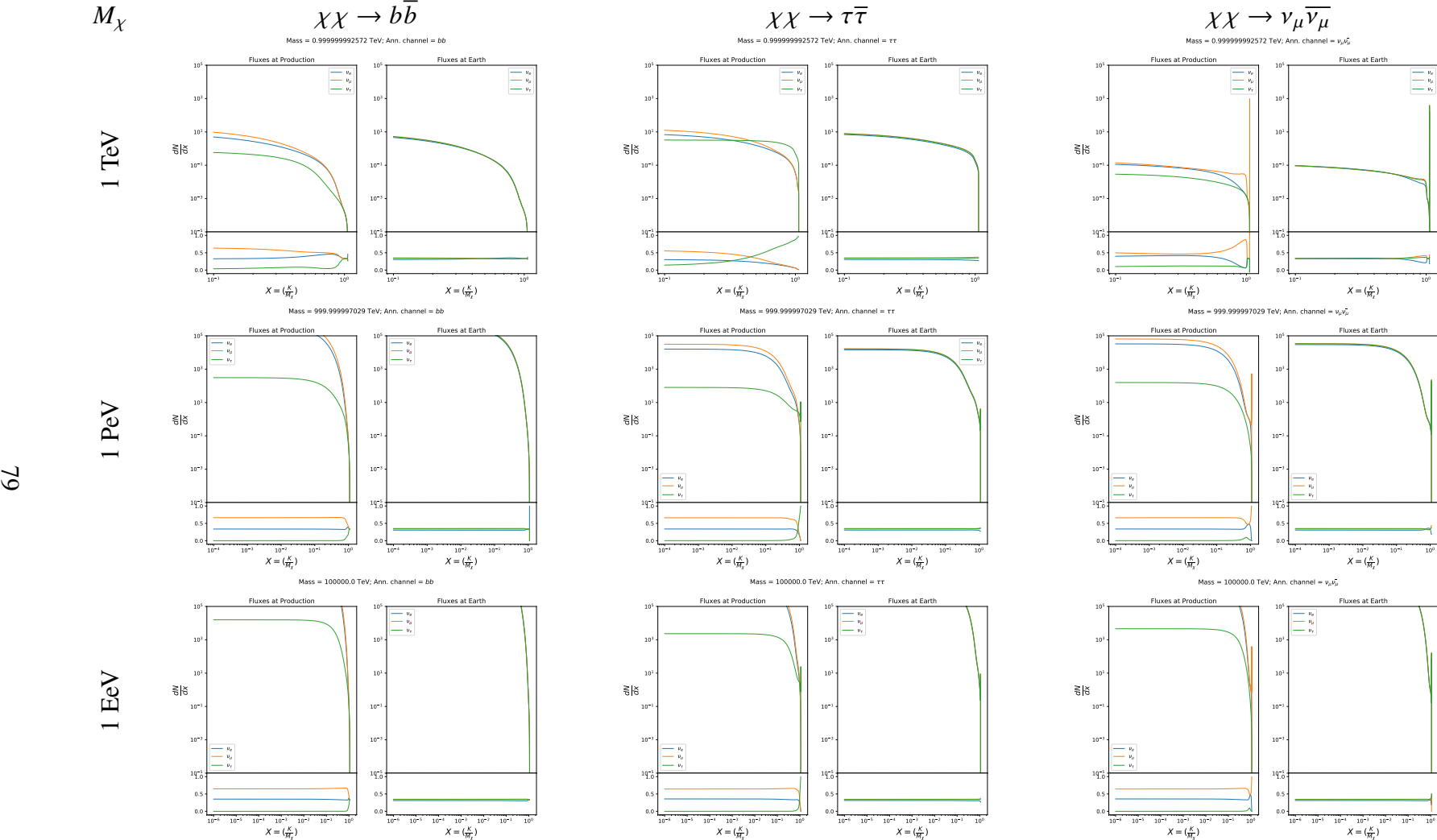


Figure 7.1 Neutrino spectra at production (left panels) and after oscillation at Earth (right panels). Blue, orange, and green lines are the ν_e , ν_μ , and ν_τ spectra respectively. Top panels show the spectra in $\frac{dN}{dE}$. Lower panels plot the flavor ratio to $\nu_e + \nu_\mu + \nu_\tau$. SM annihilation channels $b\bar{b}$, $\tau\bar{\tau}$, and $\nu_\mu \bar{\nu}_\mu$ are shown for $M_\chi = 1$ PeV, TeV, and EeV.

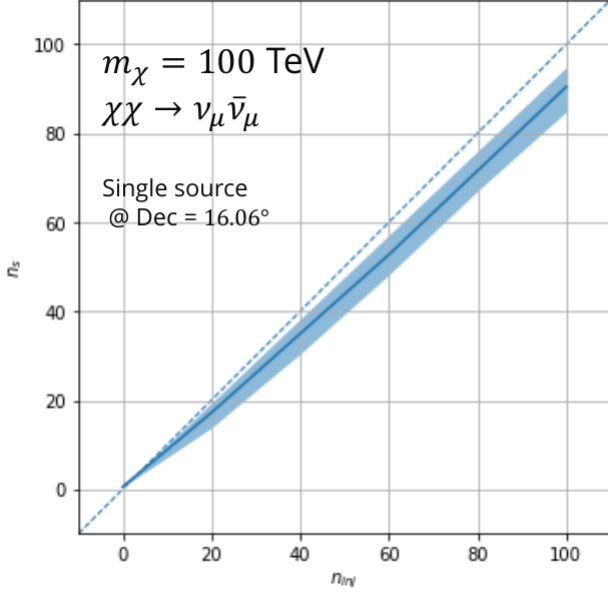


Figure 7.2 Signal recovery for 100 TeV DM annihilation into $\nu_\mu \bar{\nu}_\mu$ for a source at Dec = 16.06°. n_{inj} is the number of injected signal events in simulation. n_s is the number of reconstructed signal events from the simulation. Although the uncertainties are small and tight, the reconstructed n_s are systematically underestimated.

1494 7.3.1.1 Treatment of Neutrino Line Features

1495 All leptonic DM annihilation channels $\chi\chi \rightarrow [\nu_{e,\mu,\tau}, e, \mu, \tau]$ develop a prominent and narrow

1496 spectral line feature. For all neutrino flavors, this line is visible and prominent in all mass models

1497 studied for this analysis. For charged leptons, the feature only really shows up at the larger DM

1498 mass models. Examples for lines in both neutrinos and charged leptons annihilation are provided

1499 in Fig. 7.1. This line feature is so narrow relative the sampled energy range that the MC rarely

1500 samples within the neutrino line. As a result, often the best fit to simulation of background will

1501 always floor to TS = 0 and the signal recovery tends to be conservative.

1502 To remedy this, a similar approach to the IceCube’s decay analysis [TODO: refer to Minjin’s](#)

1503 [page](#). 2 kernels were tested (Gaussian, uniform (flat)) to smooth out the line feature. The widths

1504 were tuned such that the signal recovery approached unity for DM mass 100 TeV to 1 PeV.

1505 Additionally, the tuning was performed only for a source at declination 16.06 (Segue 1). This is

1506 to avoid confusion loss in signal recovery from too narrow a line and from Earth’s attenuation of

1507 high energy neutrinos. The convolution also needed to as close as possible preserve the integrated

1508 counts of neutrinos. The optimized kernel window for all lines is summarized as:

- 1509 • Gaussian kernel w/ 2σ width = $3.5E-3 \cdot m_\chi$
- 1510 • Minimum energy included in convolution = $\text{MIN}[0.995 \cdot m_\chi, En(\nu_{line}) - 4\sigma]$
- 1511 • Maximum energy included in convolution = $\text{MAX}[1.005 \cdot m_\chi, En(\nu_{line}) + 4\sigma]$

1512 where $En(\nu_{line})$ is the neutrino energy where the neutrino line is at the maximum.

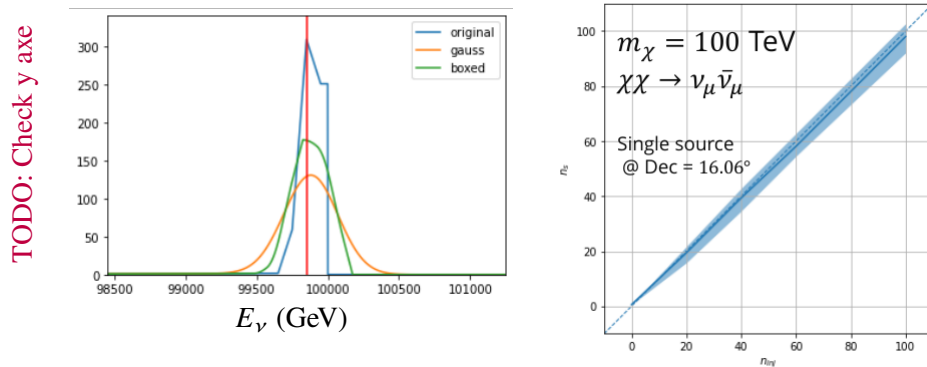


Figure 7.3 Top left panel shows the two kernels overlayed the original spectrum from Charon. delta I is the difference in the integral of the peaks with respect to the original spectrum. The vertical red line indicated where the original neutrino line is maximized. Lower right shows the signal recoveries of the DM model using the Gaussian kernel with parameters enumerated above.

1513 These parameters broadly improved the signal recovery of the line spectra. An example is
1514 provided below. Signal recovery plots of the full analysis are provided much further down.

1515 7.3.1.2 Spline Fitting

1516 In an effort to reduce computational work, memory burden, and align with point source methods
1517 used for NGC1068 and Seyfert analyses, spectral splines were created and adopted for estimating
1518 the neutrino flux for the different annihilation. Software was written to generate, handle, and
1519 calculate values on the splines. When using splines, one has to be careful of the goodness to fit.
1520 There are critical caveats when testing the goodness to fit to MC generated above for all channels.

- 1521 • The splines must be Log10(*) in Energy and dN/dE to account for the exponential nature of
1522 the flux
- 1523 • The fidelity of the fit matters more at $E_\nu \approx m_\chi$ where the model uncertainties are minimal
1524 and physical considerations (like the cut-off) are most apparent.

- 1525 • The fidelity of the fit matters less at low E_ν as the model uncertainties are large AND
 1526 IceCube's sensitivity diminishes significantly below 500 GeV
- 1527 • Total integrated counts should be well preserved, however, the resolution of the MC is much
 1528 higher than IceCube's energy resolution.
- 1529 – Meaning over several steps in E, the integral is preserved
- 1530 – the step size enters the cost function
- 1531 – Oscillating residuals, so long as they are very small and well centered, are not penalized
- 1532 as this gets averaged out.

1533 The resulting cost function to evaluate the goodness of fit was used to account for the above
 1534 considerations.

$$e_i = x_i \cdot \left(\frac{dN_i}{dE_i} - 10^{\hat{e}_i} \right) \quad (7.3)$$

1535 Where \hat{e}_i is the spline estimator's value for x_i . $x_i = E_{\nu_i}/m_\chi$. $\frac{dN_i}{dE_i}$ is the flux value from MC.

$$\text{err} = \sqrt{\frac{1}{x_{\max} - x_{\min}} \int_{x_{\min}}^{x_{\max}} e^2 dx} \quad (7.4)$$

1536 I then take the RMS of the error distribution and the resulting value (err) is used to evaluate
 1537 the fidelity of the spectral spline. Each SM channel had different tolerances for 'err'. Channels
 1538 with very hard cut-offs had looser tolerance for err because a lot of error would be generated from
 1539 the cut-off being estimated to occur slightly early or late. Soft channels don't have this issue and
 1540 therefore the tolerance is very strict. The table blow summarizes the tolerances for the SM channels.

1541
 1542 The errors are then plotted in two ways. First, FAIL and OK are directly plotted with e_i as a
 1543 function of x, and the full spline and MC. Second, a summary plot of all the splines is plotted and
 1544 colors coded.

1545 Figure C.1 are the spline summaries and represent the current, up-to-date status of the splines.
 1546 The goal broadly is to eliminate all red and inspect yellow. ν_e is not considered in this analysis
 1547 among the neutrino final states and so no work was done to converge the spline fits for this flavor.

$\chi\chi \rightarrow$	GOOD	OK	FAIL	Limits of err calc [X_{min}, X_{max}]
$Z^0 Z^0, W^+ W^-$	1.0E-3	1.0E-3, 1.0E-2	1.0E-2	MAX[100GeV/ m_χ , 10^{-6}], 1.0
$t\bar{t}, hh$	1.0E-5	1.0E-5, 1.0E-4	1.0E-4	MAX[100GeV/ m_χ , 10^{-6}], 1.0
$b\bar{b}, d\bar{d}, u\bar{u}$	9.0E-7	9.0E-7, 9.0E-6	9.0E-6	MAX[100GeV/ m_χ , 10^{-6}], 1.0
$\nu\bar{\nu}_{e,\mu,\tau}$	1.0E-3	1.0E-3, 1.0E-2	1.0E-2	MAX[100GeV/ m_χ , 10^{-6}], MIN[0.995, ($E_n(\nu_{line}) - 4\sigma$)/ M_χ]
$e\bar{e}, \mu\bar{\mu}, \tau\bar{\tau}$	1.0E-3	1.0E-3, 1.0E-2	1.0E-2	MAX[100GeV/ m_χ , 10^{-6}], MIN[0.995, ($E_n(\nu_{line}) - 4\sigma$)/ M_χ]

Table 7.1 TODO: fill me daddy

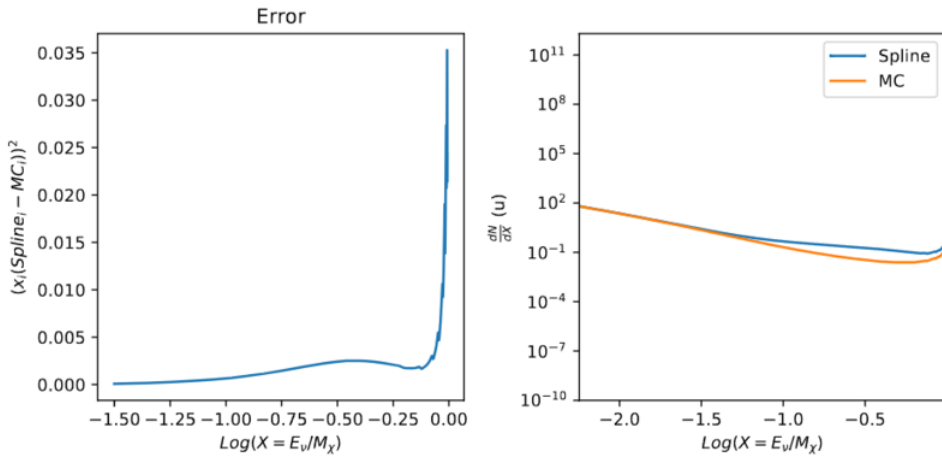


Figure 7.4 Example spline that failed the fit. Failed splined are corrected on a case by case basis unless the SM channel has a systematic problem fitting the splines. In this case, I made a bookkeeping error and loaded the incorrected neutrino flavor

1548 A Final inspection of the splines by eye was done to verify that the spline fitting did not introduce
 1549 spurious features into the distribution that would corrupt the LLH fitting.

1550 7.3.1.3 Composite Neutrino Spectra

1551 With all of the previously mentioned pieces, we are ready to fully assemble a comprehensive
 1552 description of the particle physics term dN/dE in Eq. (7.1).

$$\frac{dN_\nu}{dE_{\nu \oplus}} = \left(\frac{dN_{\nu_e}}{dE_{\nu_e}} + \frac{dN_{\nu_\mu}}{dE_{\nu_\mu}} + \frac{dN_{\nu_\tau}}{dE_{\nu_\tau}} \right)_{\text{src}} \cdot \mathbf{P}(\nu_\alpha \rightarrow \nu_\beta) \quad (7.5)$$

1553 Figure 7.5 shows the spectral models that required Gaussian smoothing, the leptonic annihilation
 1554 channels. The remaining models where the only processing was the spline fitting are documented
 1555 in the TODO: refer to apdxNotice that the different neutrino flavors are unique, especially in their
 1556 low energy tails. Therefore, this analysis will be sensitive to DM annihilating to the distinct neutrino

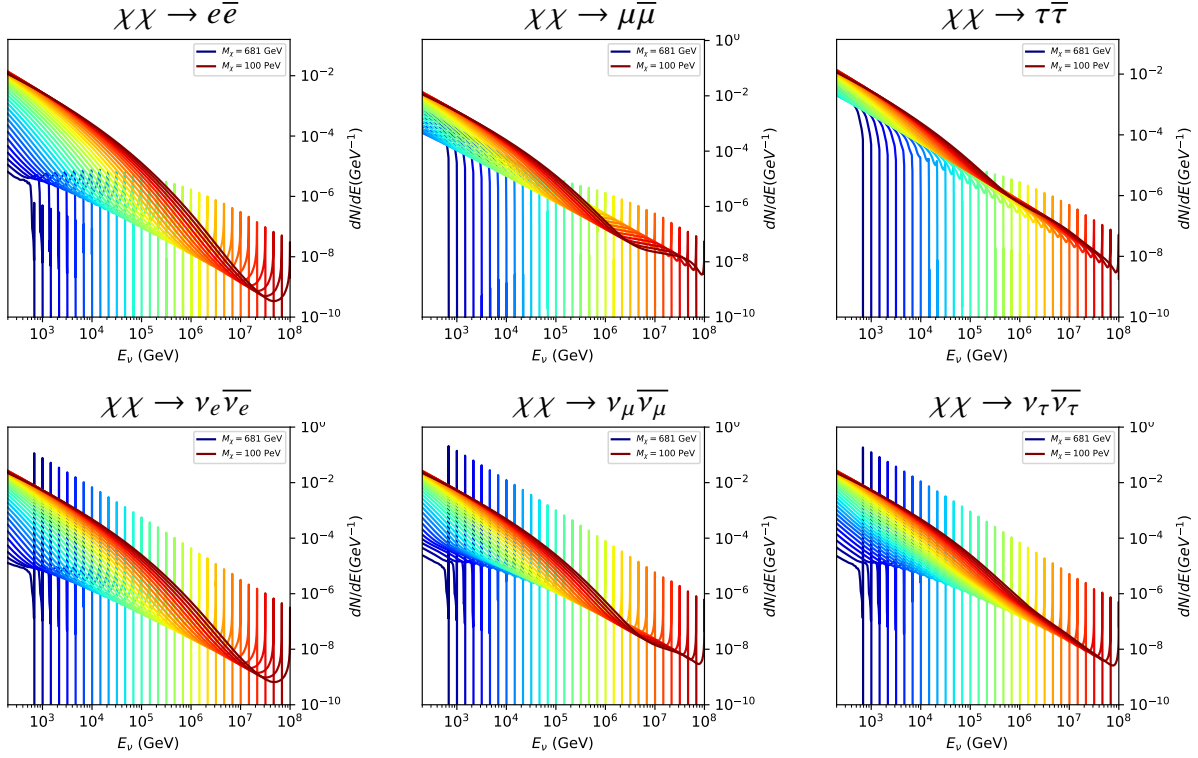


Figure 7.5 Summary of input spectral models that were smoothed with Gaussian kernel. Spectral models are for $\chi\chi \rightarrow e\bar{e}$, $\mu\bar{\mu}\tau\bar{\tau}$, $\nu_e\bar{\nu}_e$, $\nu_\mu\bar{\nu}_\mu$, and $\nu_\tau\bar{\nu}_\tau$. These spectra are the composite ($\nu_\mu + \nu_\tau$) of neutrino flavors. Every spectral model used for this analysis is featured as a colored solid line. Bluer lines are for lower DM mass spectral models. DM masses range from 681 GeV to 100 PeV. HDM [64], χ arov [68], and Photospline [70] are used to generate these spectra. Energy (x-axis) was chosen to roughly represent the energy sensitivity of NST.

1557 flavors. All leptonic channels show prominent, hard features around $E_\nu = m_\chi$.

1558 7.3.2 J- Astrophysical Component

1559 The expected neutrino counts from a dwarf spheroidal galaxy depends also on the the 'astro-
 1560 physical factor'. The value for this (in our specific case) J-factor for a target depends on its dark
 1561 matter density distribution, ρ_χ and how far it is l . For this analysis, we adopt the \mathcal{GS} model used
 1562 in Sec. 5 for dSph from [45]. These models are based on a modified Navarro-Frenk-White (NFW)
 1563 profile where the indices of the NFW (traditionally 1,3,1) are allowed to float. More specifically,
 1564 these DM distributions are described using the Zhao profile. The Zhao profile is written as:

1565 where θ is the angular distance from the center of the source. For the case annihilation, the
 1566 source diameter, [<https://iopscience.iop.org/article/10.1088/0004-637X/801/2/74> here] defined as

1567 the $2\theta_{\max}$, of these dwarves is typically under 1° with the largest in the catalog, Fornax, extending
 1568 to 2.61° . Fornax is not in the northern sky and the remaining sources are notably below this angular
 1569 size. Therefore, the sources are treated as point sources because the typical source diameter is under
 1570 1 degree. The J-factor used for the point source assumption is the total J emitted from θ_{\max} . These
 1571 values are enumerated in Geringer-Sameth 2015 and again in the table below with their coordinates.
 1572 Coordinates are given in J200.0 equatorial coordinates. IceCube uses identical sources to Tab. 5.1
 1573 except we analyze source with declinations above 0.0 degrees.

1574 7.3.3 Source Selection and Annihilation Channels

1575 We use all of the dSphs presented in IceCube's previous dSph DM search [69]. IceCube's
 1576 sources for these simulation studies include Bootes I, Canes VenaticiI, Canes Venatici II, Coma
 1577 Berenices, Draco, Hercules, Leo I, Leo II, Leo V, Leo T, Segue 1, Segue 2, Ursa Major I, Ursa Major
 1578 II, and Ursa Minor. A full description of all sources used in Table 5.1. Sources with declinations
 1579 less than 0.0 are excluded from this analysis.

1580 This analysis improves on the previous IceCube dSph paper [69] in the following ways. Pre-
 1581 viously, the IceCube detector was not yet completed to the 86 string configuration. Many more
 1582 dSphs will be observed, from 4 to 15. Previously, the particle physics model used for neutrino-ray
 1583 spectra from DM annihilation did not have EW corrections where they are now included [64]. The
 1584 spectral models also predict substantial differences between the neutrino flavors, so this analysis
 1585 will be the first DM dwarf analysis to discriminate between primary neutrino flavors. The study
 1586 performed here studies 10.4 years of data.

1587 The SM annihilation channels probed for this study include $b\bar{b}$, $t\bar{t}$, $u\bar{u}$, $d\bar{d}$, $e\bar{e}$, $\mu\bar{\mu}$, $\tau\bar{\tau}$, ZZ ,
 1588 W^+W^- , $\nu_e\bar{\nu}_e$, $\nu_\mu\bar{\nu}_\mu$, and $\nu_\tau\bar{\nu}_\tau$.

1589 7.4 Likelihood Methods

1590 I use the Point-Source search likelihood which is widely used in IceCube analyses. The
 1591 likelihood function is defined as the following:

$$L(n_s) = \prod_{i=1}^N \left[\frac{n_s}{N} S_i + \left(1 - \frac{n_s}{N}\right) B_i \right] \quad (7.6)$$

1592 where i is an event index, S and B are the signal PDF and background PDF respectively. For a joint
1593 analysis where the sources are stacked the likelihood is expanded in the simplified way:

$$L(n_s) = \prod_{i=1}^{N_{\text{sources}}} L_i(n_s) \quad (7.7)$$

1594 Where L_i is the likelihood from the i -th source in the stacked analysis. The test statistic definition
1595 remains the same as Eq. (5.6)

1596 7.5 Background Simulation

1597 Before we look at data, we must first analyze background and signal injection to validate our
1598 analysis. The following sections show the results of the likelihood fitting for a suite of background
1599 trials for the DM models we set out to study in [TODO: refer to the section](#). We study the TS
1600 distributions first for each source, then for the stacked analysis.

1601 The TS distributions are not expected to behave according to a chi-squared distribution with 1
1602 degree of freedom. This is in large part due to the distinct spectral shapes demonstrated earlier.
1603 These can vary significantly between DM mass and annihilation models. Therefore, Wilks' theorem
1604 may not be applicable to the analysis. Instead, a critical value is defined from a large number of
1605 background trials.

1606 I assume that TS values are physical: $\text{TS} \geq 0$. η denotes the fraction of positive TS values
1607 above the threshold and written in the legend. $\epsilon[x]$ indicate the fraction of events where $\text{TS} < x$.
1608 For TS plots shown here, the decimal values of x are $1.0\text{e-}2$ and $1.0\text{e-}3$. The following plots show
1609 the background TS distributions obtained from Segue1, a source with little Earth attenuation and
1610 large J-factor, assuming that dark matter annihilates into $b\bar{b}$. I also show the 15 source stack TS
1611 distributions with identical DM models.

1612 7.5.1 TS per Source

1613 Below I present the TS distributions for Segue1 and $\chi\chi \rightarrow b\bar{b}$. All remaining channels and
1614 source TS panels are hosted on [TODO: Change this text, it will all be here](#).

1615 Although it was not expected, almost every distribution produced follows a chi2 distribution
1616 with 1 degree of freedom. This is important for future assumptions made (in multi-messenger) and

1617 may justify statistical calculations assuming Wilk's theorem is valid.

1618 TODO: add text saying that you show: bb, numu, and tau??? specs for Seg1 and UMa2?

1619 **7.5.2 Stacked TS**

1620 The presentation of these plots are identical to the previous 'per Source' section. I use csky
1621 source software to calculate the TS distributions. Bugs were found when implementing, however
1622 were rectified. Warning to future users performing a stacked analysis with custom spectra. In
1623 using the above, I am making the implicit assumption that the primary/only cause to a difference in
1624 neutrino counts from the sources is accounted for through the J-factors. The J-factors are therefor
1625 used as weights for the stacking where an individual source's weight is defined as:

1626 Each subplot, except the final, is the TS distribution for a specific DM mass listed in the subplot.
1627 The final subplot plots the all DM spectral models used as input for the TS distribution calculations
1628 with bluer lines indicating lower DM mass and redder indicating higher DM mass. Below is an
1629 image of bb. The full resolution pdfs were provided in links above.

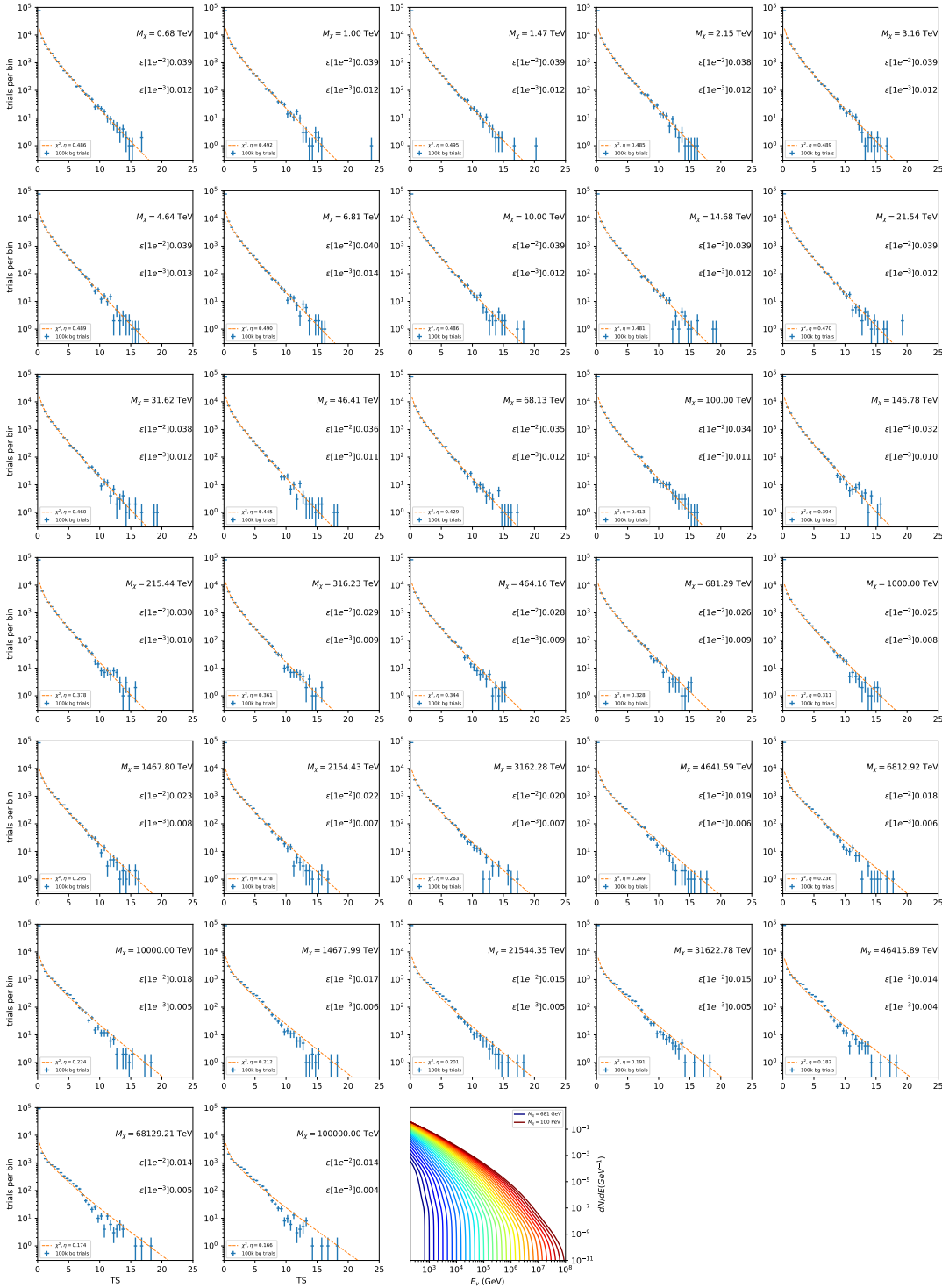


Figure 7.6 Test statistic (TS) distributions for Segue 1 and $\chi\chi \rightarrow b\bar{b}$. Each subplot, except the final, is the TS distribution for a specific DM mass listed in the subplot. Orange dashed lines are the traces for a χ^2 distribution with 1 degree of freedom. $\epsilon[\cdot]$ is the fraction of trials smaller than the bracketed value. The final subplot plots the all DM spectral models, similar to Fig. 7.5, used as input for the TS distributions.

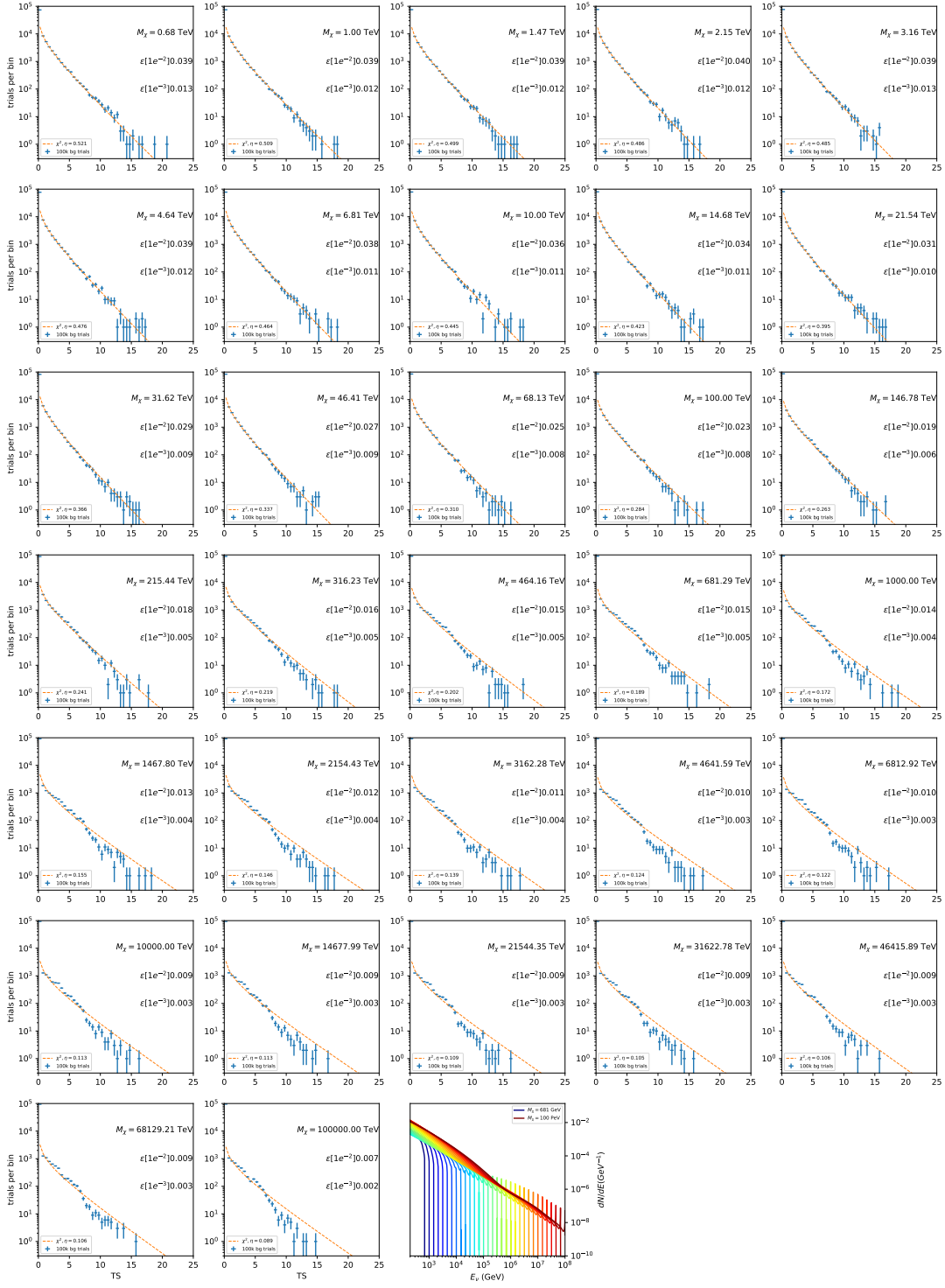


Figure 7.7 Same as Fig. 7.6 for Segue 1 $\chi\chi \rightarrow \tau\bar{\tau}$.

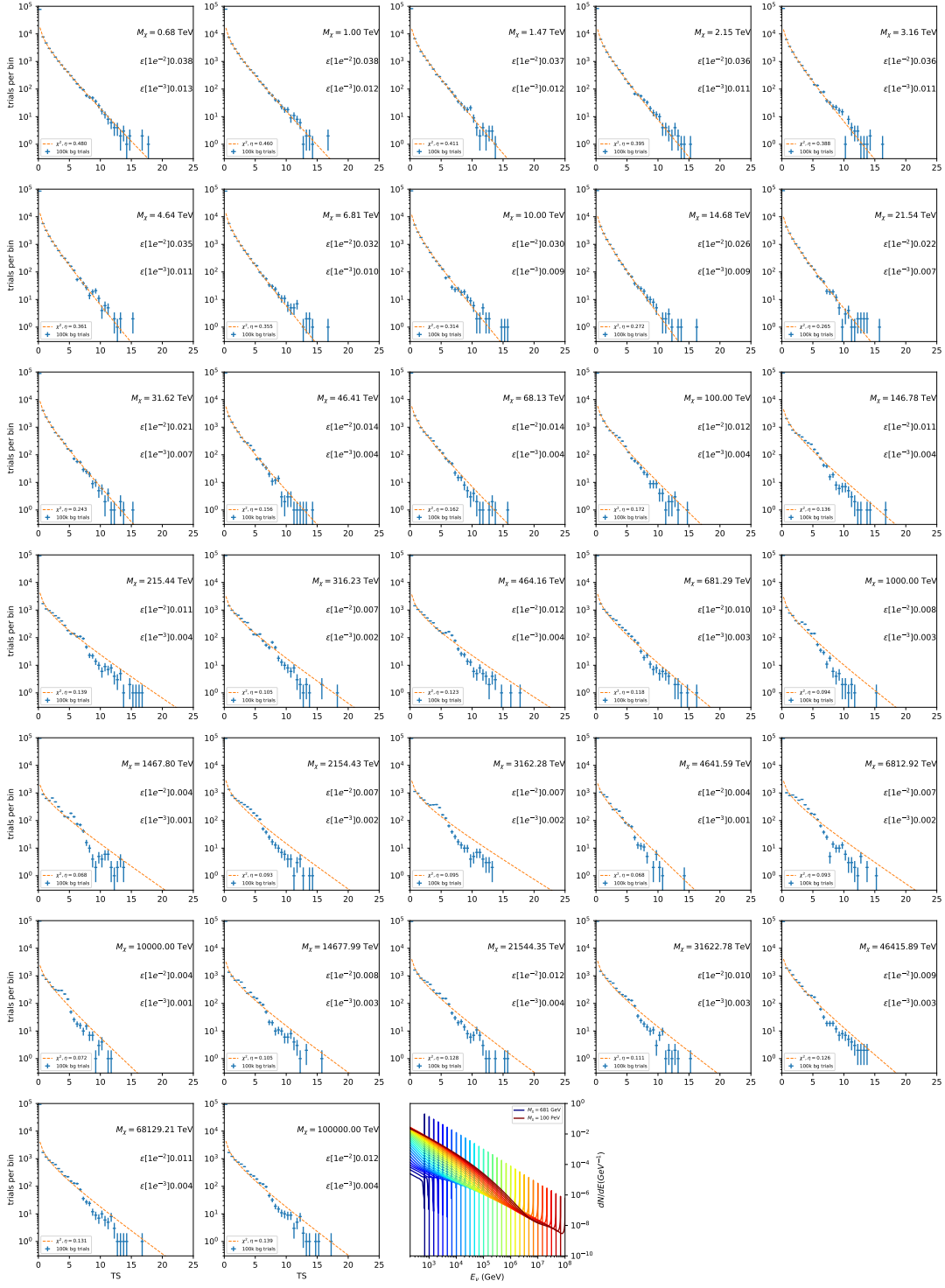


Figure 7.8 Same as Fig. 7.6 for Segue 1 $\chi\chi \rightarrow \nu_\mu\bar{\nu}_\mu$.

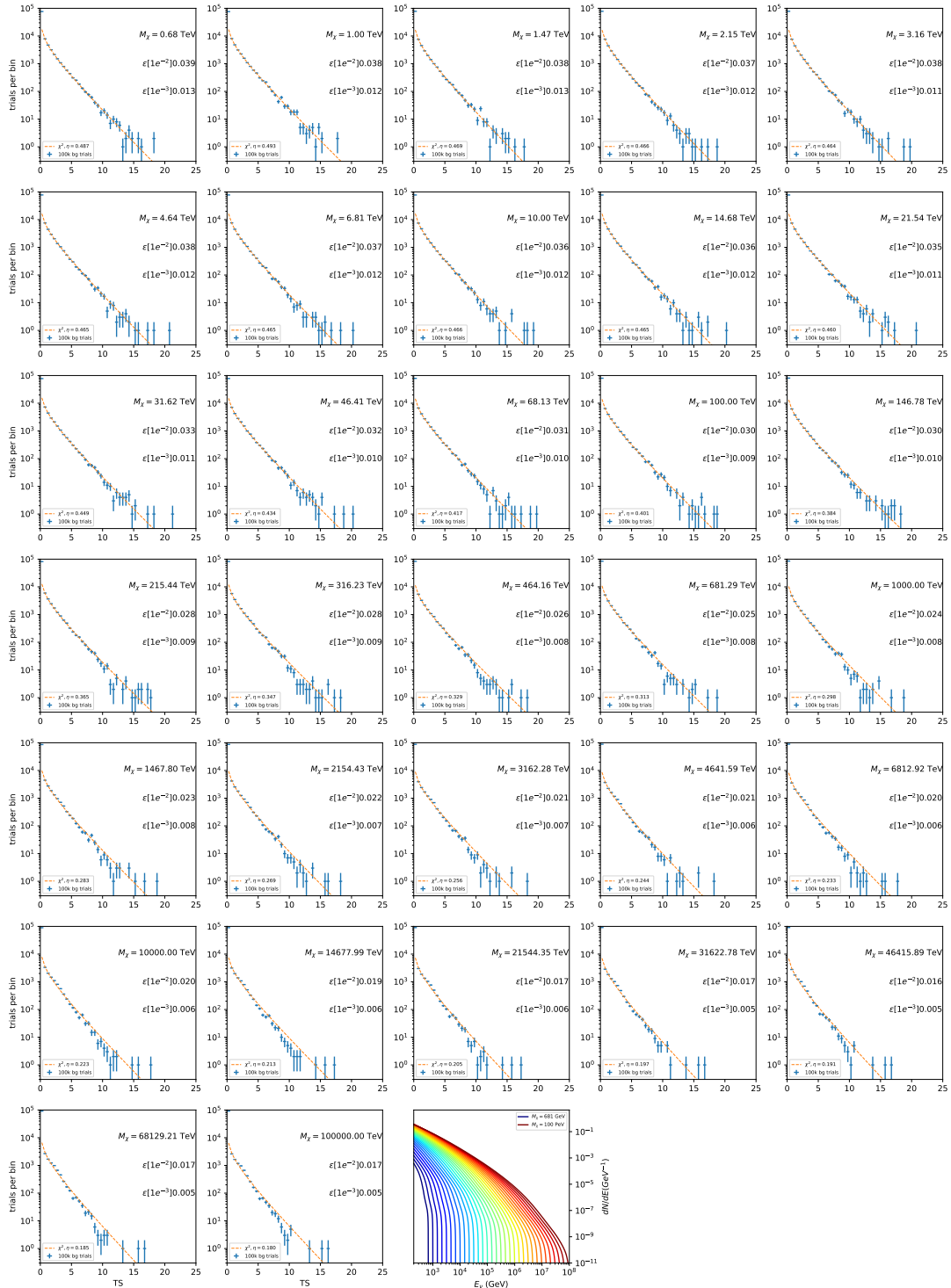


Figure 7.9 Same as Fig. 7.6 for Ursa Major II 1 $\chi\chi \rightarrow b\bar{b}$.

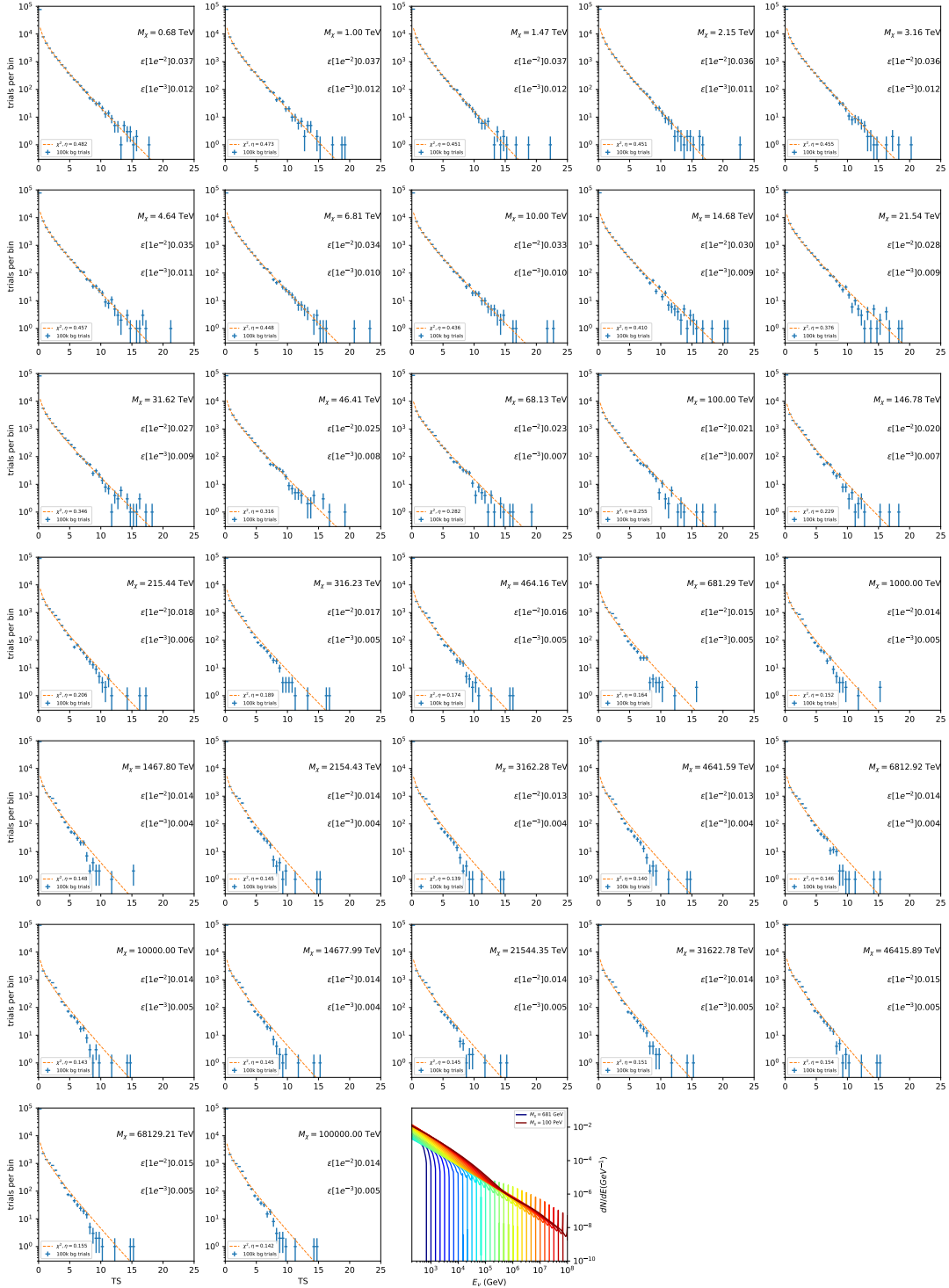


Figure 7.10 Same as Fig. 7.6 for Ursus Major II 1 $\chi\chi \rightarrow \tau\bar{\tau}$.

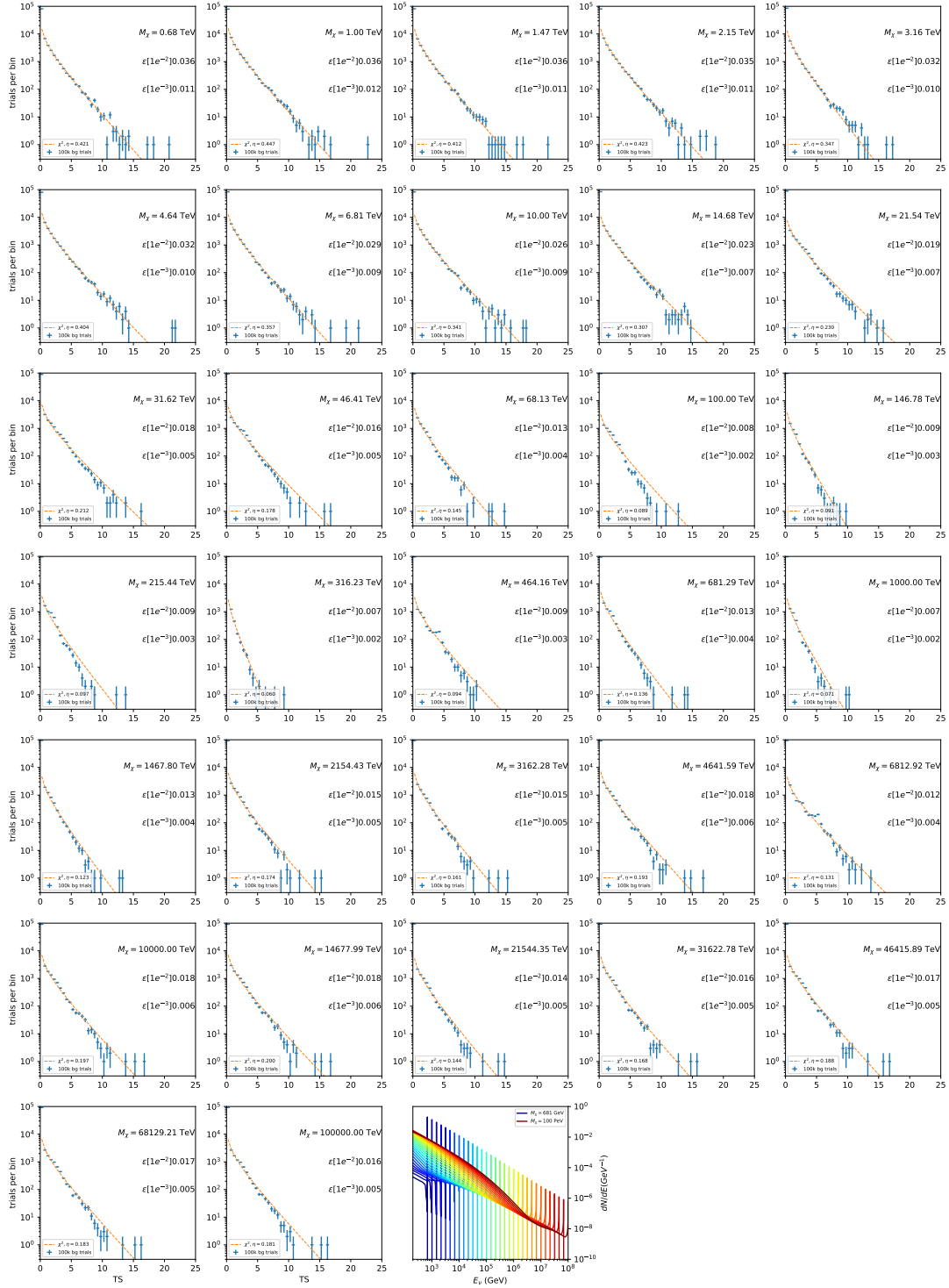


Figure 7.11 Same as Fig. 7.6 for Ursa Major II 1 $\chi\chi \rightarrow \nu_\mu \bar{\nu}_\mu$.

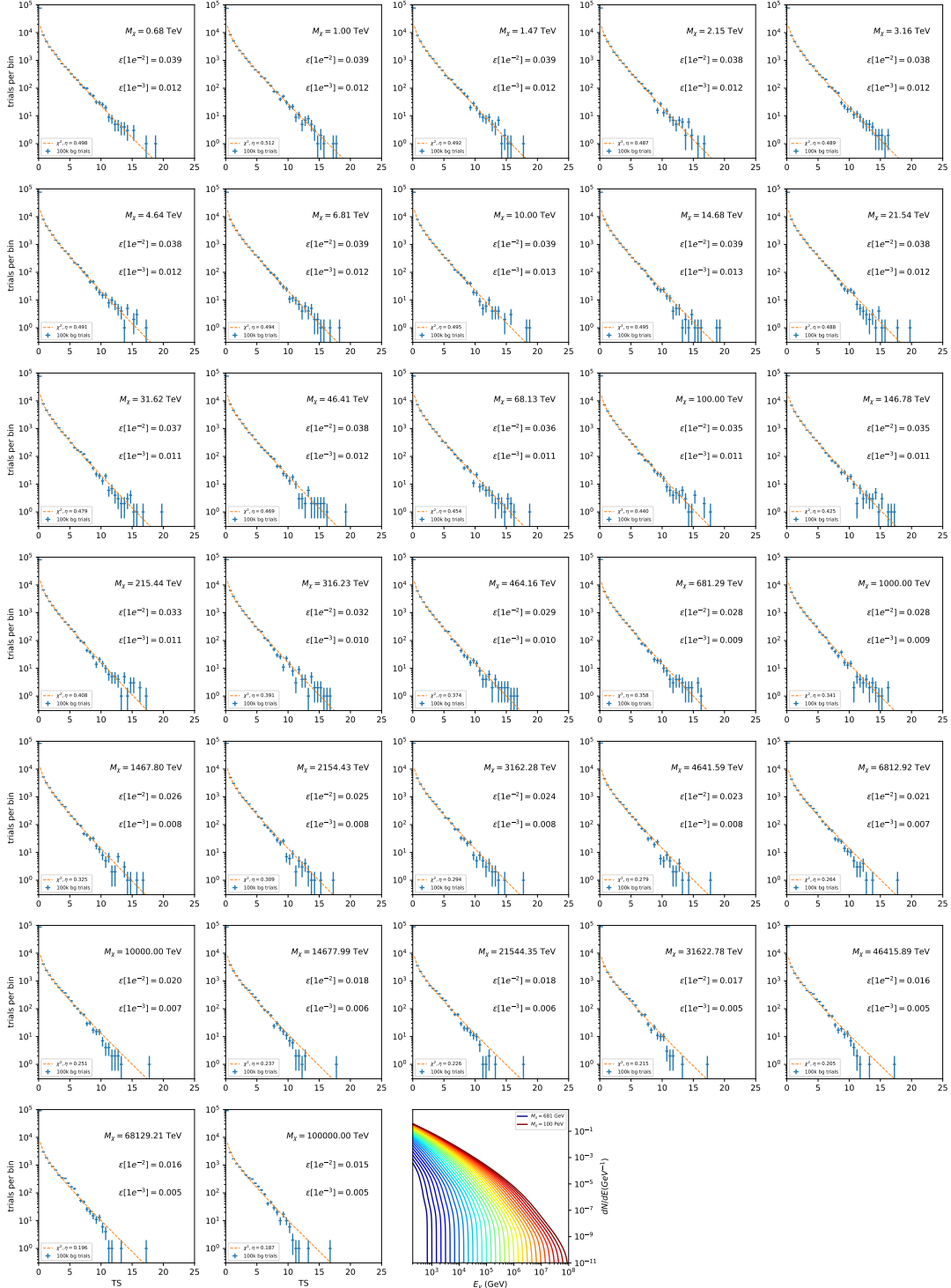


Figure 7.12 Same as Fig. 7.6 for 15, $\mathcal{G}\mathcal{S}$ J-factor, stacked sources and $\chi\chi \rightarrow b\bar{b}$.

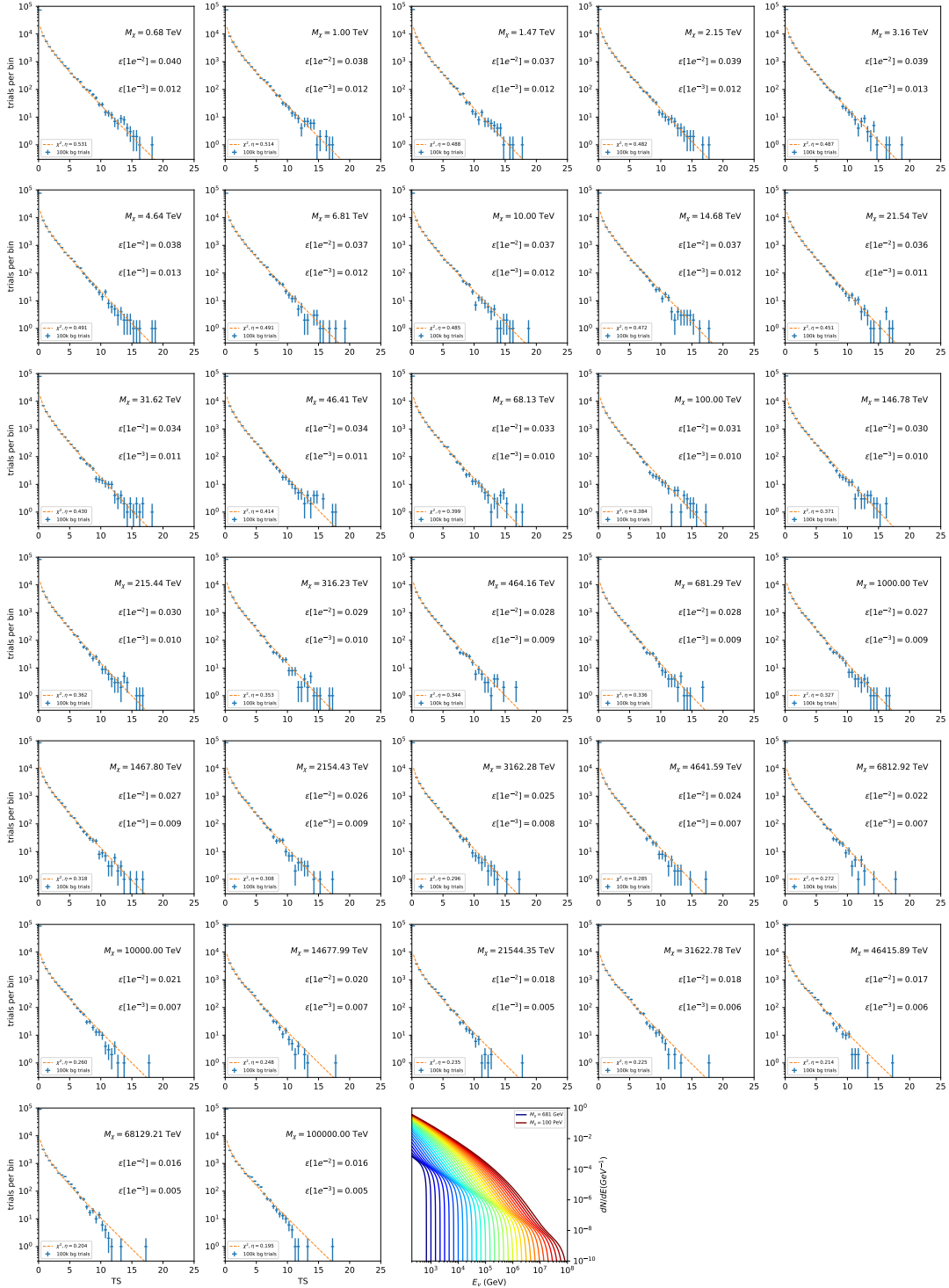


Figure 7.13 Same as Fig. 7.6 for 15, GS J-factor, stacked sources and $\chi\chi \rightarrow t\bar{t}$.

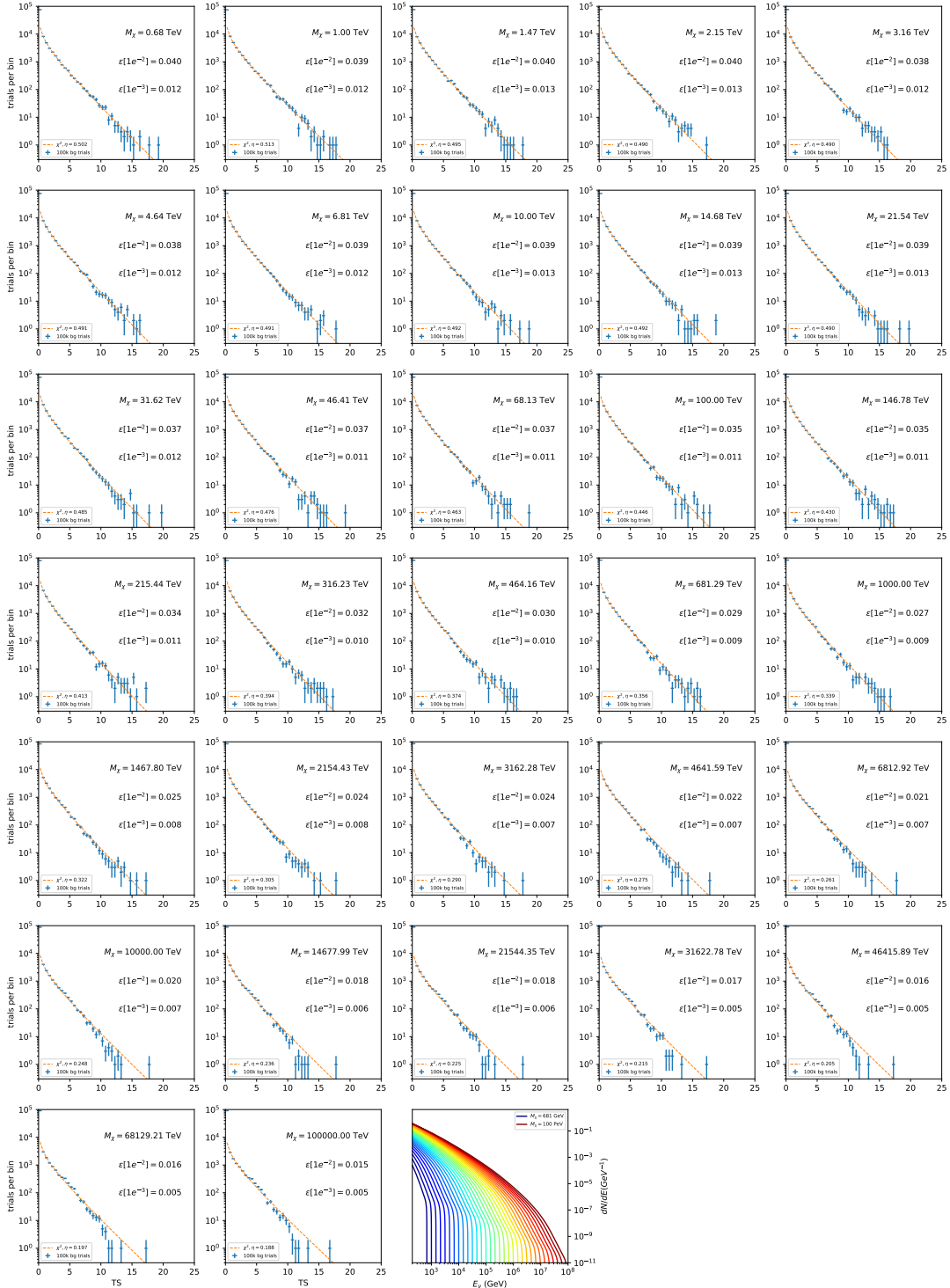


Figure 7.14 Same as Fig. 7.6 for 15, $\mathcal{G}\mathcal{S}$ J -factor, stacked sources and $\chi\chi \rightarrow u\bar{u}$.

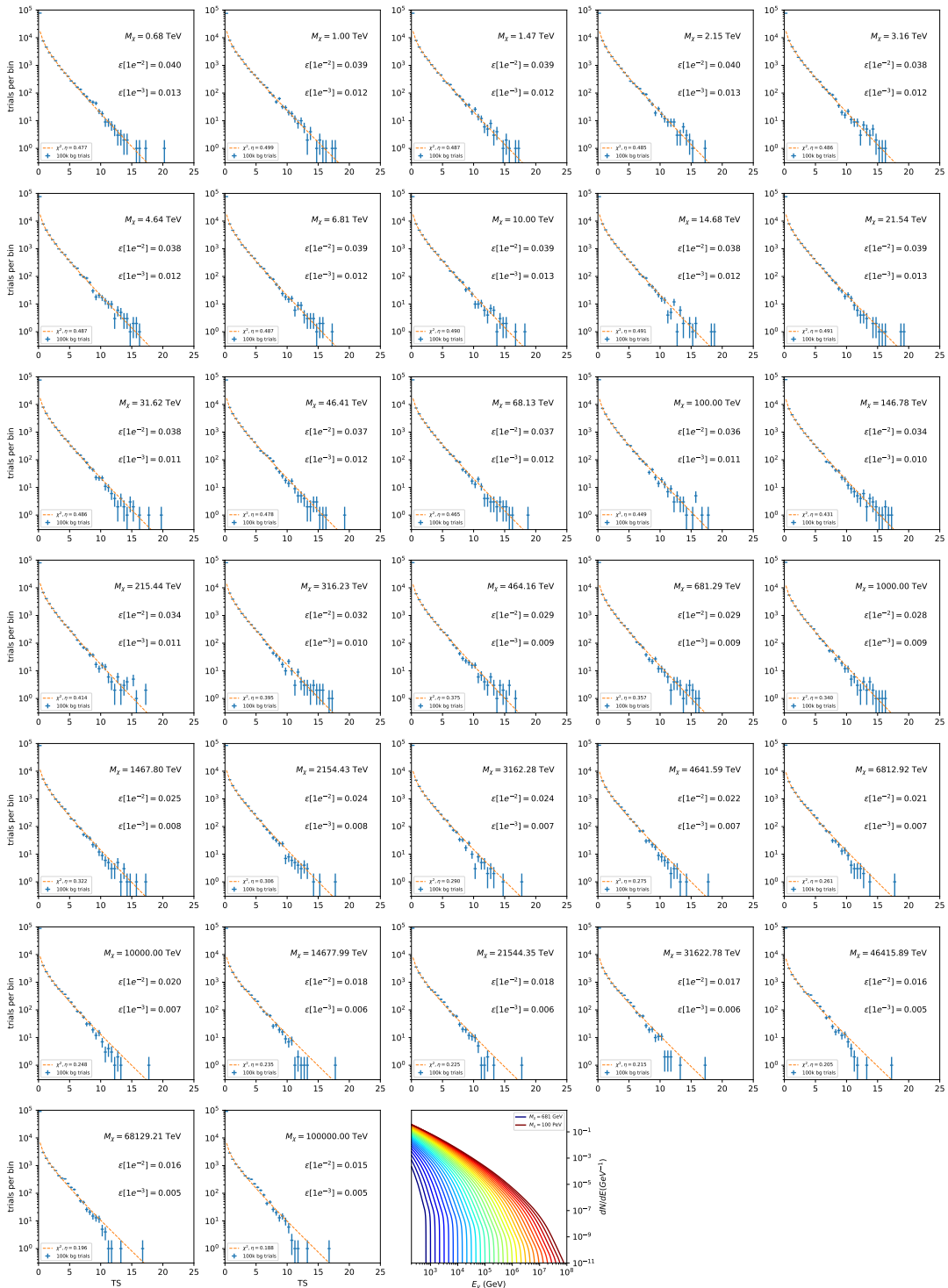


Figure 7.15 Same as Fig. 7.6 for 15, \mathcal{GS} J-factor, stacked sources and $\chi\chi \rightarrow d\bar{d}$.

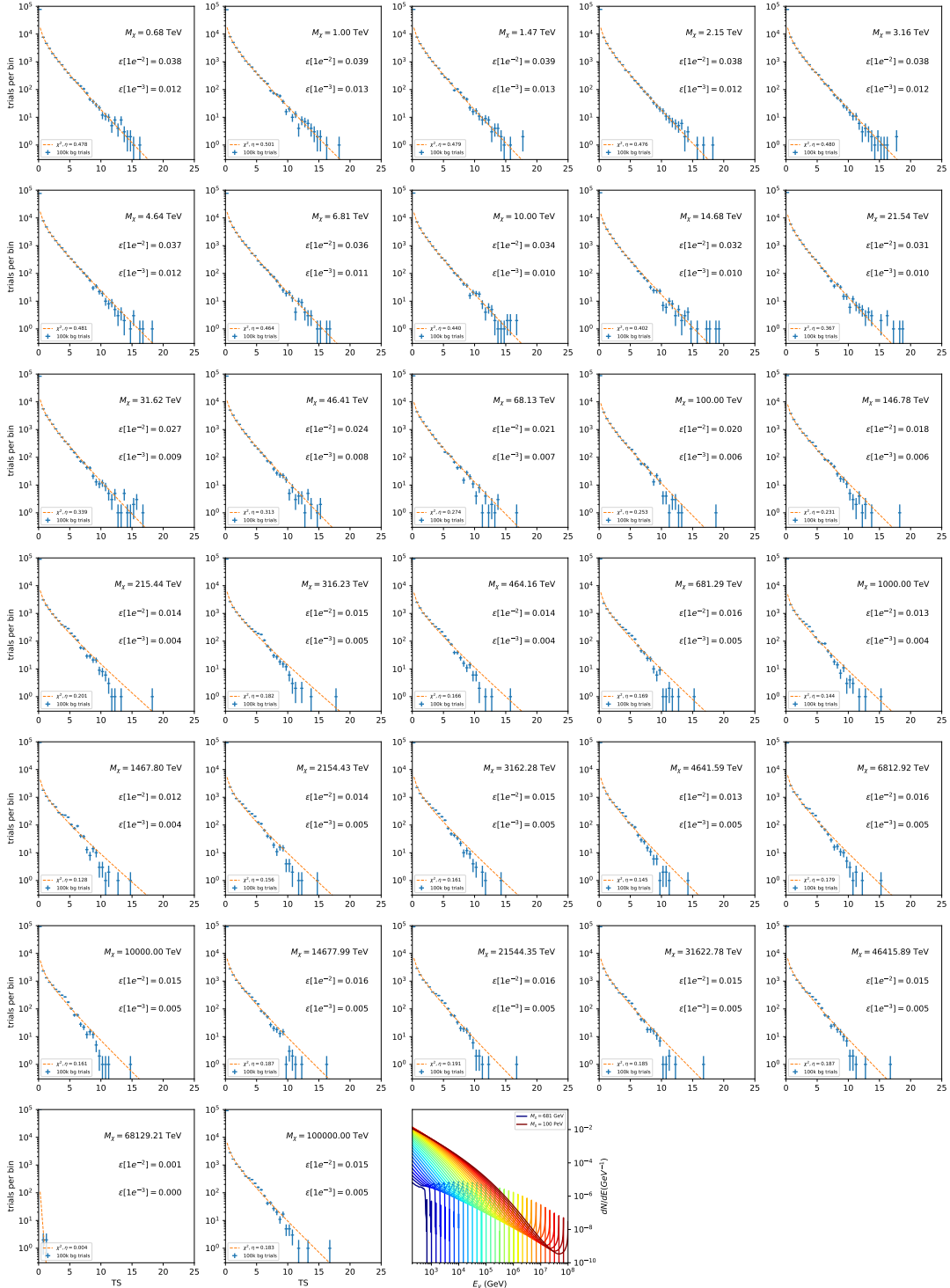


Figure 7.16 Same as Fig. 7.6 for 15, $\mathcal{G}\mathcal{S}$ J-factor, stacked sources and $\chi\chi \rightarrow e\bar{e}$.

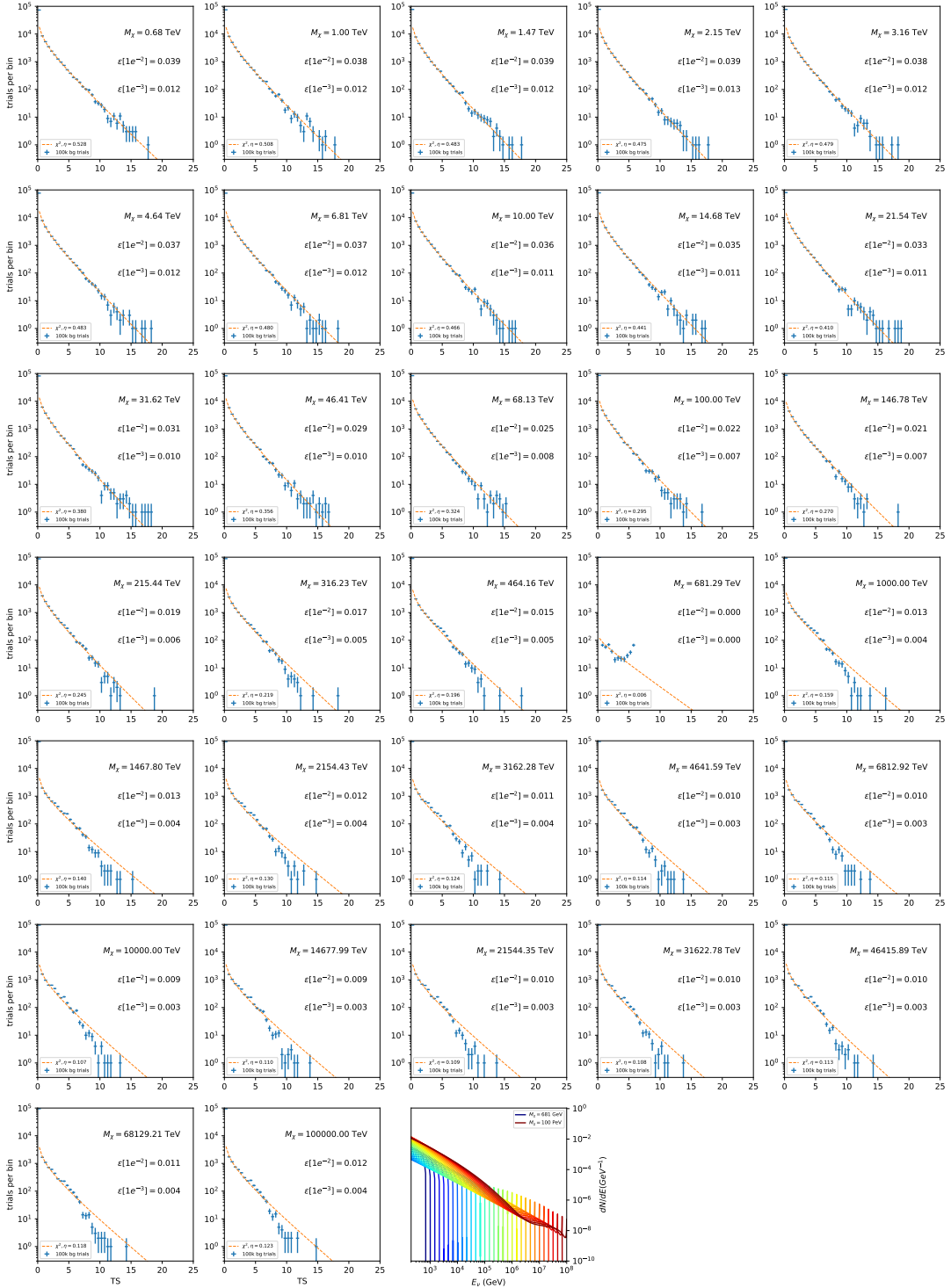


Figure 7.17 Same as Fig. 7.6 for 15, \mathcal{GS} J -factor, stacked sources and $\chi\chi \rightarrow \mu\bar{\mu}$.

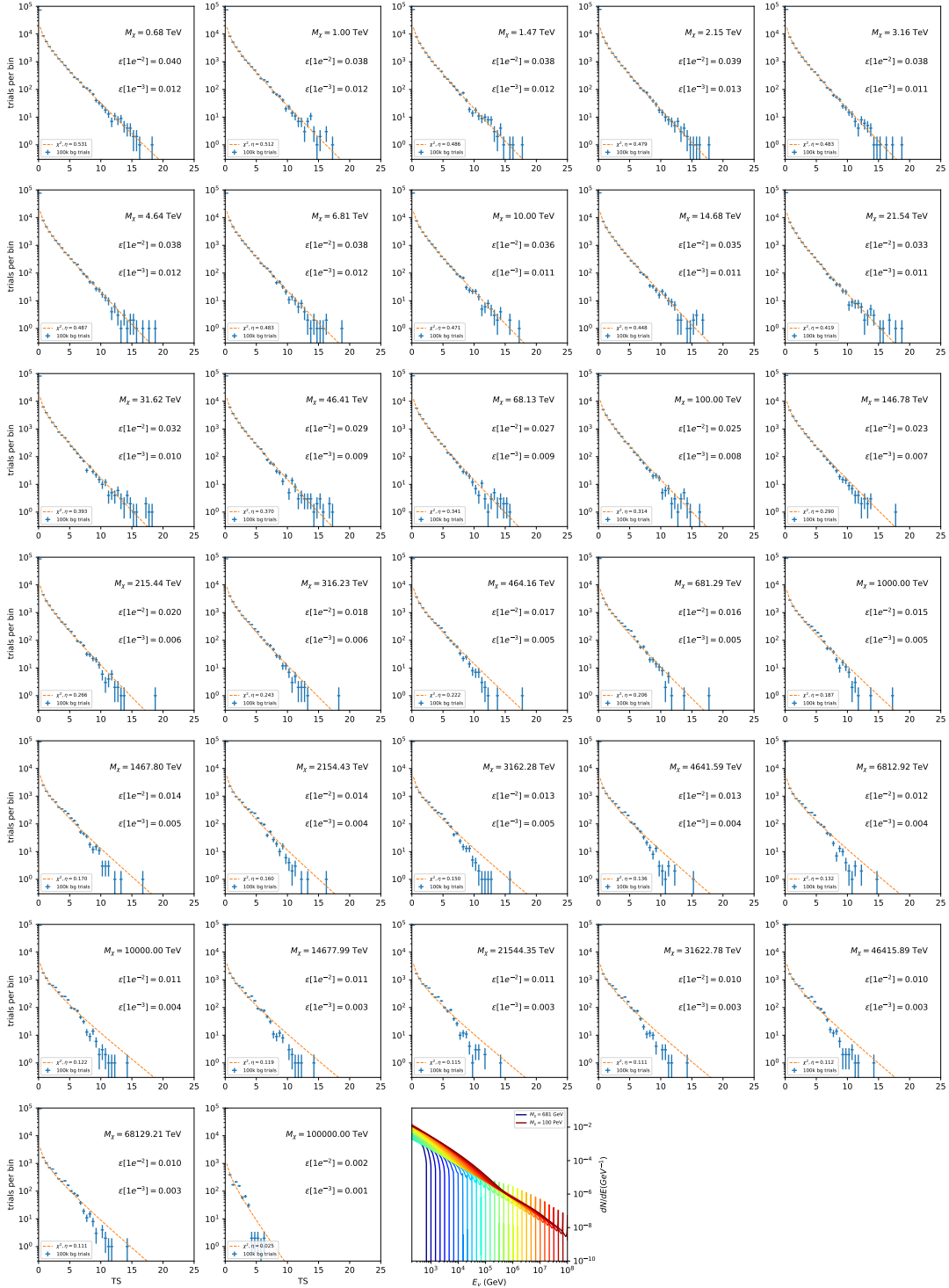


Figure 7.18 Same as Fig. 7.6 for 15, \mathcal{GS} J -factor, stacked sources and $\chi\chi \rightarrow \tau\bar{\tau}$.

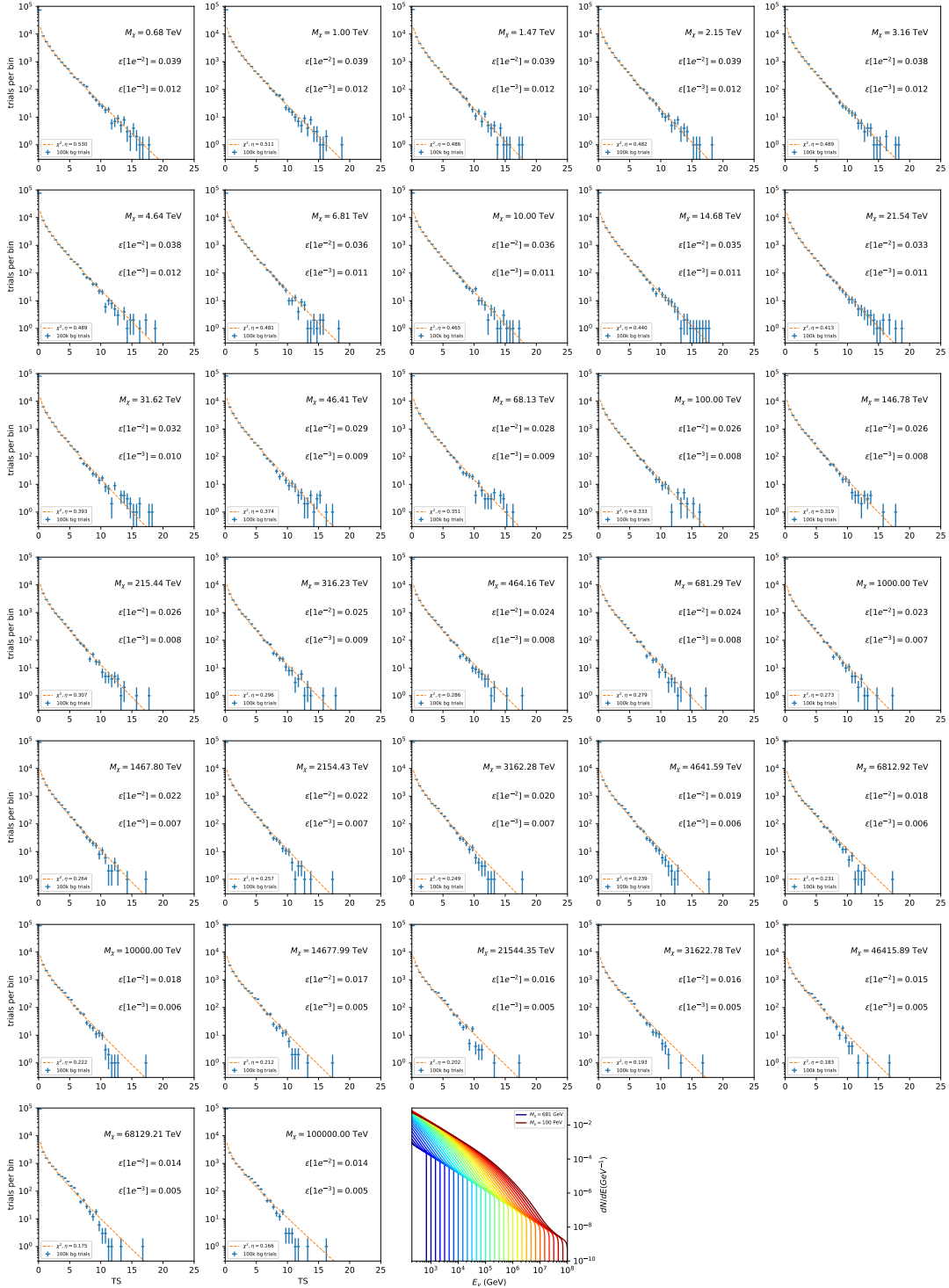


Figure 7.19 Same as Fig. 7.6 for 15, \mathcal{GS} J-factor, stacked sources and $\chi\chi \rightarrow W^+W^-$.

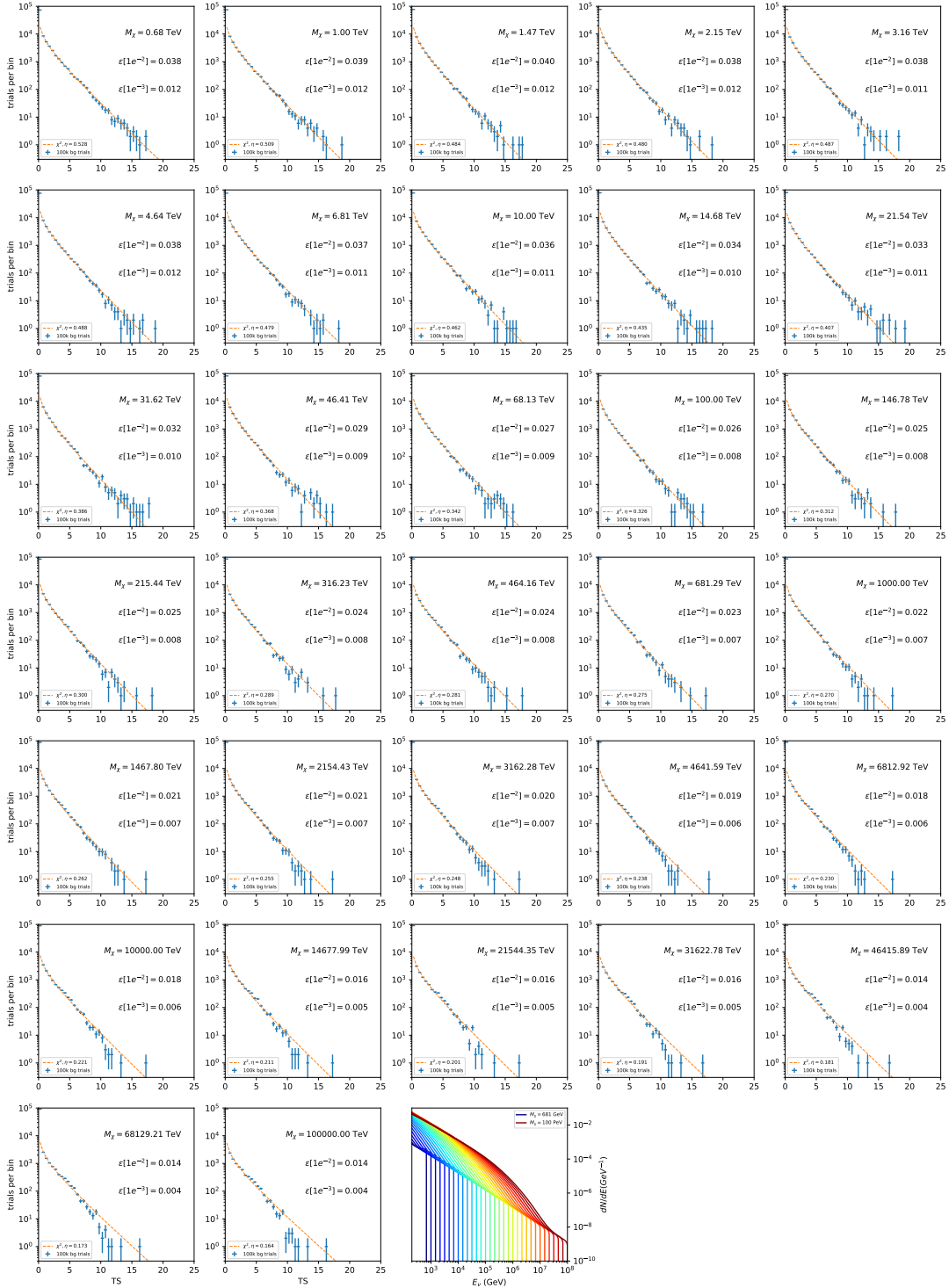


Figure 7.20 Same as Fig. 7.6 for 15, \mathcal{GS} J-factor, stacked sources and $\chi\chi \rightarrow ZZ$.

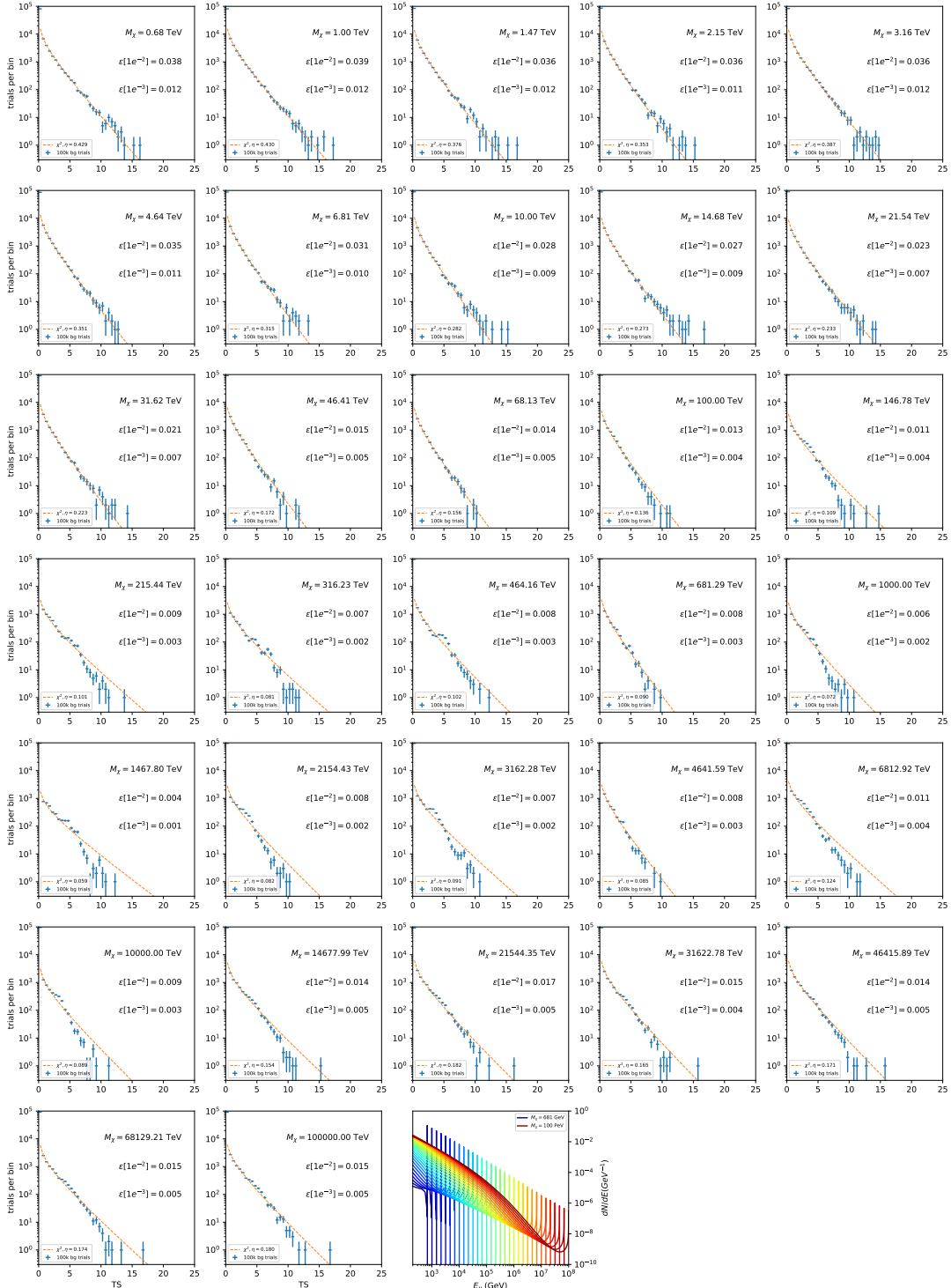


Figure 7.21 Same as Fig. 7.6 for 15, \mathcal{GS} J-factor, stacked sources and $\chi\chi \rightarrow \nu_e \bar{\nu}_e$.

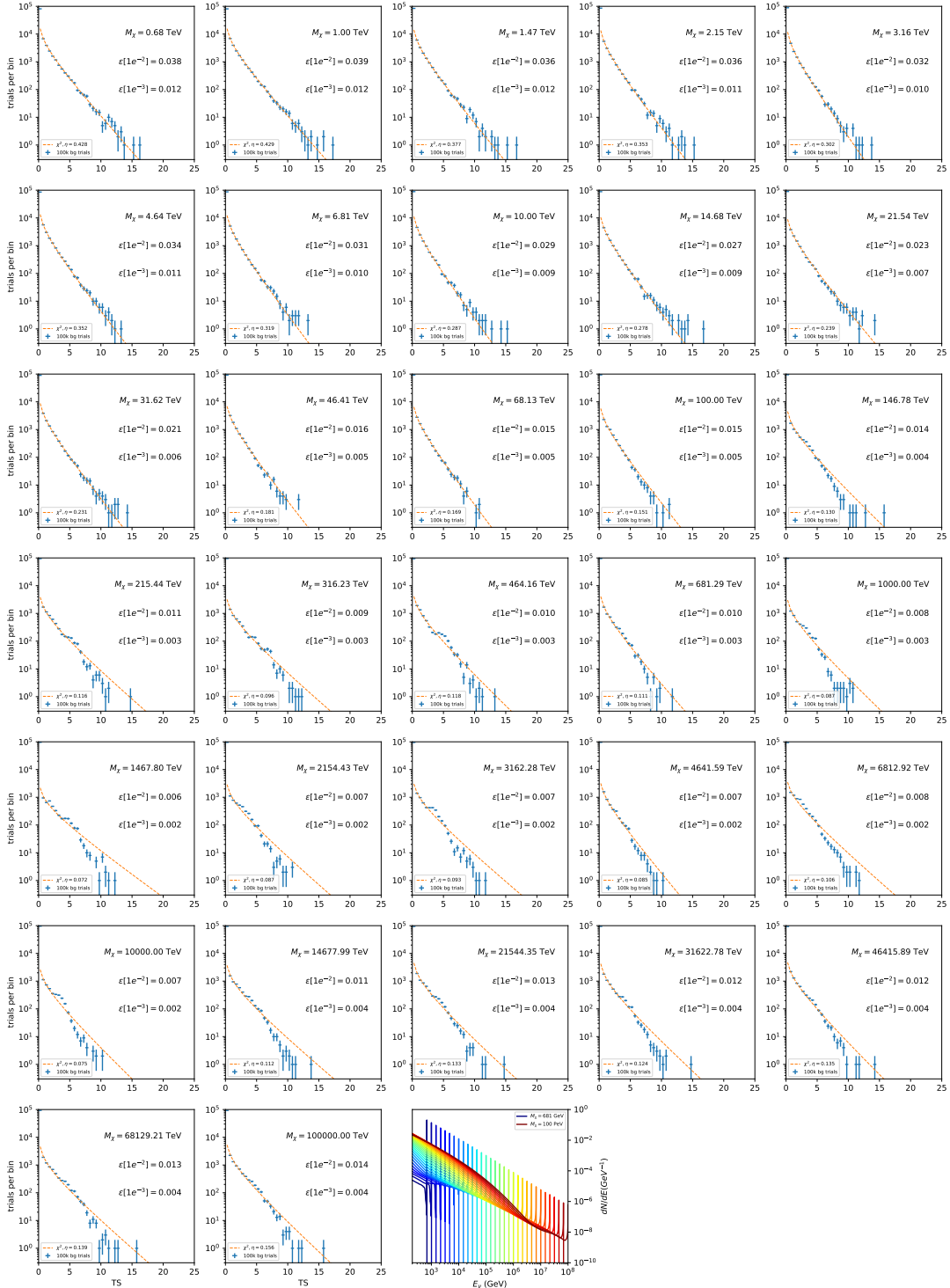


Figure 7.22 Same as Fig. 7.6 for 15, GS J-factor, stacked sources and $\chi\chi \rightarrow \nu_\mu \bar{\nu}_\mu$.

1630

CHAPTER 8

NU DUCK

MULTI-EXPERIMENT SUPPLEMENTARY FIGURES

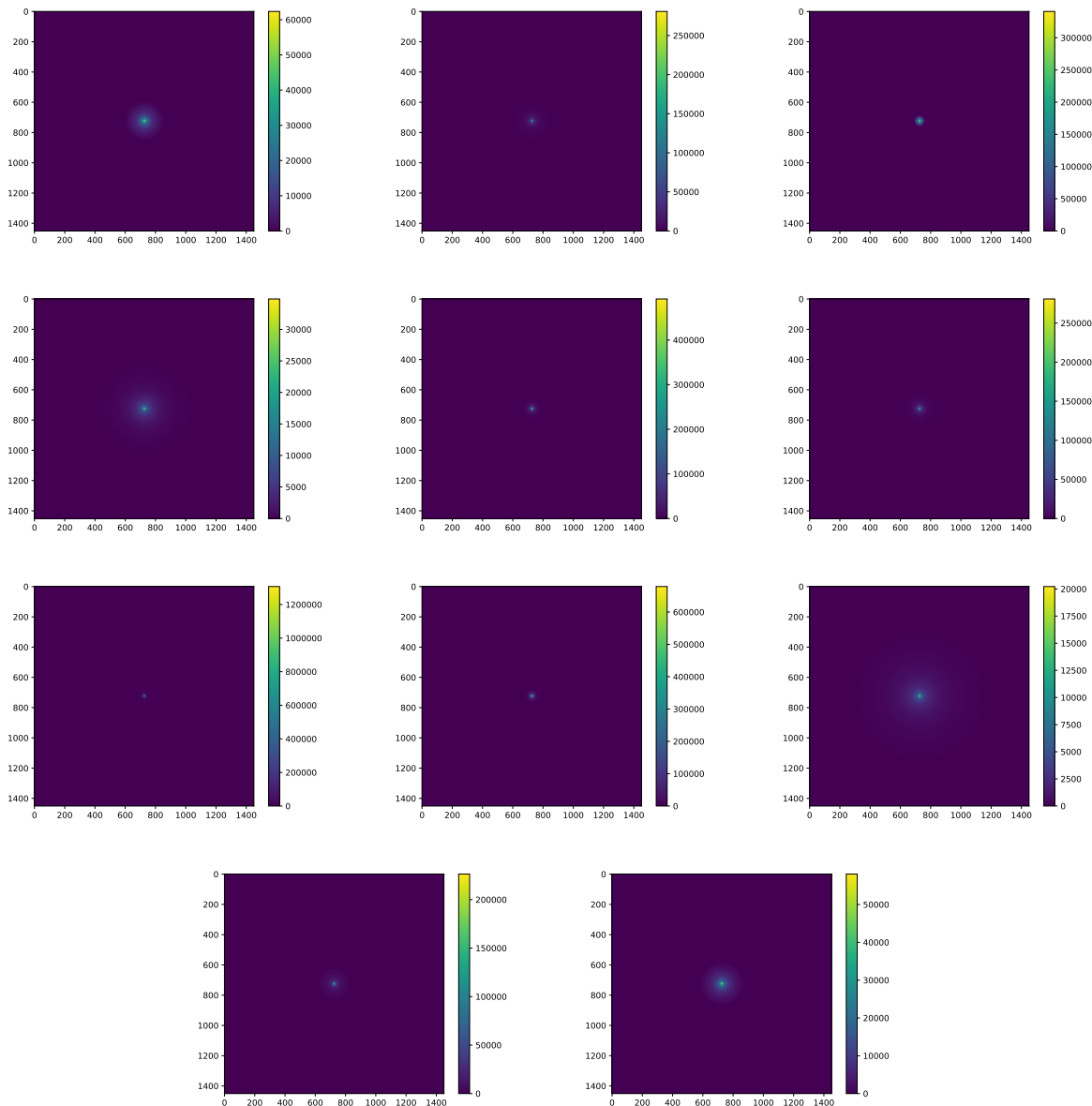


Figure A.1 Sister figure to Figure 5.3. Sources in the first row from left to right: Bootes I, Canes Venatici I, II. In second row: Draco, Hercules, Leo I. In the first row: Leo II, Leo IV, Sextans. In the final row: Ursa Major I, Ursa Major II.

APPENDIX B

1632 MULTITHREADING DARK MATTER ANALYSES SUPPLEMENTARY MATERIAL

1633 B.1 Remaining Spectral Models

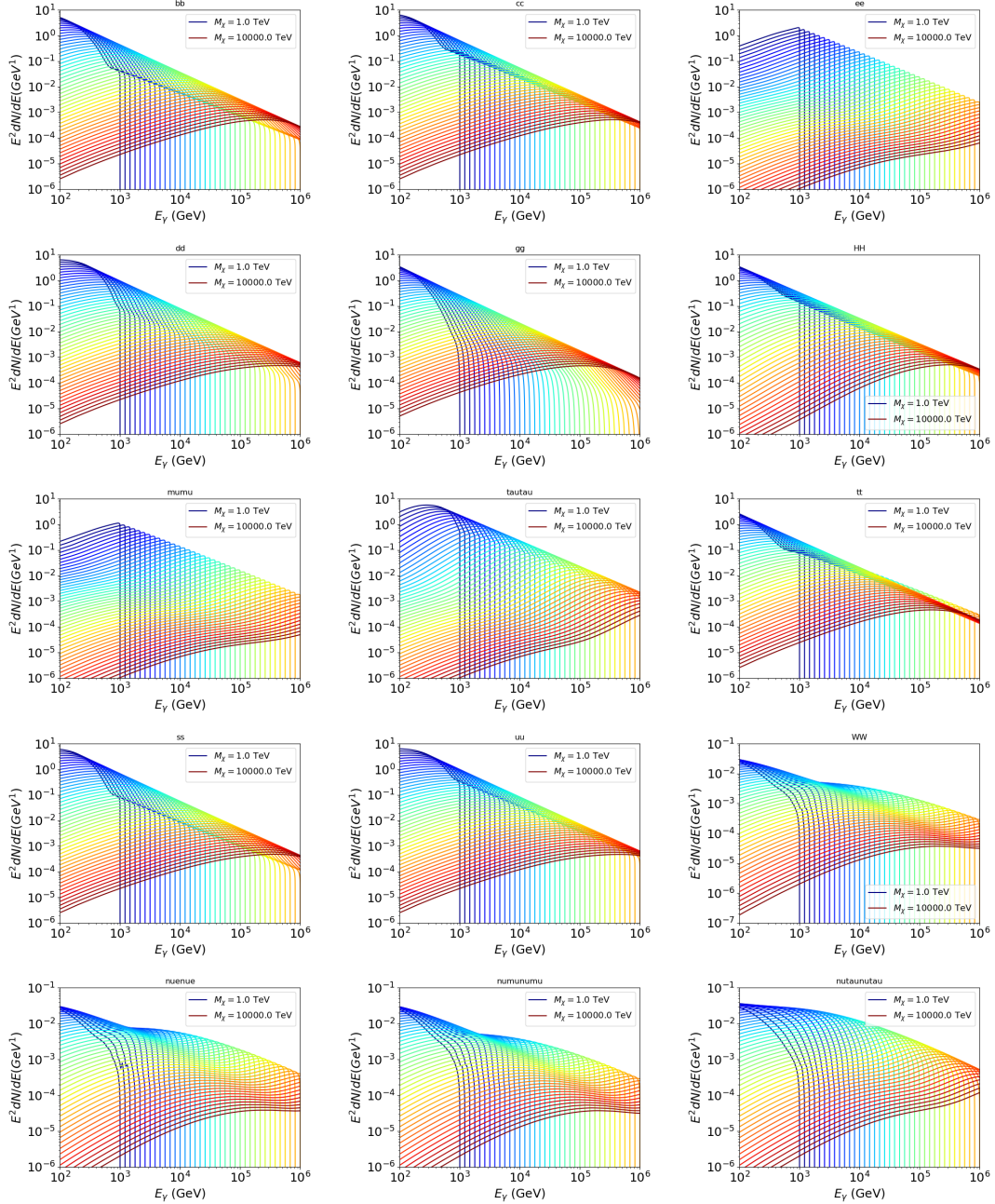


Figure B.1 Sister figure to Figure 6.2 for remaining SM primary annihilation channels studied for this thesis. These did not require any post generation smoothing and so are directly pulled from [64] with a binning scheme most helpful for a HAWC analysis.

1634 **B.2 mpu_analysis.py**

```
16351 import warnings
16362 with warnings.catch_warnings():
16373     warnings.simplefilter("ignore")
16384 # Python base libraries
16395 import os
16406 import sys
16417 import time
16428 # Import general libraries with namespace
16439 import matplotlib
16440 # Necessary for computing on cluster
16451 matplotlib.use("agg")
16462 import numpy as np
16473 import multiprocessing as mp
16484 # Import HAWC software
16495 sys.path.insert(1, os.path.join(os.environ['HOME'], 'hawc_software', 'threeML-
1650     analysis-scripts', 'fitModel'))
16516 from analysis_modules import *
16527 from threeML import *
16538 from hawc_hal import HAL, HealpixConeROI
16549 from threeML.minimizer.minimization import FitFailed
16550 # Import Dark Matter HAWC Libraries
16561 import analysis_utils as au
16572 import spectra as spec
16583 import sources as srcs
16594
16605 #* READ ONLY PATHS This block will change eventually
16616 MASS_LIST = './plotting/studies/nd/masses.txt'
16627 CHAN_LIST = './plotting/studies/nd/chans.txt'
16638
16649 #* WRITE PATHS, default location is to scratch
16650 OUT_PATH = os.path.join(os.environ["SCRATCH"], os.environ["USER"], 'New_duck')
```

```

16661 print('Our out path is going to be {}'.format(OUT_PATH))
16672
16683 # Define parallel Function. Can also be run serially
16694 def some_mass_fit(sigVs, datalist, shape, dSph, jfactor, mass_chan,
16705                 progress=None, log_file='', queue=None, i_job=0):
16716
16727     if progress is None:
16738         progress = [0]
16749     else: # Create log files for each thread
16750         log_file = log_file.replace('.log', '_ThreadNo_')
16761         log_file = log_file + str(i_job) + ".log"
16772         sys.stdout = open(log_file, "w")
16783
16794     fits = []
16805
16816     try:
16827         for m_c in mass_chan:
16838             print(f'Mass chan tuple: {m_c}')
16849             mass = int(m_c[0])
16850             ch = m_c[1]
16861             # Build path to output files
16872             outPath = os.path.join(OUT_PATH, ch, dSph)
16883             au.ut.ensure_dir(outPath)
16894
16905             if progress[i_job] < 0:
16916                 # If the master gets a Keyboard interrupt, commit suicide.
16927                     break
16938
16949                 ### Start Model Building for DM mass and SM channel #####
16950                 spectrum = spec.DM_models.HDMSpectra()
16961                 spectrum.set_channel(ch)
16972
16983                 myDwarf = ExtendedSource(dSph, spatial_shape=shape,

```

```

16994                     spectral_shape=spectrum)
17005
17016     spectrum.J = jfactor * u.GeV**2 / u.cm**5
17027     spectrum.sigmav = 1e-24 * u.cm**3 / u.s
17038     spectrum.set_dm_mass(mass * u.GeV)
17049
17050     spectrum.sigmav.bounds = (1e-30, 1e-12)
17061     model = Model(myDwarf)
17072     ##### End model Building #####
17083
17094     jl = JointLikelihood(model, datalist, verbose=False)
17105
17116     try:
17127         result, lhdf = jl.fit(compute_covariance=False)
17138         ts = -2.* (jl.minus_log_like_profile(1e-30) - jl.
1714         _current_minimum)
17159         # Also profile the LLH vs sv
17160         ll = jl.get_contours(spectrum.sigmav, sigVs[0],
17171                         sigVs[-1], len(sigVs),
17182                         progress=False, log=['False'])
17193
17204         sigv_ll = au.ut.calc_95_from_profile(ll[0], ll[2])
17215         # Write results to file
17226         outFileLL = outPath+f"/LL_{dSph}_{ch}_mass{int(mass)}_GD.txt"
17237         np.savetxt(outFileLL, (sigVs, ll[2]),
17248                         delimiter='\t', header='sigV\tLL\n')
17259
17260         with open(outPath+f"/results_{dSph}_{ch}_mass{int(mass)}_GD.
1727 txt", "w") as results_file:
17281             results_file.write("mDM [GeV]\tsigV_95\tsigV_B.F.\n")
17292
17303             results_file.write("%i\t%.5E\t%.5E\t%.5E"%(mass, sigv_ll,
17314                                         ts, result.value[0]))

```

```

17325         # End write to file
17336     except FitFailed: # Don't kill all threads if a fit fails
17347         print("Fit failed. Go back and calculate this spectral model
17348 later")
17350
17351         fits.append((ch, mass, -1, -1))
17352
17353     with open(log_file+'.fail', 'w') as f_file:
17354         f_file.write(f'{ch}, {mass}\n')
17355
17356
17357     progress[i_job] += 1
17358
17359     matplotlib.pyplot.close() # Prevent leaky memory
17360
17361
17362     fits.append((ch, mass, result.value[0], ts))
17363
17364     progress[i_job] += 1
17365
17366     matplotlib.pyplot.close()
17367
17368 except KeyboardInterrupt:
17369     progress[i_job] = -1
17370
17371
17372     fits = np.array(fits)
17373
17374     if queue is None:
17375         return fits
17376
17377     else:
17378
17379         queue.put((i_job, fits))
17380
17381
17382 def main(args):
17383
17384     masses = np.loadtxt(MASS_LIST, dtype=int)
17385
17386     chans = np.loadtxt(CHAN_LIST, delimiter=',', dtype=str)
17387
17388     mass_chan = au.ut.permute_lists(chans, masses)
17389
17390
17391     print(f"DM masses for this study are: {masses}")
17392
17393     print(f"SM Channels for this study are XX -> {chans}")
17394
17395     print(mass_chan)
17396
17397
17398     # extract information from input argument

```

```

17657 dSph = args.dSph
17668 data_mngr = au.ut.Data_Selector('P5_NN_2D')
17679 dm_profile = srcts.Spatial_DM(args.catalog, dSph, args.sigma, args.decay)
17680
17691     ### Extract Source Information ####
17702 if dm_profile.get_dec() < -22.0 or dm_profile.get_dec() > 62.0:
17713     raise ValueError("HAWC can't see this source D: Exitting now...")
17724
17735 print(f'{dSph} information')
17746 print(f'jfac: {dm_profile.get_factor()}\tRA: {dm_profile.get_ra()}\tDec: {dm_profile.get_dec()}\n')
1775
17767
17778 shape = SpatialTemplate_2D(fits_file=dm_profile.get_src_fits())
17789     ### Finish Extract Source Information ####
17790
17801     ### LOAD HAWC DATA ####
17812 roi = HealpixConeROI(data_radius=2.0, model_radius=8.0,
17823                         ra=dm_profile.get_ra(), dec=dm_profile.get_dec())
17834 bins = choose_bins.analysis_bins(args, dec=dm_profile.get_dec())
17845
17856 hawc = HAL(dSph, data_mngr.get_datmap(), data_mngr.get_detres(), roi)
17867 hawc.set_active_measurements(bin_list=bins)
17878 datalist = DataList(hawc)
17889     ### FINISH LOAD HAWC DATA ####
17890
17901 # set up SigV sampling. This sample is somewhat standardized
17912 sigVs = np.logspace(-28,-18, 1001, endpoint=True) # NOTE This will change
1792 with HDM
17933
17944 if args.n_threads == 1:
17955     # No need to start || programming just iterate over the masses
17966     kw_arg = dict(sigVs=sigVs, datalist=datalist, shape=shape, dSph=dSph,
17977                     jfactor=dm_profile.get_factor(), mass_chan=mass_chan,

```

```

17988                 log_file=args.log)
17999             some_mass_fit(**kw_arg)
18000         else:
18011             # I Really want to suppress TQMD output
18022             from tqdm import tqdm
18033             from functools import partialmethod
18044             tqdm.__init__ = partialmethod(tqdm.__init__, disable=True)
18055
18066             x = np.array_split(mass_chan, args.n_threads)
18077             n_jobs = len(x)
18088
18099             print("Thread jobs summary by mass and SM channel")
18100             for xi in x:
18111                 print(f'{xi}')
18122
18133             queue = mp.Queue()
18144             progress = mp.Array('i', np.zeros(n_jobs, dtype=int))
18155
18166             # Define task pool that will be split amongsts threads
18177             kw_args = [dict(sigVs=sigVs, datalist=datalist, shape=shape,
18188                             dSph=dSph, jfactor=dm_profile.get_factor(),
18199                             mass_chan=mass_chan, progress=progress,
18200                             queue=queue, i_job=i, log_file=args.log)
18211                 for i, mass_chan in enumerate(x)]
18222
18233             # Define each process
18244             procs = [mp.Process(target=some_mass_fit, kwargs=kw_args[i]) \
18255                 for i in range(n_jobs)]
18266
18277             ### Start MASTER Thread only code block ###
18288             # Begin running all child threads
18299             for proc in procs: proc.start()
18300

```

```

18311     try:
18312
18313         # In this case, the master does nothing except monitor progress of
18314         # the threads
18315
18316         # In an ideal world, the master thread also does some computation.
18317
18318         n_complete = np.sum(progress)
18319
18320         while_count = 0
18321
18322
18323         while n_complete < len(mass_chan):
18324
18325             if np.any(np.asarray(progress) < 0):
18326
18327                 # This was no threads are stranded when killing the script
18328
18329                 raise KeyboardInterrupt()
18330
18331             if while_count%1000 == 0:
18332
18333                 print(f"{np.sum(progress)} of {len(mass_chan)} finished")
18334
18335
18336             n_complete = np.sum(progress)
18337
18338             time.sleep(.25)
18339
18340             while_count += 1
18341
18342
18343         except KeyboardInterrupt:
18344
18345             # signal to jobs that it's time to stop
18346
18347             for i in range(n_jobs):
18348
18349                 progress[i] = -2
18350
18351             print('\nKeyboardInterrupt: terminating early.')
18352
18353             ### End MASTER Thread only code block ###
18354
18355
18356
18357             fitss = [queue.get() for proc in procs]
18358
18359             print(f'Thread statuses: {progress[:]}')
18360
18361
18362             # putting results in a file
18363
18364
18365             print("QUACK! All Done!")

```

```

18643
18654
18665 if __name__ == '__main__':
18676     import argparse
18687
18698     p = argparse.ArgumentParser(description="Run a DM annihilation analysis on
1870         a dwarf spheroidal for a specific SM channel for DM masses [1 TeV to 10
1871         PeV]")
18729
18730     # Dwarf spatial modeling arguements
18741     p.add_argument("-ds", "--dSph", type=str,
18752                     help="dwarf spheroidal galaxy to be studied", required=
1876         True)
18773     p.add_argument("-cat", "--catalog", type=str, choices=['GS15', 'LS20'],
18784                     default='LS20', help="source catalog used")
18795     p.add_argument("-sig", "--sigma", type=int, choices=[-1, 0, 1], default=0,
18806                     help="Spatial model uncertainty. 0 corresponds to the
1881 median. +/-1 correspond to the +/-1sigma uncertainty respectively.")
18827
18838     # Arguements for the energy estimators
18849     p.add_argument("-e", "--estimator", type=str,
18850                     choices=['P5_NHIT', 'P5_NN_2D'],
18861                     default="P5_NN_2D", required=False,
18872                     help="The energy estimator choice. Options are: P5_NHIT,
1888 P5_NN_2D. GP not supported (yet).")
18893     p.add_argument("--use-bins", default=None, nargs="*",
18904                     help="Bins to use for the analysis", dest="use_bins")
18915     p.add_argument('--select_bins_by_energy', default=None, nargs="*",
18926                     help="Does nothing. May fill in later once better
1893 understood")
18947     p.add_argument('--select_bins_by_fhit', default=None, nargs="*",
18958                     help="Also does nothing see above")
18969     p.add_argument( '-ex', '--exclude', default=None, nargs="*",

```

```

18970         help="Exclude Bins", dest="exclude")

18981

18992     # Computing and logging arguements.

19003     p.add_argument('-nt', '--n_threads', type=int, default=1,
19044             help='Maximum number of threads spawned by script. Default
1902      is 4')

19035     p.add_argument('-log', '--log', type=str, required=True,
19046             help='Name for log files. Especially needed for threads')

19057

19068     p.add_argument('--decay', action="store_true",
19079             help='Set spectral DM hypothesis to decay')

19080

19091     args = p.parse_args()

19102     print(args.decay)

19113     if args.exclude is None: # default exclude bins 0 and 1
19124         args.exclude = ['B0C0Ea', 'B0C0Eb', 'B0C0Ec', 'B0C0Ed', 'B0C0Ee']

19135

19146     if args.decay: OUT_PATH += '_dec'
19157     else: OUT_PATH += '_ann'

19168

19179     OUT_PATH = OUT_PATH + '_' + args.catalog
19180     if args.sigma != 0: OUT_PATH += f'_{args.sigma}sig'

19191

19202     main(args)

```

1921 B.3 Comparison with Glory Duck

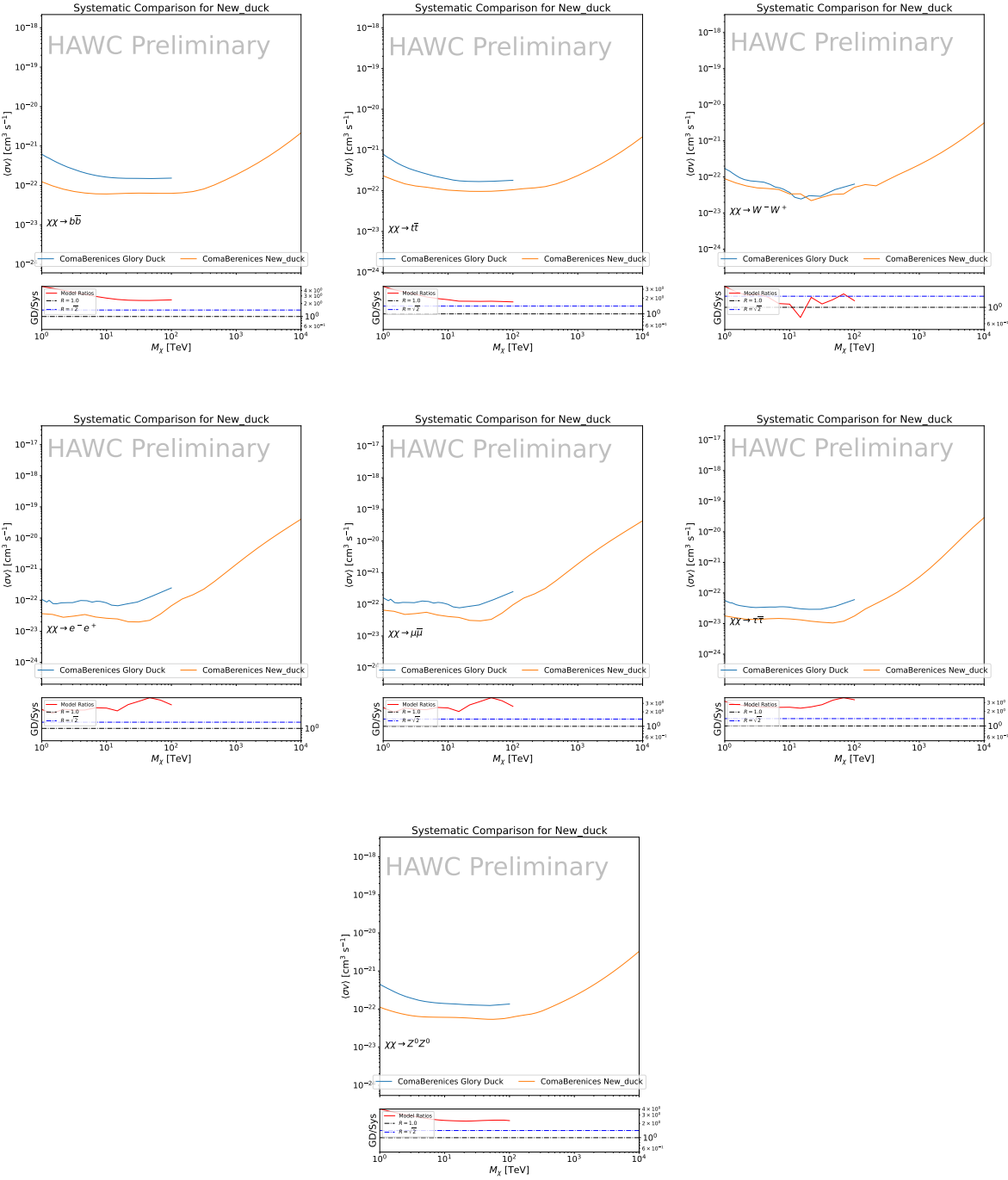


Figure B.2 TODO: fill this out

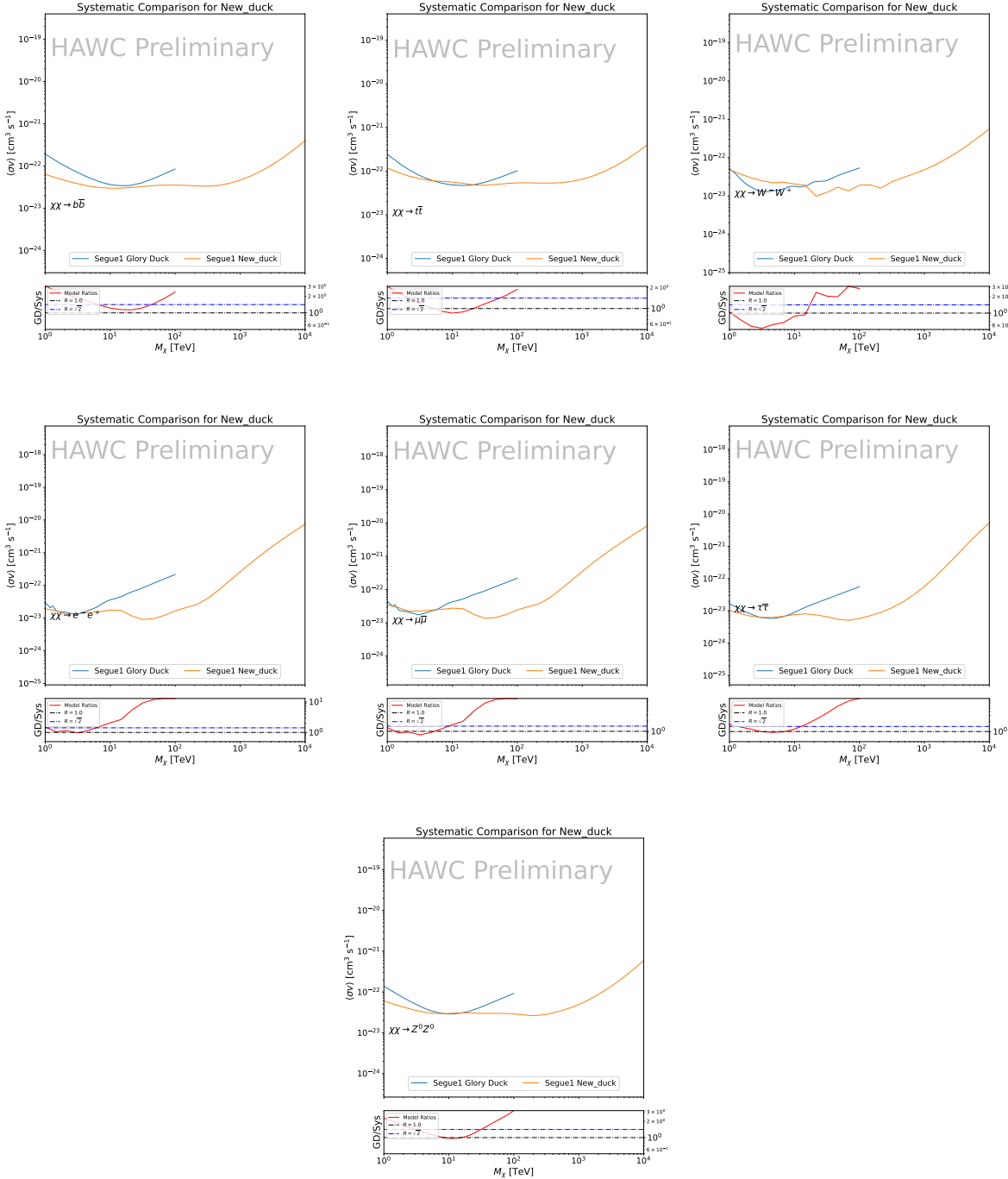


Figure B.3 TODO: fill this out

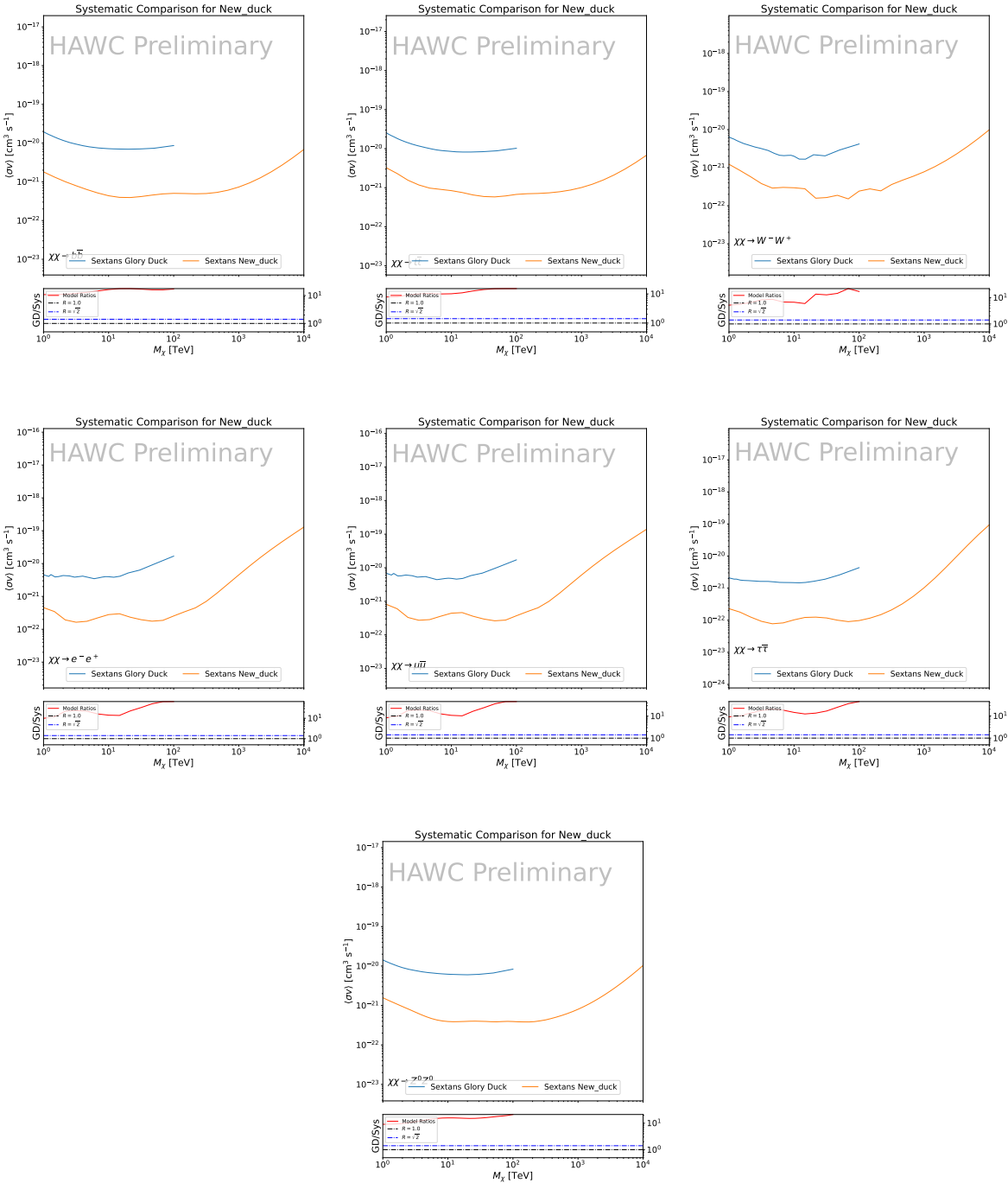


Figure B.4 TODO: fill this out

APPENDIX C

1922 ICECUBE HEAVY DARK MATTER ANALYSIS SUPPLEMENTARY MATERIAL

1923 C.1 Docker Image for Oscillating Neutrino Spectra

```
1924 1 FROM ubuntu:18.04
1925 2
1926 3 # Execute commands to install software packages
1927 4 RUN apt -y update
1928 5
1929 6     # Install utility programs
1930 7 RUN apt -y install vim wget git cmake
1931 8
1932 9 ARG DEBIAN_FRONTEND=noninteractive
1933 0
1934 1     # Install python
1935 2 RUN apt -y install python python-dev python-pip libjpeg-dev zlib1g-dev
1936 3
1937 4     # We need Python2 for installing Charon.
1938 5 RUN apt -y install python-numpy python-sympy python-matplotlib \
1939 6             python-sympy python-h5py python-astropy python-ipython
1940 7
1941 8     # Install dependencies of Charon : SQuIDS, NuSQuIDS
1942 9 RUN apt -y install libgsl-dev libgslcblas0 libgsl23 gsl-bin pkg-config
1943 0     # Install SQuIDS
1944 1 RUN mkdir /home/SQuIDS /home/SQuIDS_install
1945 2 WORKDIR /home/SQuIDS
1946 3 RUN git clone https://github.com/jsalvado/SQuIDS.git
1947 4 WORKDIR /home/SQuIDS/SQuIDS
1948 5 RUN git checkout 7ad9ba7c6ad06d1f0fa8418f937ebf1a403fef90
1949 6     # Before executing "make install" an environmental variable has to be set.
1950 7 ENV PKG_CONFIG_PATH=/home/SQuIDS/SQuIDS/lib
1951 8 RUN ./configure --prefix=../SQuIDS_install \
```

```

19529     && make
19530 RUN make install
19541
19552     # Set up an environmental variable that is required to install nuSQuIDS..
19563 ENV SQuIDS=/home/SQuIDS/SQuIDS
19574 ENV LD_LIBRARY_PATH=$SQuIDS/lib:$LD_LIBRARY_PATH
19585
19596     # Install NuSQuIDS
19607 RUN mkdir /home/nuSQuIDS
19618 WORKDIR /home/nuSQuIDS
19629 RUN git clone https://github.com/qrliu/nuSQuIDS.git
19630 WORKDIR /home/nuSQuIDS/nuSQuIDS
19641 RUN git checkout 072d8ef740e2fc7330f1fabaea94f0f4540c46f9
19652 RUN apt -y install libhdf5-dev hdf5-tools
19663 RUN apt -y install libboost1.65-all-dev
19674 RUN ./configure --with-squids=$SQuIDS --with-python-bindings --prefix=../
1968     nuSQuIDS_install \
19695     && make \
19706     && make install
19717
19728     # Set up an environmental variable for nuSQuIDS.
19739 ENV nuSQuIDS=/home/nuSQuIDS/nuSQuIDS
19740 ENV LD_LIBRARY_PATH=$nuSQuIDS/lib:$LD_LIBRARY_PATH
19751
19762     # Build the python bindings
19773 WORKDIR /home/nuSQuIDS/nuSQuIDS/resources/python/src
19784 RUN make
19795
19806     # Set up an environmental variable for the python bindings.
19817 ENV PYTHONPATH=$nuSQuIDS/resources/python/bindings/:$PYTHONPATH
19828
19839     # Install Charon in the /home/Charon/charon directory.
19840 RUN mkdir /home/Charon

```

```
19851 WORKDIR /home/Charon
19862 RUN git clone https://github.com/icecube/charon.git \
19873     && apt -y install unzip python-scipy
19884 WORKDIR charon
19895 RUN git checkout c531efe4e01dc364a60d1c83f950f04526ccd771
19906 RUN unzip ./charon/xsec/xsec.zip -d charon/xsec/ \
19917
19928 # Download neutrino spectra tables in the /home/Charon/charon/data directory
1993 .
19949 && mkdir ./charon/data
19950 WORKDIR ./charon/data
19961 RUN wget --no-check-certificate https://icecube.wisc.edu/~qliu/charon/
1997     SpectraEW.hdf5 \
19982 && wget --no-check-certificate https://icecube.wisc.edu/~qliu/charon/
1999     Spectra_PYTHIA.hdf5 \
20003 && wget --no-check-certificate https://icecube.wisc.edu/~qliu/charon/
2001     Spectra_noEW.hdf5
20024
20035 WORKDIR ../../
20046 RUN python setup.py install
20057 WORKDIR /home
```

2006 C.2 Spline Fitting Statuses

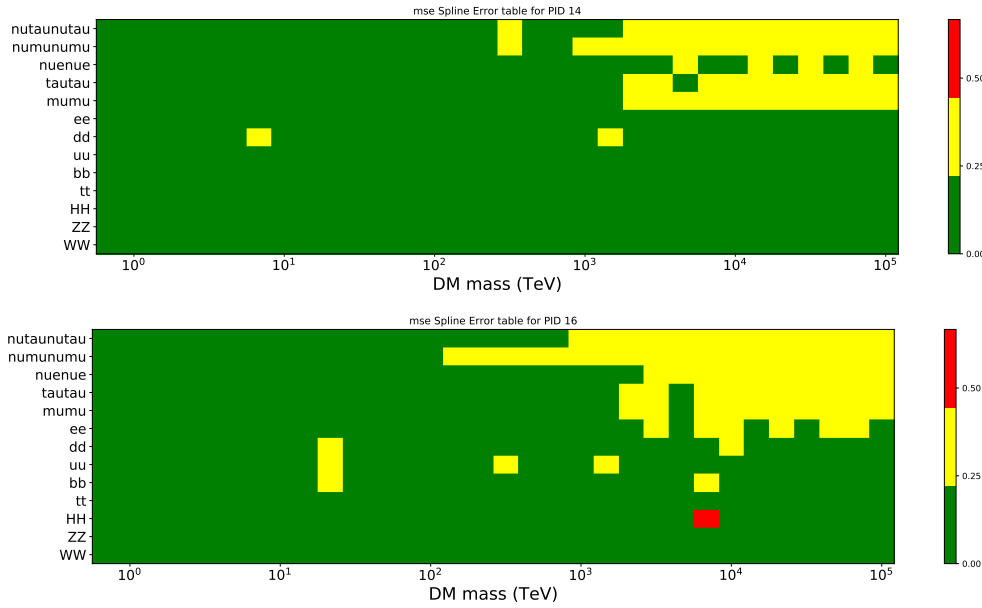


Figure C.1 TODO: fill me daddy

2007 C.3 Full Test statistic Background Simulation Per Source



Figure C.2 TODO: Fill this out eventually. I think I want all the plots generated first[NEEDS A SOURCE][FACT CHECK THIS]

2008

BIBLIOGRAPHY

- 2009 [1] Anne M. Green. “Dark matter in astrophysics/cosmology”. In: *SciPost Phys. Lect. Notes* (2022), p. 37. doi: [10.21468/SciPostPhysLectNotes.37](https://doi.org/10.21468/SciPostPhysLectNotes.37). URL: <https://scipost.org/10.21468/SciPostPhysLectNotes.37>.
- 2010 [2] Bing-Lin Young. “A survey of dark matter and related topics in cosmology”. In: *Frontiers of Physics* 12 (Oct. 2016). doi: <https://doi.org/10.1007/s11467-016-0583-4>. URL: <https://doi.org/10.1007/s11467-016-0583-4>.
- 2011 [3] Gianfranco Bertone, Dan Hooper, and Joseph Silk. “Particle dark matter: evidence, candidates and constraints”. In: *Physics Reports* 405.5 (2005), pp. 279–390. issn: 0370-1573. doi: <https://doi.org/10.1016/j.physrep.2004.08.031>. URL: <https://www.sciencedirect.com/science/article/pii/S0370157304003515>.
- 2012 [4] Gianfranco Bertone and Dan Hooper. “History of dark matter”. In: *Rev. Mod. Phys.* 90 (4 Aug. 2018), p. 045002. doi: [10.1103/RevModPhys.90.045002](https://doi.org/10.1103/RevModPhys.90.045002). URL: <https://link.aps.org/doi/10.1103/RevModPhys.90.045002>.
- 2013 [5] Fritz Zwicky. “The Redshift of Extragalactic Nebulae”. In: *Helvetica Physica Acta* 6. (1933), pp. 110–127. doi: [10.5169/seals-110267](https://doi.org/10.5169/seals-110267).
- 2014 [6] Vera C. Rubin and Jr. Ford W. Kent. “Rotation of the Andromeda Nebula from a Spectroscopic Survey of Emission Regions”. In: *ApJ* 159 (Feb. 1970), p. 379. doi: [10.1086/150317](https://doi.org/10.1086/150317).
- 2015 [7] K. G. Begeman, A. H. Broeils, and R. H. Sanders. “Extended rotation curves of spiral galaxies: dark haloes and modified dynamics”. In: *Monthly Notices of the Royal Astronomical Society* 249.3 (Apr. 1991), pp. 523–537. issn: 0035-8711. doi: [10.1093/mnras/249.3.523](https://doi.org/10.1093/mnras/249.3.523). eprint: <https://academic.oup.com/mnras/article-pdf/249/3/523/18160929/mnras249-0523.pdf>. URL: <https://doi.org/10.1093/mnras/249.3.523>.
- 2016 [8] *Different types of gravitational lenses*. website. Feb. 2004. URL: <https://esahubble.org/images/heic0404b/>.
- 2017 [9] Douglas Clowe et al. “A Direct Empirical Proof of the Existence of Dark Matter”. In: *apjl* 648.2 (Sept. 2006), pp. L109–L113. doi: [10.1086/508162](https://doi.org/10.1086/508162). arXiv: [astro-ph/0608407 \[astro-ph\]](https://arxiv.org/abs/astro-ph/0608407).
- 2018 [10] Planck Collaboration and N. et. al. Aghanim. “Planck 2018 results I. Overview and the cosmological legacy of Planck”. In: *A&A* 641 (2020). doi: [10.1051/0004-6361/201833880](https://doi.org/10.1051/0004-6361/201833880). URL: <https://doi.org/10.1051/0004-6361/201833880>.
- 2019 [11] Wayne Hu. *Matter Density Animation*. web. 2024. URL: <http://background.uchicago.edu/~whu/animbut/anim2.html>.

- 2042 [12] Wenlong Yuan et al. “A First Look at Cepheids in a Type Ia Supernova Host with JWST”. in:
2043 *The Astrophysical Journal Letters* 940.1 (Nov. 2022). doi: [10.3847/2041-8213/ac9b27](https://doi.org/10.3847/2041-8213/ac9b27).
2044 URL: <https://dx.doi.org/10.3847/2041-8213/ac9b27>.
- 2045 [13] Wendy L. Freedman. “Measurements of the Hubble Constant: Tensions in Perspective”. In:
2046 *The Astrophysical Journal* 919.1 (Sept. 2021), p. 16. doi: [10.3847/1538-4357/ac0e95](https://doi.org/10.3847/1538-4357/ac0e95).
2047 URL: <https://dx.doi.org/10.3847/1538-4357/ac0e95>.
- 2048 [14] Jodi Cooley. “Dark Matter direct detection of classical WIMPs”. In: *SciPost Phys. Lect.
2049 Notes* (2022), p. 55. doi: [10.21468/SciPostPhysLectNotes.55](https://doi.org/10.21468/SciPostPhysLectNotes.55). URL: <https://scipost.org/10.21468/SciPostPhysLectNotes.55>.
- 2050
2051 [15] “Search for new phenomena in events with an energetic jet and missing transverse momentum
2052 in pp collisions at $\sqrt{s} = 13$ TeV with the ATLAS detector”. In: *Phys. Rev. D* 103
2053 (11 July 2021), p. 112006. doi: [10.1103/PhysRevD.103.112006](https://doi.org/10.1103/PhysRevD.103.112006). URL: <https://link.aps.org/doi/10.1103/PhysRevD.103.112006>.
- 2054
2055 [16] *Jetting into the dark side: a precision search for dark matter*. website. July 2020. URL:
2056 <https://atlas.cern/updates/briefing/precision-search-dark-matter>.
- 2057 [17] Celine Armand et. al. “Combined dark matter searches towards dwarf spheroidal galaxies
2058 with Fermi-LAT, HAWC, H.E.S.S., MAGIC, and VERITAS”. in: *Proceedings of Science*.
2059 Vol. 395. Mar. 2022. doi: <https://doi.org/10.22323/1.395.0528>.
- 2060 [18] Tracy R. Slatyer. “Les Houches Lectures on Indirect Detection of Dark Matter”. In: *SciPost
2061 Phys. Lect. Notes* (2022), p. 53. doi: [10.21468/SciPostPhysLectNotes.53](https://doi.org/10.21468/SciPostPhysLectNotes.53). URL:
2062 <https://scipost.org/10.21468/SciPostPhysLectNotes.53>.
- 2063 [19] Christian W Bauer, Nicholas L. Rodd, and Bryan R. Webber. “Dark matter spectra from
2064 the electroweak to the Planck scale”. In: *Journal of High Energy Physics* 2021.1029-8479
2065 (June 2021). doi: [https://doi.org/10.1007/JHEP06\(2021\)121](https://doi.org/10.1007/JHEP06(2021)121).
- 2066 [20] Riccardo Catena and Piero Ullio. “A novel determination of the local dark matter density”.
2067 In: *Journal of Cosmology and Astroparticle Physics* 2010.08 (Aug. 2010), p. 004. doi:
2068 [10.1088/1475-7516/2010/08/004](https://doi.org/10.1088/1475-7516/2010/08/004). URL: <https://dx.doi.org/10.1088/1475-7516/2010/08/004>.
- 2069
2070 [21] B. P. Abbott et al. “Observation of Gravitational Waves from a Binary Black Hole Merger”.
2071 In: *Phys. Rev. Lett.* 116 (6 Feb. 2016), p. 061102. doi: [10.1103/PhysRevLett.116.061102](https://doi.org/10.1103/PhysRevLett.116.061102). URL: <https://link.aps.org/doi/10.1103/PhysRevLett.116.061102>.
- 2072
2073 [22] R. Abbasi et. al. “Observation of high-energy neutrinos from the Galactic plane”. In: *Science*
2074 380.6652 (June 2023), pp. 1338–1343.
- 2075 [23] NASA Goddard Space Flight Center. *Fermi’s 12-year view of the gamma-ray sky*. website.

- 2076 2022. URL: <https://svs.gsfc.nasa.gov/14090>.
- 2077 [24] Marco Cirelli et al. “PPPC 4 DM ID: a poor particle physicist cookbook for dark matter
2078 indirect detection”. In: *Journal of Cosmology and Astroparticle Physics* 2011.03 (Mar.
2079 2011), p. 051. doi: [10.1088/1475-7516/2011/03/051](https://doi.org/10.1088/1475-7516/2011/03/051). URL: <https://dx.doi.org/10.1088/1475-7516/2011/03/051>.
- 2081 [25] Javier Rico. “Gamma-Ray Dark Matter Searches in Milky Way Satellites—A Comparative
2082 Review of Data Analysis Methods and Current Results”. In: *Galaxies* 8.1 (Mar. 2020), p. 25.
2083 doi: [10.3390/galaxies8010025](https://doi.org/10.3390/galaxies8010025). arXiv: [2003.13482 \[astro-ph.HE\]](https://arxiv.org/abs/2003.13482).
- 2084 [26] W. B. Atwood et al. “The Large Area Telescope on the Fermi Gamma-Ray Space Telescope
2085 Mission”. In: *apj* 697.2 (June 2009), pp. 1071–1102. doi: [10.1088/0004-637X/697/2/1071](https://doi.org/10.1088/0004-637X/697/2/1071). arXiv: [0902.1089 \[astro-ph.IM\]](https://arxiv.org/abs/0902.1089).
- 2087 [27] M. Ackermann et al. “Searching for Dark Matter Annihilation from Milky Way Dwarf
2088 Spheroidal Galaxies with Six Years of Fermi Large Area Telescope Data”. In: *prl* 115.23,
2089 231301 (Dec. 2015), p. 231301. doi: [10.1103/PhysRevLett.115.231301](https://doi.org/10.1103/PhysRevLett.115.231301). arXiv:
2090 [1503.02641 \[astro-ph.HE\]](https://arxiv.org/abs/1503.02641).
- 2091 [28] Mattia Di Mauro, Martin Stref, and Francesca Calore. “Investigating the effect of Milky
2092 Way dwarf spheroidal galaxies extension on dark matter searches with Fermi-LAT data”.
2093 In: *Phys. Rev. D* 106 (12 Dec. 2022), p. 123032. doi: [10.1103/PhysRevD.106.123032](https://doi.org/10.1103/PhysRevD.106.123032).
2094 URL: <https://link.aps.org/doi/10.1103/PhysRevD.106.123032>.
- 2095 [29] F. et al. Aharonian. “Observations of the Crab Nebula with H.E.S.S.”. In: *Astron. Astrophys.*
2096 457 (2006), pp. 899–915. doi: [10.1051/0004-6361:20065351](https://doi.org/10.1051/0004-6361:20065351). arXiv: [astro-ph/0607333](https://arxiv.org/abs/astro-ph/0607333).
- 2098 [30] J. Albert et al. “VHE γ -Ray Observation of the Crab Nebula and its Pulsar with the MAGIC
2099 Telescope”. In: *The Astrophysical Journal* 674.2 (Feb. 2008), p. 1037. doi: [10.1086/525270](https://doi.org/10.1086/525270). URL: <https://dx.doi.org/10.1086/525270>.
- 2101 [31] N. Park. “Performance of the VERITAS experiment”. In: *Proceedings, 34th International
2102 Cosmic Ray Conference (ICRC2015): The Hague, The Netherlands, July, 30th July - 6th
2103 August*. Vol. 34. 2015, p. 771. arXiv: [1508.07070 \[astro-ph.IM\]](https://arxiv.org/abs/1508.07070).
- 2104 [32] A. Abramowski et al. “H.E.S.S. constraints on Dark Matter annihilations towards the Sculptor
2105 and Carina Dwarf Galaxies”. In: *Astropart. Phys.* 34 (2011), pp. 608–616. doi: [10.1016/j.astropartphys.2010.12.006](https://doi.org/10.1016/j.astropartphys.2010.12.006). arXiv: [1012.5602 \[astro-ph.HE\]](https://arxiv.org/abs/1012.5602).
- 2107 [33] A. Abramowski et al. “Search for dark matter annihilation signatures in H.E.S.S. observations
2108 of Dwarf Spheroidal Galaxies”. In: *Phys. Rev. D* 90 (2014), p. 112012. doi: [10.1103/PhysRevD.90.112012](https://doi.org/10.1103/PhysRevD.90.112012). arXiv: [1410.2589 \[astro-ph.HE\]](https://arxiv.org/abs/1410.2589).

- 2110 [34] H. Abdalla et al. “Searches for gamma-ray lines and ‘pure WIMP’ spectra from Dark
2111 Matter annihilations in dwarf galaxies with H.E.S.S”. in: *JCAP* 11 (2018), p. 037. doi:
2112 [10.1088/1475-7516/2018/11/037](https://doi.org/10.1088/1475-7516/2018/11/037). arXiv: [1810.00995 \[astro-ph.HE\]](https://arxiv.org/abs/1810.00995).
- 2113 [35] J. Aleksić et al. “Optimized dark matter searches in deep observations of Segue 1 with
2114 MAGIC”. in: *JCAP* 1402 (2014), p. 008. doi: [10.1088/1475-7516/2014/02/008](https://doi.org/10.1088/1475-7516/2014/02/008).
2115 arXiv: [1312.1535 \[hep-ph\]](https://arxiv.org/abs/1312.1535).
- 2116 [36] V.A. Acciari et al. “Combined searches for dark matter in dwarf spheroidal galaxies observed
2117 with the MAGIC telescopes, including new data from Coma Berenices and Draco”. In: *Physics of the Dark Universe* (2021), p. 100912. issn: 2212-6864. doi: <https://doi.org/10.1016/j.dark.2021.100912>. URL: <https://www.sciencedirect.com/science/article/pii/S2212686421001370>.
- 2121 [37] M. L. Ahnen et al. “Indirect dark matter searches in the dwarf satellite galaxy Ursa Major II
2122 with the MAGIC Telescopes”. In: *JCAP* 1803.03 (2018), p. 009. doi: [10.1088/1475-7516/2018/03/009](https://doi.org/10.1088/1475-7516/2018/03/009). arXiv: [1712.03095 \[astro-ph.HE\]](https://arxiv.org/abs/1712.03095).
- 2124 [38] S. et al. Archambault. “Dark matter constraints from a joint analysis of dwarf Spheroidal
2125 galaxy observations with VERITAS”. in: *prd* 95.8 (Apr. 2017). doi: [10.1103/PhysRevD.95.082001](https://doi.org/10.1103/PhysRevD.95.082001). arXiv: [1703.04937 \[astro-ph.HE\]](https://arxiv.org/abs/1703.04937).
- 2127 [39] Louise Oakes et al. “Combined Dark Matter searches towards dwarf spheroidal galaxies with
2128 Fermi-LAT, HAWC, HESS, MAGIC and VERITAS”. in: *Proceedings of Science*. 2019.
- 2129 [40] Celine Armand et al. on behalf of the Fermi-LAT, HAWC, HESS, MAGIC, VERITAS.
2130 “Combined Dark Matter searches towards dwarf spheroidal galaxies with Fermi-LAT,
2131 HAWC, HESS, MAGIC and VERITAS”. in: *Proceedings of Science*. 2021.
- 2132 [41] Daniel Kerszberg et al. on behalf of the Fermi-LAT, HAWC, HESS, MAGIC, and VER-
2133 TIAS collaborations. “Search for dark matter annihilation with a combined analysis of
2134 dwarf spheroidal galaxies from Fermi-LAT, HAWC, H.E.S.S., MAGIC and VERITAS”. in:
2135 *Proceedings of Science*. 2023.
- 2136 [42] A. U. Abeysekara et al. “Observation of the Crab Nebula with the HAWC Gamma-Ray
2137 Observatory”. In: *The Astrophysical Journal* 843.1 (June 2017), p. 39. doi: [10.3847/1538-4357/aa7555](https://doi.org/10.3847/1538-4357/aa7555). URL: <https://doi.org/10.3847/1538-4357/aa7555>.
- 2139 [43] Giacomo Vianello et al. *The Multi-Mission Maximum Likelihood framework (3ML)*. 2015.
2140 arXiv: [1507.08343 \[astro-ph.HE\]](https://arxiv.org/abs/1507.08343).
- 2141 [44] Marco Cirelli et al. “PPPC 4 DM ID: a poor particle physicist cookbook for dark matter
2142 indirect detection”. In: *Journal of Cosmology and Astroparticle Physics* 2011.03 (Mar.
2143 2011). issn: 1475-7516. doi: [10.1088/1475-7516/2011/03/051](https://doi.org/10.1088/1475-7516/2011/03/051). URL: <http://dx.doi.org/10.1088/1475-7516/2011/03/051>.

- 2145 [45] Alex Geringer-Sameth, Savvas M. Koushiappas, and Matthew Walker. “DWARF GALAXY
2146 ANNIHILATION AND DECAY EMISSION PROFILES FOR DARK MATTER EXPERI-
2147 MENTS”. in: *The Astrophysical Journal* 801.2 (Mar. 2015), p. 74. ISSN: 1538-4357. doi:
2148 [10.1088/0004-637X/801/2/74](https://doi.org/10.1088/0004-637X/801/2/74). URL: <http://dx.doi.org/10.1088/0004-637X/801/2/74>.
- 2150 [46] A. Albert et al. “Dark Matter Limits from Dwarf Spheroidal Galaxies with the HAWC
2151 Gamma-Ray Observatory”. In: *The Astrophysical Journal* 853.2 (Feb. 2018), p. 154. ISSN:
2152 1538-4357. doi: [10.3847/1538-4357/aaa6d8](https://doi.org/10.3847/1538-4357/aaa6d8). URL: <http://dx.doi.org/10.3847/1538-4357/aaa6d8>.
- 2154 [47] V. Bonnivard et al. “Spherical Jeans analysis for dark matter indirect detection in dwarf
2155 spheroidal galaxies - Impact of physical parameters and triaxiality”. In: *Mon. Not. Roy.
2156 Astron. Soc.* 446 (2015), pp. 3002–3021. doi: [10.1093/mnras/stu2296](https://doi.org/10.1093/mnras/stu2296). arXiv:
2157 [1407.7822 \[astro-ph.HE\]](https://arxiv.org/abs/1407.7822).
- 2158 [48] M. Ackermann et al. “Searching for Dark Matter Annihilation from Milky Way Dwarf
2159 Spheroidal Galaxies with Six Years of Fermi Large Area Telescope Data”. In: *prl* 115.23,
2160 231301 (Dec. 2015), p. 231301. doi: [10.1103/PhysRevLett.115.231301](https://doi.org/10.1103/PhysRevLett.115.231301). arXiv:
2161 [1503.02641 \[astro-ph.HE\]](https://arxiv.org/abs/1503.02641).
- 2162 [49] M. L. Ahnen et al. “Limits to Dark Matter Annihilation Cross-Section from a Combined
2163 Analysis of MAGIC and Fermi-LAT Observations of Dwarf Satellite Galaxies”. In: *JCAP*
2164 1602.02 (2016), p. 039. doi: [10.1088/1475-7516/2016/02/039](https://doi.org/10.1088/1475-7516/2016/02/039). arXiv: [1601.06590](https://arxiv.org/abs/1601.06590)
2165 [astro-ph.HE].
- 2166 [50] Javier Rico et al. *gLike: numerical maximization of heterogeneous joint
2167 likelihood functions of a common free parameter plus nuisance parameters*.
2168 <https://doi.org/10.5281/zenodo.4601451>. Version v0.09.03. Mar. 2021. doi: [10.5281/zenodo.4601451](https://doi.org/10.5281/zenodo.4601451). URL: <https://doi.org/10.5281/zenodo.4601451>.
- 2170 [51] Tjark Miener and Daniel Nieto. *LklCom: Combining likelihoods from different experiments*.
2171 <https://doi.org/10.5281/zenodo.4597500>. Version v0.5.3. Mar. 2021. doi: [10.5281/zenodo.4597500](https://doi.org/10.5281/zenodo.4597500). URL: <https://doi.org/10.5281/zenodo.4597500>.
- 2173 [52] T. Miener et al. “Open-source Analysis Tools for Multi-instrument Dark Matter Searches”.
2174 In: *arXiv e-prints*, arXiv:2112.01818 (Dec. 2021), arXiv:2112.01818. arXiv: [2112.01818](https://arxiv.org/abs/2112.01818)
2175 [astro-ph.IM].
- 2176 [53] Alex Geringer-Sameth and Matthew Koushiappas Savvas M. and Walker. “Dwarf galaxy
2177 annihilation and decay emission profiles for dark matter experiments”. In: *Astrophys.
2178 J.* 801.2 (2015), p. 74. doi: [10.1088/0004-637X/801/2/74](https://doi.org/10.1088/0004-637X/801/2/74). arXiv: [1408.0002](https://arxiv.org/abs/1408.0002)
2179 [astro-ph.CO].
- 2180 [54] Gianfranco Bertone, Dan Hooper, and Joseph Silk. “Particle dark matter: evidence, can-

- 2181 didates and constraints”. In: *Physics Reports* 405.5-6 (Jan. 2005), pp. 279–390. ISSN:
2182 0370-1573. doi: [10.1016/j.physrep.2004.08.031](https://doi.org/10.1016/j.physrep.2004.08.031). URL: <http://dx.doi.org/10.1016/j.physrep.2004.08.031>.
- 2184 [55] V. Bonnivard et al. “Dark matter annihilation and decay in dwarf spheroidal galaxies: The
2185 classical and ultrafaint dSphs”. In: *Mon. Not. Roy. Astron. Soc.* 453.1 (2015), pp. 849–867.
2186 doi: [10.1093/mnras/stv1601](https://doi.org/10.1093/mnras/stv1601). arXiv: [1504.02048 \[astro-ph.HE\]](https://arxiv.org/abs/1504.02048).
- 2187 [56] A. et al. Albert. “Searching for Dark Matter Annihilation in Recently Discovered Milky Way
2188 Satellites with Fermi-LAT”. in: *Astrophys. J.* 834.2 (2017), p. 110. doi: [10.3847/1538-4357/834/2/110](https://doi.org/10.3847/1538-4357/834/2/110). arXiv: [1611.03184 \[astro-ph.HE\]](https://arxiv.org/abs/1611.03184).
- 2190 [57] Mattia Di Mauro and Martin Wolfgang Winkler. “Multimessenger constraints on the dark
2191 matter interpretation of the Fermi-LAT Galactic Center excess”. In: *prd* 103.12, 123005
2192 (June 2021), p. 123005. doi: [10.1103/PhysRevD.103.123005](https://doi.org/10.1103/PhysRevD.103.123005). arXiv: [2101.11027 \[astro-ph.HE\]](https://arxiv.org/abs/2101.11027).
- 2194 [58] HongSheng Zhao. “Analytical models for galactic nuclei”. In: *Mon. Not. Roy. Astron. Soc.*
2195 278 (1996), pp. 488–496. doi: [10.1093/mnras/278.2.488](https://doi.org/10.1093/mnras/278.2.488). arXiv: [astro-ph/9509122 \[astro-ph\]](https://arxiv.org/abs/astro-ph/9509122).
- 2197 [59] H. C. Plummer. “On the Problem of Distribution in Globular Star Clusters: (Plate 8.)”
2198 In: *Monthly Notices of the Royal Astronomical Society* 71.5 (Mar. 1911), pp. 460–470.
2199 ISSN: 0035-8711. doi: [10.1093/mnras/71.5.460](https://doi.org/10.1093/mnras/71.5.460). eprint: <https://academic.oup.com/mnras/article-pdf/71/5/460/2937497/mnras71-0460.pdf>. URL:
2200 <https://doi.org/10.1093/mnras/71.5.460>.
- 2202 [60] Daniel R. Hunter. “Derivation of the anisotropy profile, constraints on the local velocity
2203 dispersion, and implications for direct detection”. In: *JCAP* 02 (2014), p. 023. doi:
2204 [10.1088/1475-7516/2014/02/023](https://doi.org/10.1088/1475-7516/2014/02/023). arXiv: [1311.0256 \[astro-ph.CO\]](https://arxiv.org/abs/1311.0256).
- 2205 [61] Barun Kumar Dhar and Liliya L. R. Williams. “Surface mass density of the Einasto family
2206 of dark matter haloes: are they Sersic-like?” In: *Mon. Not. Roy. Astron. Soc.* (2010). doi:
2207 [10.1111/j.1365-2966.2010.16446.x](https://doi.org/10.1111/j.1365-2966.2010.16446.x).
- 2208 [62] M. Baes and E. Van Hese. “Dynamical models with a general anisotropy profile”. In:
2209 *Astron. Astrophys.* 471 (2007), p. 419. doi: [10.1051/0004-6361:20077672](https://doi.org/10.1051/0004-6361:20077672). arXiv:
2210 [0705.4109 \[astro-ph\]](https://arxiv.org/abs/0705.4109).
- 2211 [63] Matthew G. Walker, Edward W. Olszewski, and Mario Mateo. “Bayesian analysis of re-
2212 solved stellar spectra: application to MMT/Hectochelle observations of the Draco dwarf
2213 spheroidal”. In: *mnras* 448.3 (Apr. 2015), pp. 2717–2732. doi: [10.1093/mnras/stv099](https://doi.org/10.1093/mnras/stv099).
2214 arXiv: [1503.02589 \[astro-ph.GA\]](https://arxiv.org/abs/1503.02589).
- 2215 [64] Nicholas L. Rodd et al. “Dark matter spectra from the electroweak to the Planck scale”. In:

- 2216 *J. High Energy Physics* 121.10.1007 (June 2021).
- 2217 [65] Pace, Andrew B and Strigari, Louis E. “Scaling relations for dark matter annihilation and
2218 decay profiles in dwarf spheroidal galaxies”. In: *Monthly Notices of the Royal Astronomical
2219 Society* 482.3 (Oct. 2018), pp. 3480–3496. ISSN: 0035-8711. doi: [10.1093/mnras/sty2839](https://doi.org/10.1093/mnras/sty2839).
- 2221 [66] Albert, A. et al. “Search for gamma-ray spectral lines from dark matter annihilation in
2222 dwarf galaxies with the High-Altitude Water Cherenkov observatory”. In: *Phys. Rev. D* 101 (10 May 2020), p. 103001. doi: [10.1103/PhysRevD.101.103001](https://doi.org/10.1103/PhysRevD.101.103001). URL:
2224 <https://link.aps.org/doi/10.1103/PhysRevD.101.103001>.
- 2225 [67] Victor Eijkhout and Edmund Show and Robert van de Geijn. *The Science of Computing.
2226 The Art of High Performance Computing*. Vol. 3. Open Copy published under CC-BY 4.0
2227 license, 2023, pp. 63–66.
- 2228 [68] Qinrui Liu and Jeffrey Lazar and Carlos A. Argüelles and Ali Kheirandish. “ χ aro: a tool
2229 for neutrino flux generation from WIMPs”. In: *Journal of Cosmology and Astroparticle
2230 Physics* 2020.10 (Oct. 2020), p. 043. doi: [10.1088/1475-7516/2020/10/043](https://doi.org/10.1088/1475-7516/2020/10/043). URL:
2231 <https://dx.doi.org/10.1088/1475-7516/2020/10/043>.
- 2232 [69] Aartsen, M. et al. “IceCube search for dark matter annihilation in nearby galaxies and galaxy
2233 clusters”. In: *Phys. Rev. D* 88 (12 Dec. 2013), p. 122001. doi: [10.1103/PhysRevD.88.122001](https://doi.org/10.1103/PhysRevD.88.122001). URL: <https://link.aps.org/doi/10.1103/PhysRevD.88.122001>.
- 2235 [70] Nathan Whitehorn and Jakob van Santen. *Photospline*. IceCube: GitHub.